A Combined Remote Sensing/Modelling Approach for the Retrieval of Sea ice Thickness in East Antarctica

By

Clemente Soares Hungria, BSc

Submitted in fulfilment of the requirements for the degree of
Doctor of Philosophy

Institute of Antarctic and Southern Ocean Studies (IASOS)

University of Tasmania

May, 2002

I met Master Chief Severino de Andrade for the first time on the bridge of the "Barão de Teffé" during my second trip to Antarctica in the summer of 1992/93. For his last assignment before retirement from the Brazilian Navy, he was given the post of Chief of the Boat in recognition for his long and distinguished career as a submarine pilot. This was the first (and last) time he would see ice and snow. As he put it: his "coldest journey ever."

At four o'clock on an early December morning, when we got to the entrance of Admiralty Bay on King George Island, the sun was rising on a rare and glorious day of calm seas and no winds. The ship was moving slowly, brushing aside melting icebergs that had the most beautiful colours and intricate forms. Since he and I were the only souls on the bridge at that odd time, I decided to keep to myself and enjoy the view. Foolishly, I considered myself a "specialist", a true Antarctic scientist. As such, I did not want to engage in any meaningful conversation with such a simple man. I guess I was lucky he did not feel the same way.

It did not take long for him to start chatting, commenting on the beauty of the landscape, and asking all sorts of questions about the work that researchers do in Antarctica. As my impatience grew, he simply smiled and, without taking his eyes off the wheel, said: "You know what? I finally understand why you people (by "people" I guess he meant scientists) are so interested in this place." Here we go, I thought, another pearl of military thinking for my personal dictionary of silly quotes. "Enlighten me, then." was my sarcastic reply. He said: "You guys are looking for God. I am sure He used to live here before He got tired of humanity and moved to Heaven. If you keep working with faith, you might be able to find traces of His presence."

After seven trips to Antarctica and almost ten years dedicating my time to study the Great White, I believe Sgt. Severino was right to start with. Of course, whenever we meet to revive our friendship with a chat and a drink every couple of years, I never tell him so.

But then again, I don't have to. I am sure he already knows...

Declaration

This thesis contains no material which has been accepted for a degree or diploma by the University of Tasmania or any other institution, except by way of background information that is duly acknowledged. To the best of my knowledge and belief, this thesis contains no material previously published or written by another person, except where due acknowledgement is made in the text

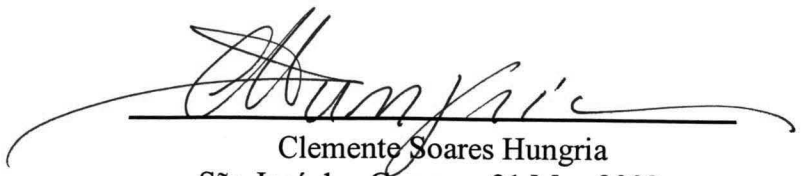

Clemente Soares Hungria
São José dos Campos, 31 May 2002.

Authority of Access

This thesis may be available for loan and limited copying in accordance with the *Copyright Act 1968*.

Clemente Soares Hungria
São José dos Campos, 31 May 2002.

Abstract

Sea ice thickness is an essential parameter for the estimation of energy, mass and momentum exchange and sea ice mass balance in the Southern Hemisphere. *In situ* methods of estimating the ice thickness distribution cannot provide the necessary areal coverage, while the coarse resolution of numerical models is unsuitable for parameterising small-scale processes. Remote sensing technology has the potential to address these issues of areal coverage and spatial resolution.

A procedure for estimating the distribution of sea ice thickness using remote sensing data from the AVHRR[1] sensor is presented. This procedure is based on the method described by *Yu and Rothrock* [1996] for Arctic sea ice and relies upon the assumptions *a)* that the surface temperature of thin sea ice is closely related to its thickness and *b)* that there is a linear vertical temperature gradient across the recently-formed sea ice. Considerable modifications have been made to the *Yu and Rothrock* method in order to apply it to Antarctic conditions.

Broadband albedo, ice/snow surface temperature and near-surface air temperature were estimated for cloud-free AVHRR pixels identified by an "expert system" algorithm. These variables were used as inputs to a thermodynamic model to estimate ice thickness for two areas of the East Antarctic sector during the austral winter of 1995 and spring of 1996. The sensitivity of the model was examined with reference to the estimation of near-surface air temperature, effective thermal conductivity of snow, bulk transfer coefficients for heat and evaporation and the calibration of the satellite sensor's gain.

Resultant ice thickness maps and frequency distribution histograms were compared with concurrent ship-based sea ice observations and digital aerial photography. Comparisons were also made with historical ("climatological") data including drill-hole measurements, ship-based observations and SSM/I[2]-derived sea ice extent data. In spite of the relative lack of concurrent data to validate the results, the analysis of the 1996 data showed good agreement with ship-based observations from previous years and with estimates of areal coverage obtained from passive microwave data. The ice thickness distribution in the Prydz Bay area for the months of October and November is also consistent with ice drift patterns, regional iceberg distribution and ocean circulation described in the literature for that area. Important by-products of the method proposed are maps of ice/snow surface physical temperature and albedo.

Comparisons with near-contemporary digital aerial photography demonstrated the procedure's ability to resolve features such as icebergs and large floes and the transition between areas of open water and/or thin ice and areas of thick, snow-covered ice. The model's response to the presence of more than one surface type within a single pixel depends on their radiometric characteristics and relative concentration. The small number of images from August 1995 precluded a more detailed analysis, but it was clear that the larger solar zenith angles that occur in winter significantly affected the result. In spite of these problems, it was possible to interpret the thickness distribution in terms of the meteorological and geophysical conditions.

---

[1] Advanced Very High Resolution Radiometer

[2] Special Sensor Microwave/Imager

Acknowledgements

The completion of this doctorate programme would not have been possible without the financial support of Brazil's National Council for the Development of Science and Technology (CNPq). I am acutely aware of the difficulties in providing such support, given the social and economic problems endured by many Brazilians. I feel honoured and fortunate for being given this opportunity. I am also grateful to IASOS and the Polar Waters sub-program of the Co-operative Research Centre for Antarctica and the Southern Ocean (Antarctic CRC) for their support during the final months of my stay in Australia.

I extend my sincerest thanks to my supervisors Dr. Kelvin Michael and Dr. Robert Massom. Their knowledge, dedication and patience have been far beyond the call of duty and I sincerely hope I have met their expectations. They have been excellent supervisors, colleagues and above all good friends, who created an association that I would be delighted to maintain.

Thanks are also due to several people within IASOS: to my friend Katrina Hill and to Dr. Glenn Hyland for their patience and support in numerous occasions, helping me with the intricacies of the world of computer programming. To Mr. Neil Adams, Mr. Vito Dirita, Dr. Simon Marsland, Dr. Phil Reid and Prof. Jörg Wolff for providing much valuable data. To Prof. Bill Budd and Dr. Ray Williams, Dr. Xingren Wu, Dr. Mike Pook, Dr. Vicky Lytle and Dr. Tony Worby for their comments and support during various stages of this project. To the masters and crew of the RSV *Aurora Australis* and the RSV *Ary Rongel* for their support during the field trips. I also received valuable comments from Dr. Peter Guest of the Naval Postgraduate School in Monterey, California and Dr. Jeff Key of the University of Wisconsin, Madison. In Brazil, I wish to thank Mr. Leandro Andrade, Mr. Richard Günther and Mr. Carlos Torres who provided much valuable support during the final stages of this project and Mrs. Helena Hungria who revised the final version of the text. These and many others have had a decisive influence in the outcomes of this thesis and for that I am grateful.

To my family. I have been and will always be deeply influenced by the examples set by several generations of *Hungrias*. Their great respect for knowledge, unrivalled dedication to both their families and professional lives and an almost unbelievable joy for living are truly compelling. One of its brightest minds, my uncle Dr. José Hungria, has recently completed his healing mission on this side of the world. In spite of the sadness of knowing that I will not be able to shake hands with him again, I am comforted by the thought that, up from where he is now, he is probably looking for a very good pair of glasses just to be able to read my thesis.

To my wife Sueli and my daughters Talita and Thais. They have been my true north and an endless source of inspiration for the past five years. They helped me put things into perspective, and patiently and lovingly shared the good and bad days that come with the writing of a thesis.

Finally - and most importantly - to my father, the silent supporter.

Table of Contents

List of Figures

List of Tables

List of Symbols

α ..... Albedo.

αF_r ..... Reflected short-wave radiation, where α is the surface albedo ($W \cdot m^{-2}$).

$\alpha_{i(TOA)}$ ..... Top of the atmosphere narrow band albedo for AVHRR channel *i*.

α_i ..... Narrow band albedo for AVHRR channel *i*.

δ ..... Optical depth (μm).

δ_p ..... Microwave volume scattering coefficient.

δT ..... Air-surface temperature difference (K).

ΔT ..... Skin effect (K). Difference between the temperature observed by traditional methods (bulk temperature) and the temperature sensed by a radiometer (skin temperature).

ε_{sfc} ..... Longwave surface emissivity.

ε_{air} ..... Effective atmospheric emissivity.

ϕ ..... Sun-satellite azimuth (radians).

λ ..... Wavelength (cm).

μ ..... Cosine of the solar zenith angle (radians).

θ ..... Sensor zenith angle (radians).

θ_0 ..... Solar zenith angle (radians).

τ ..... Transmitted portion of the shortwave radiation ($W \cdot m^{-2}$).

σ ..... Stefan-Boltzmann constant (5.6693×10^{-8} $W \cdot m^{-2} \cdot K^{-4}$).

σ_o ..... Microwave backscatter cross section.

ρ_a ..... Air density (1.295 $kg \cdot m^{-3}$).

ρ_s ..... Density of snow ($kg \cdot m^{-3}$).

ξ ..... Surface roughness parameter (cm).

c ..... Speed of light (3×10^8 $m \cdot s^{-1}$).

C_d ..... Bulk transfer coefficient for momentum (drag coefficient).

C_e ..... Bulk transfer coefficient for evaporation.

C_h ..... Bulk transfer coefficient for heat.

c_p ..... Specific heat of air (1004.4 $J \cdot kg^{-1} \cdot K^{-1}$).

e_a ..... Surface water vapour pressure (hPa).

e_{sa} ..... Saturation vapour pressure (hPa).

f ..... Relative humidity (%).

$f(\theta_0, \theta, \phi)$ ..... Broadband reflectance factor (sr^{-1}).

F_c ..... Conductive heat flux ($W \cdot m^{-2}$).

F_i ..... Integrated solar spectral irradiance, weighted by the spectral response function of AVHRR channel *i* ($W \cdot m^{-2}$).

F_L ..... Incoming long-wave radiation from atmosphere and clouds ($W \cdot m^{-2}$).

F_l ..... Latent heat flux ($W \cdot m^{-2}$).

F_r ..... Incoming solar shortwave radiation ($W \cdot m^{-2}$).

F_s ..... Sensible heat ($W \cdot m^{-2}$).

F_w ..... Oceanic turbulent heat flux ($W \cdot m^{-2}$).

G ..... Geostrophic wind.

g_i ..... Gains for AVHRR's visible channels (counts·W·m^{-2}·sr^{-1} ·μm^{-1}).

h ..... Planck's constant (6.62 x 10^{34} J).

H_C ..... Conductive heat flux (W·m^{-2}).

H_L ..... Latent heat flux (W·m^{-2}).

H_S ..... Turbulent sensible heat flux (W·m^{-2}).

I_0 ..... Flux of radiative energy across the surface and into the ice (W·m^{-2}).

k ..... Boltzmann's constant (1.38 x 10^{-23} J·K^{-1})

K^* ..... Net shortwave flux (W·m^{-2}).

k_i ..... Thermal conductivity of ice (W·m^{-1}·K^{-1}).

k_s ..... Effective thermal conductivity of snow (W·m^{-1}·K^{-1}).

L ..... Latent heat of vaporisation (2.49 x 10^6 J·kg^{-1}).

L_i ..... Calibrated narrowband radiance for the AVHRR channels 1 and 2 (W·m^{-2}·sr^{-1}·μm^{-1}).

M ..... Radiant exitance (W·m^{-2}).

o_i ..... Instrument offset for the AVHRR channels 1and 2 (counts).

P_0 ..... Surface atmospheric pressure (1013.0 hPa).

$Q_{L\uparrow}$ ..... Upward longwave radiation (W·m^{-2}).

$Q_{L\downarrow}$ ..... Downward longwave radiation (W·m^{-2}).

Q_S ..... Incoming solar shortwave radiation (W·m^{-2}).

R ..... Spectrally-integrated albedo.

$R_i(\theta_0, \theta, \phi)$ ..... Corrected narrowband reflectance.

S ..... Salinity of sea ice (psu).

S_w ..... Salinity of sea water (psu).

T_{Air} ..... Near-surface air temperature, usually measured at 2 m (K).

T_b ..... Brightness temperature (K).

T_f ..... Temperature of sea water (K).

T_i ..... Brightness temperature measured by the satellite (K). Same as T_n.

T_{Ice} ..... Ice surface physical temperature (K). Same as T_{Sfc}.

T_n ..... Brightness temperature of AVHRR channel n (n = 3, 4 and 5) (K).

T_r ..... Internal temperature of a radiometer (K).

T_{Sfc} ..... Temperature measured at the top of the snow or ice surface (K).

u ..... Wind speed at 2 m above the surface (m·s^{-1}).

u_{O_3} ..... Integrated ozone content (cm NTP).

u_{H_2O} ..... Water vapour content (g·cm^{-2}).

W_i ..... Equivalent width of the spectral response function for AVHRR channel i (μm).

Z_0 ..... Roughness length (m).

Z_{AVHRR} ..... AVHRR-derived sea ice thickness (m).

Z_i ..... Sea ice thickness (m).

Z_{Obs} ..... Weighted-average ice thickness from ship-based observations (m).

Z_s ..... Snow thickness (m).

List of Acronyms and Abbreviations

AABW ..... Antarctic Bottom Water.
ABL ..... Atmospheric Boundary Layer.
ACC ..... Antarctic Circumpolar Current.
ALOS ..... Advanced Land Observing Satellite.
AMC ..... Antarctic Meteorological Centre.
ANARE ..... Australian National Antarctic Research Expeditions.
AnSITP ..... Antarctic Sea Ice Thickness Project.
Antarctic CRC ..... Co-operative Research Centre for Antarctica and the Southern Ocean.
ASAR ..... Advanced SAR.
ASPeCt ..... Antarctic Sea Ice Processes and Climate.
ATSR ..... Along-Track Scanning Radiometer.
AVHRR ..... Advanced Very High Resolution Radiometer.
CCCO ..... Committee on Climatic Changes in the Ocean
CLIC ..... Climate and Cryosphere [Programme].
CNPq ..... National Council for the Development of Science and Technology.
CSIRO ..... Commonwealth Scientific & Industrial Research Organisation.
CZCS ..... Coastal Zone Color Scanner.
DISIMP ..... Device Independent Software for Image Processing.
DLS ..... Data Logger System.
DMSP ..... Defence Meteorological Satellite Program.
ERS ..... European Remote Sensing Satellite.
ESA ..... European Space Agency.
EWD ..... East Wind Drift
FOV ..... Field of View.
GAC ..... Global Area Coverage.
GASP ..... Global Assimilation and Prediction System.
GCM ..... General Circulation Model.
GCTP ..... General Cartographic Transformation Package.
GLOCHANT ..... [SCAR] Global Change Programme.
HLS ..... Hue, Lightness and Saturation [Colour Model].
IASOS ..... Institute of Antarctic and Southern Ocean Studies.
IBM® ..... International Business Machines Corporation.
IAnZone ..... International Antarctic Zone Programme.
IDL® ..... Interactive Data Language.
IPAB ..... International Programme for Antarctic Buoys.
IGY ..... International Geophysical Year.
ISCCP ..... International Satellite Cloud Climatology Project.
IST ..... Ice Surface Temperature.
LAC ..... Local Area Coverage.
LOWTRAN ..... Low Resolution Atmospheric Transmission [Code].

LST ..... Land Surface Temperature.
MODIS ..... Moderate-Resolution Imaging Radiometer.
NASA ..... National Aeronautics and Space Administration.
NOAA ..... National Oceanic and Atmospheric Administration.
NSIDC ..... National Snow and Ice Data Center
NTP ..... Normal Temperature and Pressure
OLS ..... Operational Line Scan.
OOSDP ..... Ocean Observing System Development Panel.
PALSAR ..... Phased Array Type L-band Synthetic Aperture Radar.
PBL ..... Planetary Boundary Layer [Model].
PCMCIA ..... Personal Computer Memory Card International Association.
PVC ..... Polyvinyl Chloride.
PWL ..... Piecewise Linear [Calibration Method].
RGPS ..... Radarsat Geophysical Processor System.
RMS ..... Root mean square [Error].
SAR ..... Synthetic Aperture Radar.
SCAR ..... Scientific Committee on Antarctic Research.
SCOR ..... Scientific Committee on Oceanic Research.
SLAR ..... Side-Looking Airborne Radar.
SMMR ..... Scanning Multichannel Microwave Radiometer.
SMOS ..... Soil Moisture and Ocean Salinity Mission
SSM/I ..... Special Sensor Microwave/Imager.
SST ..... Sea Surface Temperature.
TERSS ..... Tasmanian Earth Resources Satellite Station.
THIR ..... Temperature Humidity Infrared Radiometer
TIF ..... Tagged Image File.
TIROS ..... Television and Infra-Red Observational Satellite.
TOA ..... Top of the Atmosphere.
TOVS ..... TIROS Operational Vertical Sounder.
ULS ..... Upward Looking Sonar.
USGCRP ..... United States Global Change Research Programme.
VHS ..... Video Home System.
WCRP ..... World Climate Research Programme.
WMO ..... World Meteorological Organisation.

Introduction

Our knowledge of the sea ice cover in the Southern Ocean is relatively new. It was not until the second half of the 19th century that the concept of the *Terra Australis Incognita* was effectively verified. Although early references to the Arctic sea ice can be traced as far as the first century BC, when geographers like Strabo and Pliny the Elder refer to a *Mare Concretum* visited by Pythias of Massilia almost three hundred years earlier [*Weeks*, 1998b], the existence of a large continent below 60° S was postulated by Greek philosophers purely as a way of counterbalancing the land masses known at the time thereby, reinforcing the idea of the "sphericity of the Earth" [*Gurney*, 1998].

Several exploratory and commercial expeditions in the 18th and 19th centuries encountered and reported the outer edge of the Antarctic pack ice. However, these expeditions were restricted to spring and summer months, mainly because of limitations in navigation techniques, naval technology and the lack of accurate charts. Even as late as the 1840s, when the first landings in Antarctica occurred, there was insufficient evidence to dismiss the idea suggested by some explorers, that the land found south of 62° S comprised solely of islands surrounded by an impenetrable mass of sea ice that stretched all the way to the South Pole [*Gurney*, 1998; *Walton*, 1987].

The collection of *in situ* data in the Antarctic sea ice cover did not start until the times of the early explorers like Adrien de Gerlache in 1898 and Erich Von Drygalsky in 1902 [*Walton*, 1987]. For most of the 20th century, and even after the International Geophysical Year (IGY) and the establishment of the Antarctic Treaty in the late 1950s, Antarctic sea ice studies have relied entirely upon information gathered by ships on an occasional basis [*Walton*, 1987]. Today, the number of expeditions dedicated to the study of this region is still limited by high costs and logistical difficulties. Because of its inaccessibility, harsh conditions, large expanse and variability, Antarctic sea ice can be better studied from space [*Gurney, et al.*, 1993].

1.1 Antarctic Sea Ice and Climate

Geophysical processes occurring at high latitudes are an important component of the Earth's atmospheric and oceanic systems. Of particular concern are issues such as ozone layer depletion in the stratosphere, the enhanced greenhouse effect and climate change [*Budd*, 1991; *Thomas*, 1992]. Recent advances in the methods of collecting geophysical data over large portions of the globe (satellite remote sensing technology in particular) have provided scientists with tools capable of determining whether and how human-induced changes can modify these systems [*Budd*, 1982; *Gordon*, 1981; *Thomas*, 1992].

Sea ice is a key component of the climate system in both polar regions [*Budyko*, 1966]. In the Southern Ocean it covers, at its maximum in September, a vast area, estimated from satellite passive microwave data to be approximately 19×10^6 km^2 [*Gloersen, et al.*, 1992]. At its minimum in February, the area covered by Antarctic sea ice is about 3.5×10^6 km^2. This annual cycle represents one of the greatest seasonal geophysical changes on Earth [*Allison*, 1997]. Because of its large extent, annual variability and its unique physical properties, sea ice has a profound impact on the interactions between the ocean and atmosphere, significantly altering the transfer of mass, energy and momentum between these two media and ultimately affecting global atmospheric and oceanic circulations [*Ackley*, 1981; *Allison*, 1997; *Nicol and Allison*, 1997]. The variability in sea ice extent, concentration and thickness are key parameters determining the extent and magnitude to which the sea ice cover modifies a wide range of air-sea-ice and indeed -biota interactions. The primary impacts of sea ice on the global climatic system can be summarised as:

a) Mass Exchange.

The presence of a sea ice cover inhibits the release of water vapour from the ocean to the atmosphere [*King and Turner*, 1997]. The exchange of gases such as carbon dioxide (CO_2) and oxygen (O_2) in the Southern Ocean also displays a strong seasonal cycle that is governed by the presence of a sea ice cover [*Budd*, 1991]. The melting of sea ice in spring produces a layer of fresh water that suppresses vertical circulation and stabilises the mixed layer, thereby promoting the growth of algal blooms. The subsequent process of salt rejection due to the freezing in winter re-establishes vertical mixing [*Budd*, 1991].

b) *Ocean Circulation.*

The freezing of sea water causes the rejection of salt to the underlying ocean [*Weeks and Ackley*, 1986], increasing the density of the water mass and leading to water mass modification. In some places of the Southern Ocean, this process contributes to the formation of the Antarctic Bottom Water (AABW) which is responsible for the cooling and ventilation of most of the world's deep oceans [*Jacobs and Comiso*, 1993; *Rintoul*, 1998]. Furthermore, the vertical convective circulation generated by this process causes the transport of heat towards the surface, controlling the zonal circulation of the Southern Ocean and the subsequent redistribution of heat between the Equator and higher latitudes [*Pinet*, 1996; *Tomczak and Godfrey*, 1994].

c) *Thermal Insulation.*

The presence of a sea ice cover causes a drastic reduction in the amount of energy released by the ocean in the form of turbulent heat fluxes [*Allison, et al.*, 1982; *Andreas and Makshtas*, 1985]. *Maykut* [1986] states, for example, that maximum temperature gradients of up to 20 $K \cdot m^{-1}$ between the atmosphere and the ocean can occur in areas covered by thick sea ice. During winter, when the temperature difference between the cold polar atmosphere and the relatively warm ocean surface reaches its maximum, intense heat transfer is essentially limited to regions of open water and/or thin ice. In these regions, the flux of oceanic heat to the atmosphere can be up to two orders of magnitude greater than that through an adjacent thicker floe. Therefore, the distribution of open water and thin classes of sea ice is very important in determining the regional heat balance [*Makshtas*, 1994; *Maykut*, 1986]. The presence of a snow cover significantly compounds this insulative effect [*Massom, et al.*, in press-a; *Sturm, et al.*, 1998].

d) *Momentum Exchange.*

Generally, the presence of sea ice reduces the transfer of momentum between the atmosphere and the ocean [*Maykut*, 1986]. Sea ice itself exhibits a range of surface roughness characteristics, depending on the degree of deformation (ridging) and snow cover thickness and distribution relative to the wind direction [*Andreas and Claffey*, 1995]. Furthermore, floe bottom topography also affects ice-water drag coefficients [*Andreas, et al.*, 1993].

Budd [1982] mentions that, while the Antarctic continent is relatively stable in terms of its climate, the analysis of satellite data suggests that the sea ice cover experiences substantial changes throughout the year and on larger time scales. The detection and comprehension of such annual and interannual variability requires the collection of further ground truth information, along with the improvement of satellite technology and the use of high-resolution general circulation models (GCM).

The change in albedo (α) - defined as the ratio of reflected to incident shortwave radiation - is perhaps the most evident aspect of this annual variability. Typical values can vary from 0.21 for grease ice to 0.85 for snow-covered first-year ice during winter [*Grenfell and Maykut*, 1977; *Perovich*, 1998]. These variations ultimately determine how the sea ice interacts with short wave radiation [*Allison, et al.*, 1993; *Untersteiner*, 1986].

Large variations in sea ice coverage are not a passive phenomenon caused solely by oceanic and atmospheric conditions. Feedback mechanisms, both positive and negative, are an important part of the system, and one of the most important is a direct consequence of the abrupt changes in the sea-surface albedo during each annual freeze-up. Where a positive anomaly in sea ice extent occurs, for example, the amount of short wave radiation available for heating the surface will decrease, thereby increasing the amount of freezing and consequently favouring the expansion of the ice cover in a positive feedback [*Nicol and Allison*, 1997; *Satiamurty, et al.*, 1989; *Untersteiner*, 1986].

Many of the large-scale features and phenomena occurring in the Antarctic sea ice zone have a close relationship with atmospheric and oceanic circulation and temperatures. For example, the position of the outer edge of the ice pack is related to deflections in the Antarctic Circumpolar Current (ACC), as it encounters topographic features in the deep ocean [*Gloersen, et al.*, 1992]. On the synoptic scale, the location of the ice edge influences regional weather. Under certain circumstances, the presence of a sharp thermal boundary between the open ocean and the sea ice can give rise to violent weather patterns known as polar lows [*Gloersen, et al.*, 1992].

Recent studies suggest that the observation of trends in the Antarctic sea ice extent, thickness and volume may be employed as an early indicator of signs of global climate change due to enhanced greenhouse warming [*Key, et al.*, 1997a; *Key, et al.*, 1994; *Manabe, et al.*, 1991; *Thomas*, 1992]. Several numerical models [*Gordon and O'Farrell*, 1997; *Maykut and Untersteiner*, 1971; *Washington, et al.*, 1976] have demonstrated that the variability in sea ice extent and thickness may be key factors in amplifying the climatic effects of small changes in global heating [*Fletcher*, 1969]. Interannual variability in Antarctic sea ice has also been linked to other global phenomena such as El Niño events [*Simmonds and Jacka*, 1995] and the Antarctic Circumpolar Wave [*White and Peterson*, 1996].

The features and processes described above, and many others outside the scope of this study, are evidence of the importance of sea ice to the Southern Ocean and indeed global atmospheric/climatic system. In addition to its relevance to geophysical processes, Antarctic sea ice also provides vital habitat for whales, seals and penguins and a growth environment for phytoplankton [*Eicken*, 1992; *Nicol and Allison*, 1997]. It also limits shipping activities at high latitudes [*Gurney, et al.*, 1993].

In spite its importance, however, Antarctic sea ice remains one of the least studied components of the polar environment, and a complete understanding of its role in global atmospheric and oceanic circulation is yet to be achieved [*Massom*, 1995; *Steffen, et al.*, 1993]. This situation is caused primarily by the harshness of the polar environment which makes the collection of consistent long-term data sets difficult and expensive [*Gurney, et al.*, 1993]. Satellite technology has improved this situation considerably, although there is still a great need for further *in situ* and remote observations. The work presented in this study will exploit the unique attributes of satellite remote sensing in an effort to derive information on a key component of the Antarctic air-sea-ice interaction system - the sea ice thickness distribution.

1.2 Rationale

The importance of Antarctic sea ice in the climate system has been emphasised in a number of recent multidisciplinary research fora such as the Climate and Cryosphere (CLIC) Programme of the World Climate Research Programme (WCRP) [*Allison, et al.*, 2000] and the United States Global Change Research Program (USGCRP). In its report on the Global Change Modelling Forum [*USGCRP*, 1995], the USGCRP concluded that, in any future global warming scenario, Northern Hemisphere sea ice will probably be reduced. However, projected changes and their timing in Southern Hemisphere sea ice extent and thickness are less certain. At present, these changes are impossible to ascertain due to a lack of knowledge of the Antarctic sea ice thickness distribution [*Worby and Regester-Young*, 1999].

The Antarctic Sea ice Processes and Climate Programme (ASPeCt) is a multi-disciplinary research initiative that exists within the Scientific Committee on Antarctic Research (SCAR) Global Change Programme (GLOCHANT). It was created with the objective of improving the understanding of the role played by the Antarctic sea ice zone in the global climate system, through ASPeCt activities and through the interaction with existing sea ice research programmes such as the International Antarctic Zone Programme (IAnZone) and the Antarctic Sea Ice Thickness Project (AnSITP) [*Worby and Regester-Young*, 1999]. In order to achieve this objective, ASPeCt aims to answer a number of key scientific questions. One such question is: "*What are the broad-scale time-varying distributions of the ice and snow-cover thickness, ice composition and other physical characteristics in the Antarctic sea ice zone?*".

In a recent document, the Scientific Committee on Oceanic Research (SCOR) Ocean Observing System Development Panel (OOSDP) highlighted two major deficiencies in our current ability to monitor high-latitude oceans: *a)* the lack of any technique to determine sea ice thickness or volume on global scales, and *b)* the inability to accurately estimate thin-ice and open-water fractions [*CCCO*, 1996]. While satellite remote sensing has, over the past 30 years, revolutionised our ability to detect and monitor many important aspects of the Antarctic sea ice cover, including its extent, motion and concentration [*Massom*, 1995], sea ice thickness cannot currently be measured directly from space. The present study aims to address this issue through the combined use of satellite remotely sensed data from the National Oceanic and Atmospheric Administration (NOAA) Advanced Very High

Resolution Radiometer (AVHRR) and *in situ* data in a thermodynamic model, exploiting the relative strengths of each method.

In order to achieve this objective of combining remote sensing with *in situ* information to produce sea ice thickness data, this study aims to capitalise on the relatively large amount of data collected in the East Antarctic pack ice zone (between 75° and 150° E) by the Sea Ice sub-programme of the Antarctic CRC, on eight cruises since 1991. This dataset comprises ship-based sea ice observations, ice cores and snow pits, ice and snow thickness transects, electromagnetic induction-derived sea ice thickness data and digital aerial photography [*Lytle, et al.*, 1998b; *Worby, et al.*, 1998].

The availability of remote sensing data was also an important factor in the planning of this study. AVHRR images covering the study areas have been routinely collected at Casey Station in Antarctica and in Hobart since 1990. For periods coinciding with cruises since 1995, Synthetic Aperture Radar (SAR) images collected at McMurdo Station and the Tasmanian Earth Resources Satellite Station (TERSS) in Hobart have also been obtained from the Canadian, European, and Japanese space agencies. These data are archived at the Antarctic CRC, providing an unique opportunity to combine remote sensing and *in situ* information in an effort to better characterise the Antarctic sea ice thickness distribution.

Computer models of sea ice behaviour have become an important tool in the effort to understand the climate system. Thermodynamic sea ice models such as those of *Maykut and Untersteiner* [1971] and *Parkinson and Washington* [1979] offer the possibility of estimating the sea ice thickness distribution and temperature through the principle of conservation of energy, at a low cost and without geographical and temporal limitations. The combination of moderate-resolution remote sensing data with a thermodynamic sea ice model, as proposed in this study, represents an intermediate step between the coarse resolution of most numerical models and the limited areal coverage of the *in situ* methods. Furthermore, the digital format inherent in satellite images ensures a flexibility that allows advanced processing, such as geolocation, unsupervised classification and combination of sensors with different geometric and radiometric characteristics, i.e., synergism.

In this context, the AVHRR sensor, which provides the main body of data for this study, is a particularly useful tool. It possesses features such as a moderately good spatial resolution (1.1 km at nadir), excellent temporal and spatial coverage (across a 2750 km-wide swath), low acquisition cost and a relatively long dataset that extends back for more than two decades [*Kidwell*, 1998]. The sensor's visible and thermal infrared channels are suitable for the derivation of broadband albedo and ice/snow surface temperature via a number of well-documented algorithms. However, important problems such as cloud/ice discrimination and the resolution of sub-pixel features are still being investigated by the polar research community [*Key, et al.*, 1994; *Key, et al.*, 1997b; *Steffen*, 1995; *Steffen, et al.*, 1993]. These issues will be further discussed in Chapter 2. The current study builds upon the work of *Yu and Rothrock* [1996] in the Arctic, but with considerable modification and improvement to adapt the algorithm to Antarctic conditions.

1.3 Objectives

The primary scientific objective of this study is to obtain instantaneous "snapshots" of the sea ice thickness distribution from cloud-free regions of the Southern Ocean, through the combination of *in situ* and remote sensing data. This is addressed through the development of an unsupervised procedure for obtaining ice thickness via the incorporation of these data into a one-dimensional thermodynamic sea ice model. This procedure is tested with time series of NOAA-14 images and *in situ* data collected during the austral winter of 1995 and the spring of 1996, during field campaigns onboard the RSV *Aurora Australis*.

A secondary objective is the extended application of this algorithm, once properly tested and validated, to larger areas of the East Antarctic pack ice zone i.e. from the ice edge to the Antarctic coast, establishing the foundations for an Antarctic sea ice thickness algorithm based on remote sensing data alone.

Important by-products of this study are the large-scale maps and distributions of total albedo and surface physical temperature of the Antarctic sea-ice zone, the variability of which is intimately tied to the variability in the sea-ice thickness distribution. In themselves, these are also key parameters in the global climate system and are likely to respond to global climate change.

The ice-albedo feedback, wherein warming leads to a reduced albedo which in turn leads to further warming is, for example, a key topic in the discussion of global climate change [*Chu*, 1996; *Rind, et al.*, 1995]. Sea ice/snow surface temperature is closely linked to the near-surface air temperature and drives the longwave radiation flux. The data from the current technique will complement those from the National Snow and Ice Data Center's (NSIDC) NOAA Polar Pathfinder compilation of AVHRR data, which covers the period 1983-1996 [*Maslanik, et al.*, 1998], also forming a useful dataset with which to run and test existing coupled models.

The various energy fluxes represented in the thermodynamic sea ice model described in this study were originally identified by *Maykut and Untersteiner* [1971]. *Yu and Rothrock* [1996] employed *Maykut and Untersteiner*'s equation for the conservation of energy at the top of the ice/snow layer (Equation 8) in conjunction with AVHRR data to estimate the sea ice thickness distribution for two high-latitude areas of the Northern Hemisphere. The general principles of these two studies comprise the basis for the establishment of the objectives mentioned above.

However, given the marked differences in the sea ice characteristics between the two polar regions (discussed in Section 2.1.1), and also the nature and availability of *in situ* data to be employed in the validation process, a simple adaptation of *Yu and Rothrock*'s work to create a AVHRR-based sea ice thickness algorithm for the Southern Ocean is neither practical nor feasible. Therefore, this study aims to reconstruct the model (including its code) and improve on the principles of *Maykut and Untersteiner* and *Yu and Rothrock* studies using additional knowledge on processes and conditions within the Antarctic sea-ice zone in order to establish the foundations for an algorithm that is more in tune with Antarctic sea ice conditions, providing much needed data for the scientific community.

Because of the characteristics of the AVHRR data, its applicability to the method proposed and the availability of *in situ* data for validation, some important assumptions are made regarding factors such as the presence of a linear temperature profile in the snow/ice column and variations in snow depth and properties over different areas in the ice pack. These assumptions, and the way they can affect the results, are discussed in detail throughout Chapter 4, while the expected limitations caused by them are mentioned in Chapter 6 (Section 6.2), along with possible sources of additional *in situ* data that can be employed to minimise this problem and generalise the application of the method (Senction 6.3).

1.4 Outline

This study is divided into five sections: Chapter 2 constitutes a literature review which presents a more detailed characterisation of Antarctic sea ice. This is followed by a review of the *in situ* and remote sensing techniques (concentrating on the AVHRR sensor) currently employed to gather information on sea ice thickness, and a brief discussion on the use of numerical models for the characterisation of sea ice.

The methods employed to collect and analyse the *in situ* and remote sensing data are described in Chapter 3. This chapter also contains a description of the techniques employed to transform the AVHRR data from their original format into the products required by the experiment.

Chapter 4 details the development of a procedure to estimate sea ice thickness using AVHRR data as input into a thermodynamic sea ice model. It outlines the steps involved in the construction of this model, placing it in the context of the work of *Yu and Rothrock* [1996]. It also describes the integration of meteorological data into the system, and presents sensitivity tests and an error analysis carried out.

The results of the application of this model, in the form of image products from 1995 and 1996, are presented in Chapter 5. A data summary is followed by the characterisation of the ice thickness distributions obtained through this method, which are interpreted in the light of historical remote sensing and *in situ* data. The following section presents comparisons between the AVHRR-derived ice thickness distributions and concurrent *in situ* sea ice thickness estimates from digital aerial photography and ship-based sea ice observations. Comparisons are also made with "climatological" data constituting drill-hole measurements and ship-based observations. The chapter is concluded with a discussion of the results.

Conclusions are presented in Chapter 6, where an assessment of the results is given in terms of the objectives set out in the current chapter. A comparative analysis with *Yu and Rothrock*'s study is made, considering the improvements that were introduced and the steps that led to the establishment of an Antarctic sea ice thickness algorithm. This is followed by a description of the limitations of the method, an investigation of its operational feasibility and the identification of future improvements and further research requirements. Finally, a description of future remote sensing techniques with the potential to generate sea ice thickness products is presented along with a summary of the study.

Theory and Background

2.1 Characterisation of Antarctic Sea Ice

2.1.1 Polar Contrasts

Marked differences exist between the sea ice covers in both hemispheres as a result of geographical disparities between the two polar regions. Understanding these differences is an essential prerequisite to this study, as remote sensing and modelling techniques previously developed for the Arctic (e.g. *Yu and Rothrock* [1996] and *Key and Haefliger* [1992]) cannot be applied to the Southern Ocean without significant modification. Moreover, the accurate parameterisation of differences outlined in this section is essential to the effective modelling of the large-scale behaviour of Antarctic sea ice.

Compared to the Antarctic, the northern sea ice cover is much more strongly influenced by land along its equatorward extent. The Arctic Ocean basin is predominantly land-locked, with only a small fraction of ice advected out of the area each year, mostly via Fram Strait (between Greenland and Svalbard). While land encloses the Arctic Ocean, its effects upon sea ice formation also allow Arctic sea ice to extend well into the middle northern latitudes [*Parkinson, et al.*, 1987].

In contrast, since it is unconstrained by land to the north and subject to strong circumpolar winds, the Antarctic ice pack is largely divergent, resulting in a comparatively higher fraction of open water and thin ice, a lower fraction of multiyear ice [*Andreas and Ackley*, 1982; *Gloersen, et al.*, 1992; *Worby*, 1998] and highly variable ice drift rates [*Heil and Allison*, 1999; *Worby, et al.*, 1998]. In the Southern Ocean, large-scale patterns in the sea ice distribution are related to atmospheric and oceanic temperature and circulation patterns [*Gloersen, et al.*, 1992], whereas the influence of land is less important.

From an atmospheric perspective, mean wind speeds are highest during austral spring and autumn, when the position of the circumpolar low-pressure trough migrates closer to the Antarctic continent [*King and Turner*, 1997]. The westerly movement of low pressure systems around the Southern Ocean and the frequent occurrence of storms [*Budd*, 1987] contribute to the drift and deformation of the pack ice [*Heil and Allison*, 1999; *Worby, et al.*, 1998]. Antarctic sea ice is also constantly affected by wave-ice interaction processes around its outer margin (marginal ice zone), and by swell propagating from the Southern Ocean [*Massom, et al.*, 1999], a phenomenon that does not typically occur in the Arctic Basin. Such dynamic processes cause Antarctic sea ice floes to break up, altering the floe-size distribution and affecting the heat exchange [*Langhorne, et al.*, 1998].

Antarctic sea ice is thinner and younger than in the Arctic, its maximum thickness being largely regulated by sea-ice dynamics. In the Arctic Basin, the thickness distribution is typically characterised by two peaks: one for first-year ice at approximately 2 m, the other for multiyear ice at 3 to 5 m [*Allison and Moritz*, 1995]. Moreover, the tale in the thickness distribution can stretch beyond 20 m due to the abundance of ridges and hummocks [*Wadhams*, 1981].

In Antarctica, the modal thickness is only about 0.5 to 0.7 m, with few ridges thicker than 5 to 10 m [*Allison and Moritz*, 1995]. In areas of multiyear ice such as the western Weddell Sea, the modal thickness is still only about 1.5 m [*Lange and Eicken*, 1991]. Beyond 0.3 to 0.5 m, the dynamic, mechanical deformation processes of rafting and ridging and the so-called "pancake cycle" [*Lange, et al.*, 1989] become the dominant mechanisms by which Antarctic ice thickens [*Allison and Worby*, 1994; *Worby, et al.*, 1998]. The maximum age and thus thickness of the ice cover in Antarctica is therefore regulated by sea ice dynamics and the resultant ice cover is typically a mix of different ice thicknesses and types, with young ice comprising a significant fraction of the total [*Worby, et al.*, 1998].

Within the Antarctic pack, frazil crystals which form under turbulent conditions in open water areas [*Weeks*, 1998a] make a major contribution to the total ice mass [*Lange and Eicken*, 1991; *Worby and Massom*, 1995]. Wave-ice interaction and the pancake-ice formation cycle play important roles in ice formation in the Southern Ocean (Section 2.1.2). As sea ice in the Arctic Basin is not as mobile, fewer open water areas occur and frazil ice growth makes a smaller contribution to the total ice mass in comparison to columnar or congelation ice growth [*Gow and Tucker III.*, 1990]. Antarctic sea ice is also more saline than Arctic sea ice [*Gow and Tucker III.*, 1990] due to its more rapid growth rate [*Weeks and Ackley*, 1986]. Ice thickening due to the rafting of floes under wave action makes a smaller contribution in the Arctic, although large pressure ridges are common [*Wadhams*, 1998].

Snow cover is another important difference between Arctic and Antarctic sea ice In the Antarctic, snow is relatively thick compared to the sea ice thickness. In fact, recent studies such as *Massom et al.* [in press-a], *Sturm et al.* [1998] and *Wadhams et al.* [1987] have shown that the snow mass is sufficient to push the sea-ice surface below sea level, leading to flooding of the ice surface and the formation of snow or meteoric ice by the subsequent freezing of the resultant slush. Indeed, ice core analyses (textural and oxygen isotopic) have shown that snow-ice makes a significant yet variable contribution to the overall sea-ice mass around Antarctica [*Eicken, et al.*, 1995; *Jeffries, et al.*, 1998b; *Lange and Eicken*, 1991; *Lange, et al.*, 1990], with mean regional proportions of snow-ice, calculated from ice cores, varying from 8 to 38% [*Massom, et al.*, in press-a]. Such flooding and snow-ice formation is not common in the central Arctic, although it may occur in marginal seas such as the Bering and Greenland Seas [*Warren, et al.*, 1999]. To a lesser extent, the formation of superimposed ice, as a result of melted snow refreezing at the snow/ice interface, also contributes to a meteoric component of Antarctic sea-ice [*Jeffries, et al.*, 1998a; *Massom, et al.*, in press-a; *Worby, et al.*, 1998].

Another major difference between Arctic and Antarctic sea ice is observed during the respective melt seasons [*Andreas and Ackley*, 1982]. In the Arctic, melting occurs mainly at the surface, with the formation of melt ponds. In Antarctica, melt ponds are rarely seen on the surface [*Drinkwater and Liu*, 2000] and melting occurs mainly from the bottom and the sides of the floes [*Andreas and Ackley*, 1982; *Gloersen, et al.*, 1992; *Worby*, 1998]. The increasing fraction of open water within the ice pack allows more absorption of solar radiation and the warming of the ocean's surface layer, triggering the positive feedback mechanism responsible for large-scale melting [*Worby and Regester-Young*, 1999]. This process is also linked to the rapid increase in the rate of melting of Antarctic sea ice from November through December.

Because of the processes mentioned above, large seasonal differences exist in the areas covered by sea ice in both polar regions. Satellite passive microwave data collected since 1973 [*Gloersen, et al.*, 1992; *Parkinson, et al.*, 1987; *Zwally, et al.*, 1983] show that in the Arctic, the seasonal cycle varies, on average, from a minimum extent of 9×10^6 km^2 in September to a maximum of 16×10^6 km^2 in March. The Arctic Ocean basin retains a significant proportion of multiyear ice up to several metres thick and up to ten years old [*Parkinson and Cavalieri*, 1989; *Parkinson, et al.*, 1987]. In the Antarctic, on the other hand, the mean annual areal extent varies from 3.5×10^6 km^2 in February to 19×10^6 km^2 in September. As such, much less Antarctic sea ice survives the summer melt and the seasonal sea ice zone is significantly larger [*Gloersen, et al.*, 1992]. As the result of the differences outlined in this section and many others outside the scope of this study, the resulting sea ice cover in the Southern Ocean forms a surface that is more complex and with substantially different radiometric properties than its Arctic counterpart.

2.1.2 Sea Ice Formation, Classification and Structure

Sea water with a salinity of 35 psu freezes at approximately 271.35 K. Unlike freshwater, sea water continues to increase in density as its temperature decreases. This cold salty water tends to sink and cause convection which brings warmer waters to the surface. Therefore, a surface layer of several metres in thickness has to be cooled to the freezing point for ice to begin to form [*Nicol and Allison*, 1997; *Weeks*, 1998a]. However, in shallow areas where convection currents reach the bottom, the temperature of the entire water body must reach freezing point for the ice to start its formation. There is a general lack of information concerning the details of the freezing processes in sea water, although they do appear to be similar to those in fresh water [*Weeks*, 1998a; *Weeks and Ackley*, 1986].

The first sign of freezing is the appearance of small circular crystals that give the water an oily appearance. These crystals develop from diminutive spherical structures to discs with dimensions of 1 to 2 mm across, under the influence of wind-induced turbulence, which happens more readily in the open ocean than in calm waters. The addition of snow crystals and the further effects of wind and waves are responsible for subsequent agglomeration which can then assume various forms such as grease ice, shuga and pancake ice [*Lange, et al.*, 1989; *Nicol and Allison*, 1997; *Weeks and Ackley*, 1986].

As mentioned previously in section 2.1.1, Antarctic sea ice generally forms in turbulent open water areas by frazil ice formation and accretion [*Weeks*, 1998a]. Formation also occurs more slowly by accretion of ice to the base of existing sheets, by heat loss upwards through the ice to form columnar crystal growth. Frazil pancakes form in the more turbulent outer pack [*Lange, et al.*, 1989], where wave-ice interaction is the dominant process [*Squire*, 1998]. The pancake-ice formation cycle in the upper ocean waters appears to be an important mechanism driving the rapid advance and growth of the sea-ice edge in the austral autumn [*Lange, et al.*, 1989]. Under more quiescent conditions (e.g. in leads in the inner pack), nilas formation predominates. Around Antarctica, the conductive heat loss at the ice-water interface may be partially balanced by heat gain from the underlying ocean. As a result, sea ice thermodynamic growth (and decay) is very sensitive to vertical oceanic heat flux [*Lytle, et al.*, in press-a; *Martinson*, 1998].

Figure 1 is a conceptual model of the evolution of East Antarctic sea ice as a result of the interaction of thermodynamic and dynamic processes. The synoptic-scale alternation between divergent (**b**) and convergent (**c**) conditions is governed by changing surface winds, ocean currents and the occurrence of ocean swell which can penetrate hundreds of kilometres into the pack ice (**a**), all associated with the passage of storms [*Worby*, 1998]. Cold and dry air masses of continental origin create divergent conditions which cause the ice areal extent to expand northwards, creating regions of open water within the pack which rapidly freeze in winter. Strong katabatic winds near the Antarctic coast in a zone a few tens of kilometres in extent (**a**), cause the offshore movement of ice, contributing to the formation of coastal latent heat polynyas (Section 2.1.4).

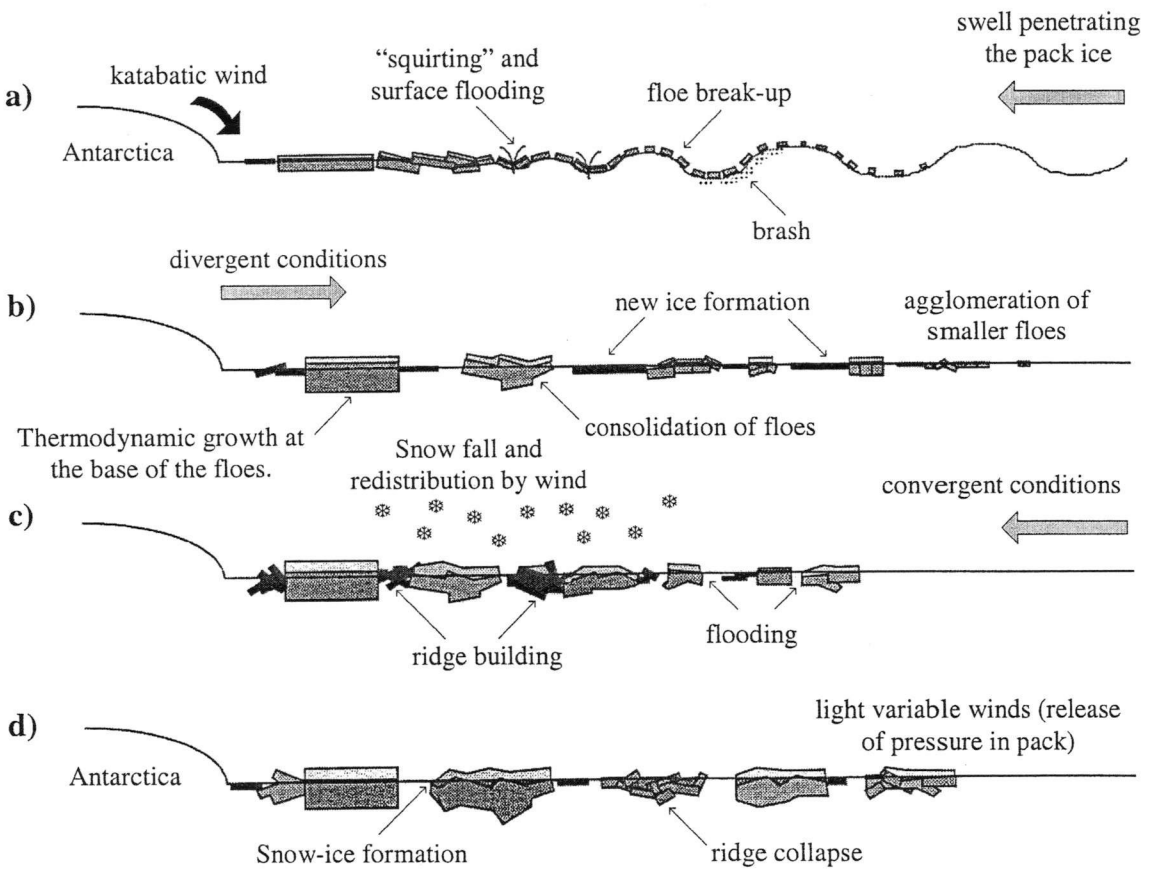

Figure 1 A conceptual model of the dynamic and thermodynamic processes observed in the East Antarctic sea ice pack. Adapted from *Worby et al.* [1998] and *Worby* [1998].

The passage of synoptic weather systems contributes to the creation of convergent conditions (**c**) whereby ice is compacted and the ice edge is pushed south, causing newly formed thin ice to raft and ridge into thicker floes [*Worby*, 1998]. In these conditions, the warm and moist air masses of oceanic origin favour widespread snowfall and slow thermodynamic growth [*Worby*, 1998; *Worby, et al.*, 1998]. In light wind conditions (**d**), the pressure within the pack ice is relieved and newly formed ridges may collapse, creating broken ice blocks with saturated snow [*Worby*, 1998]. The processes described above can occur simultaneously increasing the complexity of the East Antarctic sea ice region. The effect of such diversity is reflected in parameters such as thickness, topography, salinity and crystal structure and the identification of regional patterns and long-term trends in those properties is further complicated [*Worby, et al.*, 1998].

This study adopts the classification proposed by the World Meteorological Organisation [*WMO*, 1970] where sea ice is named according to thickness and the various phases of its development, as shown in Table 6. Although this section concentrates upon Antarctic sea ice, this classification is also valid for the Arctic. In terms of its dynamics, sea ice can be affected by convergent and divergent processes. The former causes rafting and ridging and the latter causes the development of leads and openings [*WMO*, 1970].

On the micro-scale, sea-ice crystal structure, obtained from the analysis of ice cores, is an indication of the conditions under which sea ice was formed and subsequently developed. From the analysis of ice cores, it is possible to infer the history of ice development for a given ice type. The structural inhomogeneity of Antarctic pack ice is recognised as one of the main characteristics differentiating it from Arctic sea ice [*Worby*, 1998; *Worby, et al.*, 1998].

In terms of structure, the Antarctic pack is dominated by three types of ice: frazil ice, snow-ice and columnar ice [*Buynitskiy*, 1967; *Worby*, 1998]. In a crystallographic analysis of 153 cores from the East Antarctic pack (supported by stable isotope and salinity measurements), *Worby* [1998] showed that 47.5% comprised frazil ice (turbulent growth conditions), 39% columnar ice (grown under more quiescent conditions) and 13.5% snow ice.

Due to the turbulent near-surface conditions in Antarctica, and the importance of leads and polynyas, frazil-ice formation is the dominant sea ice formation process in the Southern Ocean [*Jeffries, et al.*, 1997; *Lange and Eicken*, 1991; *Worby and Massom*, 1995; *Worby, et al.*, 1998]. Once the sea surface is completely covered by ice, columnar ice forms underneath by vertical one-dimensional growth in a process known as geometric selection [*Perey and Pounder*, 1958; *Weeks and Ackley*, 1986]. A transition layer of truncated columnar crystals between the initial layer and the columnar ice below is commonly found in Antarctic sea ice [*Worby*, 1998].

Snow-ice forms when the weight of snow cover on a floe depresses the ice surface below sea level, flooding the lower part of the snow cover. Subsequent freezing of this slush forms a solid ice layer [*Massom, et al.*, in press-a; *Nicol and Allison*, 1997; *Weeks and Ackley*, 1986; *Worby, et al.*, 1998]. In East Antarctica, *Worby et al.* [1998] estimated that snow-ice contributed a range of 12% to almost 46% of the volume of sea ice sampled as cores from four East Antarctic cruises. For comparison, fractions of 16% and 24 to 27% have been reported from the Weddell Sea [*Lange and Eicken*, 1991] and the Bellingshausen and Amundsen Seas [*Jeffries, et al.*, 1997] respectively.

Detailed information on sea ice structural properties in East Antarctica is given by *Worby et al.* [1998], *Worby and Massom* [1995], *Worby* [1998], and *Lytle et al.* [1998b], and on snow cover characteristics by *Massom et al.* [1998b] and *Massom et al.* [in press-a].

2.1.3 Main Ice Regimes

Allison and Moritz [1995] identify three spatial scales at which Antarctic sea ice can be studied. On scales up to 100 m, significant variability is observed in sea ice and snow cover thickness which can be associated with surface phenomena (such as pressure ridges). At the scale of 100 m to 100 km, the ice is fractured into floes and floe assemblages, which are separated by leads, shear zones and cracks. At the largest scale (100 km or more), significant spatial variability is observed in ice characteristics and properties.

In the Southern Ocean, thermodynamic and mechanical processes, contribute to the creation of a complex mix of different ice types with regions of open water. However, large scale regimes are discernible. For example, *Massom et al.* [1999] and *Morris et al.* [1998] described similar patterns of zonation for the Antarctic pack ice zone: the inner pack which is dominated by coastal polynyas, the central pack dominated by consolidated ice advected from the east and south and the outer pack dominated by floes and brash fractured by wave-ice interactions. In East Antarctica, sea ice at maximum extent forms a narrow and highly mobile band only a few hundred kilometres wide, making it vulnerable to the effects of wave and swell penetration and storms [*Massom, et al.*, 1999].

The outer pack, or marginal ice zone, is located north of the Antarctic Divergence at maximum sea ice extent. It is dominated by wave-ice interaction processes which play a significant role not only in ice formation but also in the break-up and reworking of existing floes [*Squire*, 1998]. The marginal ice zone also absorbs much of the incident wave/swell energy, largely protecting the inner pack to the south [*Liu and Häkkinen*, 1993]. The central zone comprises mostly first-year ice formed to the south and advected northwards. Older ice and vast fragmented fast ice floes (some as thick as 5 m) advected from the east in the East Wind Drift (EWD) are commonly found. Snow cover is substantially thicker in the central zone than in the outer pack, where wave over-washing can remove much of the snow [*Massom, et al.*, in press-b].

At places along the Antarctic coast, and particularly in protected embayments and regions containing lines of grounded icebergs, fast ice forms a very thick sea ice cover that can persist over a number of years before breaking out [*Massom, et al.*, in press-b]. Fast ice is differentiated from pack ice in that it remains stationary, or "land-fast" [*WMO*, 1970], rather than drifting in response to wind forcing, ocean currents, water drag, the Coriolis force, or internal ice stress [*Leppäranta*, 1998]. Fast ice in the Prydz Bay region, for example maintains a slow thermodynamic growth rate, from March to late September, with some bottom melting and surface ablation occurring before it typically breaks out between December and February [*Heil, et al.*, 1996]. To the south of the inner pack ice zone, leads and coastal polynyas dominate the areas adjacent to the Antarctic coast [*Massom, et al.*, in press-b].

2.1.4 Polynyas and Leads

In spite of comprising a small percentage of the total area of the pack ice, polynyas and leads are key components of the Antarctic sea ice zone, being responsible for substantial alterations in the atmosphere/ocean heat and fresh water exchange patterns [*Gordon*, 1988; *Massom, et al.*, 1998a; *Smith, et al.*, 1990]. Polynyas form regions of open water and thin ice in the lee of blocking features, such as coastal promontories and floating glacier tongues. Leads are elongated channels of open water (0.1 to 10 km scale), that last for periods of a few hours to a few days. In contrast, polynyas have a scale of tens of kilometres and tend to be recurrent and persistent features in certain locations [*WMO*, 1970].

There are two types of polynyas: those forming in the open ocean to the north and those forming along the coast of the continent. Coastal polynyas, also known as latent heat polynyas, are maintained by atmospheric forcing by both katabatic winds and synoptic-scale systems, which can generate prevailing winds with a strong easterly component adjacent to the coast, as can be seen in Figure 1 (**a**) [*Lytle, et al.*, in press-b; *Massom, et al.*, 1998a]. Significantly, coastal polynyas are thought of as "ice factories" of the Antarctic sea ice zone in which considerable amounts of ice are generated and quickly transported away from the coast, with resultant ice-production rates being up to ten times greater than in regions of consolidated sea ice.

In this case, the heat flux into the atmosphere is balanced by heat released during ice formation [*Cavalieri and Martin*, 1985; *Lytle, et al.*, in press-b; *Zwally, et al.*, 1985]. From a sea ice thickness perspective, coastal polynyas are highly important in that, over a growing season, they produce an equivalent thickness of sea ice in excess of 8 to 11 $m \cdot yr^{-1}$ per unit area [*Lytle, et al.*, in press-b], compared to less than 1 $m \cdot yr^{-1}$ within the surrounding pack [*Haas, et al.*, 1998; *Worby, et al.*, 1998].

Coastal polynyas are responsible both for the formation AABW, through the processes described previously in Section 1.1 [*Foster*, 1995; *Gordon*, 1988] and the exchange of large quantities of energy, water and gases between the ocean and atmosphere [*Worby and Ackley*, 2000]. They also play an important role in marine biological systems and in the control of biogeochemical fluxes [*Eicken*, 1992; *Massom, et al.*, 1998a]. Table 1 presents a list of key polynyas found in the regions of interest of this study.

Polynya Location	*Lat.* (°S)	*Lon.* (°E)	*Mean Area* (75%)
Davis Area			
Cape Darnley	67.6	69.1	17,853
Mackenzie Bay	68.8	71.4	3,460
Amery Ice Shelf	69.8	74.2	492
Prydz Bay	67.1	78.1	13,750
Barrier Bay	67.4	81.9	5,431
Mertz Area			
Dibble Iceberg Tongue	66.9	134.2	6,833
Mertz Glacier	66.5	145.4	23,300
Ninnis Glacier	68.2	149.1	1,883
Cape Hudson	68.3	153.1	1,063

Table 1 Locations and areal characteristics (in km^2) of coastal polynyas found in the regions of interest of this study (the definition of both regions is given in Figure 4). Mean areas are based upon a 75% ice-concentration threshold applied to monthly SSM/I images. Adapted from *Massom et al.* [1998a].

Open-ocean polynyas, also referred to as sensible heat polynyas, are maintained by the upward flux of deep and relatively warm water, balanced by the downward flux of surface cold water in convective cells with a horizontal scale of tens of kilometres. Many of these convective cells are required to maintain an open-ocean polynya. In this case, the heat flux into the atmosphere is balanced by heat transferred by vertical convection. However, we cannot yet claim to have a complete understanding of the mechanisms that control the formation and maintenance of open-ocean polynyas [*Gordon*, 1988; *Massom, et al.*, 1998a; *Pease*, 1987].

2.1.5 Sea ice Extent and Seasonal Fluctuations

In this study, Antarctic sectors referred to in the text are based upon the division suggested by *Zwally and Gloersen* [1977], namely: the Weddell Sea, the Indian Ocean, the Pacific Ocean, the Ross Sea and the Bellingshausen-Amundsen Seas. Table 2 shows the area and longitude range of each of these sectors. Although there exist some other classifications, such as the inner and outer zones proposed by *Weller* [1980], the division into five sectors presented in this section is the most common approach and will be employed in this study.

Sector	*Longitude Range* (Degrees)	*Area* (10^6 km^2)
Bellingshausen-Amundsen	60° W - 130° W	7.94
Western Pacific Ocean	90° E - 160° E	7.76
Indian Ocean	20° E - 90° E	9.00
Weddell Sea	60° W - 20° E	12.36
Ross Sea	160° E - 130° W	9.64

Table 2 Area and longitude range of the five sea ice sectors of the Southern Ocean. Adapted from *Gloersen et al.* [1992].

As stated in Sections 1.1 and 2.1.1, the Antarctic seasonal sea ice zone is subjected to large annual variations in total extent. Furthermore, interannual anomalies have been recorded in sea ice areal coverage within the individual sectors and values within sectors vary considerably from the average [*Gloersen, et al.*, 1992; *Parkinson and Gloersen*, 1993].

Around Antarctica the annual sea-ice growth-decay cycle is characterised by seven months of growth and five months of decay [*Worby, et al.*, 1998]. In February, at minimum extent, most of the ice is concentrated in the Weddell, Amundsen, Bellingshausen and eastern Ross Seas [*Gloersen, et al.*, 1992]. The equatorward advance of the ice edge starts generally in late summer, primarily in the Ross and Weddell seas. By May, the pack ice reaches as far north as 65° S. Growth continues around the continent for the next four to five months, when it reaches its maximum equatorward extent, between 55° and 65° S, depending on the sector. Ice decay starts very slowly in early spring but then proceeds rapidly from October until January, closing the annual cycle [*Parkinson and Gloersen*, 1993]. The large-scale patterns of ice growth and decay in Antarctica are discussed in more detail by *Zwally et al.* [1983].

Worby et al. [1998] presented mean monthly ice edge location maps for East Antarctica from 1991 to 1995 obtained from passive microwave data from the Special Sensor Microwave/Imager (SSM/I) sensor. These data suggest a strong seasonal cycle of ice advance and retreat and a significant degree of interannual variability. In East Antarctica for example, ice expansion begins in March and continues until September or October when the maximum extent is reached. Ice edge advance is most evident in July, reaching values of up to 450 km per month in regions near Davis Station [*Worby, et al.*, 1998].

Ice retreat begins in November and continues throughout February. In the warmer months, areas of open water that were sites of enhanced ice production in winter, contribute to the decay of the ice through the uptake of solar radiation. Therefore, ice decay occurs not only through the retreat of the ice edge southwards but also "from within", through the positive feedback mechanism in the open water areas [*Worby, et al.*, 1998].

Figure 2 shows an example of the variability found in sea ice extent of the Weddell and Bellingshausen Seas obtained from AVHRR images and ship information over a period of ten years. The most noticeable feature is an atypical increase of almost 1×10^6 km^2 in the Weddell Sea ice extent in 1980. This increase was apparently "compensated" by a decrease in the Bellingshausen Sea [*Comiso*, 1996, pers. comm.]. *Jacobs and Comiso* [1993] and *Parkinson* [1995] described a more recent decrease in the summertime ice coverage of the Bellingshausen Sea between 1989 and 1991, caused by interannual differences in surface winds and air temperature. *Bevilaqua et al.* [1994] suggested that temperature anomalies in the tropical sectors of the Atlantic and Pacific Oceans might be related to these variations in ice extent through the exchange of atmospheric mass between middle and high latitudes.

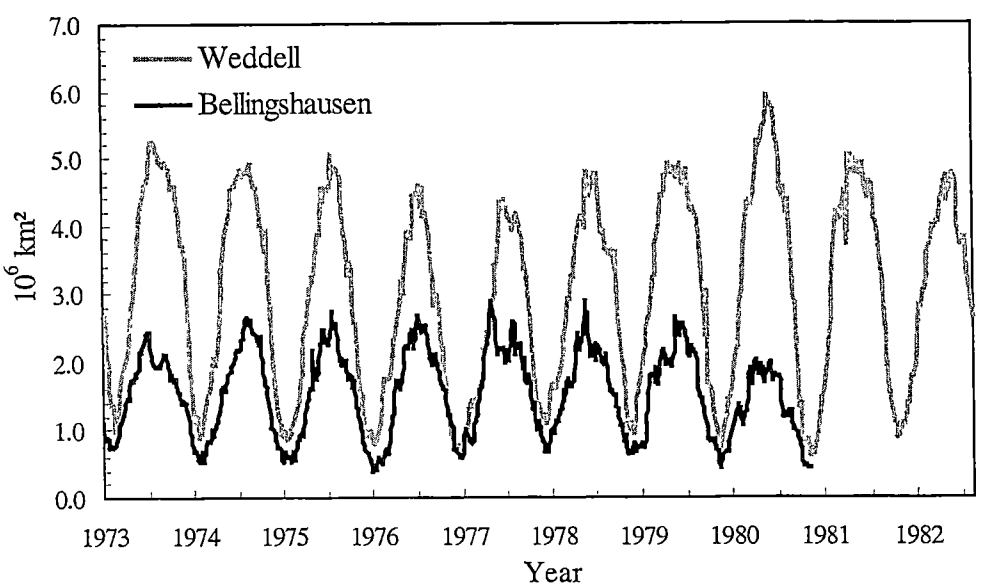

Figure 2 Variations of sea ice extent in the Bellingshausen and Weddell seas from 1973 to 1983. Adapted from *Setzer and Hungria* [1994].

2.1.6 Sea ice Drift/Motion

Knowledge of sea ice drift and the subsequent effect of floe interactions on the ice thickness distribution are essential for a complete understanding of the interactions between the sea ice cover, the atmosphere and the ocean [*Heil and Allison*, 1999]. Antarctic pack ice drift is highly variable in space and time. It is governed by a number of environmental processes such as wind velocity, roughness and drag of ice floes and ocean current [*Heil and Allison*, 1999; *Hibler and Zhang*, 1995]. It also affects the net transport of fresh water and the location of the ice edge [*Worby*, 1998].

This study concentrates on the region of Antarctic sea ice contained within East Antarctica (between 60° and 150° E), where a number of large-scale sea ice drift regimes are apparent in satellite-tracked drifting buoy data [*Allison*, 1989; *Heil and Allison*, 1999; *Worby, et al.*, 1998], iceberg data [*Tchernia and Jeannin*, 1984], and also in large-scale satellite-derived sea ice motion fields [*Emery, et al.*, 1997]. These regimes are related to the presence of the Antarctic Divergence, which is a narrow circumpolar belt separating the zone of mean eastward oceanic winds from the coastal zone of mean westward winds. *Heil and Allison* [1999] further define the Antarctic Divergence as a region of high zonal shear in the sea ice velocity distribution, dividing the predominantly eastward-flowing ACC to the north from the westward-flowing coastal current (the EWD). This east-west shear coincides with a zone of oceanic upwelling. Ekman transport results in coastal convergence in the EWD, but divergence in the ice drift field in the ACC [*Allison*, 1989].

Drifting buoys are the main source of *in situ* sea ice drift information. Analysing data from 32 buoys deployed in the East Antarctic pack between 1985 and 1996, *Worby et al.* [1998] reported highly variable daily drift rates for East Antarctica, ranging from 0.05 $m \cdot s^{-1}$ to 0.9 $m \cdot s^{-1}$ with an average of 0.22 $m \cdot s^{-1}$. *Allison* [1989] found lower values (0.13 - 0.3 $m \cdot s^{-1}$) from three buoys deployed in the Prydz Bay region and even lower values (0.06 - 0.18 $m \cdot s^{-1}$) were reported by *Massom* [1992] for the western Weddell sea, although this region is considered atypical. Through the analysis of ten years of drifting buoy data, *Heil and Allison* [1999] concluded that ice drift shows strong seasonal variability in East Antarctica. Furthermore, the authors suggested that interannual variability in maximum ice-edge position in the western Pacific sector (90° - 160° E) may be associated with interannual changes in mean ice motion south of the Antarctic Divergence.

2.1.7 Narrow-Band Albedo and Optical Properties

Surface albedo (α) can be defined as the proportion of the direct solar radiative flux reflected from the surface under clear skies [*Lindsay and Rothrock*, 1994a]. The interaction of shortwave radiation with sea ice is an important component of the ice cover heat balance [*Ebert and Curry*, 1993; *Maykut and Untersteiner*, 1971; *Thorndike, et al.*, 1992]. Important processes in the thermodynamic growth and decay of sea ice are the absorption, transmission and reflection of shortwave radiation by the ice and its snow cover. The presence of the latter has a very significant impact [*Grenfell and Maykut*, 1977; *Perovich*, 1998; *Warren*, 1982] with even a thin snow layer greatly reducing light transmission through the ice [*Perovich*, 1998].

Sea ice significantly modifies the albedo of the polar oceans, especially in Antarctica, where annual fluctuations are most evident. Ice-free ocean generally has albedos ranging from 0.06 to 0.08 [*Lamb*, 1982; *Payne*, 1972] whereas thick, snow-covered sea ice albedos average about 0.80 [*Grenfell*, 1983]. These values are influenced by several factors such as the solar incidence angle, snow grain size and geometry, impurities in the snow, surface topography and the water content of the snow [*Grenfell*, 1983; *Steffen, et al.*, 1993; *Warren and Wiscombe*, 1980; *Wiscombe and Warren*, 1980]. Other types of polar surfaces can present very diverse values such as 0.98 (fresh snow) and 0.21 (grease ice), increasing the complexity of the system [*Grenfell and Maykut*, 1977; *Vowinkel and Orvig*, 1970]. An important factor which is exploited in this study is that albedo is sensitive to ice thickness during the initial stages of sea ice growth [*Perovich*, 1998], as can be seen in Table 3.

Several studies have presented values of albedo related to ice type collected *in situ* or by means of remote sensing [*Allison, et al.*, 1993; *De Abreu, et al.*, 1994; *Grenfell and Maykut*, 1977; *Perovich*, 1996; *Perovich, et al.*, 1986; *Schweiger, et al.*, 1993; *Stroeve, et al.*, 1997]. The values in Table 3 generally agree with those studies, and discrepancies can be attributed to factors such as the presence or absence of clouds, snow cover, solar zenith angle, regional differences etc. [*Grenfell*, 1983; *Koepke*, 1989; *Warren and Wiscombe*, 1980; *Wiscombe and Warren*, 1980].

Ice Type (Thickness)	*Snow Cover (m)*		
	Snow-free	< 0.03	> 0.03
Open water	0.07	-	-
Grease	0.09	-	-
Nilas (<0.1 m)	0.16*	0.42	-
Young Grey Ice (0.1 - 0.15 m)	0.25	(0.52)	(0.70)
Grey-White Ice (0.15 - 0.3 m)	(0.35)	(0.62)	(0.74)
First-Year Ice (0.3 - 0.7 m)	(0.42)	(0.72)	0.77
First-Year Ice (>0.7 m)	0.49	0.81	0.85

Table 3 Broadband solar albedos for cold Antarctic sea-ice types. Values in parentheses are interpolated or extrapolated, not measured. (*) Nilas albedo varies with ice thickness from 0.07 to 0.25; 0.16 is the middle of the range. Adapted from *Allison et al.* [1993] and *Massom et al.* [in press-a].

The wavelength-integrated, or total, albedo is an important quantity in sea-ice thermodynamic modelling, in that it is a measure of the total solar energy absorbed by the ice and underlying ocean [*Maykut and Perovich*, 1987; *Maykut and Untersteiner*, 1971]. Because ice-covered surfaces have such high albedos compared to ice-free areas, the presence of a sea ice cover considerably reduces the amount of radiation absorbed at the Earth's surface [*Gloersen, et al.*, 1992].

Performing sensitivity tests in a one-dimensional thermodynamic sea ice model, *Ebert and Curry* [1993] found that the equilibrium ice thickness changed by 0.6 m for only a 2% change in the net solar flux at the surface. This change could be provided by just a 0.01 change in the mean albedo if the mean albedo is 0.50. As shown by *Grenfell and Maykut* [1977], changing cloud conditions can significantly impact the incident spectral irradiance, and thus the total albedo. In this study, clear-sky conditions are assumed as clouds have been masked (Section 3.1.1).

An overview of the optical properties of sea ice, and sea ice radiative transfer models, is given by *Perovich* [1998]. As defined in that study, the term "optical" refers to the wavelength range of ~250-2500 nm in the electromagnetic spectrum, with the solar portion also being referred to as shortwave radiation. The interaction of shortwave radiation with sea ice and its snow cover is an important component of the ice cover heat balance [*Maykut and Perovich*, 1987; *Maykut and Untersteiner*, 1971; *Thorndike, et al.*, 1992].

Light transmission through the snow/ice is characterised by the transmittance, or properties of incident irradiance transmitted through the snow and ice slab [*Perovich*, 1998]. Light attenuation is typically represented by an irradiance extinction coefficient, which is a measure of loss due to scattering and absorption as light penetrates the snow/ice slab [*Grenfell and Maykut*, 1977]. Importantly from a modelling perspective, the extinction coefficient of snow is significantly higher than that of sea ice [*Thomas*, 1963; *Weller and Schwerdtfeger*, 1967]. Thermodynamic models typically include treatment of the reflection, transmission and absorption of shortwave radiation in a parameterised fashion. For example, *Maykut and Untersteiner* [1971] used total extinction coefficients in their sea-ice thermodynamic model to determine the surface heat balance and the degree of solar heating of the ice mass, which is the same approach employed in this study.

2.1.8 Snow Cover Characteristics

As it ages, sea ice accumulates an insulative snow cover which is itself highly variable in thickness and properties. The snow cover greatly amplifies the effects of sea ice in the atmospheric/oceanic system. The constant presence of strong winds redistribute the snow, and its properties constantly evolve as a result of a range of metamorphism processes [*Massom, et al.*, in press-a; *Sturm, et al.*, 1998]. However, while the importance of ice extent and ice thickness distribution is well established, the role of snow has received less attention [*Eicken, et al.*, 1995].

Snow cover has a number of important effects on the ice thickness distribution, both indirect and direct [*Massom, et al.*, in press-a]. It can reduce sea ice growth by thermally insulating the ice surface. On the other hand, it can act to increase ice growth, or at least protect it from melt in the spring/summer period, by forming a high-albedo surface which reduces the penetration of solar radiation into the ice mass. It also makes a direct contribution to Antarctic sea ice formation through flooding of the ice surface and subsequent snow-ice formation [*Lange, et al.*, 1989], as described in Section 2.1.2. The presence of a snow cover significantly increases the albedo compared to snow-free ice [*Allison, et al.*, 1993; *Wendler, et al.*, 2000]. Snow-covered ice absorbs 10 to 30% of the incoming solar radiation, compared to 40 to 80% for snow-free ice [*Grenfell and Maykut*, 1977; *Maykut*, 1986].

Due to its low thermal conductivity (about one order of magnitude lower than that of sea ice), the presence of a snow cover reduces conductive heat losses and the rate at which ice thickens by thermodynamic means [*Eicken, et al.*, 1995; *Massom, et al.*, in press-a; *Maykut and Untersteiner*, 1971; *Sturm, et al.*, 1998]. By smoothing the ice surface, the presence of a snow cover modifies the ice-air drag coefficient [*Andreas, et al.*, 1993]. Snow also affects the electro-magnetic signature of sea ice, complicating the retrieval of geophysical properties by both passive and active satellite remote sensing systems [*Comiso*, 1983; *Drinkwater, et al.*, 1995]. These effects are even more amplified if the snow is wet with either fresh or saline water [*Hallikainen and Winebrenner*, 1992; *Morris, et al.*, 1998].

The current state of our knowledge of the snow cover on Antarctic sea ice is reviewed by *Massom et al.* [in press-a] with emphasis on its implications for physical and biological modelling and remote sensing studies. Important recent findings include: the circumpolar importance of snow-ice formation, the occurrence of periodic large melt events even in winter and a more recent parameterisation of the effective thermal conductivity of snow (k_s) , with a lower value than those typically employed in sea ice models [*Massom, et al.*, in press-a]. Chapter 4 presents a more detailed discussion on the use of this new parameterisation of k_s in a one-dimensional thermodynamic model.

2.1.9 Sea ice Thickness

The most important sea ice variables in global climate and regional ocean-atmosphere interaction contexts are drift, concentration and thickness. The spatial and temporal distribution of Antarctic sea ice thickness is a key yet poorly understood component of the regional heat and mass balance of the Southern Ocean [*Allison*, 1997; *Budd*, 1991; *Nicol and Allison*, 1997; *Worby, et al.*, 1996a; *Worby, et al.*, 1998]. The degree to which the sea ice cover modifies ocean-atmosphere interaction is largely determined by the thickness and concentration of the ice, which in turn are determined by atmospheric and oceanic interaction. As such, the thickness distribution is an important descriptor of the heat and mass balance of the Southern Ocean [*Thorndike, et al.*, 1992].

With ice velocity, sea ice thickness defines the mass flux of sea ice, which is a major component of the exchange of freshwater and energy between polar and sub-polar seas [*Wadhams and Comiso*, 1992]. On its own, it affects the exchange of heat and moisture between the ocean and the atmosphere. Sea ice thickness is also a measure of the degree of deformation of the ice field [*Wadhams and Comiso*, 1992]. Improved parameterisations of the sea ice thickness distribution are an essential requirement to derive forcing and validation information for coupled climate models [*Wu, et al.*, in press; *Wu, et al.*, 1997] and to determine factors controlling the ecology of biota in the Southern Ocean [*Eicken*, 1992].

Allison and Moritz [1995] stress that knowledge of the ice thickness distribution within a given area is essential to accurately determine a number of key parameters. These include the total sea ice mass, the salt/freshwater balance of the upper ocean, the effective mechanical response and strength of the ice cover, the top and bottom surface roughness, the total surface albedo, and the penetration of light into the ice and its relation to biological productivity.

Sea ice thickness distribution interacts with a number of relevant processes in the Southern Ocean. For example, the distribution of thin sea ice classes and open water areas is a key variable in this system, as such regions are sites of high rates of ice formation and concomitant brine rejection and are responsible for the exchange of most of the turbulent heat within the ice pack, thus controlling ocean-atmosphere heat exchange [*Allison*, 1997; *Maykut*, 1982; *Worby, et al.*, 1998]. As a result, the sea ice growth rate is particularly rapid in such areas (in winter), as is the resulting brine rejection rate and the flux of salt into the underlying ocean [*Smith, et al.*, 1990]. Although the energy exchange by radiation and turbulent transfer is dominated by areas of open water and thin, snow-free ice, most of the ice mass is contained in thick floes and ridges [*Worby, et al.*, 1998]. The total mass of the ice is the parameter that controls the salt input to the ocean [*Nicol and Allison*, 1997].

That ice is present in a variety of thicknesses is of critical importance to key high-latitude air-sea interaction processes. The key role of a consolidated ice cover as an effective insulating and highly-reflective blanket separating relatively warm ocean from cold atmosphere was stressed in Chapter 1. Conversely, intense upward turbulent heat exchange (loss) occurs through regions of thin ice and open water in the form of leads and polynyas [*Maykut*, 1978; 1982].

As a result, the sea-ice growth rate is particularly rapid in such areas, as is the resulting brine rejection rate and the flux of salt into the underlying ocean [*Smith, et al.*, 1990]. Moreover, the distribution of sea-ice thickness strongly affects the surface area-averaged albedo, which affects the input of solar energy to the upper ocean [*Grenfell*, 1983] and the oceanic heat flux at the underside of ice [*Maykut and Perovich*, 1987]. As a result of the above processes, relatively small areas of open water, nilas and young ice could dominate the regional mass and heat balance of the ice pack [*Maykut*, 1982].

Other important processes that can be linked to sea ice thickness distribution are the surface long and short wave radiation budget and the effects of UV penetration [*Nunez, et al.*, 1997; *Smolskaia, et al.*, 1999] and mass and momentum exchange [*Ackley*, 1979; *Andreas*, 1987; *Andreas and Claffey*, 1995]. In terms of marine ecology, sea-ice thickness distribution also has a first-order effect. Regions of thin ice and open water provide marine mammals and birds access to the surface for air and hauling out, and to the water for food and refuge, while thick floes provide a growth environment for phytoplankton and other microorganisms [*Eicken*, 1992; *Horner, et al.*, 1992]. Sea ice thickness distribution also directly affects the ability of vessels to navigate at high latitudes.

Due to the complex processes responsible for forming, redistributing and deforming the Antarctic sea ice cover, the thickness distribution varies greatly seasonally and regionally and possibly interannually [*Worby, et al.*, 1998]. Therefore, not only is the sea ice thickness distribution important but also its variability is a key parameter. As shown in Section 2.1.2, the area-averaged mean thickness of the sea ice cover in any given region is determined not only by the thermodynamic growth (and decay) rates, but also sea ice dynamics i.e. lead formation, deformation (ridging and rafting) and advection [*Wadhams*, 1998].

As shown in Section 2.1.6, pack ice drifts in response to ocean currents, wind stress, water drag, Coriolis force and internal ice stress [*Leppäranta*, 1998]. Internal ice stress diminishes significantly with distance from the coast, and inertial forces are unimportant at time scales greater than one day [*Allison*, 1989]. Advection results in significant redistribution of sea ice, as shown in analyses of drifting buoy tracks within the East Antarctic sea ice zone [*Allison*, 1989; *Heil and Allison*, 1999].

This redistribution is a key mechanism, determining not only sea ice concentration and extent but also the sea ice thickness distribution and the overall mass budget of the pack, in that ice deformation creates both open water and thin ice areas, and thick ridged ice. The Antarctic sea ice thickness distribution is therefore a quantifiable, interpretable parameter that reflects the integration of mechanical (dynamic) and thermal forces driving the Southern Ocean sea ice cover.

Although important, developing an improved understanding of processes controlling the ice thickness distribution is beyond the scope of this study, which is concerned with the production of large-scale maps of the thickness distribution of East Antarctic sea ice. In order to achieve this objective, measured values of the various components of the heat balance equation were retrieved from satellite visible and thermal infrared data, and then applied to the determination of the thermodynamic growth of the ice cover via a model (Chapter 4). The resulting sea ice thickness for a given pixel within the satellite image may be an underestimation due to the reasons outlined above i.e. the importance of ice dynamics, although the changes in thickness for that area in a period of time will be accurately measured. These issues will be discussed in more detail in Chapters 5 and 6. However, in the absence of other large-scale data on sea ice thickness for Antarctica, this study provides an important first-order approximation.

2.2 Measurements of Antarctic Sea ice Thickness

This section reviews the techniques available for measuring Antarctic sea ice thickness, evaluates their relative strengths and weaknesses, and then places the current study into the context of previous studies. It is divided into three sub sections: *in situ* methods, near surface remote sensing methods and satellite remote sensing methods. The latter includes a more detailed description of the AVHRR sensor which is the main focus of this study.

2.2.1 *In Situ* Measurements

A number of techniques have been used to measure Antarctic sea ice thickness *in situ*. These include the drilling of holes along transects across individual floes, and the collection of estimates of sea thickness from ships traversing the sea ice zone. These techniques provide high accuracy data but cover a limited thickness range and only in local spatial scales.

Drill-hole measurements of sea ice thickness along transects on floes have been carried out all around Antarctica [*Jeffries and Adolphs*, 1997; *Jeffries, et al.*, 1998b; *Lange and Eicken*, 1991; *Wadhams, et al.*, 1987; *Worby, et al.*, 1996b], although sampling strategies vary [*Jeffries, et al.*, 1998a]. This type of measurement may be biased, in that it tends to undersample the proportion of thick ridged ice present and takes little or no account of very thin ice and open water [*Wadhams, et al.*, 1987]. While reliable and accurate, hole drilling has no value for large-scale surveying or long-term monitoring of sea ice thickness. Further discussion of inherent biases of this technique is given in *Allison and Worby* [1994] and *Worby et al.* [1996b].

Larger scale measurements are derived from hourly observations of sea ice thickness and overall ice conditions made by trained observers on the bridge of ships traversing the sea ice zone [*Allison and Worby*, 1994; *Worby and Allison*, 1999; *Worby, et al.*, 1996b]. While early measurements were somewhat biased by the sampling strategy, whereby ships avoided regions of thick deformed ice for navigation purposes, recent efforts have been made to remove biases and standardise the data collection using an internationally recognised and adopted protocol [*Worby and Allison*, 1999]. Comparisons with drilled measurements and possible sources of ambiguity are discussed in *Worby et al.* [*Worby, et al.*, 1996a] and a more detailed description of the ship-based observation technique is given in Section 3.2.2.

When drawn together, drill-hole measurements and ship-borne observations give large-scale seasonal and regional mean thickness distributions [*Worby, et al.*, 1998]. Each data point, however, represents a snapshot in space and time. Table 2.2 in *Worby* [1998] presents a summary of published sea ice and snow thickness data obtained from drilled measurements and ship-based observations in Antarctica. *Worby and Ackley* [2000] have identified a total of 11,000 individual records of *in situ* observations in Antarctica from 42 voyages between 1980 and 1997. These data are being processed and catalogued by the ASPeCt program for future release on the internet (www.antdiv.gov.au/datacentre).

2.2.2 Near-Surface Remote Sensing Measurements

Due to the large scales involved and the importance of measuring and monitoring sea ice thickness, the development of remote sensing technology has received a good deal of recent attention. Several studies have employed various forms of near-surface remote sensing techniques such as acoustic and laser profilometers, electromagnetic induction instruments and moored upward-looking sonars (ULS) in an effort to gain information on Antarctic sea ice thickness.

Moored ULSs provide information on the draft of floes moving above the sensor via the measurement of the ice draft [*Bush*, 1997; *Strass and Fahrbach*, 1998]. While useful, ULS measurements are limited in space and time and the number and location of moorings is insufficient to derive large-scale seasonal and regional estimates of ice thickness distribution. Of the 37 instruments deployed in the Southern Ocean since 1990, only seven are currently operational: five between 59° and 69° S along the Greenwich line and two between 64° and 66° S and 142° E [*AntCRC*, 1998]. Arctic studies of sea ice thickness have to a large extent been based upon the analysis of submarine upward-looking sonar data [*Rothrock, et al.*, 1999; *Wadhams*, 1994]. However, such data are not available for the Southern Ocean due to restrictions on submarine activities set out in the Antarctic Treaty.

Helicopter-borne impulse radars have been tested in the Weddell Sea by *Wadhams et al.* [1987]. The authors found that, while results were in some cases reasonable and agreed with drill-hole calibration measurements, superimposition of the bottom and surface echoes undermined the ability of the sensor to measure sea ice thinner than 1 m. Moreover, the slowness of data gathering due to the necessary slow speed of the helicopter when flying such sensors is also a serious limitation.

Electromagnetic induction instruments attached to ships provide information on ice plus snow thickness [*Haas, et al.*, 1998]. When combined with laser altimetry, a method that provides information on the height of the snow/ice surface, electromagnetic induction techniques can give a profile of ice thickness while the ship is in motion. Although the results are highly promising, ambiguities still occur in regions where water-filled interstices are present in the ice and further studies are necessary until this method becomes operational [*Worby, et al.*, 1999].

Menashi et al. [1993] tested a long-wavelength (50 cm, frequency 611 MHz) passive microwave system onboard the RV *Polarstern* during winter in the Weddell Sea. This technique showed potential for ice thickness measurement (for thicknesses up to 0.7 m), but technological limitations remain to be solved before such sensors can be employed operationally [*Wadhams and Comiso*, 1992]. Difficulties also remain regarding the unambiguous interpretation of the microwave emissivity as it relates to ice thickness, given the complexity of Antarctic sea ice and its snow cover [*Massom, et al.*, 1999].

Laser profilometry has been extensively carried out in the Arctic Ocean over the past 30 years (e.g. *Tucker et al* [1979], *Wadhams* [1976], *Weeks et al.* [1971]), but in a much more limited fashion in the Antarctic sea-ice zone [*Weeks, et al.*, 1989]. Analysing the results of previous Arctic experiments, *Wadhams and Comiso* [1992] suggest that in regions with mean ice thickness varying in the range of 4 m to 6 m, the accuracy of this technique is approximately ± 0.12 m in mean ice thickness. According to *Wadhams* [1998] and *Wadhams and Comiso* [1992] more validation is necessary before laser profilometry can provide routine sea ice thickness data in Antarctica. Latterly, it has been used in conjunction with an electromagnetic induction sensor on a boom extending out from the ship as it traverses the pack ice in East Antarctica [*Worby*, 2000, pers. comm.].

Analysis of aerial photography provides a qualitative estimate of sea ice thickness, whereby greyscales can be related to sea ice type as a proxy for ice thickness. *Eppler and Farmer* [1992] suggest that the thickness distribution of new and young ice (less than 0.3 m) can be obtained through the analysis of differences in grey tones which arises from changes in albedo, reflectivity and absorption. This thickness-grey tone relationship enables the collection of information on the thickness distribution at the thin end of the spectrum, which would be difficult to obtain with other methods. The technique employed by *Eppler and Farmer* [1992] and others in the Arctic and *Ackley et al.* [1992] in the Weddell Sea involved the use of digitised pictures (512 x 512 pixels) with the aid of a PC-based interactive image processor software. In both studies, the classification was based on the WMO scheme [*WMO*, 1970] and the analysts also employed additional information such as the presence and morphology of deformational features such as rafts, ridges and fractures. Digital aerial photography is employed in this study as a source of data with which the results are calibrated (Section 5.3.1).

2.2.3 Satellite Remote Sensing Measurements

Whereas near-surface remote sensing and *in situ* measurements are limited in both space and time, satellite remote sensing offers the potential means to obtain information on important sea ice variables over large areas on a repetitive basis. The use of remote sensing for measuring such parameters in the polar regions and monitoring their short and long-term behaviour presents several advantages: large areal coverage (ranging from 100 km^2 per image to mosaics that encompass the whole Antarctic continent), good temporal resolution (ranging from a few hours in the case of polar orbiting satellites to a few weeks in the case of spacecraft carrying narrow-swath, high-resolution imaging sensors), cost-effectiveness, data uniformity, and data availability [*Massom*, 1995]. An overview of the various remote sensing techniques employed to infer the sea ice thickness distribution is given by *Wadhams and Comiso* [1992] and *Thorndike et al.* [1992].

Large-scale information on Antarctic sea ice drift is available from satellite data, including the AVHRR [*Emery, et al.*, 1997], passive microwave [*Kwok, et al.*, 1998; *Liu and Cavalieri*, 1998], radar scatterometer [*Drinkwater*, 1995; *Drinkwater and Lytle*, 1997; *Long and Drinkwater*, 1999] and SAR [*Holt, et al.*, 1992]. Reasonably accurate global sea ice concentrations are derived from passive microwave sensors as reviewed by *Steffen et al.* [1992]. Observations of sea ice thickness are, however, far more limited [*Carsey, et al.*, 1992], and are largely derived from *in situ* or near-surface remote sensing measurements, which are inherently limited in space and time. This is due to the fact that no direct measurements of sea ice thickness are possible from space using current technology.

Satellite instruments do not sense the bottom surface of sea ice. Rather, they measure radiation emitted or scattered from the upper surface, the volume of the snow cover, or the volume of the upper few tens of centimetres of the ice [*Hallikainen and Winebrenner*, 1992]. *Lindsay and Rothrock* [1993] identified three groups of techniques for inferring sea ice thickness using satellite remote sensing technology. Two involve microwave (radar and passive microwave) and the third involves thermal infrared sensors. Brief discussions of passive microwave and radar techniques employed in recent studies are given below. Thermal infrared techniques are presented in more detail in Section 2.2.4, with emphasis in the AVHRR sensor.

The first satellite-borne instruments with real potential for sea ice investigation were passive microwave sensors. Following successful experiences in the late 1960s and early 1970s, the development of the Scanning Multichannel Microwave Radiometer (SMMR), which operated on the Nimbus 7 satellite from 1978 to 1987, led to the establishment of a very useful long-term data set [*Gloersen, et al.*, 1992]. In 1987 the Defence Meteorological Satellite Programme (DMSP) launched the SSM/I, extending the long-term daily record of passive microwave information over the Southern Ocean.

Efforts have been made to relate surface radiative and microwave properties to ice thickness through a mixture of empiricism and physics. For example, *Cavalieri* [1994] mapped the distribution of new, young and first-year Arctic sea ice using microwave spectral and polarisation data from the SSM/I sensor. *Zabel et al.* [1996] developed a method to determine the thickness of artificially-grown sea ice via changes in radar backscatter as they relate to surface roughness and dielectric properties. *Wensnahan et al.* [1993] employed principal component analysis to distinguish Arctic thin ice types. *Massom et al.* [1999] used a cluster analysis technique with input from four channels of the SSM/I to distinguish large-scale sea ice regimes of differing thicknesses within the East Antarctic sea ice zone.

Another approach employed by *Cavalieri et al.* [1984] has been to distinguish multiyear ice from first-year ice in the Arctic, based upon the contrast in their respective passive microwave signatures as measured from space, using algorithms reviewed by *Eppler et al.* [1992]. However, this technique is not applicable in Antarctica, where the radiometric contrast between annual and perennial sea ice is not as great due to different environmental conditions [*Comiso, et al.*, 1992]. Moreover, current passive microwave algorithms perform relatively badly in regions of predominantly thin ice, partly due to limitations in the spatial resolution of passive-microwave radiometers (25 x 25 km for sea ice products derived from current SSM/I data) and the mixed-pixel effect [*Grenfell, et al.*, 1992]. Other issues regarding the microwave remote sensing of Antarctic sea ice are reviewed by *Comiso et al.* [1992].

The second type of instruments with potential for inferring sea ice thickness are active microwave (radar) systems. Unlike passive microwave systems such as the SSM/I that measure the blackbody radiation emitted by the surface, airborne and spaceborne radar instruments generate a series of microwave pulses and measure the intensity and delay of the returned backscattered signal. These pulses interact with the surface (surface scattering) and can also penetrate the target (volume scattering) or, in some cases like new ice, be absorbed. The backscattered energy as detected by the satellite instrument contain information about the state and physical properties of the surface.

While the spatial resolution of real-aperture radar instruments, like the Side-Looking Airborne Radar (SLAR), is limited by the size of the antenna and the range to the target, SAR instruments rely on the motion of the satellite to simulate (synthesise) a larger antenna and therefore achieve a finer spatial resolution of up to 10 metres which is suitable for sea ice studies [*Kwok, et al.*, 1992].

A technique employed in studies such as *Barber and LeDrew* [1989] and *Kwok et al.* [1992] is to estimate sea ice thickness from SAR data in the Arctic region is to identify the sea ice type and use it as a proxy for thickness. Another approach is presented by *Haverkamp et al.* [1994] who developed an automated system for the determination of sea ice thickness from SAR data using a combination of algorithmic and heuristic methods. The application of this system to a set of Arctic European Remote Sensing Satellite (ERS-1) SAR images showed promising results. However, the authors of that study acknowledge that further studies are necessary to assess the effectiveness of this method as the analysis of the results was made only by visual judgement.

More recent studies such as *Kwok* [in press] and *Kwok and Holt* [2000] have outlined a new technique which uses time series of Radarsat SAR data to create gridded fields of sea ice thickness (as well as ice motion and deformation). Operating within the Radarsat Geophysical Processor System (RGPS), this technique estimates ice age and thickness from repeat observations of Lagrangian cells in sequential SAR imagery. Further details of this technique are given in *Kwok et al.* [1999]. However, at present and in the foreseeable future, the application of this technique is limited to the Arctic Ocean basin. It has yet to be tested in the seasonal sea ice zone, and it is unlikely to produce accurate results in Antarctica without considerable development.

The most evident advantage of SAR and passive microwave over visible and thermal infrared sensors is the fact that its microwave pulses can penetrate cloud cover and the polar night. Furthermore, while visible and infrared sensors are mostly sensitive to chemical and thermal properties of the observing medium, SAR has the ability to sense physical (morphology, roughness, geometric shape, etc.) and electrical properties of the surface and subsurface in great detail.

While promising however, the approaches described in this section depend largely on the knowledge of surface conditions, and a good understanding of the complex relationships between electromagnetic radiation and the ice and snow surface roughness, electrical properties, and their structure and salinity [*Hallikainen and Winebrenner*, 1992]. Furthermore, these techniques are yet to be tested on an operational basis.

2.2.4 AVHRR

The third satellite-based technique for estimation of sea ice thickness involves the use of visible and thermal infrared data. By estimating the albedo and temperature of the snow/ice surface, together with knowledge of the near-surface air temperature, it is possible to estimate ice thickness from a thermal balance [*Lindsay and Rothrock*, 1993]. This study focuses on the use of the AVHRR sensor.

2.2.4.1 Remote Sensing of Surface Physical Temperature From Space

Before entering into a discussion on the use of the AVHRR sensor for the retrieval of polar geophysical parameters, it is important to briefly review the theory on which this sensor is based, especially the physical processes that control the interactions between thermal energy and matter, which constitute the foundation for the AVHRR's ability to detect and record thermal radiation. Formal and more detailed discussions of the principles presented in this section can be found in remote sensing texts such as *Lillesand and Kiefer* [1987] and *Colwell* [1983].

The spectral distribution of the radiation produced by a blackbody (defined as an ideal radiator of thermal radiant energy) is defined by Planck's equation as:

$$M_\lambda = \frac{2\pi hc^2}{\lambda^5}\left(\frac{1}{e^{hc/\lambda kT}-1}\right) \qquad \textbf{Equation 1}$$

where $h = 6.62 \times 10^{-34}$ J·s^{-1} is Planck's constant, $k = 1.38 \times 10^{-23}$ J·K^{-1} is Boltzmann's constant, c is the speed of light, T is the temperature (in K) and λ is the wavelength.. The radiant exitance (the flow of energy per unit time per area) is obtained by integrating Planck's formula over all wavelengths. The result is known as the Stefan-Boltzmann Law:

$$M = \sigma T^4 \qquad \textbf{Equation 2}$$

where $\sigma = 5.6693 \times 10^{-8}$ W·m^{-2}·K^{-4} is the Stefan-Boltzmann constant. For a non-black body, the Stefan-Boltzmann Law is modified to $M = \varepsilon\sigma T^4$ where ε is the emissivity, which is a physical property that depends only on the nature of the substance/surface, being independent of temperature but possibly dependent on wavelength.

Therefore, by measuring the radiant exitance of a particular object in a part of the electromagnetic spectrum, and with knowledge of the appropriate emissivity, it is possible to determine the physical temperature of the object. This is the principle utilised by a radiometer placed at a short distance from an object. For an instrument located above the atmosphere, one has to consider a number of additional sources of radiant energy: direct atmospheric emissions, direct cloud emissions, reflected cloud emissions, and - of less importance in the thermal infrared - solar emissions scattered into the satellite's field of view and reflected solar energy.

In summary, the three most important atmospheric effects which must be quantified when remotely sensing surface physical temperatures are: direct atmospheric emissions, scattering and absorption. A component of the radiant energy reaching the Earth is emitted by the atmosphere itself, especially from clouds. A proportion of the radiation emitted by the atmosphere combines with radiation from the surface and is sensed by an instrument at the top of the atmosphere.

Molecular absorption, caused by the presence of gases in the atmosphere, removes energy from the beam of radiation as it travels through the atmosphere. This energy is generally re-radiated in all directions at longer wavelengths. The primary mechanism for absorption by gases is the transfer of energy from the electromagnetic wave to a gaseous molecule or atom. These exchanges of energy are quantised i.e. each change in energy is associated with a particular frequency or wavelength. Because of this variation of atmospheric absorption with frequency/wavelength, there are a number of *windows* in the electromagnetic spectrum in which the atmosphere is relatively transparent, allowing the observation of the surface from space.

Scattering is the process by which the particles in the atmosphere (water droplets, smoke, haze etc.) can change the direction of propagation of the beam of radiation without altering its wavelength. Scattering usually dominates over absorption. Furthermore, the influence of scattering by particles in the atmosphere is complicated by a number of factors such as the polarisation of the scattered energy, the strong dependence of scattering on the size of the particles relative to the wavelength of radiation, the strong directional properties of scattered radiation and multiple scattering which can both remove and add energy to the beam of radiation.

Scattering can be classified into three different categories, based on the relationship between the particle's diameter (a) and the wavelength of the propagating radiation (λ): Isotropic or non-selective scattering occurs when $\lambda << a$. At visible wavelengths isotropic scattering is associated with thick clouds or fog, containing water droplets with radii of the order of 5 - 10 μm. Rayleigh scattering occurs when the wavelength of the propagating radiation is much larger than the diameter of the particles ($\lambda >> a$). In this case the amount of energy scattered is smaller than the amount of energy absorbed. Mie scattering occurs when the wavelength of the propagating radiation is of the same order as the diameter of the particles ($\lambda \approx a$). Mie theory is applied to most practical situations such as atmospheres containing dust, water vapour, sea spray, aerosols etc.

At near infrared wavelengths, Rayleigh scattering is not valid, and Mie scattering theory must be applied. The interaction of electromagnetic radiation with the atmosphere, its effects on satellite remote sensing of temperatures and correction techniques are discussed in detail in several studies such as *Colwell* [1983], *Cracknell* [1997], *Cracknell and Hayes* [1991], *Kaufman* [1989], *Slater* [1980] and *Wolfe* [1996].

Since NOAA-7 was launched in 1981, carrying the first AVHRR/2 on board, a number of algorithms, both theoretically- and/or empirically-based have been developed, to make the best estimate of the target's temperature when observed from TOA. These algorithms generally utilise two or more channels in an effort to eliminate atmospheric effects from surface physical temperature data retrieved from satellite thermal infrared measurements. These techniques are called "split-window" algorithms and have been largely employed in the estimation of ice and sea surface temperatures [*Skirving*, 2001].

The split-window technique is based on the principle that the emissivities for water and ice in the 10.3 - 11.3 μm (AVHRR channel 4) and 11.5 - 12.5 μm (AVHRR channel 5) are effectively equal. AVHRR channel 4 coincides with the middle of the thermal infrared water vapour window, whilst channel 5 is just off-centre. Therefore, channel 4 has less atmospheric effect than channel 5 and the AVHRR channel 4 / channel 5 difference can be related to the amount of atmospheric attenuation associated with water vapour [*Skirving*, 2001]. A description of the theory and detailed discussions about the development of split window algorithms can be found in *McMillin and Crosby* [1984], *Barton* [1995] and *Walton et al.* [1998]. Section 2.2.4.5 presents a more detailed discussion of split-window algorithms designed to estimate sea ice surface temperature from thermal infrared AVHRR data.

2.2.4.2 Radiometric Techniques

Portable radiometers have been used in several studies over the past fifty years to derive the temperature of different types of surfaces [*Ball*, 1954; *Saunders*, 1967; *Woodcock and Stommel*, 1947]. They are particularly useful in the measurement of water and ice/snow surface temperatures on a large scale [*Campbell, et al.*, 1976; *Coppin, et al.*, 1991; *Guest and Davidson*, 1994; *Rapier*, 1995; *Schluessel, et al.*, 1990; *Schluessel, et al.*, 1987] as the amount of data collected using traditional methods such as drifting buoys, oceanographic cruises or ice stations is insufficient and sometimes inaccurate.

The operational use of spaceborne radiometers to retrieve accurate estimates of the temperature of polar surfaces is yet to be achieved, mostly because of the issues to be discussed in Section 2.2.4.5. Therefore, performing *in situ* radiometric measurements along with traditional temperature measurements is essential for the validation of algorithms to derive water and ice/snow surface physical temperatures from satellites [*Barton, et al.*, 1989; *Coppin, et al.*, 1991]. Studies of radiative measurements over polar surfaces are less frequent than those of sea surface temperature (SST). The main reasons are the high cost and logistic difficulties involved in conducting voyages or setting ice stations in the Arctic or Antarctic. Most of the studies found in the literature describe experiments carried out in the Arctic pack ice to correlate *in situ* measurements with AVHRR-derived ice surface temperature (IST) data e.g. *Massom and Comiso* [1994].

Guest and Davidson [1994] for example demonstrated that, during the Arctic winter, the near-surface air temperature (T_{Air}) is usually closely linked to the temperature measured at the top of the snow or ice surface (T_{Sfc}) through turbulent heat transfer processes, in spite of the constant presence of low-level temperature inversions. With the exception of light wind periods (less than 2 $m \cdot s^{-1}$), the authors concluded that the difference between T_{Air} and T_{Sfc} was less than 2 K. Although this study is specific to the Arctic winter, its results are important as they confirm that sensors such as the AVHRR can be used as operational tools for IST retrieval.

In order to validate the algorithm proposed by *Key and Haefliger* [1992] to derive Arctic IST from AVHRR images, *Key et al.* [1994] performed a series of radiometric measurements during the Sea Ice Monitoring and Modelling Site (SIMMS) in 1992. In this Arctic study, AVHRR-derived IST data were compared to near-surface air temperatures, surface temperatures derived from upwelling longwave radiation measured by a pyrgeometer, snow/ice interface temperatures measured by thermocouples below the snow surface and skin temperatures measured by a hand-held infrared radiometer. *Key et al.* found that the difference between the skin temperature and the upwelling longwave radiation-derived surface temperature was small (0.33 K). However, the difference between the AVHRR-derived temperature and the pyrgeometer temperature varied between < 0.1 K and >3 K, with the satellite estimates always less than the *in situ* measurements. This difference was attributed to undetected clouds, spatial and temporal variability of the temperature field and incorrect assumptions made in the retrieval procedures.

Haefliger et al. [1993] conducted a similar experiment on the Greenland Ice Sheet in 1991 to derive temperature and narrow band-albedo estimates from AVHRR imagery using the Low Resolution Atmospheric Transmission Code (LOWTRAN) radiative transfer model. Results showed an RMS error of 0.3 K between the *in situ* and the AVHRR-derived IST.

Michael et al. [1998] utilised two thermal infrared radiometers installed on the RSV *Aurora Australis* to collect surface temperature data on the East Antarctic sea ice during the austral autumn of 1993. Additional information on the characteristics of the targets were obtained through standardised ship-based sea ice observations and environmental/meteorological data collected by the ship's sensors. As the two radiometers failed to produce consistent results, a *composite temperature* was created to retain the full temporal resolution of approximately 30 seconds and the stability of calibration under the low air temperatures found in the Southern Ocean at this time of the year. The results showed a broad agreement between the *in situ* IST and the composite radiometric surface temperature, and the variability observed in the latter could be explained by changes in the snow and ice conditions as the ship traversed the sea ice pack. To ensure the successful application of this method in the future, the authors recommended that the instruments should be calibrated as frequently as possible. Furthermore, the quantitative interpretation of results can only be achieved with a very detailed record of the sea ice conditions.

2.2.4.3 Characteristics of the AVHRR Sensor

The AVHRR sensor is a cross-tracking scanning instrument that has been flown on the NOAA polar orbiting series of satellites since October 1978. Since then, at least two satellites have usually been in orbit at any one time, with a period of approximately 102 minutes, and at an orbital inclination of about 99°. The sensor swath width is 2750 km, or 25° of latitude, and the pixel resolution at nadir is approximately 1.1 km. At the time of writing of this document, NOAA operated two polar orbiting satellites: NOAA-14, which was launched in December 1994 and carries the AVHRR/2 sensor and NOAA-15, launched in May 1998, which is the first satellite to carry a new series of sensors that include the AVHRR/3. This instrument has an additional channel (3A) centred on 1.61 μm. AVHRR data are available at two spatial resolutions: Local Area Coverage (LAC) data have resolution of 1.1 km, while that of Global Area Coverage (GAC) is of 4 km. Further information on the characteristics of this sensor can be obtained from *Kidwell* [1998] and *Cracknell* [1997]. The use of AVHRR data for the retrieval of geophysical parameters of the sea ice cover in the Southern Ocean has several benefits compared to *in situ* methods and other remote sensing platforms. These include the following:

a) Data Availability.

AVHRR sensors have been in operation since the late 1970s and similar instruments are planned for the next decade or so [*Massom*, 1995], providing a long and uninterrupted dataset for climatological studies. The images are easy to obtain at a reasonably low cost. Furthermore, because of their application in operational weather forecasting, the number of stations capable of receiving AVHRR images in Antarctica has grown considerably in the past ten years [*Turner, et al.*, 2000].

b) Resolution, Coverage and Radiometric Range.

The AVHRR's moderately high spatial resolution and large spatial coverage are suitable for geophysical applications and its revisit time is excellent in the polar regions, with up to 15 passes a day available from up to three different satellites, both in ascending and descending mode. Another important aspect of this sensor is its radiometric range that covers the visible, near-infrared and thermal infrared areas of the electromagnetic spectrum with 4, 5 or 6 channels.

c) *Processing Techniques.*

The basic image pre-processing techniques, such as navigation and mapping, have been developed within the wider remote sensing community, which has facilitated the development of more advanced algorithms capable of addressing issues such as the retrieval of IST and albedo.

Table 4 presents the parameters for each of the AVHRR channels in the NOAA satellites. These, along with the characteristics described above, make the AVHRR a very useful resource. However, in spite of its potential, the sensor has not been widely applied to Antarctic sea ice research and, until recently, most of the studies have been conducted on a demonstration and/or case study basis, without attaining a monitoring capacity [*Steffen, et al.*, 1993].

Channel	*Wavelength (μm) NOAA-6,8,10*	*Wavelength (μm) NOAA-7,9,11,12,14*	*FOV* (miliradians)
1. Visible	0.58 - 0.68	0.58 - 0.68	1.39
2. Near Infrared	0.73 - 1.10	0.73 - 1.10	1.41
3. Infrared	3.55 - 3.93	3.55 - 3.93	1.51
4. Thermal Infrared	10.50 - 11.50	10.30 - 11.30	1.41
5. Thermal Infrared	-	11.50 - 12.50	1.30

Table 4 Characteristics of the AVHRR channels. Adapted from *Fetterer and Hawkins* [1993], *Steffen et al.* [1993] and *Kidwell* [1998]. This table does not include the characteristics of the AVHRR/3 sensor, recently launched onboard the NOAA-15.

The main reason for this lack of application has not been of methodology, but difficulties in understanding aspects of the polar atmosphere such as temperature, humidity and aerosol as well as the microphysical properties of polar clouds [*Key and Haefliger*, 1992]. Cloudiness is a major limitation, especially during the summer. Even in situations where there are "holes" in the cloud cover, the differentiation between the snow and/or ice surface and the clouds can be quite difficult, as they tend to have similar spectral signatures in the AVHRR channels. In 1992, a workshop held in Colorado on snow and ice applications of AVHRR in polar regions discussed a number of key research topics to be developed in the future which could improve the use of this important remote sensing tool in high latitudes [*Steffen, et al.*, 1993]. The following sections will elaborate upon issues featured in the *Steffen et al.* paper such as cloud masking, ice surface temperature, and narrow-band albedo, also incorporating newer references when available.

2.2.4.4 Cloud Masking

The method proposed in this study depends on the ability to discriminate between clouds and snow/ice surfaces in AVHRR scenes, hence the discussion presented below. The fact that clouds and polar surfaces have similar characteristics in both the visible and the infrared parts of the electromagnetic spectrum makes the screening of polar scenes a very challenging task.

Many authors have reported difficulties with the screening of clouds in polar regions. *Welch et al.* [1992], for instance, found that clouds can be warmer and darker than the background ice and snow, and can easily be confused with melt ponds, thin ice and pancake ice in Arctic Landsat imagery. In addition to simple obscuration of the surface, parameters such as albedo and ice temperature can be biased by the presence of optically thin clouds such as high level cirrus, stratus and low-level fog [*Steffen, et al.*, 1993].

One set of algorithms used to mask clouds relies on visible and infrared thresholds. Reflectance thresholds are generally set at about 3% above the background value, while thermal thresholds are set at 3 K below the surface target value [*Steffen, et al.*, 1993]. However, those techniques were developed for tropical, subtropical and temperate regions, where the contrast between clouds and the surface is much more evident.

Other studies [*Key*, 1990; *Welch, et al.*, 1992] indicate that a combination of spectral measures based upon AVHRR channels 1, 3, and 4 and textural measures computed from channels 1 and 4, can effectively detect polar clouds. Some success has also been achieved using channel differences, such as [channel 1 - channel 2] and [channel 3 - channel 4], and band ratios such as [channel 3 / channel 1] [*Steffen, et al.*, 1993].

Four general approaches to cloud masking have been described in the literature: *a)* spectral thresholding; *b)* statistical and clustering; *c)* textural and *d)* a combination of spectral, statistical and textural. The relative merits of each of these techniques are evaluated by *Comiso et al.* [1992]. *Darzi* [1992] presented a review of methods for detecting and screening cloud contamination on images from the AVHRR and the Coastal Zone Color Scanner (CZCS) sensors. The work of *Steffen et al.* [1993] contains a similar review. This section presents a brief description and update of some of these techniques found in recent publications and cited here in chronological order.

Welch et al. [1990] used Landsat images to generate two different sets of textural features for polar scene discrimination. Textural features can be described as statistical measures of the spatial distribution of grey levels in an image. Results showed that typical polar surfaces such as consolidated sea ice, glaciers, open water, snow-covered mountains and cloud-covered areas have distinguishable textural features, suggesting that this technique could successfully discriminate clouds in polar scenes. However, some problems were experienced in distinguishing between broken sea ice and stratocumulus and thin cirrus clouds.

Welch et al. [1992] found overall accuracies of 85.6%, 87.6% and 87.0% using three different types of polar cloud and surface classifiers respectively: *a)* the stepwise discriminant analysis method; *b)* the feed-forward back-propagation neural network and *c)* the probabilistic neural network. Among the 10 classes of surface, clouds or cloud/surface selected, the "Cirrus Over Ice" class presented the best results (94.34%, 93.09% and 94.48% for each of the classifiers respectively). However, other cloud classes presented lower accuracies.

Lindsay and Rothrock [1993] developed a subjective cloud masking procedure that relies solely on combinations of AVHRR channel reflectances, such as the [channel 4 - channel 3] difference for sunlit scenes and the [channel 4 - channel 5] difference at night. The results showed some uncertainties in the screening of cloudy areas which affected the estimates of surface albedo.

Gallegos et al. [1993] applied a multiple band approach to produce signatures not readily available in single-channel data, an edge detection technique to locate features in the clouds and a polygon identification technique to remove noise and separate clear regions from cloud-contaminated areas. The authors reported encouraging results, especially in the discrimination of very cold clouds, on a limited dataset of AVHRR images. However, this technique fails to detect the presence of thin cirrus and low level clouds.

Massom and Comiso [1994] used the [channel 3 - channel 4] difference and empirical threshold values in daylight conditions to separate clouds from the rest of the scene. This technique was applied on a case-by-case basis, as the spectral response of clouds within a given scene varies with cloud type, height, and sensor geometry. However, the detection of low level and subpixel-scale clouds remained a source of uncertainty.

Yhann and Simpson [1995] applied two different types of neural network for cloud screening of AVHRR data. The first involved an interactive cloud screening technique, whereby a simple network was trained on a set of data points selected from the image to be screened. The second approach, which was designed to handle a large number of images, incorporated a more complex network. Results were promising, with accuracies above 95% in some cases. However, the 7-year AVHRR dataset employed in that study mostly comprised low-latitude open ocean data. Using a similar approach, *Turner et al.* [1996] achieved approximately 98% accuracy in the discrimination of regions of sea ice, ocean and cloud cover for a limited data set of AVHRR images of the Antarctic sea ice.

From the techniques described above, it can be seen that there is no consensus as to what technique can be used to achieve a consistent polar cloud classifier, although it is generally agreed that spectral information alone is inadequate. Difference and ratio methods, textural measures and neural networks techniques appear to have varying degrees of success, but all require further testing using broader polar AVHRR datasets, particularly in the Southern Ocean. Another common limitation is that almost all the cloud screening algorithms found in the literature are effective only during daylight hours, thus precluding the polar night.

In addition to the techniques discussed in this section, other methods have been tested involving the combination of sensors, such as the Television and Infra-Red Observational Satellite (TIROS) Operational Vertical Sounder (TOVS), used to improve the detection of thin clouds, or the coupling of AVHRR data with passive microwave retrievals [*Comiso*, 1994]. Another approach is based on temporal analysis, through the subtraction of consecutive images to evaluate cloud motion [*Steffen, et al.*, 1993]. This latter technique relies on the fact that the sea ice is relatively static compared to clouds. It is clear from the studies mentioned above that the best techniques presently available are capable of fairly high levels of accuracy (more than 90%) on a case-by-case basis.

2.2.4.5 Ice Surface Temperature

Ice surface temperature is an essential prerequisite to the accurate estimation of turbulent and radiative fluxes in polar regions. A number of studies have exploited data from AVHRR channels 4 and 5 to derive large-scale maps of IST [*Key, et al.*, 1997a; *Lindsay and Rothrock*, 1994b; *Massom and Comiso*, 1994]. However, limitations in our knowledge of atmospheric temperature, humidity, the spatial and temporal distribution of aerosols, micro-physical properties of polar clouds and the spectral characteristics of snow, water and ice surfaces have caused difficulties in the development of more robust IST algorithms using satellite data as input [*Key and Haefliger*, 1992; *Steffen, et al.*, 1993].

IST algorithms are adaptations of similar techniques designed to retrieve SST information from satellite thermal infrared data. In contrast to the open ocean, where the surface is relatively homogeneous, dark and warm, polar scenes present a great number of different surfaces, even within the space of a single AVHRR pixel. The spatially-integrated emissivity/temperature will depend upon the exact proportion of types of ice encountered, along with the amount of open water and snow cover present.

The general form of the algorithm proposed by *Barton et al.* [1989] for the retrieval of SST takes into account the correction for atmospheric attenuation of upwelling radiation primarily due to water vapour absorption:

$$T = a(\theta) + \sum_{i=3}^{5} b_i(\theta) T_i \qquad \textbf{Equation 3}$$

where θ is the sensor scan angle, a and b_i are satellite angle-dependent coefficients and T_i is the satellite-measured brightness temperature in each of the three AVHRR thermal infrared channels. The coefficients are determined through a least squares regression procedure, where surface temperatures are regressed against modelled brightness temperatures.

Consistent with the general approach to estimate IST from the AVHRR's thermal infrared channels, *Massom and Comiso* [1994] sought to correlate the satellite data with *in situ* observations. An IST algorithm was developed by correlating thermal infrared data from the 10.8 and 12.0 μm channels with surface temperature data from the Bering Sea through a regression model. The RMS differences of this algorithm, when compared with the *in situ* data, are estimated to be about 0.5 K over leads and 0.5 K - 1.5 K over thick ice.

In the absence of corresponding *in situ* measurements, satellite radiances or brightness temperatures can be modelled using radiative transfer models. This method has been used by several authors to obtain SST data with an accuracy as high as 0.5 K - 1 K [*Barton, et al.*, 1989; *Hepplewhite*, 1989; *Schluessel, et al.*, 1987]. On the other hand, land surface temperatures (LST), estimated using the same approach, showed accuracies of 2 K - 3 K, mainly because of the larger variability in the surface conditions affecting emissivity [*Barton and Takashima*, 1986; *Kerr, et al.*, 1992].

Key and Haefliger [1992] used Arctic atmospheric temperature and humidity data from radiosonde profiles to develop an IST algorithm using AVHRR thermal infrared channels. Instead of using a different set of coefficients for each scan angle (as in Equation 3), the authors applied an equation that explicitly included the scan angle:

$$T_{ice} = a + bT_4 + cT_5 + d[(T_4 - T_5)\sec\theta] \qquad \textbf{Equation 4}$$

where T_{ice} is the IST, a, b, c and d are the calculated coefficients and T_4 and T_5 are the AVHRR channels 4 and 5 brightness temperatures, respectively. Among the different equations tested in that study, Equation 4 produced the smallest RMS error.

Coefficients appropriate to three Arctic clear-sky "seasons" (spring, summer and winter) were created through statistical analysis of the atmospheric profiles for the NOAA 7, 9 and 11 satellites. Results showed the overall RMS error for all seasons to be less than 0.1 K. However, this value is based on the regression analysis of the modelled data only. *Lindsay and Rothrock* [1993] applied the same coefficients to summer data from Arctic drifting buoys and reported a bias of +4 K which they ascribed to the presence of ice crystal precipitation (also known as "diamond dust").

The same approach was taken by *Haefliger et al.* [1993], who used thermal radiances from AVHRR channels 4 and 5 of NOAA 11 and temperature, pressure and humidity profiles collected over the Greenland Ice Sheet. The *in situ* data were used in the LOWTRAN 7 radiative transfer model to retrieve the correction coefficients for atmospheric effects. The comparison between measured IST and the calculated AVHRR IST showed differences of +0.5 to -0.6 K, with a mean difference of approximately -0.2 K and a RMS error of 0.3 K.

Maslanik and Key [1993] used co-located sets of AVHRR and SSM/I passive microwave imagery to estimate IST in the Arctic. The authors used the coefficients from *Key and Haefliger* [1992] to estimate the surface temperatures in 25 x 25 km cells. In spite of the errors reported (up to 4 K), the authors concluded that this technique could be improved if smaller cells were used. The advantage of the method is the small amount of AVHRR data necessary to calibrate the SSM/I imagery, which can be then used to calculate physical temperatures on a larger scale. However, it should be noted that sea ice, snow and ocean emissivities at microwave frequencies cover a wider range.

Key et al. [1997a] subsequently presented an improvement to the *Key and Haefliger* [1992] method which could be applied to thermal data from the Along-Track Scanning Radiometer (ATSR) and the AVHRR sensors both in the Arctic and in Antarctica, over ocean and land. For the AVHRR sensors in the Southern Ocean, the equation proposed is:

$$T_{ice} = a + bT_4 + c(T_4 - T_5) + d[(T_4 - T_5)(\sec\theta - 1)] \qquad \textbf{Equation 5}$$

where θ is the scan angle and a, b, c and d are the scan-angle dependent coefficients.

The AVHRR radiances were simulated via LOWTRAN 7 using more than 1000 radiosonde profiles from 18 Antarctic stations between 1982 and 1990 and the coefficients a, b, c and d were derived separately for three temperature ranges ($T_4 < 240$ K, $240 < T_4 < 260$ and $T_4 > 260$) in order to increase the algorithm's flexibility. The validation process, which utilised satellite data coincident with surface observations made at two sites in the Arctic, showed an improvement over previous studies: the accuracies found varied between 0.3 and 2.1 K (RMS errors). The authors concluded that this method is suitable for application over homogeneous surfaces, even when applied in conjunction with current cloud-masking techniques.

IST retrievals using the methods described above have an accuracy of 0.1 K - 0.2 K in the case of modelled data or 1 K - 4 K if more realistic approaches are considered, including accounting for uncertainties in the measurements and physical (atmospheric and surface) systems. The resultant errors in the longwave upwelling fluxes obtained with these values vary from 3 to 11 $W \cdot m^{-2}$ at 230 K and from 5 to 18 $W \cdot m^{-2}$ at 270 K. These values are of the same order of magnitude as the variations expected in a monitoring scenario [*Steffen, et al.*, 1993].

2.2.4.6 Narrow-Band Albedo

Satellite visible and near-infrared sensors provide the only effective means of evaluating large-scale spatial and temporal changes in the albedo of sea ice covered areas [*Lindsay and Rothrock*, 1994a]. The AVHRR's multi-spectral narrow-band radiometer scanners, with their small fields of view (see Table 4 - Channels 1 and 2), can be used to estimate the broad-band (planetary) albedo for the shortwave spectrum (from 0.24 to 4.2 μm), provided the scattering and absorbing effects of the atmosphere are properly considered. This can be achieved by numerical simulation or by using radiative transfer models [*Koepke*, 1989; *Steffen, et al.*, 1993]. A review of recent attempts to derive albedo from AVHRR data is presented in this section.

Haefliger et al. [1993] used NOAA 11 radiances from channels 1 and 2 and *in situ* data to derive albedos for the Greenland Ice Sheet. The results for the AVHRR-derived narrow-band albedo, when compared to ground observations modelled by LOWTRAN 7, showed a difference of less than 0.02 in the visible band. However, for the near infrared channel, the difference was 0.14, probably due to inaccuracies in the aerosol scattering modelling.

Lindsay and Rothrock [1993; 1994a] estimated the surface albedo by applying the following steps to a NOAA-10 and NOAA-11 AVHRR Arctic dataset: *a)* obtain the digital counts from the AVHRR images; *b)* determine the narrow-band radiances; *c)* calculate the TOA reflectance assuming a Lambertian surface; *d)* account for the anisotropic reflectance of the ice and atmosphere; *e)* correct for atmospheric interference; *f)* convert the narrow-band (AVHRR channel) reflectance to broad-band albedo, and *g)* normalise to a common solar zenith angle of 70°. These steps are discussed in more detail in Chapter 4 (Section 4.3.2.1), as *Lindsay and Rothrock's* method is employed in this study.

Lindsay and Rothrock reported many uncertainties in both studies, exacerbated by the lack of adequate surface-based data with which to evaluate the results independently. However, they acknowledge that the results can be improved by incorporating better data on the characteristics of the polar atmosphere such as aerosol concentration and ozone distribution. In spite of recent efforts in this field, the post-launch calibration of the radiometers remains the largest source of uncertainty of this method.

Schweiger et al. [1993] carried out a comparison between spatial patterns of Arctic monthly surface albedo derived from DMSP Operational Line Scan (OLS) data and values derived from AVHRR channel 1 for the International Satellite Cloud Climatology Programme (ISCCP). Results showed that the albedo values from both techniques are in general agreement, although systematic differences of 5% - 10% were found, probably related to uncertainties in the parameterisations used in the DMSP analysis.

The error sources described by *Lindsay and Rothrock* [1994a], along with cloud contamination of pixels and sensor degradation, are common to all of the narrow-band albedo retrieval attempts made so far. At this stage, the expected error can be as large as 10%, which, after the calculation of the heat flux budget, can be equated to a difference of 3 K in the air temperature on an annual mean basis. This value is too large to permit the use of these techniques in examinations of climate sensitivity. Further studies involving AVHRR Antarctic imagery are necessary. *Steffen et al.* [1993] recommended the following improvements:

a) Measurements of humidity, aerosol and ozone concentrations to characterise the atmospheric conditions and account for absorption and scattering;

b) A reduction in the uncertainties for a possible large-scale operational retrieval of albedo values, through a statistical climatology of aerosol, ozone and humidity distribution, including different regions of the Arctic and Antarctic;

c) The use of high spectral resolution radiative transfer models in order to correct the absorption and scattering effects, and;

d) Careful monitoring of AVHRR radiometric degradation over time. The issue of monitoring the time-dependent calibration coefficients for the visible channels of AVHRR have been addressed in recent studies [*Cihlar and Teillet*, 1995; *Rao and Chen*, 1994; *Teillet and Holben*, 1994].

Knap and Oerlemans [1996] applied a method similar to that of *Lindsay and Rothrock* [1994a] to derive the surface albedo of the Greenland Ice Sheet during the 1991 melting season. However, the authors assumed that the reflected radiation field is isotropic, so that the planetary albedo would equal the spectrally-integrated albedo. Because of the homogeneity of the Greenland Ice Sheet, it was possible to set a representative value of the surface albedo and then calculate the atmospheric attenuation coefficients, avoiding the use of radiative transfer models, a method which would not be as successful if applied to the much more heterogeneous Antarctic sea ice surface. A comparison between the measured and modelled data showed a high degree of consistency in temporal variability. However, large and consistent average differences (up to 0.08) between the satellite and the ground albedos were found. The authors attributed these differences to variations of the albedo on a sub-pixel scale and also to errors introduced by the method employed to retrieve the satellite albedo.

Stroeve et al. [1997] compared AVHRR-derived and *in situ* surface albedos over the Greenland Ice Sheet between 1990 and 1993. Their study used the 6S radiative transfer model to determine the coefficients for atmospheric correction. It also incorporated an improved relationship between channel 1 and 2 narrow-band reflectances and the broad-band albedo based on regression statistics from measurements carried out in the field. More importantly, the authors also modelled the anisotropic reflection function (f) using a discrete-ordinate radiative transfer model, which, for AVHRR channel 2, showed a direct proportionality between f and snow grain size. These results agree with the observations of *Wiscombe and Warren* [1980] who proposed that, for the near-infrared wavelengths, snow becomes more forward scattering with an increase in grain size. The comparison between the AVHRR-derived and surface-measured broadband albedo in *Stroeve et al.* [1997] showed good agreement before the snow began to melt. However, the improvements of this method are somewhat restricted to the homogeneous conditions of the Greenland Ice Sheet and are linked to long-term field measurements of radiative fluxes, spectral reflectance, ice and air temperature, humidity, pressure and cloud observations.

2.3 Modelling of Sea Ice Thickness

In response to the need for large-scale mapping of the Antarctic sea ice thickness distribution, this study seeks to develop a technique which melds remote sensing with numerical modelling techniques. In so doing, it exploits the relatively high spatial resolution of the AVHRR and the more complete spatial and temporal coverage offered by satellite remote sensing. A brief history of the development of numerical models is followed by a review of studies where this technique is applied to gather information and predict the future behaviour of key properties of the sea ice cover in the polar regions.

The interaction between the atmosphere and ocean at high latitudes is considerably affected by the presence of sea ice. Being essentially inhomogeneous, the sea ice cover responds to both dynamic and thermodynamic forcing in a very complex manner which ultimately reflects on changes in the atmospheric and oceanic circulation patterns. Therefore, accurate modelling of the sea ice cover is an essential prerequisite to the improvement of numerical investigations of potential climate changes [*Hibler*, 1980].

The concept that the physical laws which govern the atmosphere, the oceans and the cryosphere could be used to simulate and predict future conditions is the basic principle of numerical modelling of the climate system. By the end of the nineteenth century, the fundamental principles of classical Newtonian mechanics and the laws of thermodynamics were already available, which led to the first developments in the science of accurate prediction through means of numerical calculation [*Washington and Parkinson*, 1986].

It soon became obvious that the equations involved in those calculations are highly complex and could not be solved without the aid of electronic computing resources which became available only in the late 1940s. This was the framework in which the first weather forecasting models were created. With the advance of computational technology in the mid-1960s, the atmospheric models were soon followed by large-scale ocean models and calculations aimed to investigate the role of the land, biosphere and cryosphere. However, the incorporation of all these components into large scale models only began to take place in the early 1980s [*Washington and Parkinson*, 1986]

Sea ice models can be classified broadly as *dynamic*, *thermodynamic* and *coupled dynamic-thermodynamic* [*Hibler*, 1980]. Thermodynamic sea ice models seek to calculate the thickness and temperature structure of the sea ice, making use of the principle of conservation of energy, while dynamic sea ice models are based on the principle of conservation of momentum and focus on the drift of sea ice. Coupled dynamic-thermodynamic models are concerned with the large-scale variability of sea ice and seek to predict ice drift, thickness and concentration [*Häkkinen*, 1990; *Washington and Parkinson*, 1986].

Coupled dynamic-thermodynamic models comprise four components, namely: *a)* thickness distribution equations describing the evolution of ice thickness due to thermodynamic and dynamic effects; *b)* a momentum balance describing ice drift; *c)* an ice rheology relating ice stress to ice thickness and deformation characteristics; and *d)* ice thermodynamics. The work of *Parkinson and Washington* [1979] and *Hibler* [1979] in the Arctic, and *Parkinson* [1983] in the Antarctic are representative of this type of sea ice model.

Unlike ocean and atmospheric models, which focus on determining the properties of the water and air, sea ice models used in climate simulations focus on a given geographical location and time step, determining the presence or absence of ice. In cases where ice is present, the models seek to calculate its areal concentration and thickness [*Washington and Parkinson*, 1986]. The present section will concentrate on the review of literature published on thermodynamic sea ice models which relate more closely to the scope of this study.

Several authors have attempted to develop empirical relationships to predict the sea ice growth, based on temperatures observed at its surface [*Barnes*, 1928; *Bilello*, 1961; *Bilello*, 1964]. Notwithstanding the practical value of those studies, they do not include a physical background which is realistic enough to describe the phenomenon [*Maykut and Untersteiner*, 1971]. Improvements in the speed of computational methods allowed the development of numerical models to simulate the thickness and the horizontal extent of the pack ice. The work of *Untersteiner* [1966] and *Budyko* [1966] are representative of these developments.

Maykut and Untersteiner [1971] proposed a one-dimensional thermodynamic sea ice model which laid the foundation for future studies. Its calculations accounted for the effects of ice salinity, snow cover, and internal heating caused by the penetration of solar radiation. In this model, sea ice is assumed to be an infinite horizontally homogeneous slab with energy fluxes occurring at both surfaces: the snow/ice - atmosphere boundary and the ice - ocean boundary.

Heat balance equations relate the various energy fluxes towards and away from the boundaries to the rates of freezing and melting. Figure 3 shows the heat balance in an atmosphere - snow/ice - ocean system as described in the *Maykut and Untersteiner* [1971] study. The fluxes that occur in this system are:

F_L	Incoming long-wave radiation from the atmosphere and clouds
F_r	Incoming solar short-wave radiation
αF_r	Reflected short-wave radiation, where α is the surface albedo
$\varepsilon_L \sigma T^4$	Outgoing long-wave radiation, where ε_L is the long-wave emissivity and is σ the Stefan-Boltzman constant
F_s	Sensible heat
F_l	Latent heat
F_c	Conductive heat flux in the ice or snow
I_0	Flux of radiative energy through the surface into the ice
F_w	Oceanic turbulent heat flux

Monthly values of F_r, F_L, F_s and α for the Arctic perennial sea ice, proposed by *Fletcher* [1965], were employed by *Maykut and Untersteiner* to provide the boundary values (energy fluxes) for the model's initial conditions. Average values of snow cover and ice salinity were also suggested and the initial thickness was set to 3.40 m.

The results showed an average equilibrium thickness of 2.88 m with a maximum of 3.14 m and a minimum of 2.71 m. The amount of surface ablation predicted was 0.4 m. Although these values and the predicted temperature field differ somewhat from contemporary submarine data available at the time, they are in good agreement with data from drifting stations established on the Arctic pack ice. According to *Maykut and Untersteiner*, the main limitations of this model are: *a)* its inability to account for the effects of the wind in producing mechanical stresses in the ice; *b)* the fact that it requires an existing layer of ice and; *c)* the fact that F_r, F_l and F_w are assumed to be independent of growth rate and the physical state of the ice at the boundaries, i.e., the environment affects the ice but not *vice versa.*

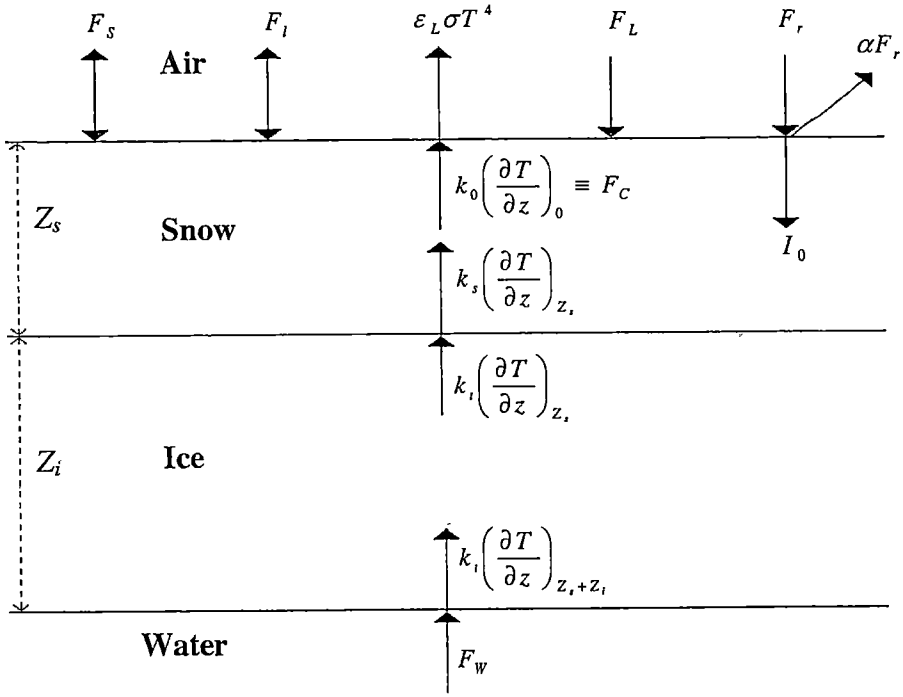

Figure 3 Schematic illustration of *Maykut and Untersteiner*'s [1971] sea ice model. The coefficients k_i and k_s represent the thermal conductivity of ice and snow and Z_i and Z_s are the thicknesses of the ice and snow respectively.

After *Maykut and Untersteiner* [1971], several studies have addressed the thermodynamic growth and decay of sea ice using models under different conditions, both in the Arctic and Antarctica [*Bintanja and Oerlemans*, 1995; *Grumbine*, 1994; *Heil, et al.*, 1996; *Ramstein and Joussaume*, 1995; *Semtner*, 1976].

Key et al. [1996] evaluated recent parameterisations for downwelling shortwave and longwave radiative fluxes that can be used in thermodynamic sea ice models and concluded that existing methods perform reasonably well for clear sky conditions (RMS errors of 4% and 6% for shortwave and longwave fluxes respectively). With the advent of satellite technology, it became evident that thermal infrared and visible imagery could be used in association with thermodynamical models to characterise the sea ice and predict changes.

Maykut [1986] provided the theoretical foundation for the calculation of ice thickness with known ice surface temperature, surface air temperature, and the freezing temperature of sea water. In this review, *Maykut* presents the various components of the surface heat balance of the Arctic sea ice, introducing recent parameterisations obtained from several different authors.

Groves and Stringer [1991] proposed the use of AVHRR imagery to distinguish between ice and open water areas in the Chukchi Polynya in the Arctic, to calculate its area and also to provide data for ice thickness calculations. For these calculations, the authors tested two empirical equations proposed respectively by *Anderson* [1961] and *Maykut* and two models proposed by *Maykut* [1986] and *Kuhn* [1975]. *Maykut's* model showed results that appear to be more realistic for the ice thickness distribution within the polynya, although the movement of floes in its later stages of formation caused problems with the thickness calculations.

Yu and Rothrock [1996] made quantitative estimates of the thickness of thin ice in the Beaufort and Greenland Seas in early winter and spring using AVHRR imagery. *Maykut and Untersteiner's* [1971] model was combined with satellite observations of albedo and snow/ice surface temperature to produce estimates of the sea ice thickness for each pixel in the images. These thicknesses were then binned to produce the thickness distribution of ice up to a metre thick in each scene. The equation for conservation of energy at the top of the ice/snow surface was specified according to *Maykut and Untersteiner's* model as:

$$(1-\alpha)F_r - I_0 - \varepsilon_L \sigma T^4 + F_L + F_s + F_l + F_c = 0 \qquad \textbf{Equation 6}$$

The definition of the fluxes in Equation 6 is given on page 214 above.

This equation allows the solution of the model for ice thickness (Z_i) using AVHRR estimations of the surface albedo (α) and the snow/ice surface temperature (T_{Sfc}). Further details on *Yu and Rothrock's* method and its adaptation for the sea ice conditions found in the Southern Ocean will be discussed in Chapters 4 and 5.

Yu and Rothrock conducted an assessment of the uncertainties associated with the heat fluxes and surface albedo at two different ice thicknesses (0.2 m and 0.8 m) for the winter and spring seasons, with the objective of determining the magnitude of the error of this method. They found that the largest sources of error came from downward radiation and sensible heat flux in winter and from solar radiation and surface albedo in spring. The variance in the thickness error is about half the ice thickness, but the uncertainty of the cumulative distribution in three examples was no more than 3% for ice thinner than 0.2 m and 9% for ice thinner than 0.8 m.

A comparison between the AVHRR-derived thicknesses and ULS data from three locations inside the study area showed that, in spite of the satellite's limited temporal sampling and its inability to resolve sub-pixel features, the difference between the two methods was generally less than 2%. The authors concluded that this method was suitable for monitoring the thin end of the ice thickness distribution in the Arctic.

Data Collection and Processing

This chapter consists of a description of the data used in this study and the methods employed to collect and analyse them. It is divided into two sections: Satellite data and *in situ* data. Visible/near infrared and thermal infrared remote sensing data (i.e. from the AVHRR sensor) are employed to generate estimates of albedo and ice/snow surface physical temperature, respectively. This information is the main input to an algorithm designed to estimate sea ice thickness (see Chapter 4). *In situ* data are then employed to compare and validate the results.

3.1 Satellite Data and Techniques

Satellite data from two areas of the East Antarctic pack ice were selected for this study. The first area (named Mertz hereafter) is located around the Mertz Glacier Tongue (≈ 67° S, ≈ 145° E) and extends northwards to 58° S (covering an area approximately 1250 km by 760 km). The second area (named Davis hereafter) has its southern end located around the Prydz Bay area, including Davis Station (66° 15' S, 110° 32' E), with the northern end at approximately 57° S (covering an area approximately 1500 km by 500 km). These areas were selected to coincide with the regions visited by two cruises which are described in Section 3.2.1. Figure 4 shows the location of the Davis and Mertz areas, along with the RSV *Aurora Australis'* track for the two voyages from which *in situ* data were employed (see Section 3.2).

3.1.1 AVHRR

The primary set of remote sensing data for this study were AVHRR images from the NOAA-14 polar orbiting satellite. A description of the general characteristics of the spacecraft and the sensor can be found in the literature review (Section 2.2.4.3) or in texts such as *Kidwell* [1998] and *Cracknell* [1997]. These images were routinely collected by the Commonwealth Scientific and Industrial Research Organisation (CSIRO) Marine Research Laboratories in Hobart and by the Antarctic Meteorological Centre (AMC) at Casey Station. All of the AVHRR passes that fell inside the study areas were extracted from the original dataset and recorded onto DAT tapes.

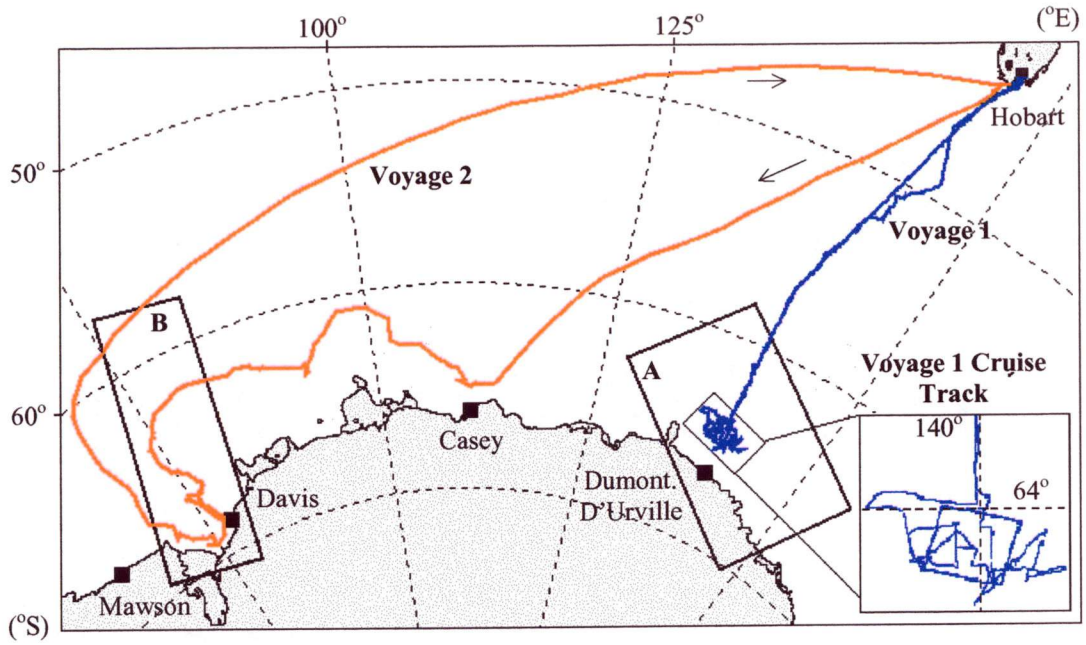

Figure 4 Location of the two study areas: Mertz (**A**) and Davis (**B**), along with the cruise tracks for Voyage 1 - 1995 (Blue) and Voyage 2 - 1996 (Red). See section 3.2.1 for details on the cruises.

The preliminary processing of the images took place at the Antarctic CRC as part of an on going large-scale initiative including several projects such as a survey of polynyas and mapping of UV radiation in the East Antarctic sector. The methods of decoding, calibration, navigation and cloud screening are described in more detail below. Additional information can be found in *Hill* [2000].

The main steps in the processing are as follows:

a) Retrieving raw data from tape.

The raw AVHRR pass data consists of a TBUS file (which contains all the meta-data necessary to geolocate and navigate the image) and the data themselves. In this first step, they are retrieved from the original tapes and converted into a format compatible with the Device Independent Software for Image Processing (DISIMP) software which has been developed by CSIRO for the display, processing and analysis of digital images. The orbit number, the pass ID and the position of each image on the tape are specified in a separate file also recorded on the tape. The conversion into the DISMP format includes the incorporation of gain and intercept values needed for the calibration of the visible and infrared channels and the application of a propagation model to predict the satellite's orbit [*Hill*, 2000].

b) Placement of the data into a region of interest.

To conform with the objectives established by the Antarctic CRC for the uses of AVHRR data mentioned above, the East Antarctic coast was divided into seven rectangular regions of interest, defined by minimum and maximum false eastings and northings (X,Y co-ordinates that correspond to the number of pixels from a pre-established origin) and one pair of latitude and longitude locations for each of the four corners. The Davis and Mertz areas coincide with two of these regions (see Figure 4). The reference X and Y co-ordinates and the latitudes and longitudes of the corners of both areas are presented in Table 5. In this step, the information contained in the TBUS file is analysed, providing the system with the necessary information to decide if the pass that is being processed contains data that fall into one of the regions of interest.

X	*Y*	*Latitude (°S)*	*Longitude (°E)*
		Davis Area	
2060	4400	70.859	79.011
2060	4900	69.522	66.400
3560	4900	57.102	75.812
3560	4400	57.865	83.589
		Mertz Area	
1150	1400	70.220	147.995
1150	2160	58.240	137.291
2400	1400	62.676	127.476
2400	2160	64.259	156.140

Table 5 Location of the four corners of the Davis and Mertz areas. Adapted from *Hill* [2000].

c) Conversion of raw data into geophysical parameters.

This routine transforms the raw digital counts (integer values from 0 to 1023) from each of the five channels into albedos (for channels 1 and 2) and brightness temperatures (for channels 3 to 5). These calibrations are performed using fixed coefficients, taken from every 50^{th} line of the original image. Further details on the calibration of the solar reflective and thermal infrared channels can be found in *Hill* [2000] and *Kidwell* [1998]. The routine also produces a "solar zenith angle" band (with a precision of two decimal places) to be used in the next step.

d) Solar zenith angle correction.

The signal sensed by AVHRR channels 1 and 2 is affected at any given time by the position of the sun. If the sun is lower in the sky, this would result in relatively little radiation being received by the sensor which would produce lower albedo estimates. To normalise the data for this effect, the albedos of each pixel obtained through the conversion routine mentioned above are divided by the cosine of their corresponding solar zenith angle (θ_0). This normalisation routine also discards pixels with θ_0 greater than 85°. Similar cut-off values have been suggested in other AVHRR polar studies such as *Lindsay and Rothrock* [1994a].

e) Re-warping the image to a polar stereographic projection.

This routine redefines the albedos and brightness temperatures into the selected areas of interest by re-mapping the data into a polar stereographic projection centred at 71° S with its central meridian at 180° E (Figure 5). This displacement of the origin was chosen to ensure that X and Y co-ordinates in all regions of interest in East Antarctica are positive. The equations for the projection conversion are taken from the General Cartographic Transformation Package (GCTP) developed by the U.S Geological Survey [*Snyder*, 1987]. This routine also replaces the "solar zenith angle" band created in step *c)* by a file (*angles.dat*) containing more precise values of the direction cosine for the sun and the satellite.

f) Checking of the solar zenith angle.

After re-warping, there is the possibility that portions of images with acceptable values of θ_0 may have been discarded due to the use of the less precise "solar zenith angle" band. This routine uses the better resolution of the *angles.dat* file created in *e)* to reclaim data that were discarded erroneously.

g) Rotating the image and angle data.

In order to ensure that all images are navigated with north in the same position (*i.e.* to the right), this routine checks each image of the dataset and performs a 90° rotation in both the data and the *angles.dat* file, if necessary.

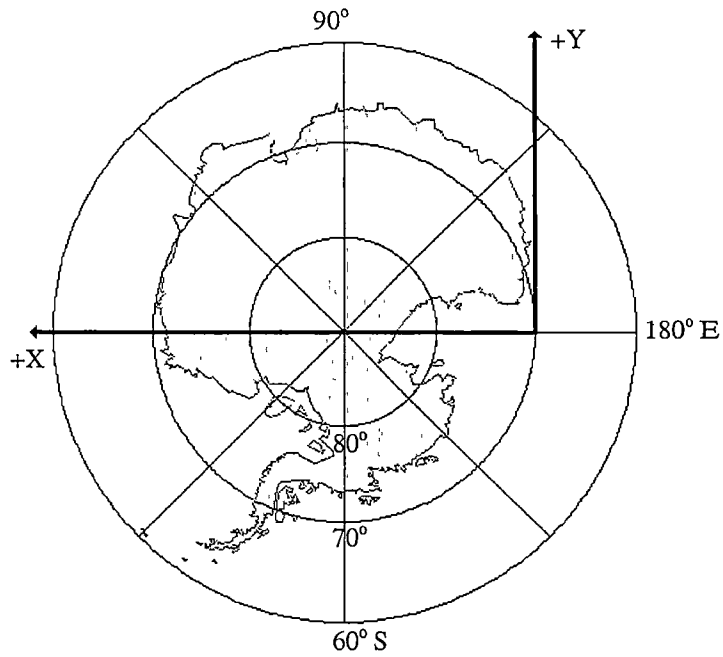

Figure 5 Positions of the X and Y axis in the polar stereographic projection employed by the Antarctic CRC to re-map the AVHRR dataset.

h) Creation of the ice classification map.

This step consists of applying an automated image-analysis system to detect cloud-covered pixels and classify sea ice pixels according to their concentration. This system, known as ICEMAPPER, was developed as a tool to assist forecasters at the AMC in the interpretation of Antarctic AVHRR imagery and the production of sea ice maps for navigation and logistical purposes. It utilises the calibrated albedo values from channels 1 and 2 and the brightness temperatures from channels 3, 4 and 5. Its basic principle is to determine a set of relationships between various albedo and brightness temperature values that characterise different ice classes, such as nilas, snow-free young ice, first-year ice etc.

ICEMAPPER drastically reduces both the time required for this task (compared to manual interpretation and production of maps) and the possible ambiguity in distinguishing between clouds and sea ice [*Williams, et al.*, in press]. A comparison between ICEMAPPER outputs and the manual interpretation of 1406 pixels from two test images from East Antarctica was conducted by *Williams et al.* [in press]. This comparison showed that the system produced a correct identification in 79.1% of cases. However, the mis-classification rate increases considerably in autumn and winter images and in those images where the solar zenith angle is greater than 75°.

An appropriate class for each pixel in the image is then determined by applying those relationships through a set of rules. These rules were derived from information gained from current sea ice and cloud research [*Ebert*, 1992; *Gesell*, 1989; *Massom and Comiso*, 1994; *Zibordi and Van Woert*, 1993] and from the analysis of 20 summer images (from December 1996 to April 1997) of the East Antarctic performed by an expert image interpreter [*Williams, et al.*, in press].

While ICEMAPPER requires some development and validation, it provided useful output by separating the image into areas of cloud, water and ice. Even though the output also included a sea-ice concentration product, this was not incorporated into the present study.

i) Spatial filtering.

The last step of the preliminary processing aims to reduce the number of mis-classified pixels through a spatial filter that operates on the ice map created in step *h)*. A manual analysis of selected images showed that those pixels could be safely classified as interference or noise because of their random distribution throughout the scene and their exceptionally high digital count values. The filter flagged as invalid the pixels with extreme values (i.e. albedos higher than 1 and brightness temperatures higher than 273 K or lower than 220 K). Random noise is removed through the application of a low pass spatial filter based on a matrix with dimensions of 3 x 3 pixels.

The final result of the preliminary processing is an image containing seven bands: the five AVHRR bands (two albedo and three brightness temperature bands), an "angles" band (containing information on the solar zenith angle, satellite zenith angle and sun-satellite azimuth angle) and the classified band (i.e. ice map) which is an output from the ICEMAPPER system. The dimensions of each band are: 501 columns by 1501 lines for the Davis area and 760 columns by 1250 lines for the Mertz area. The pixel size in both cases is approximately 1.0 km^2. The classified band contains integer values that correspond to 12 different classes, which were used to separate valid sea ice pixels from clouds, land and null data. Figure 6 shows ICEMAPPER classes and their corresponding colours and codes, along with an example of a classified image.

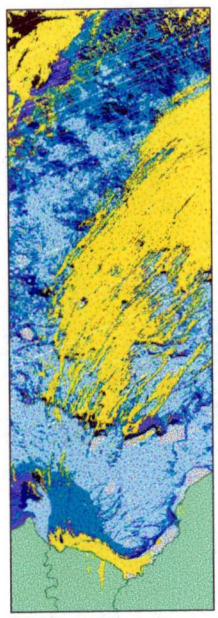

Colour	*Class*	*Code*	*Concentration*
	Open Water	0	-
	Null Data	1	-
	Cloud	5	-
	Coastline	25	-
	Land (Bare)	27	-
	Land (Ice)	29	-
	Continental Ice	23	-
	Compact Sea Ice	23	Fast Ice/Icebergs
	Very Close Sea Ice*	12	9/10
	Close Sea Ice*	7	7/10 to 8/10
	Open Sea Ice*	19	4/10 to 6/10
	Very Open Sea Ice*	17	1/10 to 3/10

Figure 6 An example of ice map from the Davis area based on an NOAA-14 image from 30-Sep-1996 at 0909 Z. The table shows the classes generated by the ICEMAPPER system. The asterisk (*) denotes classes containing valid sea ice pixels. The descriptors of each class and the associated concentrations (as defined by the WMO classification) are presented in the methods of *Williams et al.* [in press].

3.2 *In Situ* Data

The techniques employed to collect *in situ* sea ice data from East Antarctica, both for input into the algorithm and for validation purposes, are described in this section. Data sources include ship-based sea ice observations, environmental and meteorological data, ship-borne radiometric data, digital aerial photography and video footage.

3.2.1 Description of the Cruises

Data employed in this study were collected during two cruises - Voyage 1 (95) and Voyage 2 (96) - of the RSV *Aurora Australis* (Figure 7) to the East Antarctic as part of the Australian National Antarctic Research Expeditions (ANARE) programme. These cruises are part of a multiyear investigation which has been conducted by the Sea Ice Sub-Programme of the Antarctic CRC since 1991 to determine the regional and interannual variability in the characteristics and physical properties of the pack ice from 75° to 150° E and 60° to 70° S [*Worby and Allison*, 1999; *Worby and Massom*, 1995]. To date, sea ice research has been performed on nine cruises between 1991 and 2000.

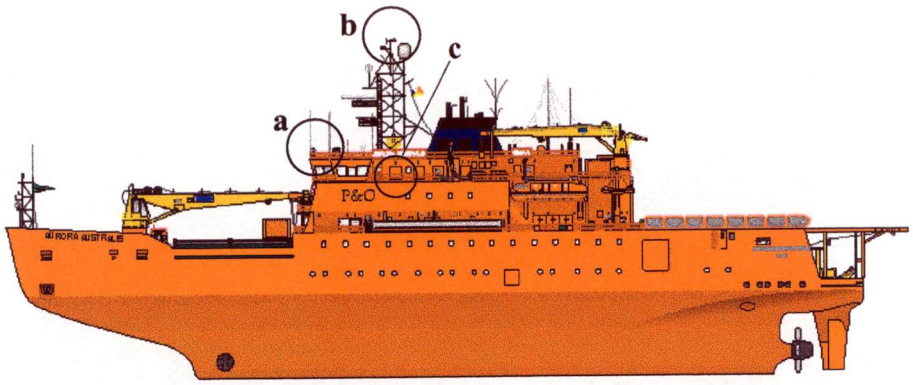

Figure 7 The RSV *Aurora Australis*. The location of the meteorological instruments mentioned in Section 3.2.3 is shown in (**a**) and (**b**). The position of the radiometer described in Section 3.2.4 is shown in (**c**).

Voyage 1 (95) was dedicated to a multi-disciplinary study conducted between August and September 1995 to understand the interactions between atmosphere, sea ice and the ocean in the East Antarctic pack ice during winter. Its objectives were: to provide quantitative estimates of various components of the surface energy balance, to determine the processes of ice formation and thickening and to quantify the mass budget of the East Antarctic sea ice. Further details on this experiment can be found in *Lytle et al.* [1998b], *Massom et al.* [1998b], *Worby et al.* [1996b] and *Worby et al.* [1998].

Voyage 2 (96) occurred between September and November 1996 and included both a scientific programme and re-supply operations at Casey (68° 35' S; 77° 59' E) and Davis (66° 15' S; 110° 32' E) stations. Along with the activities carried out as part of the Antarctic CRC's multiyear investigation of sea ice described above, four other related experiments occurred on this cruise: the measurement and modelling of UV-B radiation, the measurement of physical, thermal and optical properties of various types of sea ice, the analysis of solar radiation processes in the sea ice and thermal infrared radiometric measurements of sea ice and open water. Figure 4 shows the tracks of the RSV *Aurora Australis* for the two cruises, along with information on satellite data described in Section 3.1. These cruises were chosen primarily because of the availability of remote sensing data and the collection of *in situ* thermal infrared radiometric data which was specifically designed for this study.

3.2.2 Ship-Based Sea Ice Observations

Ship-based observation is a particularly useful method as it allows the characterisation of the pack ice at a relatively fine scale of 100s of metres and provides a quasi-synoptic coverage of the area visited by the ship [*Worby and Allison*, 1999]. The method of observation employed in this study was developed by the Sea Ice sub-programme of the Antarctic CRC and has been used on several cruises in East Antarctica since 1988 [*Allison, et al.*, 1993; *Allison and Worby*, 1994; *Worby, et al.*, 1998]. *Worby and Allison* [1999] described this observational method, which has been endorsed and adopted by the SCAR/ASPeCt programme as the preferred protocol for conducting ship-based observations of sea ice characteristics.

According to *Worby* [1998], the accuracy of the method varies with ice thickness. For thin ice types (< 0.3 m) it is estimated to be 20% of the actual thickness, while for ice types thicker than 0.3 m, the accuracy improves to 10%. For ice types thicker than 1 m, the error increases primarily because of deformation processes. Thickness estimates are not made for deformed floes.

Sea ice thickness data obtained from these observations, supplemented by video footage and meteorological information, were directly compared with the results of the satellite-based procedure developed in this study (see Section 5.3.1). Each observation was treated as a data point. Although video imagery cannot be used for a quantitative analysis, it can assist in the interpretation of the ship-based observations, and also in the identification of specific regions of interest.

Hourly observations were made by trained observers on the ship's bridge. The three dominant ice thickness categories - defined as those with the greatest areal concentration - were determined within a radius of approximately 0.5 nautical miles from the ship. Within these three dominant categories, the thickest is defined as the primary ice type and the thinnest as the tertiary ice type [*Worby and Allison*, 1999]. For each category, the observers estimated the following characteristics:

a) *Ice Thickness:* expressed in centimetres. A spherical buoy, 0.55 m in diameter, was suspended over the side of the ship, close to the water line, to provide a scaled reference for the thickness estimates of level floes turned sideways along the ship's hull. Thinner, snow-free ice types such as nilas and grease ice were classified according to contrasts in their apparent albedo (i.e. light nilas versus dark nilas) and the thickness of very thick floes was estimated by their freeboard [*Worby and Allison*, 1999]. Table 6 shows the range of thicknesses associated with different types of sea ice and the code used to identify them in the ship-based observation protocol.

Ice Type		*Thickness (m)*	*Code*
New Ice	Frazil	< 0.1	10
	Shuga		11
	Grease		12
	Nilas		20
Pancakes		<0.2*	30
Young grey ice		0.10 - 0.15	40
Young grey-white		0.15 - 0.30	50
First-year ice		0.30 - 0.70	60
First-year ice		0.70 - 1.20	70
First-year ice		> 1.20	80
Multiyear ice		< 20*	85
Brash		< 0.5*	90
Fast ice		< 3.0*	95

Table 6 Sea ice types and their thickness ranges according to the WMO classification, along with their corresponding ship-based observation protocol codes. The asterisk (*) indicates that the thickness range is a guide only. Adapted from *Worby and Allison* [1999] and *WMO* [1970].

b) *Ice Concentration:* an estimate of the total area covered by ice floes (in tenths);

c) *Ice Type*: classified according to the WMO [1970] sea ice nomenclature and expressed in a two digit code (see Table 6);

d) *Floe Size*: the average size (in metres) of floes assigned to the category, recorded using a three digit code. A new sheet ice code was normally used for nilas;

e) *Topography*: this category was used to estimate the areal extent and mean sail height of ridges for each ice type. The mean sail height was estimated to the nearest half-metre below 2 m, and to the nearest metre above 2 m. A three-digit code was used to classify the ridges: the first digit, from 5 to 8, described the type of the ridge. The second digit, from 0 to 9, described the areal coverage and the third, from 0 to 7, described the mean sail height to the nearest 0.5 m;

f) *Snow Cover*: an integer code between 0 and 10 was used to describe the different types of snow cover, such as fresh snow, wind-packed snow and glaze;

g) *Snow Thickness*: similarly to ice thickness, this parameter was expressed in centimetres and measured with reference to the 0.55 m spherical buoy;

h) *Open Water*: the amount of open water present in the pack was expressed by an integer code between 0 and 10 that described the size of cracks, breaks, leads and polynyas.

Additionally, the following environmental and meteorological parameters were recorded during each observation: water temperature (°C), air temperature (°C), wind speed (kt) and direction (°), visibility (km) and weather state (WMO code). Items *b)* to *h)*, along with the meteorological parameters were employed as additional sources of information to assist in the interpretation of eventual differences found between the *in situ* and the satellite-based methods.

A total of 562 ship-based observations were recorded during V1(95) and 459 during V2(96). Data were initially recorded in logbooks and then entered into a computer program designed specifically for the analysis of ship-based sea ice observation data. The main features of this system are: quality control, data editing, estimates of area-averaged ice and snow thickness and calculation of area-averaged albedo [*Worby and Dirita*, 1999]. The computer program also filters the data by removing hourly observations separated by less than 6 nautical miles, thereby avoiding the natural bias towards thicker ice (which acts to slow the ship's passage). Examples of observation sheets and the complete listing of codes used in this protocol can be found in *Worby and Allison* [1999] and *Worby* [1999a].

To assist with the interpretation of the data, a time-lapse video recorder system was installed on the ship's port rail (close to **c** in Figure 7). It consisted of a Phillips® LDH 0647/XX CCD camera mounted in an outdoor housing to protect the equipment from the elements. The camera was connected to a monitor and to a Javelin® Heliquad II video recorder installed in the ship's meteorology laboratory. The equipment was set to take approximately one frame every 8 seconds and the information was recorded on 180-minute VHS tapes. A photographic record was also maintained during both cruises, consisting of 35 mm slides taken from the bridge, whenever possible, at the time of each hourly ice observation.

3.2.3 Meteorological Data

Meteorological and environmental data from sensors installed on the RSV *Aurora Australis* were automatically recorded every 10 seconds by the ship's Data Logger System (DLS). The parameters shown in Table 7 were retrieved from the original dataset and imported into electronic spreadsheets for analysis. The air temperature and humidity sensors were mounted outboard of the port and starboard bridge wing railings, approximately 20 m above sea level (Figure 7 - **a**), while the wind sensors were mounted on the top of the main mast, 31.6 m above sea level (Figure 7 - **b**).

Parameter	*Unit*
Wind Speed*	$m \cdot s^{-1}$
Wind Direction*	°
Air Temperature*	°C
Relative Humidity*	%
Solar Radiation*	$W \cdot m^{-2}$
Ship Speed	Kt
Ship Heading (true)	°
Ship Position (lat./long.)	°
Atmospheric Pressure	hPa

Table 7 Meteorological and other parameters obtained from the RSV *Aurora Australis*' DLS. The (*) denotes the presence of instruments on both port and starboard sides.

3.2.4 Shipborne Radiometric Data

Radiometric data, collected only during Voyage 2 (96), were used to estimate the snow/ice surface temperature along the track of the ship. These data were employed to evaluate the accuracy of the snow/ice surface temperatures estimated by the AVHRR (Section 4.3.2.2) and the effectiveness of the method proposed to estimate the near-surface air temperature (Section 4.3.2.3).

One Everest® radiometer model 4000 ALCS (Figure 8 - **a**) was used to continuously measure the thermal infrared radiation emitted by water and snow/ice surfaces. The instrument, which is 0.125 m long and 0.065 m in diameter, was mounted on the ship's port-side railing (Figure 7 - **c**), approximately 15 m above sea level and was protected from salt, sea spray, rain, snow and solar radiation by a PVC shield (Figure 8 - **b**). The radiometer was connected to an IBM-compatible computer on which the resulting brightness temperatures (T_b) and the radiometer internal temperatures (T_r) were recorded approximately every 30 s.

The radiometer, viewed the target from a distance of 15 m with a beam width of approximately 1.5 and a filter band pass of 8 to 13 μm [*Rapier*, 1995]. The instrument was pointed downwards towards the surface at an angle of approximately 135° to the vertical to avoid the ship's wake and sea foam (in the case of open water measurements), to minimise the effects of reflection of sky radiation from the surface [*Schluessel, et al.*, 1990] and also to minimise contamination of the signal by the ship's superstructure.

Michael et al. [1998] made similar measurements with the Everest® radiometer during an earlier cruise of the RSV *Aurora Australis* between March and May 1993. Comparisons with a more sensitive (but less robust) thermal infrared radiometer and *in situ* ice surface temperature data showed that the Everest® performed inconsistently, probably because of the low temperatures encountered in the Southern Ocean at this time of the year, which fell outside the instrument's recommended range of operation (from 262.4 to 323.2 K). An attempt to insulate the instrument was made on Voyage 2 (96), but it was not completely successful and approximately 8% of the data from this voyage were removed from the analysis.

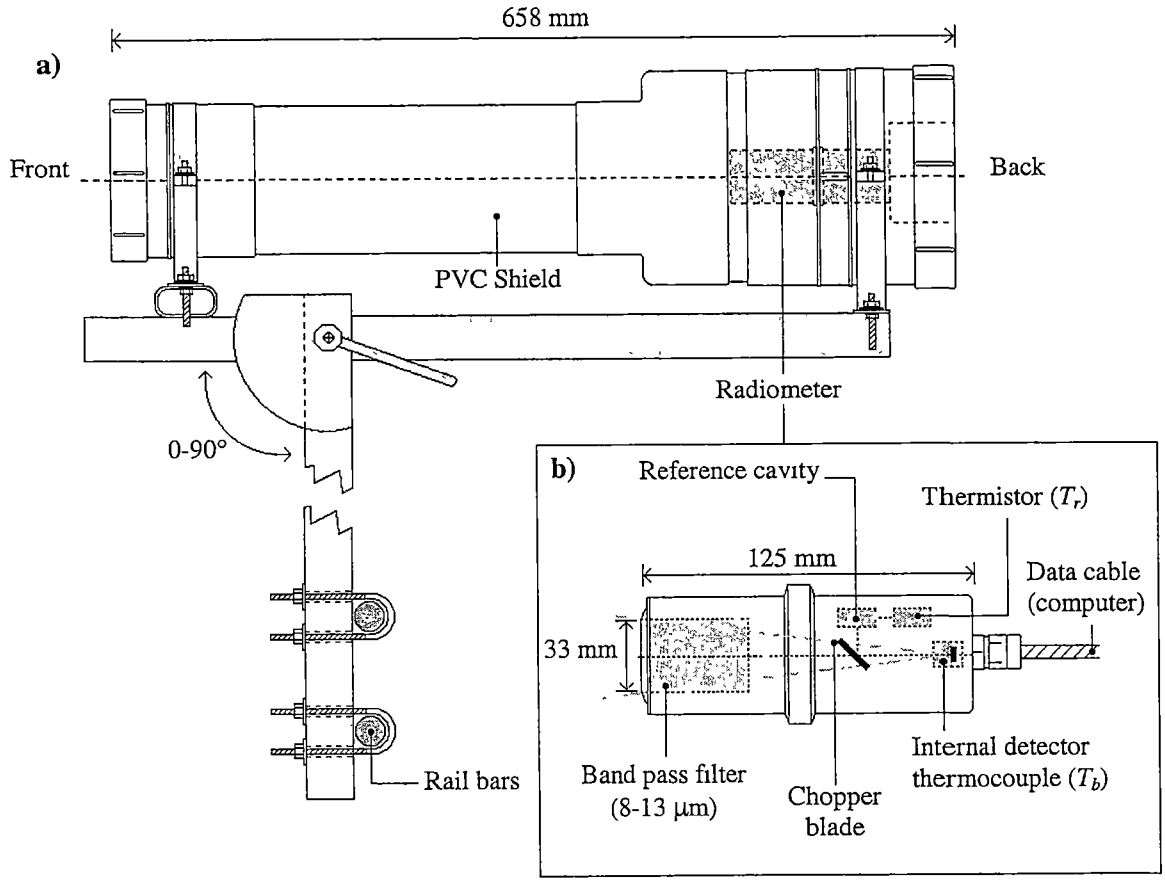

Figure 8 Schematic representation of the Everest® radiometer (**B**) and its PVC shield (**A**). Adapted from *Rapier* [1995].

To address the problem of inconsistency, a series of calibrations was made during the cruise using a calibration unit provided by the radiometer's manufacturer. The accuracy of the calibration unit was tested against a temperature probe and a Heintronics® KT19 hand-held thermal infrared radiometer (spectral range 8 to 14 μm) with satisfactory results. Nine sets of calibration measurements were made in air temperatures ranging from 263 to 298 K.

The results of these measurements, shown in Figure 9, indicate a good agreement between the temperatures of the radiometer and the calibration unit (slope $\approx$ 1.0), with the radiometer being consistently 4 K warmer. The coefficients from the calibration curve (T_r = 1.0086 T_s - 3.9808) were then used to correct the radiometer readings. Besides the procedures mentioned above, standard cold room calibrations (in temperatures ranging from 263 to 278 K) were also performed before the voyage. The methods and the equipment utilised in those calibrations are described by *Rapier* [1995].

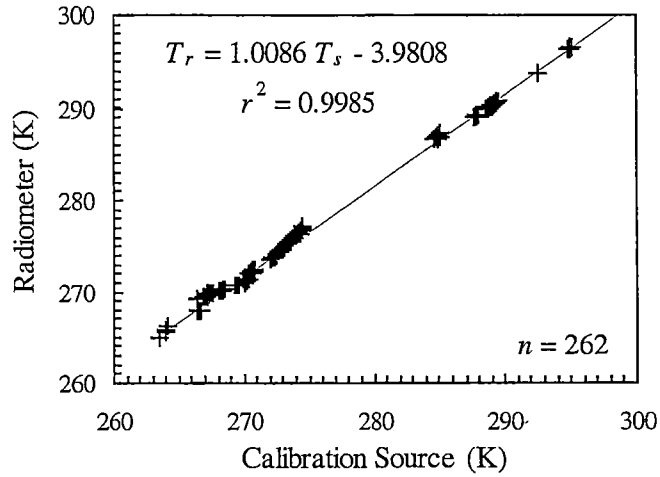

Figure 9 Correlation between the temperatures of the Everest® radiometer (T_r) and the calibration source (T_s) obtained from calibrations performed during Voyage 2 (96).

3.2.5 Digital Aerial Photography and Video Footage

Digital aerial photographs and video footage were collected on 15 flights during Voyage 1 (95) and 9 flights during Voyage 2 (96). These data were of use in interpreting AVHRR-derived ice thickness estimates (Section 5.3.1), providing important sub-pixel level information on how these estimates are affected by processes such as rafting and swell penetration. A Kodak® DCS digital camera was mounted inside the helicopter to look down vertically through a hole in the fuselage. Figure 10 and Table 8 show the details of helicopter flights from both cruises which coincided with the two study areas.

The digital camera was connected to a Macintosh® 520c laptop computer and was operated by software designed to produce overlapping images by controlling the repeat rate of the shutter and triggering it automatically during the flight [*Lytle, et al.*, 1998b]. The images (1536 x 1024 pixels, 1.5 Mb in size) were stored on PCMCIA cards during the flights and subsequently converted into a standard TIF format and downloaded onto DAT tapes. During the flights, the helicopter speed was maintained at approximately 110 knots, while the altitude varied between 800 and 2800 m. The size of the images was calculated using the following relationship:

$$X_{(m)} = \frac{(35 * Altitude_{(ft)} * 0.3048)}{28 * 2.6} \qquad \textbf{Equation 7}$$

where X is the length of the longest side of the image. The shortest side (Y) is 0.67 times this value [*Lytle, et al.*, 1998b]. Based on Equation 7 and the range of altitudes given in Table 8, the pixel size ranged from 0.25 to 0.75 m. Figure 11 shows examples of two overlapping photographs taken during Voyage 2 (96).

A Sony® Hi8 format video camera equipped with a 15-mm wide-angle lens was also mounted in the helicopter alongside the digital camera. It provided a continuous view at a substantially larger field of record than the digital photography. Footage was recorded on VHS tapes [*Lytle, et al.*, 1998b]. This information was used to pre-select areas for closer analysis and to assist in the identification of larger features such as icebergs and polynyas in the photographs.

Flight Number	*Date/Time* (GMT)	*Start Position* Lon.(°E)	Lat.(°S)	*End Position* Lon.(°E)	Lat.(°S)	*Altitude* (m)
		Voyage 1 (95)				
2	06-Aug-95 0120	141.12	64.33	140.98	64.43	1650
4	09-Aug-95 0415	140.40	64.98	140.31	64.98	825
14	19-Aug-95 0030	138.15	64.66	138.00	64.72	2640
16	19-Aug-95 2340	139.25	64.23	139.22	64.28	2640
17	20-Aug-95 0440	139.23	64.70	139.22	64.90	2640
		Voyage 2 (96)				
4	22-Oct-96 0213	74.00	63.32	74.25	62.50	1320
5	23-Oct-96 0117	74.17	64.17	74.17	64.28	990
6	25-Oct-96 0817	75.42	65.93	77.20	63.90	2640
7	26-Oct-96 0246	77.00	66.25	76.00	66.25	2640
8	26-Oct-96 0851	76.85	66.40	77.00	66.47	2640
9	27-Oct-96 0216	75.88	66.82	79.00	67.12	1650

Table 8 Information on the digital aerial photography helicopter flights which coincided with the two study areas.

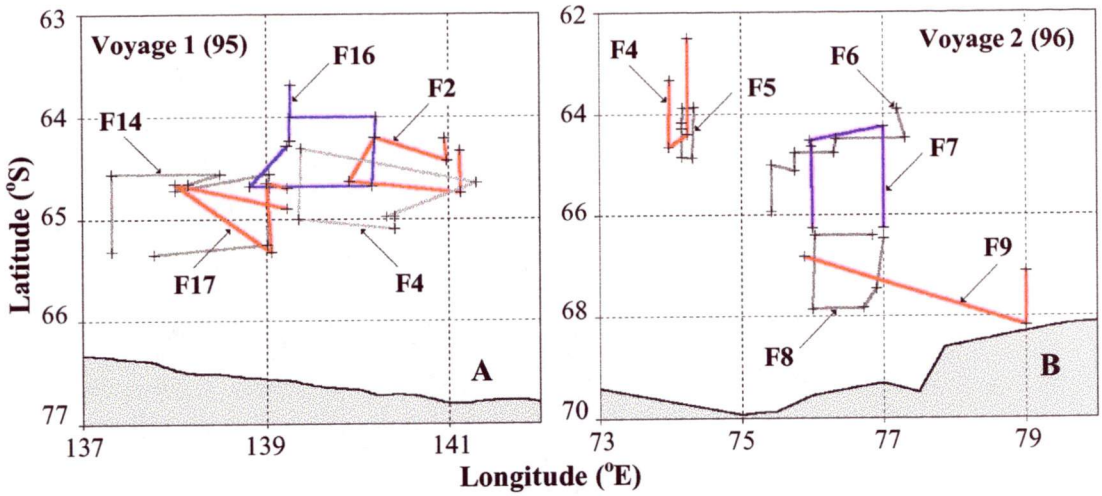

Figure 10 Helicopter tracks for the digital aerial photography flights from (**A**) Voyage 1 (95) and (**B**) Voyage 2 (96).

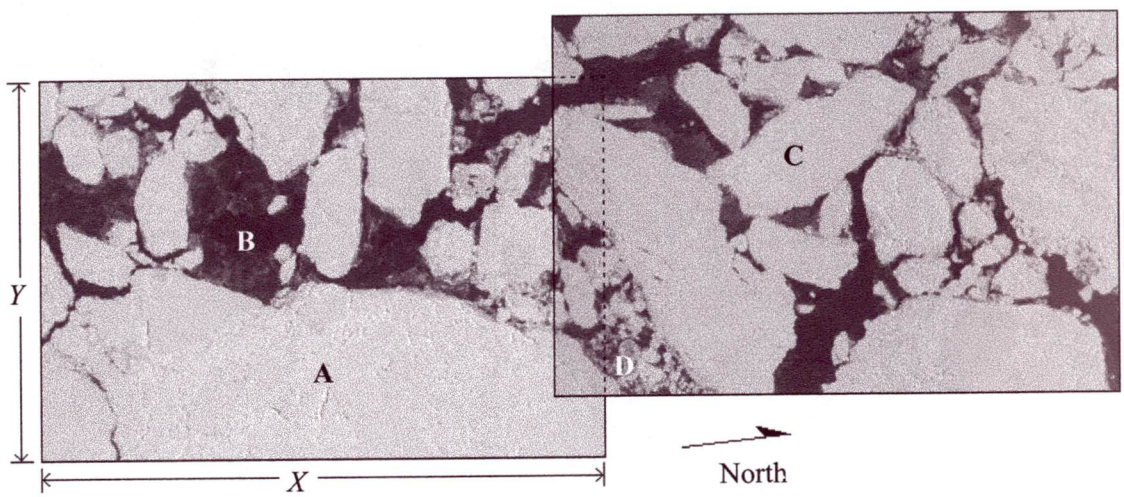

Figure 11 Two overlapping digital aerial photographs taken on 14-Oct-1996 at approximately 64° 04' S; 93° 00' E. With the aircraft at an altitude of 1650 m, the dimensions of the scenes are: $X = 914.6$ m and $Y = 612.8$ m. Noticeable features include: (**A**) large (> 500 m) snow-covered floe, (**B**) areas of open water and/or snow-free thin ice, (**C**) medium size (100-500 m), snow-covered first-year ice floes and (**D**) brash ice.

Sea Ice Thickness Model

4.1 Model Development

This section describes the procedure used to estimate sea ice thickness distributions using inputs from Antarctic AVHRR imagery. It employs the principles of a one-dimensional thermodynamic model proposed originally by *Maykut and Untersteiner* [1971]. *Yu and Rothrock* [1996] developed a method for the application of this model with input variables from Arctic AVHRR data. Section 2.3 of the literature review chapter presents a more detailed analysis of these two studies. In a similar fashion to *Yu and Rothrock* [1996], the system presented in this section utilises AVHRR-derived albedo and ice surface temperature data as inputs for *Maykut and Untersteiner*'s [1971] thermodynamic model. However, several significant structural and theoretical modifications and improvements were incorporated to *Yu and Rothrock*'s original model, leading to the development of a completely new system, adapted specifically to the sea ice conditions of the Southern Hemisphere. These modifications account for differences between Arctic and Antarctic sea ice, and accommodate the nature and availability of *in situ* and remote-sensing data employed in this study. The most important of these changes include:

a) an improved ice/snow surface temperature (T_{Sfc}) derivation;

b) an improved estimate of the near surface (2 m) air temperature (T_{Air});

c) a more robust parameterisation of the bulk transfer coefficients for heat and evaporation (C_h and C_e respectively);

d) use of a more recently-derived and realistic empirical value for the effective thermal conductivity of snow (k_s) based on data collected in the Antarctic sea ice zone and;

e) an improved relationship between ice and snow thicknesses based on field observations in the study region.

Importantly, this algorithm does not possess all the elements of a typical numerical model, as its principal aim is to estimate the *apparent ice thickness* contained within each cloud-free pixel in an AVHRR image for a given instant in time (i.e., the time of acquisition of the image). It is designed neither to detect temporal changes nor to forecast thicknesses, although some information on temporal trends can be derived if sequences of images are analysed. However, the term *sea ice thickness model* will be employed hereafter for simplicity and consistency with *Yu and Rothrock*'s work.

For the purpose of this study, sea ice can be defined ideally as a horizontally-homogeneous slab floating on its own liquid phase, with or without a homogeneous snow cover [*Maykut and Untersteiner*, 1971]. There are incoming and outgoing energy fluxes operating through both the ice/atmosphere and ice/water interfaces.

The apparent ice thickness returned by the model is the result of a thermodynamic analysis of each pixel and therefore does not account for mechanical processes that occur in the sea ice zone such as ridging, rafting and the opening and closing of cracks and leads. This issue, along with the response of the model to structures in the sea ice that are smaller than the size of the AVHRR pixel, will be addressed in later sections of chapters 5 and 6.

In a given pixel of an AVHRR image, it is possible that the *apparent ice thickness* may differ from the actual ice thickness, while still providing information related to the bulk thermodynamic properties of the snow/ice column. This difference is related to limitations of the method which are discussed throughout this chapter and analysed with in more detail in Chapter 6.

The sea ice thickness model is based upon two assumptions: *a)* that there is a linear temperature gradient across the snow and young ice layers, and *b)* that the surface temperature of thin sea ice is closely related to its thickness. These assumptions are valid primarily for snow-free ice but also for snow-covered ice, as long as there is a close relationship between snow thickness and ice thickness (Section 4.1.6) and the ice and snow are homogeneous in character [*Lytle, et al.*, 1998b; *Maykut and Untersteiner*, 1971; *Yu and Rothrock*, 1996]. For this reason, this study adopts 1 metre as the upper thickness limit of thin sea ice. The model also assumes no variability in the stratigraphic structure of the ice layer, which permits the adoption of a single value for the thermal conductivity of sea ice (k_i) that varies only with its temperature and salinity.

By assuming a linear ice/snow temperature profile, it is possible to estimate the conductive heat flux through the sea ice (H_C) using theoretical expressions such as those suggested by *Ono* [1967] and *Untersteiner* [1964]. Although the analysis of ice core and snow pit data collected in East Antarctica since 1991 demonstrates that stratigraphic uniformity is uncommon [*Lytle, et al.*, 1998b; *Worby and Massom*, 1995], many of the corresponding temperature profiles follow a linear behaviour, as can be seen in Figure 12, which supports the rationale for the choice of k_i presented above.

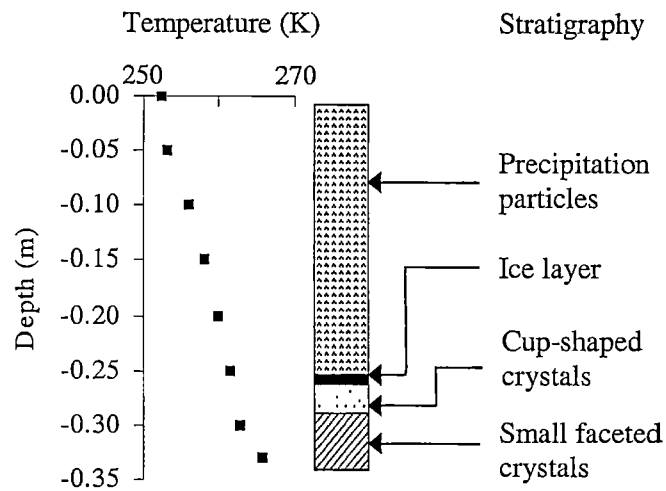

Figure 12 Temperature and stratigraphy profiles of a typical East Antarctic winter snow pit collected on 4 August during Voyage 1 (95) at 0345 Z. The location of the ice station was 65° 01' S and 141° 49' E. Adapted from *Lytle et al.* [1998b].

Maykut and Untersteiner [1971] present two possible scenarios for the energy balance at the top of the ice/snow layer. If the temperature of the snow/ice surface (T_{Sfc}) is at the melting point, then a certain amount of melting will have to occur to accommodate the excess energy flux reaching the surface. Alternatively, with T_{Sfc} below freezing point, the incoming and outgoing energy fluxes at the upper surface will balance to reach an equilibrium state, which is the situation of interest in this study (all pixels with T_{Sfc} at or above melting point are removed from ice thickness calculations). This situation is described by:

$$(1-\alpha)Q_S - \tau(1-\alpha)Q_S - Q_{L\uparrow} + Q_{L\downarrow} + H_S + H_L + H_C = 0 \qquad \textbf{Equation 8}$$

where:

α is the surface albedo;
Q_S is the incoming shortwave radiation;
τ is the transmitted portion of the shortwave radiation;
$Q_{L\uparrow}$ is the upwelling longwave radiation;
$Q_{L\downarrow}$ is the downwelling longwave radiation;
H_S is the turbulent sensible heat flux;
H_L is the latent heat flux and;
H_C is the conductive heat flux.

The terms in Equation 8 are the same as those described by *Yu and Rothrock* [1996] and mentioned previously in Chapter 2 (Equation 6). However, the current study adopts a more recent notation, following the standard terminology for electromagnetic radiation [*Lide*, 1991]. Positive signs in Equation 8 indicate fluxes directed towards the ice/snow surface, while negative signs indicate fluxes leaving the surface. The turbulent sensible and latent heat fluxes can assume either negative or positive signs, depending on the values of air temperature and humidity. Each component of the heat balance is calculated separately, based on theoretical and empirical relationships as detailed in the following sections.

4.1.1 Net Solar Radiation at the Surface

The first term of Equation 8 $[(1-\alpha)Q_S]$ is the net solar radiation at the surface, where Q_S is the incoming solar radiation and α is the AVHRR-derived surface albedo. Q_S was estimated using an empirical relationship proposed originally by *Zillman* [1972] and subsequently modified by *Shine* [1984][3]:

$$Q_S = \frac{1368.0\mu^2}{1.2\mu + (1.0+\mu)e_a 10^{-3} + 0.0455} \qquad \textbf{Equation 9}$$

[3] The formulation for Q_s found in *Yu and Rothrock* [1996] and *Yu* [1996] contains a typing error: $Q_s = 1368\,[\mu]\,[1.2\mu + (1.0+\mu)\,e_a 10^{-3} + 0.046]^{-1}$.

where μ is the cosine of the solar zenith angle and e_a is the near-surface (2 m height) water vapour pressure (in hPa), expressed as $e_a = fe_{sa}$. The value used in this study for the relative humidity (f) was 0.81, an average obtained from the RSV *Aurora Australis* DLS dataset from Voyage 2 (96). In comparison, the value employed by *Yu and Rothrock* [1996] in the Arctic was 0.90. The saturation vapour pressure at 2 m (e_{sa}) was obtained through a fourth-order polynomial which was proposed by *Maykut* [1978]:

$$e_{sa} = a_0 T_{Air}^4 + a_1 T_{Air}^3 + a_2 T_{Air}^2 + a_3 T_{Air} + a_4 \qquad \textbf{Equation 10}$$

where T_{Air} is the air temperature at 2 metres and the value of the a_n constants are: $a_0 = 2.7798 \times 10^{-6}$, $a_1 = -2.6913 \times 10^{-3}$, $a_2 = 0.9792$, $a_3 = -158.6$ and $a_4 = 9653.2$.

4.1.2 Solar Radiation Penetrating the Ice Layer

The second term in Equation 8 [$\tau(1-\alpha)Q_S$] is the solar radiation that penetrates the ice layer, where τ is the fraction of the wavelength-integrated irradiance transmitted through the ice layer. *Grenfell* [1979][4] parameterised τ as:

$$\tau = a^{(-bZ_i)} + c^{(-dZ_i)} \qquad \textbf{Equation 11}$$

where Z_i is the ice thickness and the appropriate constants for clear-sky conditions are: $a = 3894$, $b = 12.39$, $c = 0.35$ and $d = 1.578$.

4.1.3 Upwelling Longwave Radiation

The next term in Equation 8 is the upwelling longwave radiation [$Q_{L\uparrow}$], defined as $\varepsilon_{Sfc}\sigma T_{Sfc}^4$, where T_{Sfc} is the AVHRR-derived ice/snow surface temperature, σ is the Stefan-Boltzmann constant (5.6693×10^{-8} W·m^{-2}K^{-4}) and ε_{Sfc} is the surface longwave emissivity. A value of 0.9956 was used for ε_{Sfc} in this study, derived from NOAA-7 snow emissivities published by *Key and Haefliger* [1992] and calculated as an average over the range of AVHRR scan angles employed in this study.

---

[4] *Grenfell* [1979] represented τ as i_0 in his study.

4.1.4 Downwelling Longwave Radiation

The downwelling longwave radiation [$Q_{L\downarrow}$] is defined as $\varepsilon_{Air}\sigma T_{Air}^4$, where T_{Air} is the near-surface (2 m) air temperature and ε_{Air} is the effective emissivity of the atmosphere [*Oke*, 1990]. An empirical value of 0.7855 for ε_{Air}, as proposed by *Maykut and Church* [1973], was utilised in this study.

4.1.5 Turbulent and Latent Heat Fluxes

The turbulent sensible heat flux (H_S) and the latent heat flux (H_L) are estimated through the following relationships proposed by *Maykut* [1982]:

$$H_S = \rho_a c_p C_h u (T_{Air} - T_{Sfc}) \qquad \textbf{Equation 12}$$

$$H_L = \frac{0.622 \rho_a L C_e u}{p_0} (e_a - e_{so}) \qquad \textbf{Equation 13}$$

In Equation 12 and Equation 13, ρ_a is the air density (1.295 kg·m^{-3}), c_p is the specific heat of air (1004.4 J·kg^{-1}·K^{-1}), u is the wind speed 2 m above the ice/snow surface, L is the latent heat of vaporisation (2.49 x 10^6 J·kg^{-1}), e_{so} is the saturation vapour pressure at the ice/snow surface and p_0 is the surface pressure (assumed constant at 1013.0 hPa). C_h and C_e are the bulk transfer coefficients for heat and evaporation, respectively.

The values for C_h and C_e employed in this study differ from those proposed by *Yu and Rothrock* [1996]. *Andreas* [1996] demonstrated that the bulk transfer coefficients for ice and/or snow are height-dependent and strongly influenced by the stability of the atmospheric boundary layer (ABL). For a constant wind speed, C_h and C_e will increase with increasing instability within the ABL. However, recent attempts to parameterise these coefficients have met with a lack of consensus, mainly because of inherent difficulties in measuring such small quantities precisely. Although some of these measurements led to an assumption that $C_h = C_e$, *Andreas*' work demonstrated that this is not necessarily correct. Faced with a paucity of *in situ* data, *Andreas* [1987] developed a model to express C_h and C_e as a function of the bulk transfer coefficient for momentum (also known as the drag coefficient, C_d), and the near-surface wind speed. The drag coefficient is related to the surface roughness parameter (ξ) [*Andreas*, 1996].

Figure 13 shows how the modelled coefficients vary with wind speed for five different values of ξ. These values, employed by *Andreas* [1996] in his modelling study, are consistent with the range of observed roughnesses found in several Antarctic studies [*Adolphs*, 1999; *Andreas, et al.*, 1993; *Fisher and Lytle*, 1998; *Tin and Jeffries*, in press]. As the coefficients are predominantly in the range 0.001 to 0.0016, it is clear that the values of C_h and C_e employed by *Yu and Rothrock* [1996] ($C_h = C_e = 0.003$ for very thin ice; $C_h = C_e = 0.00175$ for thick ice) are overestimates at all wind speeds.

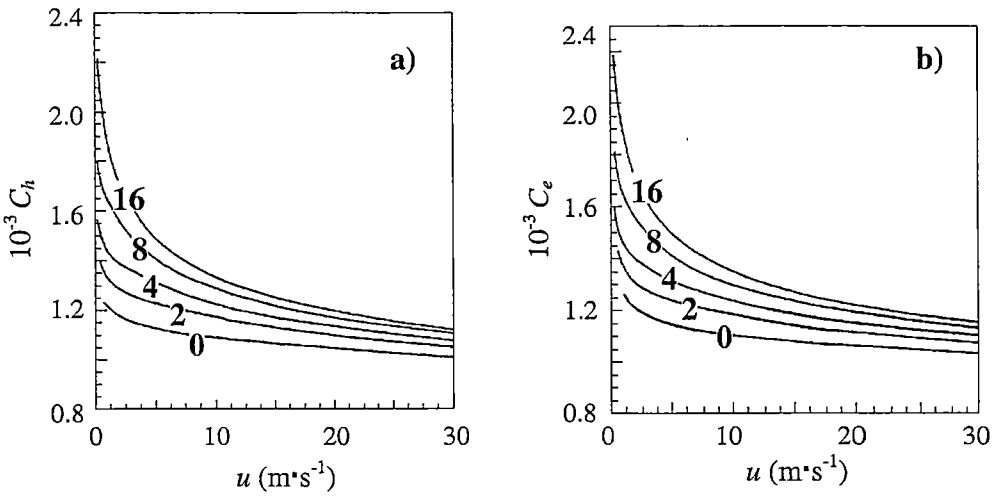

Figure 13 Model predictions of (**a**) C_h and (**b**) C_e as a function of wind speed at 2 m from *Andreas* [1987]. Each curve represents the variation of the two coefficients for five different values (0, 2, 4, 8 and 16 cm) of the surface roughness parameter. Adapted from *Andreas* [1996].

An approximation of *Andreas'* [1987] model was used to obtain C_h and C_e in this study. A direct relationship between the surface roughness parameter and ice thickness was assumed, with larger values of ξ corresponding to thicker ice types. Ice thicknesses of 0.0, 0.3, 0.6, 0.9 and 1.2 m were associated with ξ values of 0, 2, 4, 8 and 16 cm respectively. The choice of ice thickness and ξ values was based on the range of typical values encountered by *Andreas et al.* [1993] in the Weddell Sea during the austral spring of 1989. This association is also supported by more recent observations made by *Tin and Jeffries* [in press] who found statistically significant correlations between surface roughness and mean ice thickness in the Ross Sea.

Using *Andreas'* [1987] model predictions, it was possible to build linear equations (with a general form as shown by Equation 14) that relate the bulk transfer coefficients to ice thicknesses for seven wind speed intervals. These intervals were defined based on the range of values found on the DLS dataset from Voyage 2 (96).

$$C_{(h,e)} = aZ_i + b \qquad \textbf{Equation 14}$$

Table 9 shows the values of a and b for each wind-speed interval and Figure 14 shows examples of histograms of C_h and C_e calculated by this method for a NOAA-14 image from 1996. With this method, it was possible to assign specific values of the bulk transfer coefficients to each pixel of the image.

	C_h		C_e	
u (m·s^{-1})	$10^3.a$	$10^3.b$	$10^3.a$	$10^3.b$
0.0 - 2.5	0.783	1.167	0.789	1.236
2.5 - 7.5	0.301	1.131	0.312	1.168
7.5 - 12.5	0.201	1.100	0.216	1.133
12.5 - 17.5	0.154	1.075	0.170	1.106
17.5 - 22.5	1.053	0.125	0.140	1.086
22.5 - 27.5	0.109	1.032	0.118	1.069
> 27.5	0.094	1.016	0.106	1.055

Table 9 Values of a and b (as employed in Equation 14) for seven wind speed intervals, employed to calculate C_h and C_e as a function of sea ice thickness.

An alternative approach, which would greatly increase the computation time of the model, would be to utilise *in situ* measurements to generate estimates of ξ and calculate the coefficients directly from *Andreas'* [1987] model. As shown in a later section (Section 4.4.3), the model results are not particularly sensitive to changes in the bulk transfer coefficients, and there is no justification for increasing the complexity of this parameterisation within the model, even if appropriate *in situ* data were available.

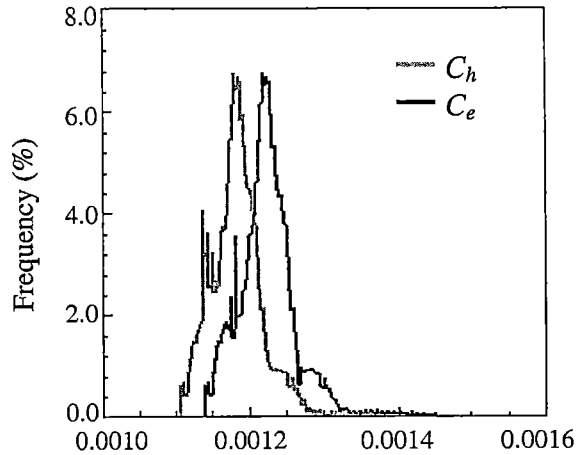

Figure 14 Example histograms of C_h and C_e calculated using *Andreas'* [1987] model with ice thicknesses obtained from a NOAA-14 AVHRR image collected on 30-Sep-1996 at 0909 Z and wind speeds obtained from the corresponding Global Assimilation and Prediction System (GASP, see Section 4.3.1) output.

4.1.6 Conductive Heat Flux

Under the assumption made at the beginning of this chapter that there is a linear temperature gradient within the ice and snow layers, the conductive heat flux (H_C) can be estimated through the following relationship:

$$H_C = \gamma(T_f - T_{Sfc}) \qquad \textbf{Equation 15}$$

where T_f is the temperature of seawater, defined as $T_f = 0.055\ S_W$, where S_W is the salinity of seawater. The value chosen for S_W is 34.2743 psu which is an average of *in situ* measurements made during the two cruises of the RSV *Aurora Australis*. The thermal conductance of the snow/ice layers (γ) is expressed by the relationship:

$$\gamma = \frac{k_i k_s}{(k_s Z_i + k_i Z_s)} \qquad \textbf{Equation 16}$$

where k_i and k_s are the effective thermal conductivities of sea ice and snow respectively, Z_i is the ice thickness and Z_s is the snow thickness. *Yu and Rothrock* [1996] utilised relationships between Z_i and Z_s based on the work of *Doronin* [1971] in the central Arctic. The empirical relationship employed in this study (shown in Figure 15) was obtained through 338 samples of Z_i and accompanying Z_s obtained from drilled transects collected during Voyage 1 (95).

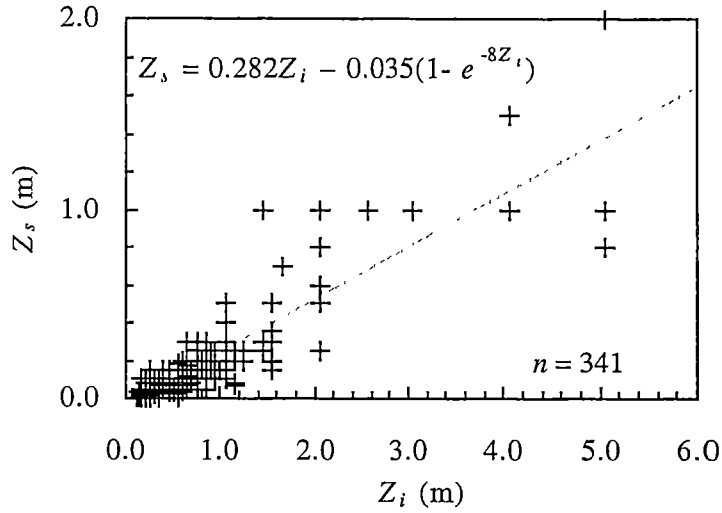

Figure 15 A scatter plot showing the empirical relationship between ice (Z_i) and snow (Z_s) thickness data collected in East Antarctica during the austral winter of 1995.

In this study, k_s was set to 0.164 $W \cdot m^{-1} \cdot K^{-1}$, based on measurements made by *Massom et al.* [1998b] using data from Voyage 1 (95) and measurements made by *Sturm et al.* [1998] in the Bellingshausen, Amundsen and Ross Seas in the 1994/95 season. Further details on the rationale for using this value, which is lower than that typically employed in sea ice models, are given in Section 4.4.3. In Equation 16, the thermal conductivity of ice (k_i) was estimated by the following relationship proposed by *Untersteiner* [1964]:

$$k_i = \frac{k_0 + \beta S}{(T_{Ice} - 273.15)} \qquad \textbf{Equation 17}$$

where k_0 is the conductivity of pure ice (taken as 2.034 $W \cdot m^{-1} \cdot K^{-1}$), β is a constant (0.13 $W \cdot m^{-2} \cdot kg^{-1}$) and S is the sea ice salinity (in psu) and T_{Ice} is the mean temperature within the ice layer. Studies by *Maykut* [1985] show that T_{Ice} depends weakly on k_i for temperatures below 269 K. Therefore, setting the value of T_{Ice} to be the same as T_{Sfc} introduces no significant error [*Yu and Rothrock*, 1996]. The sea ice salinity was estimated from an empirical relationship with ice thickness which was proposed by *Cox and Weeks* [1974][5] for the Arctic:

[5] The relationships between sea ice salinity and thickness are erroneously quoted in *Yu and Rothrock* [1996] and *Yu* [1996] as: $S = 14.24 \pm 19.39 Z_i$ for $Z_i \leq 0.4$ m and $S = 7.88 \pm 1.59 Z_i$ for $Z_i > 4$ m.

$$\text{For} \quad Z_t \leq 0.4\,\text{m} \qquad S = 14.20 - 19.39 Z_t \qquad \textbf{Equation 18}$$

$$\text{For} \quad Z_t > 0.4\,\text{m} \qquad S = 7.88 - 1.59 Z_t$$

While *Worby* [1998] presented salinity and thickness results from six Antarctic voyages between 1991 and 1995, the data fit reasonably well with *Cox and Weeks'* [1974] standard Arctic relationship. As such, the derivation of an Antarctic specific empirical relationship between ice thickness and salinity is unwarranted. Moreover, the uncertainties involved in the parameterisation of the thermal conductivity for ice (discussed later in Section 4.6) and the low sensitivity of H_C to changes in sea ice salinity do not justify the development of a new relationship.

4.2 Data Integration and Model Flow

The main input for the model is AVHRR data, pre-processed according to the methods described in Section 3.1. Each image in this dataset contains the five original AVHRR data bands, plus an "angles" band containing the solar zenith angle, satellite zenith angle and sun-satellite azimuth and a classification band generated by the ICEMAPPER algorithm. The classification band is used to eliminate invalid pixels (such as those containing clouds, land and background noise), leaving for analysis only the pixels classified as sea ice.

The next processing step consists of using bands 1 and 2 to calculate the normalised albedo (α) and bands 4 and 5 to calculate the snow/ice surface temperature (T_{Sfc}), according to the techniques proposed by *Lindsay and Rothrock* [1994a] and *Key et al.* [1997a] respectively. A detailed description of these techniques is given in Sections 4.3.2.1 and 4.3.2.2. This processing step is achieved through two separate routines, which create two new bands (i.e., an "albedo band" and a "snow/ice surface temperature band") for use in subsequent calculations.

Meteorological data from the Global Assimilation and Prediction System (GASP - see section 4.3.1) are added to the model through another routine that extracts wind speed and wind direction information from the original dataset. This routine also performs spatial and temporal interpolations to ensure that the output data match the AVHRR's spatial resolution and the time of acquisition of each image. A "wind band" is created as an output of this routine.

The last step of the model consists of calculating the *apparent sea ice thickness* within each valid pixel through the method described in Section 4.1, by combining the wind, albedo and temperature bands generated in the previous routines. The output of this routine is an "apparent sea ice thickness band " from which classified images and frequency distribution histograms are generated. Within this routine, a non-zero value of ice thickness is necessary for the computation of $\tau(1-\alpha)Q_S$, H_S, H_L and H_C. In this case, an initial thickness of 0.02 m is assumed at the beginning of the routine and the calculation of the final thickness of each pixel is performed with an incremental looping system (see Figure 16). In each iteration of the loop (n), Z_0 is increased by 0.01 m and the seven components of Equation 8 are recalculated and summed.

Pixels with a net negative balance (i.e., pixels that lose heat to the atmosphere) are kept in the loop for the next iteration, while pixels where the sum of all fluxes is zero or positive are assigned the thickness of the current iteration ($Z_i = Z0 + 0.01n$, where n starts at 0). This process is repeated until all the pixels have been assigned an equilibrium sea ice thickness. To allow for the fact that some pixels will not reach an equilibrium, the iteration is stopped when $n = 198$ (i.e., $Z_i = 2.0$ m) in the spring images, or $n = 398$ (i.e., $Zi = 4.0$ m) in the winter images. These values were chosen as they are significantly thicker than the thin sea ice limit which is the focus of the study.

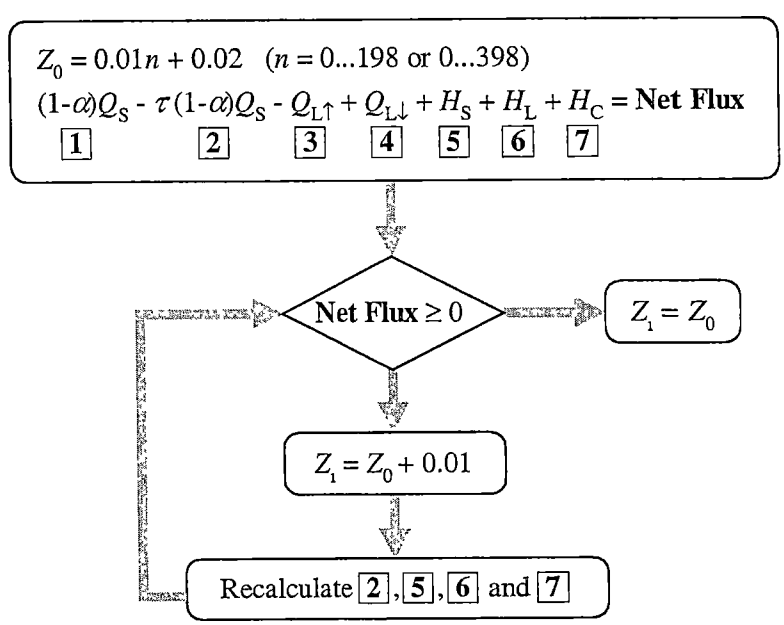

Figure 16 A flow diagram describing the looping system designed to calculate the apparent sea ice thickness.

Figure 17 is a flow diagram of the ice thickness model. The model, programmed with IDL®, consists of one main module that calls sub-routines which perform different functions, such as the spatial filtering of the classified image, the calculation of AVHRR-derived albedo and surface temperature, the calculation of the ice thickness and generation of outputs. The complete IDL® code is listed in Appendix I.

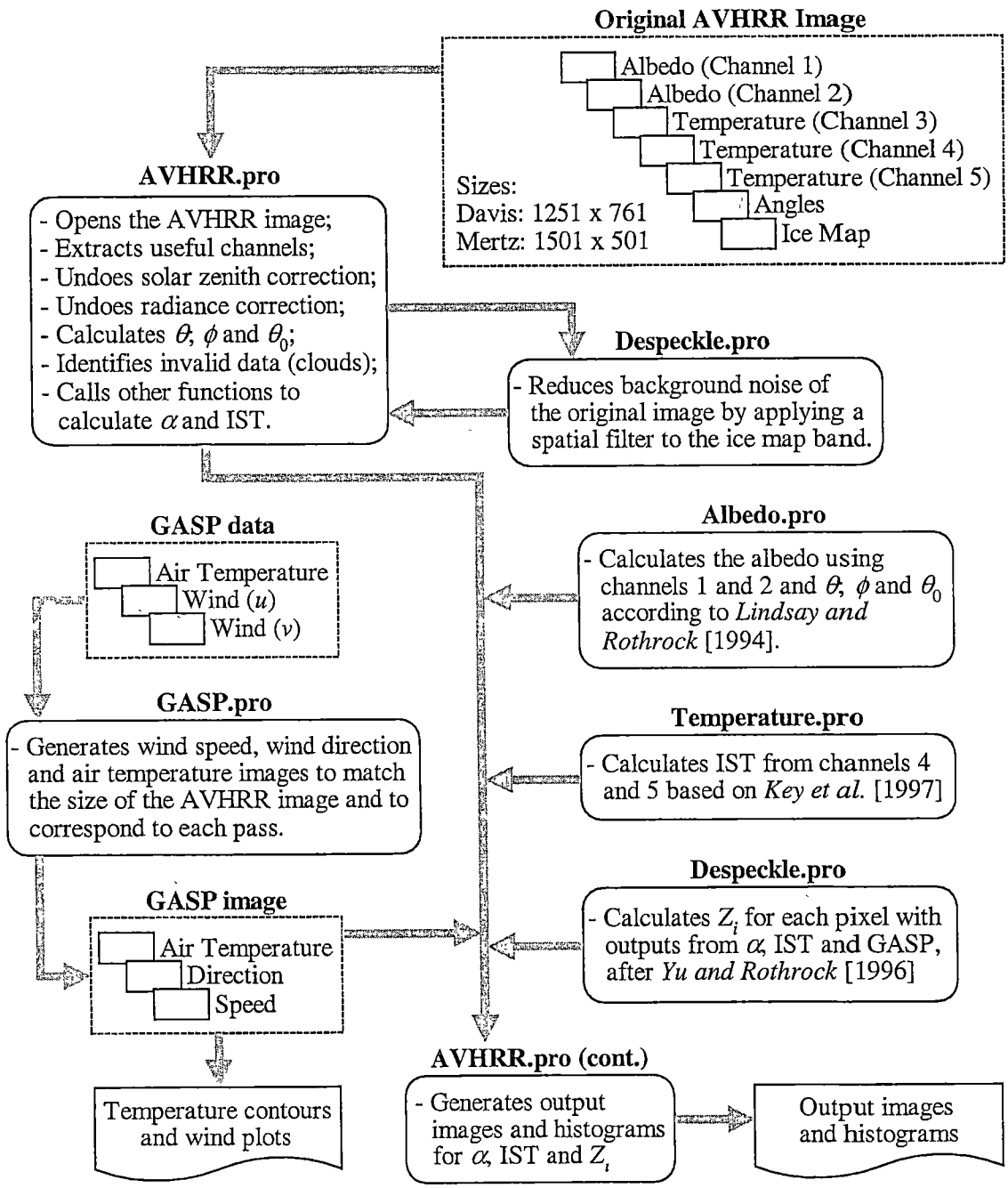

Figure 17 A flow diagram showing the sequence of events in the sea ice model. The extension *.pro denotes an IDL® routine, while dashed rectangles indicate input data. θ_0 is the solar zenith angle, θ is the satellite zenith angle and ϕ is the sun-satellite azimuth angle (see Figure 20).

4.3 Input Data

This section describes the main sources of data employed to generate the ice thickness estimates through the model. It does not include *in situ* data used to validate the relationships mentioned in previous sections.

4.3.1 Meteorological Data

Meteorological data employed in the model were obtained from the Australian Bureau of Meteorology's GASP model [*Bourke, et al.*, 1991]. The GASP model utilises a resolution of rhomboidal wave number 31 with 9 sigma levels (0.991, 0.925, 0.811, 0.663, 0.500, 0.336, 0.188, 0.074 and 0.008). Input observational data for this model include near surface observations from meteorological stations, automatic weather stations, drifting buoys, vertical profiles from radiosonde launches and NOAA-TOVS soundings. [*Reid and Budd*, 1995].

The dataset extracted consisted of arrays of wind (u and v components) and air temperature data at the lowest sigma level (0.991) from four analyses per day (at 0500, 1100, 1700 and 2300 Z) from two periods chosen to include V1 (95) and V2 (96): 01 July to 30 September 1995 and 26 September to 10 November 1996. The original spatial resolution of the GASP grid was 1.5 degrees of latitude by 1.5 degrees of longitude, but they were matched to the dimensions of the AVHRR images via a bilinear spatial interpolation. A temporal interpolation was employed to calculate the u, v components and T_{Air} arrays corresponding to the time of acquisition of each AVHRR image. The wind speed was then adjusted from the original altitude (~ 71.8 m) to the 2 m level by using the logarithmic wind profile [*Oke*, 1990]:

$$u = u_* \ln(z/z_0) \qquad \textbf{Equation 19}$$

where u is the wind speed at the original altitude, u_* is the friction velocity, z is the original altitude and z_0 is the roughness length taken as 10^{-3} m [*Oke*, 1990]. Examples of wind and temperature outputs from the GASP system are shown in Figure 18. The logarithmic profile is best applied in situations where the atmosphere is near-neutral, which will be the case over sea ice. Over open water however, the atmosphere is unstable in which case a log linear profile would be more appropriate. In the absence of any information about the degree of (in)stability of the atmosphere over each pixel, the logarithmic profile was chosen as a good approximation.

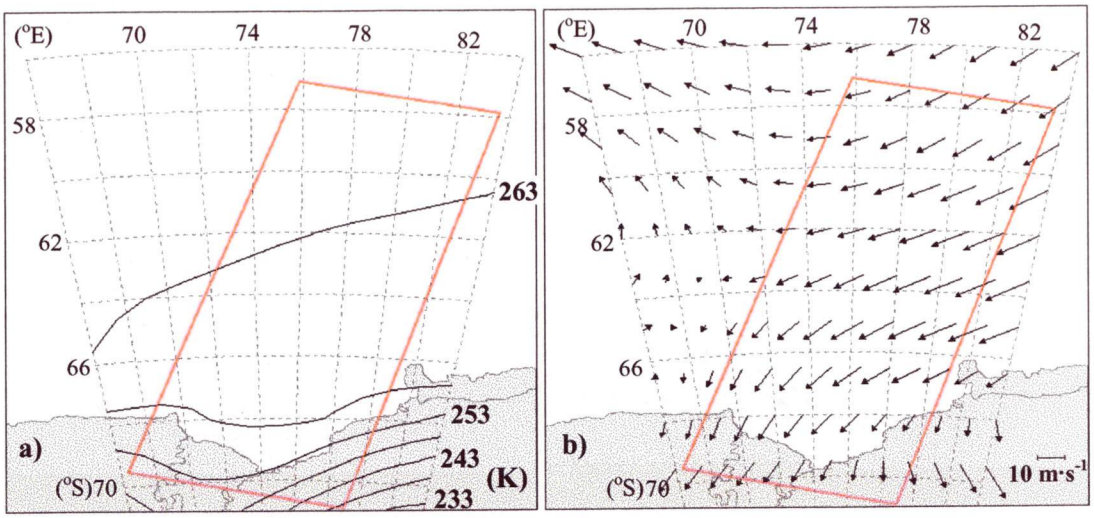

Figure 18 Examples of (**a**) 2-metre air temperature and (**b**) 2-metre wind speed and direction outputs from the GASP system, temporally interpolated to coincide with an AVHRR image from 30-Sep-1996 at 0909Z. Polygons indicate the Davis area (see Figure 4).

A comparison between the spatially interpolated air temperature data produced by the GASP system and near-simultaneous air temperature data collected by the RSV *Aurora Australis*' DLS (Figure 19) showed very little correlation ($r^2 = 0.088$). This demonstrated that GASP outputs could not be used to accurately estimate the air temperature near the surface, clearly due to its coarse spatial resolution, which is insufficient to resolve air temperature variations that occur in different ice conditions. The GASP wind speed data, however, presented a more stable behaviour ($r^2 = 0.658$) and were incorporated in the model for the estimations of the sensible and latent heat fluxes.

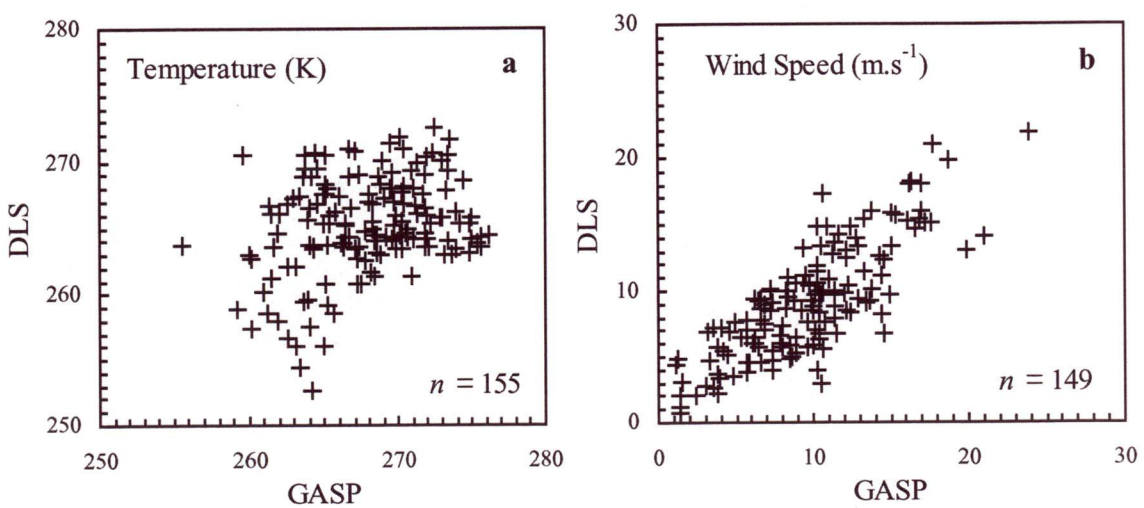

Figure 19 Comparison between coincident GASP and DLS (port side) near-surface air temperatures (**a**) and wind speed (**b**) from Voyage 2 (96). Both datasets were adjusted to a height of 2 m.

4.3.2 AVHRR-Derived Data

The 7-channel AVHRR image, pre-processed according to the methods described in Chapter 3 (Section 3.1.1), provides the main source of data for the model. The system utilises AVHRR estimates of albedo (α) and ice/snow surface temperature (T_{Sfc}), which were obtained through the methods described below (Sections 4.3.2.1 and 4.3.2.2). Estimates of near-surface air temperature at 2 m (T_{Air}) were also obtained from the AVHRR data through a relationship with T_{Sfc} described in Section 4.3.2.3.

4.3.2.1 Albedo

The method proposed by *Lindsay and Rothrock* [1994a] was employed in this study to calculate the normalised broadband surface albedo using data from AVHRR channels 1 and 2. This is the same approach as that taken by *Yu and Rothrock* [1996], and consists of six steps:

a) The calibrated narrowband radiances (L_i) from the digital counts for each visible channel (i = 1 or 2) were obtained through the following relationship:

$$L_i = \frac{Counts_i - o_i}{g_i} \qquad \textbf{Equation 20}$$

where L_i is expressed in units of $W \cdot m^{-2} \cdot sr^{-1} \cdot \mu m^{-1}$, $Counts_i$ are the digital counts from channels 1 and 2, the fixed offset (o_i) is expressed in counts and the fixed instrument gain (g_i) is expressed in units of $counts/W \cdot m^{-2} \cdot sr^{-1} \cdot \mu m^{-1}$. The gain is obtained through a relationship from *Kidwell* [1998]:

$$g_i = \frac{100\pi W_i}{s_i F_i} \qquad \textbf{Equation 21}$$

where F_i is the integrated solar spectral irradiance, weighted by the spectral response function of channel i (in $W \cdot m^{-2}$), W_i is the equivalent width of the spectral response function (in μm) and s_i is the post-launch calibration slope. The appropriate pre-launch values of F_i, W_i and s_i for NOAA-14 are presented in *Kidwell* [1998].

The post-launch drift in the calibration of AVHRR's two solar reflective channels is the largest source of uncertainty in this method. Several authors such as *Che and Price* [1992] and *Kaufman and Holben* [1993] have used different approaches to estimate the rates of change of the gain for different NOAA satellites, but the large discrepancies between these studies suggested that more attention was needed in this area [*Lindsay and Rothrock*, 1994a].

More recently, *Rao and Chen* [1994], *Teillet and Holben* [1994] and *Cihlar and Teillet* [1995], amongst others, have achieved, with various degrees of success, the goal of accounting for the temporal degradation in the performance of channels 1 and 2 on the AVHRR sensors, particularly on NOAA-14. These studies generally used areas of desert or open ocean as calibration targets, rather than ice [*Teillet and Holben*, 1994].

As with *Lindsay and Rothrock's* approach, the offset value used in this study was the pre-launch value obtained from *Kidwell* [1998], which is considered to be relatively stable. The pre-launch gains were subsequently multiplied by an empirical factor to produce a median albedo value of 0.81 for the brightest pixels of each image. This value of 0.81 was reported by *Allison et al.* [1993] as being representative of fast ice (i.e., consolidated thick ice) covered with 0.3 m of snow, based on clear-sky measurements made in the East Antarctic sector in a similar season to that covered by Voyage 2 (96). Based upon this information, the gains were calculated as:

$$Gain_t = g_t \cdot \frac{M_{23}}{0.81} \qquad \textbf{Equation 22}$$

The brightest pixels in each image were considered to be those classed as "very compact sea ice" (class 23), with a thick snow cover, in the accompanying ice map band. The median reflectance of class 23, symbolised by M_{23} in Equation 22, was employed to adjust the gains. Thirteen of the clearest NOAA-14 images from the dataset for Voyage 2 (96) were employed to calculate the average calibrated gains for each channel. These gains were then applied to all of the images using Equation 22.

Table 10 shows the calibrated gains for these images, along with the pre-launch gains calculated using the values of W_i, F_i and s_i from *Kidwell* [1998] and post-launch gains corresponding to mid-October 1996, obtained through a piecewise linear (PWL) calibration method described by *Rao and Chen* [1994]. The small difference between the calibrated gains and the gains obtained through the PWL method (2.53% for Channel 1 and 4.78% for Channel 2) indicates that this technique can produce acceptable results in spite of the uncertainties it introduces. These were thoroughly discussed by *Lindsay and Rothrock* [1994a].

Acquisition Date	*Time (Z)*	*Channel 1*	*Channel 2*
30-Sep-1996	0909	1.49	1.97
30-Sep-1996	1050	1.85	2.44
1-Oct-1996	0858	1.40	1.85
1-Oct-1996	1039	1.72	2.27
5-Oct-1996	0955	1.73	2.28
6-Oct-1996	0945	1.66	2.18
6-Oct-1996	1124	1.57	2.07
2-Nov-1996	0953	1.66	2.19
3-Nov-1996	0941	1.45	1.91
4-Nov-1996	0930	1.36	1.80
8-Nov-1996	1027	1.83	2.41
10-Nov-1996	0824	1.11	1.46
10-Nov-1996	1006	1.74	2.29
	Dataset Average	**1.58**	**2.09**
	Pre-Launch (Kidwell, 1991)	1.73	2.28
	PWL Method (Rao and Chen, 1994)	1.54	1.99

Table 10 Comparison between calibrated, post-launch and pre-launch values of gain (expressed in counts/W·m^{-2}·sr^{-1}·μm^{-1}) for channels 1 and 2 of AVHRR onboard the NOAA-14 satellite. The bold values indicate the average gains adopted in this study to calculate the albedos for the whole dataset.

b) The next step of this method consists of converting the calibrated radiance to a corrected narrowband reflectance $R_i(\theta_0,\theta,\phi)$ using the following relationship:

$$R_i(\theta_0,\theta,\phi) = \frac{\pi W_i L_i}{F_i \cos\theta_0} \qquad \textbf{Equation 23}$$

where, as before, θ is the satellite zenith angle, ϕ is the sun-satellite azimuth and θ_0 is the solar zenith angle. Figure 20 is a schematic diagram depicting θ, ϕ and θ_0. Calculations were restricted initially to pixels where θ_0 was less than 80°. In order to maximise the number of pixels available for analysis, this limit was increased to 85° for the winter images that coincided with Voyage 1 (95).

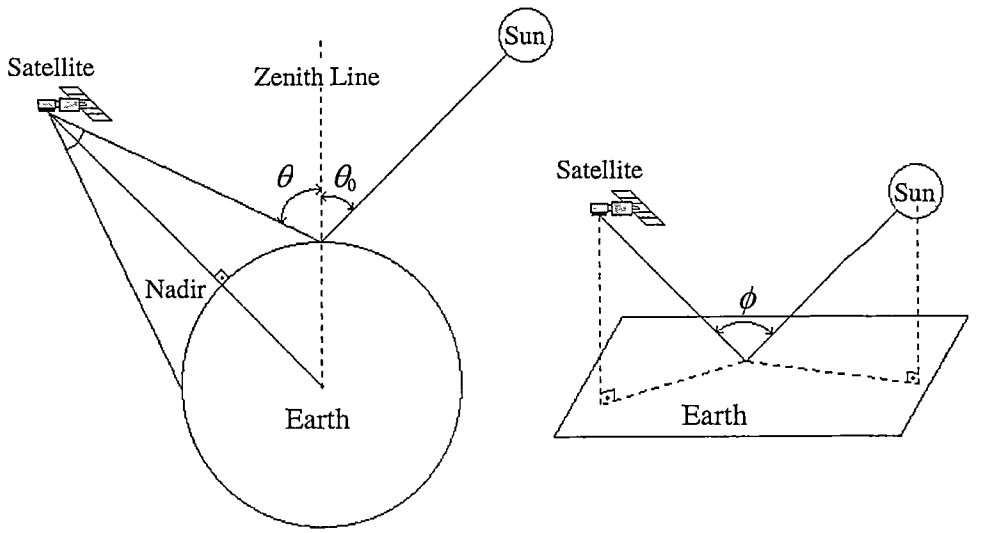

Figure 20 Angular relationships between the satellite, the Earth and the Sun. Adapted from *Kidwell* [1998].

c) From the corrected narrowband reflectance, the TOA narrowband albedo, $\alpha_{iTOA}(\theta_0)$, was obtained in the same fashion as in *Lindsay and Rothrock* [1994a], which uses a parameterised version of the broadband reflectance factor $f(\theta_0,\theta,\phi)$ from *Taylor and Stowe*'s [1984] compilation:

$$f = \beta_0 + \beta_1 x + \beta_2 y + \beta_3 \cos\theta + \beta_4 x^2 + \beta_5 y^2 + \beta_6 y \cos\theta \qquad \textbf{Equation 24}$$

where $x = \sin\theta\cos(\pi/2 - \phi)$, $y = \sin\theta\sin(\pi/2 - \phi)$ and the least-squares regression coefficients (β_n) are: $\beta_0 = 0.681$, $\beta_1 = 0.185$, $\beta_2 = -0.222$, $\beta_3 = 0.310$, $\beta_4 = 0.413$, $\beta_5 = 0.608$, and $\beta_6 = 0.338$. The TOA albedo can be then calculated through:

$$\alpha_{iTOA}(\theta_0) = \frac{R_i(\theta_0,\theta,\phi)}{f(\theta_0,\theta,\phi)} \qquad \textbf{Equation 25}$$

d) The narrowband surface albedo $\alpha_i(\theta_0)$ is obtained from the TOA albedo through a linear equation proposed by *Koepke* [1989], which accounts for the atmospheric attenuation in polar atmospheres:

$$\alpha_i(\theta_0) = \frac{\alpha_{iTOA}(\theta_0) - a_i(\theta_0)}{b_i(\theta_0)} \qquad \textbf{Equation 26}$$

The coefficients a_i and b_i depend on the atmosphere's optical depth (δ), the solar zenith angle (θ_0), and the integrated ozone content (u_{O3}) for AVHRR's Channel 1 and water vapour content (u_{H2O}) for Channel 2. *Koepke* [1989] suggested the following values for an average solar zenith angle of 70°: $\delta = 0.05$ μm, $u_{O3} = 0.24$ cm NTP and $u_{H2O} = 0.5$ g·cm^{-2}. Appropriate values for the coefficients in this case are: $a_1 = 0.086$, $b_1 = 0.791$, $a_2 = 0.035$, and $b_2 = 0.804$.

e) The broadband albedo is then estimated from the two narrowband values, α_1 and α_2. As in *Lindsay and Rothrock* [1994a], the relationship between the narrowband and the broadband albedos is obtained from measurements carried out in Antarctica by *Allison et al.* [1993] in the austral spring of 1988:

$$\alpha(\theta_0) = 0.43\alpha_1(\theta_0) + 0.47\alpha_2(\theta_0) \qquad \textbf{Equation 27}$$

f) The final step of this method consists of normalising the albedo to a solar zenith angle of 65°, a value close to the average for the dataset. This is done to account for variations in the solar zenith angle within each scene and to make albedo estimates comparable. The normalisation is achieved by multiplying the broadband albedo by a factor:

$$\alpha = \alpha(\theta_0)\left[\frac{\overline{\alpha}(65^0)}{\overline{\alpha}(\theta_0)}\right] \qquad \textbf{Equation 28}$$

where $\overline{\alpha}(\theta_0)$ is the mean albedo of an ice/snow surface at the solar zenith angle θ_0. The relationship used for $\overline{\alpha}(\theta_0)$ is the same as that employed by *Lindsay and Rothrock* [1994a], which is based on a fit to data for Antarctic snow originally published by *Liljequist* [1956]:

$$\overline{\alpha}(\theta_0) = 0.85 - 0.075\cos\theta_0 \qquad \textbf{Equation 29}$$

4.3.2.2 Ice/Snow Surface Physical Temperature

The ice/ snow surface temperature (T_{Sfc}) within each pixel was derived from the AVHRR channel 4 and 5 data following the polar multi-channel (split window) approach proposed by *Key and Haefliger* [1992], rather than estimating T_{Sfc} from channel 4 alone, which is the method employed by *Yu and Rothrock* [1996]. The *Key and Haefliger* approach was discussed in Section 2.2.4.5. This study employs an updated version of the *Key and Haefliger* [1992] algorithm presented by *Key et al.* [1997a], which incorporates angular-dependent coefficients derived especially for Antarctica (see Equation 5).

The parameterisation of the coefficients *a* through *d* in Equation 5 was based on temperature ranges for channel 4 (see Table 11 below) rather than the season-by-season approach taken in the original algorithm of *Key and Haefliger* [1992]. This technique increased the algorithm's flexibility and reduced its error [*Key, et al.*, 1997a]. Section 2.2.4.5 presents a more detailed discussion of both of these studies.

	Ch. 4 Brightness Temperature Ranges (K)		
	$T_4 < 240$	$T_4 < 260$	$T_4 > 260$
a	-1.180768	-5.647743	-6.602028
b	1.003950	1.022697	1.025938
c	1.616824	0.919952	0.963384
d	-0.729174	0.552105	0.793529

Table 11 Angular-dependent coefficients for NOAA-14 AVHRR for various ranges of channel 4 brightness temperatures [*Key*, pers. comm., 1998].

4.3.2.3 Near-Surface Air Temperature

To obtain the near-surface air temperature for their model, *Yu and Rothrock* [1996] assumed that $T_{Air} = \overline{T_{Sfc}} + \delta T$ where $\overline{T_{Sfc}}$ is the average AVHRR-derived surface temperature over a 50 km^2 area and δT has a constant value of 0.4 K for the areas of interest in the Arctic. Several studies have demonstrated that there is a close link between T_{Air} and T_{Sfc} and that, under clear-sky conditions, the snow/ice surface will be slightly cooler than the air immediately above [*Carrol*, 1982; *Guest and Davidson*, 1994; *Michael, et al.*, 1998; *Overland and Guest*, 1991; *Sverdrup*, 1933]. However, this is not necessarily valid for areas of thin ice with no snow cover.

The adoption of a constant value for δT in this study is inappropriate considering the fact that the Southern Ocean shows a greater diversity of ice types, and that Antarctic sea ice is generally thinner than is the case in the Arctic. Measurements made by *Guest* [1998] in the Weddell Sea indicate that, on average, δT is close to zero with the exception of areas of thin ice (less than 0.3 m thick) with no snow cover or when the wind is very light (less than 3 $m \cdot s^{-1}$). However, as can be seen from the linear regression in Figure 21, values of δT can vary considerably, depending on the meteorological conditions and the presence of areas of open water. *Guest* [pers. comm., 1999] suggested that the use of a linear fit to characterise the relationship between T_{Air} and T_{Sfc} would prevent an accurate modelling of the surface turbulence, and also neglect the effects of horizontal advection in the atmosphere and the associated effects of changes in wind speed and direction.

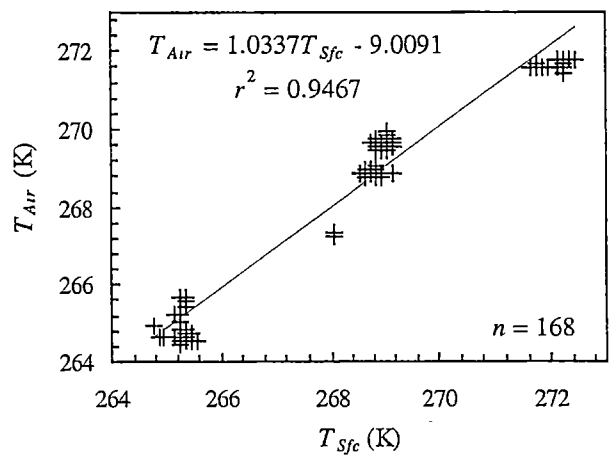

Figure 21 Relationship between T_{Air} and T_{Sfc} obtained from measurements made during five ice stations in Voyage 2 (96) using the Everest® radiometer and air temperature data (adjusted to 2 m) from the RSV *Aurora Australis*' DLS.

Also important to consider are the variations of δT when a parcel of air moves from areas of snow-covered ice to areas of open water, a very common situation in the vicinity of polynyas and leads, which are a characteristic feature of the Antarctic sea ice zone [*Worby, et al.*, 1998]. In this case, the characteristics of this air parcel, especially its relative humidity and temperature, will ultimately control the magnitude of the turbulent sensible and latent heat fluxes. *Vihma* [1995] simulated the behaviour of surface temperature and 2-m air temperature (along with other parameters) over a domain containing different fractions of ice and open water areas with a two-dimensional planetary boundary layer (PBL) model (Figure 22).

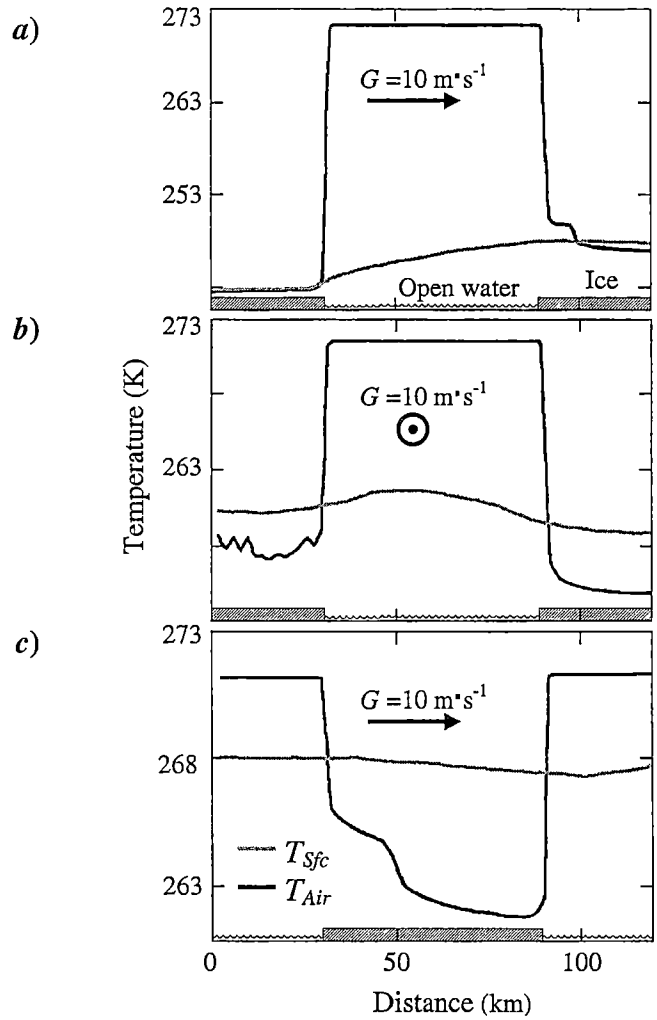

Figure 22 A PBL model simulation of surface (black) and air (grey) temperature variations over a 120 km field in three situations: (**a**) ice field with a 50% open water fraction and geostrophic wind (G) perpendicular to the ice edges, (**b**) ice field with a 50% open water fraction and G parallel to the ice edges and (**c**) single ice patch surrounded by open ocean and G perpendicular to the ice edges. Adapted from *Vihma* [1995].

As can be seen from Figure 22, the polynya-like situation of an ice-free area with the geostrophic wind perpendicular to the ice edge (***a***) shows the strong link between T_{Air} and T_{Sfc} over ice and a large temperature difference (from 25 to 27 K) over open water, with T_{Air} increasing downwind by approximately 0.1 K per kilometre. The second situation, with the geostrophic wind parallel to the ice edge (***b***), showed a similar behaviour but with higher temperatures. These were caused by surface friction which deviates the near-surface winds by 15 to 20° to the left of the geostrophic wind (in the Southern Hemisphere), producing a weak wind component across the polynya. The third situation, where a single ice floe is surrounded by open water (***c***), showed only a small variation in T_{Air}.

Based on these observations, the air temperature input for the model should ideally be from a source that is independent of the AVHRR-derived surface temperature. However, the injection of data from the GASP model did not produce acceptable results (Figure 19), mainly because of its poor spatial resolution. Other possible sources of T_{Air} data would be drifting meteorological buoys and TOVS satellite data.

The main problem with buoy data in the Southern Ocean is availability. The International Programme for Antarctic Buoys (IPAB) reported a considerable increase in buoy activities in the Antarctic sea ice zone during the years of 1995 and 1996 [*IPAB*, 1998]. However, the spatial and temporal coverage provided by the 51 units deployed throughout that two-year period was insufficient to generate air temperature fields to match the AVHRR imagery. Accuracy is another issue to be considered. *Allison* [pers. comm., 2000] mentions that a major problem with Antarctic buoy temperature data is caused by radiational effects. While modern buoys are equipped with some kind of protective shield, most historical buoy temperature data may be inaccurate, and in fact are not generally incorporated by operational meteorological agencies.

While TOVS may well provide useful additional information on surface temperature and atmospheric temperature profiles, its reliable use over ice-covered surfaces is still being investigated [*Francis*, 1994; *Lindsay, et al.*, 1997; *Schweiger and Key*, 1997]. A limiting factor is also the larger FOV (in comparison to the AVHRR) of 17-30 km. This inhibits its ability to view the surface without cloud contamination, as sub-pixel scale clouds would tend to cold-bias the TOVS surface-temperature retrieval.

In the absence of independent near-surface air temperature data, an alternative method was devised to derive T_{Air} from the AVHRR data. This approach still recognises the strong link between T_{Air} and T_{Sfc} and allows for the small δT values that typify areas with snow-covered thick (> 0.8 m) sea ice. It also addresses the effect of spatial inhomogeneity within the Antarctic sea ice zone. The method is based on the idea proposed by *Vihma* [1995] that the near-surface air temperature over open water areas will follow closely the surface temperature of the surrounding snow-covered sea ice, and that this link is governed by the wind speed and direction.

By applying this principle, the value of T_{Air} was set to the minimum value of T_{Sfc} within a rectangular shape measuring 9 x 1 pixels. This shape is oriented in the up-wind direction, as shown in Figure 23. Unfortunately, no *in situ* data were available to confirm this principle either for thick ice/thin ice situations or different wind speeds and directions. Therefore, in order to assess the effectiveness of this method, a series of sensitivity tests are presented in Section 4.4. These tests present various frequency distribution histograms of ice thickness obtained by altering the format (square or rectangular) and size of this shape.

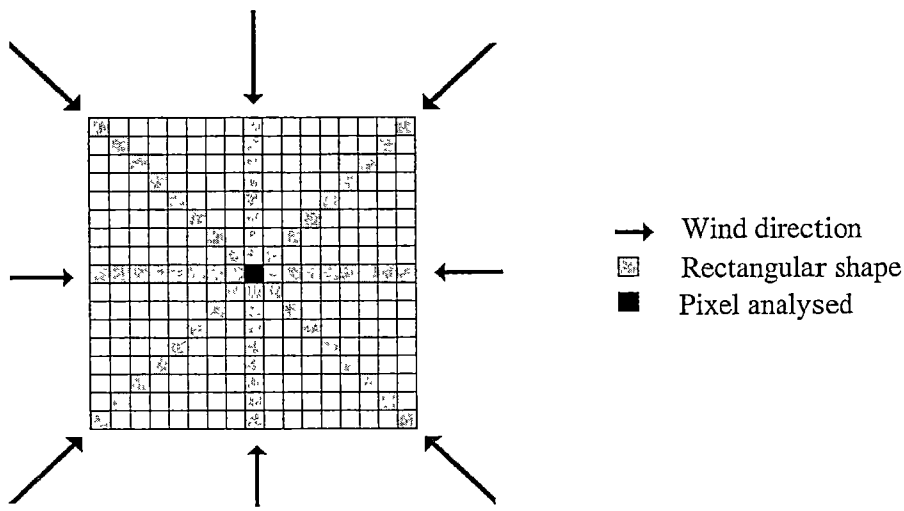

Figure 23 Eight possible positions for the 9 x 1 shape from which the minimum value of T_{Sfc} is extracted to set the value of T_{Air} for a given pixel. The position is chosen according to the wind direction of the pixel analysed.

Figure 24 shows examples of classified images (**a** and **b**) and frequency distributions histograms of T_{Air} and T_{Sfc} (**c**) and longitudinal transects of T_{Air} and T_{Sfc} located close to the Amery Ice Shelf (**d**) for an image from the spring of 1996. The relatively high temperatures (260 - 270 K) of the Cape Darnley polynya, clearly visible in the bottom left corner of both T_{Air} and T_{Sfc} images, are consistent with the expected range within an active polynya. The central lower part of the scene (between 66° and 70° S, around the Prydz Bay area) is dominated by a large region of cold pixels (T_{Air} and T_{Sfc} < 256 K). The average δT calculated from the T_{Air} and T_{Sfc} transects is less than 0.8 K, which is in agreement with modelled studies such as *Vihma* [1995], even considering that the transects cross an area of large temperature variations at the vicinity of the Cape Darnley polynya.

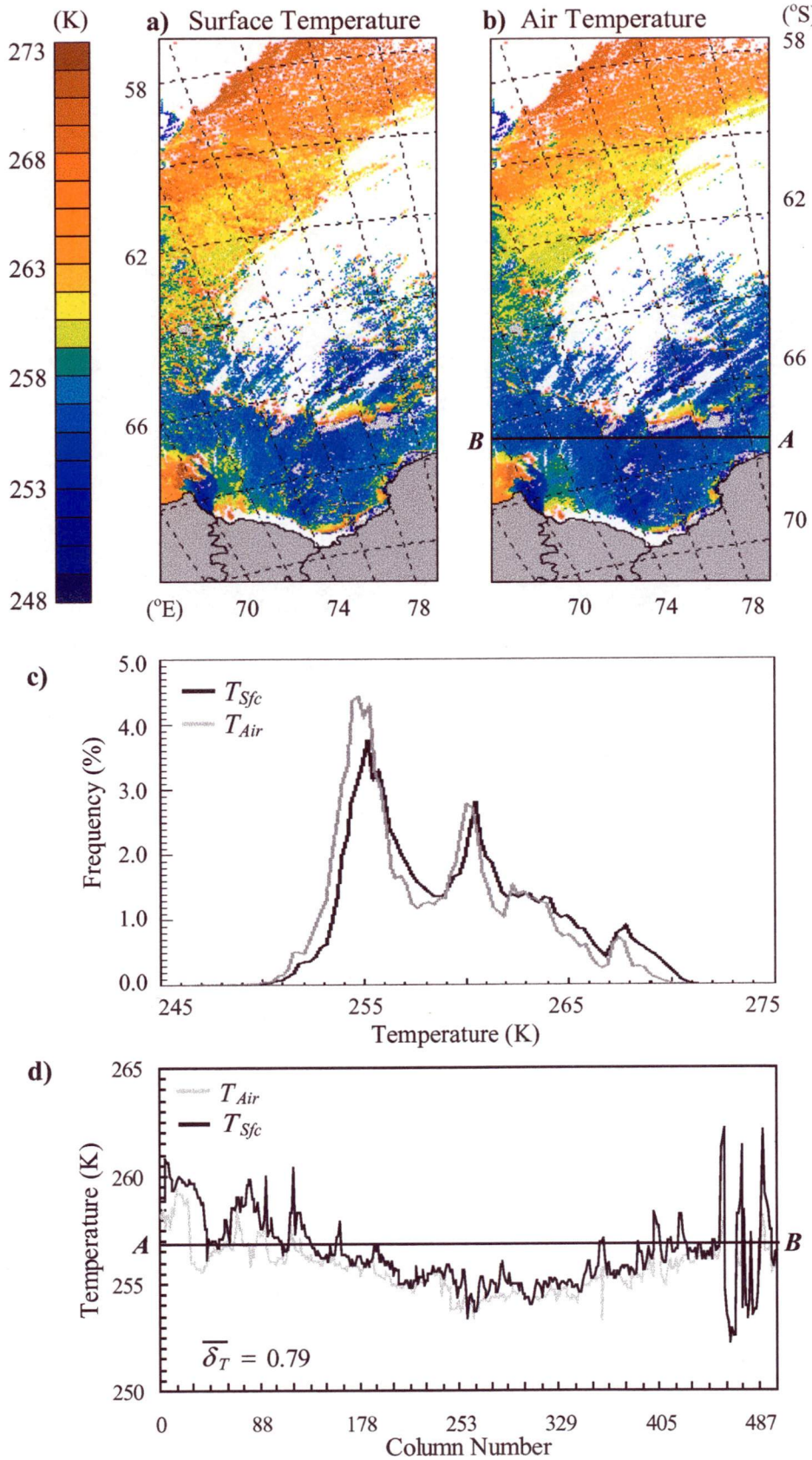

Figure 24 Classified AVHRR images of (**a**) T_{Air} and (**b**) T_{Sfc} obtained from a NOAA-14 image of the Davis area from 30-Sep-1996 at 0909 Z. Also shown is (**c**) a comparison between the two frequency distribution histograms and (**d**) longitudinal transects of T_{Air} and T_{Sfc} between *A* and *B*. The average δT for this transect is 0.79 K.

4.4 Sensitivity Tests

This section investigates the sensitivity of the model to variations in the parameters which represent the most significant areas where this study has sought to build upon *Yu and Rothrock*'s [1996] work. These parameters are: air-surface temperature difference, effective thermal conductivity of snow, bulk transfer coefficients for heat and evaporation, and the gain for calibration of channels 1 and 2 (required for the calculation of the normalised broadband albedo). By analysing the model's response to changes in these parameters, it is possible to estimate their potential contribution to errors in the estimation of ice thickness.

Two types of tests were performed for each parameter: an analysis of changes in the overall thickness histogram of a test image from the Davis area and an individual analysis of five test pixels from the same image. These pixels, detailed in Table 12, were selected to represent the broad range of values of solar zenith angle, albedo, surface temperature and wind speed and direction found in the whole dataset.

Pixel	*Location*		θ_0	α	T_{Sfc}	*Wind Speed*	*Wind Direction*
#	Column	Row	(°)		(K)	($m \cdot s^{-1}$)	(°)
1	276	30	67.87	0.092	269.12	6.19	212.5
2	467	407	69.76	0.153	268.04	5.96	251.1
3	1336	122	63.49	0.306	269.07	4.84	225.2
4	1434	496	65.93	0.640	264.45	7.94	237.2
5	364	496	70.97	0.760	258.20	5.78	248.3

Table 12 Location, solar zenith angle (θ_0), albedo (α), surface temperature (T_{Sfc}) and wind speed and direction values (obtained from GASP) for five pixels selected from the test image (30-Sep-1996, 0909 Z) for individual analysis.

4.4.1 Air-Surface Temperature Difference

The air-surface temperature difference (δT) is the most important parameter in this model, as it affects the largest number of component fluxes in Equation 8. Testing the sensitivity of the model to δT implies changing the derivation of T_{Air}, as the value of T_{Sfc} is fixed for each pixel (defined by the satellite data). An increase in T_{Air} will increase both the downwelling longwave radiation and turbulent sensible heat flux (Equation 12), thereby adding more heat to the system.

T_{Air} also has an indirect effect on the latent heat flux (through its effect on the saturation vapour pressure) and on the incoming shortwave radiation (through its effect on the surface water vapour pressure - see Equation 9) which is employed to calculate the net solar radiation at the surface and the solar radiation that penetrates the combined snow and ice layer.

Figure 25 shows variations in ice thickness of the five test pixels in response to changes in δT from -4.0 to 4.0 K. These values are one order of magnitude larger than the δT value chosen by *Yu and Rothrock* [1996], which is a constant 0.4 K. The largest changes occur in the "cold" and "bright" pixels (**4** and **5**), markedly so when δT is less than zero. Although a negative δT is rare, it can occur in areas of thin newly-forming sea ice, such as those encountered in polynyas when cold katabatic winds force the ice northwards, promoting the rapid formation of new ice [*Massom, et al.*, 1998b].

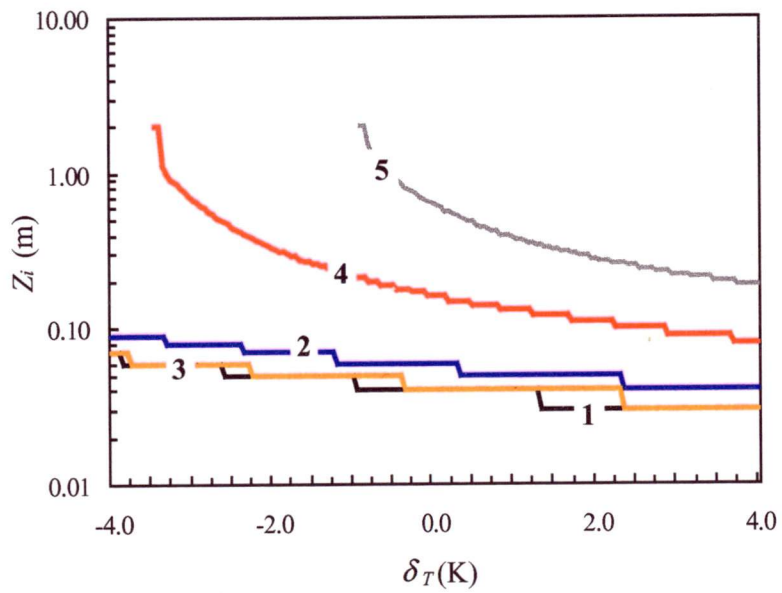

Figure 25 Variations in sea ice thickness of the test pixels **1** to **5** (see Table 12) in response to changes in δT.

Figure 26 shows a comparison between ice thickness histograms obtained by three methods of expressing T_{Air} as a linear function of T_{Sfc}, namely $T_{Air} = aT_{Sfc} + b$, using three different sets of coefficients. Table 13 presents the coefficients and the resulting median and mean thicknesses from the test image.

Histogram **1** shows results obtained by using *Yu and Rothrock*'s δT value of 0.4 ($a = 1.0$ and $b = 0.4$), histogram **2** was obtained by setting T_{Air} to the same value as T_{Sfc} ($a = 1.0$ and $b = 0.0$) and histogram **3** was derived through the empirical relationship based on field observations obtained during Voyage 2 (96) ($a = 1.03$ and b = -9.01, Figure 21). The three methods are very similar. Therefore, it is not surprising that these histograms have very similar shapes (Figure 26), although the mean and median values shown in Table 13 are slightly different.

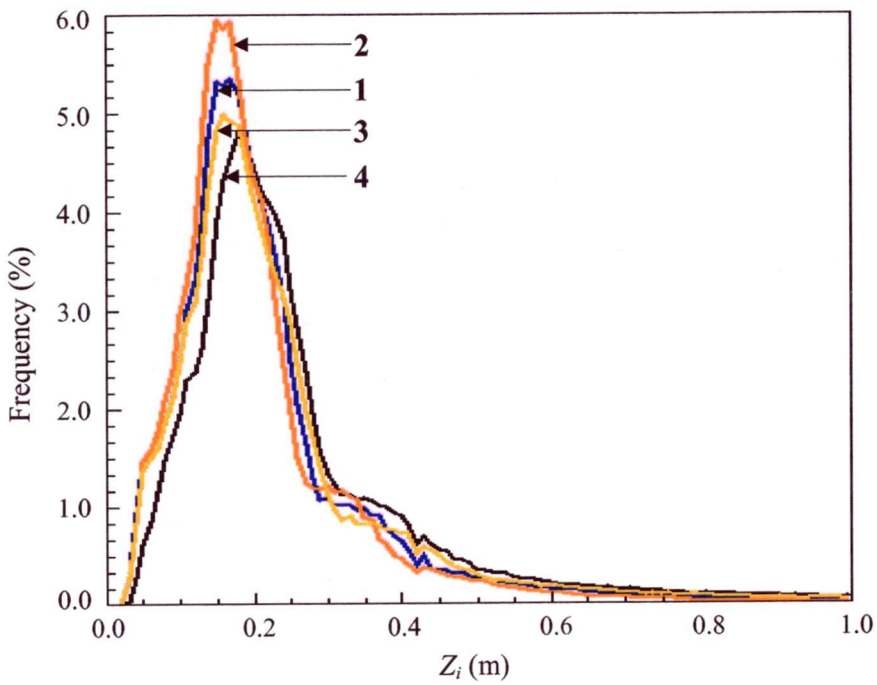

Figure 26 Frequency distribution histograms of sea ice thickness obtained with three different sets of coefficients (**1**–blue, **2**–red and **3**--yellow, according to Table 13) for estimating T_{Air} from T_{Sfc}. Also plotted is the thickness distribution histogram obtained through the method of estimating T_{Air} used in this study (**4**–black).

A fourth method of estimating T_{Air}, by equating it to the minimum value of T_{Sfc} within a box of 9 x 1 pixels (histogram **4**), produced some noticeable changes, with the resultant mean ice thickness being 0.1 m greater than that from technique 1. It is concluded from this sensitivity study that fixing the air temperature directly to the surface temperature of the pixel underneath through the use of a simple linear relationship does not produce satisfactory results. The method of setting T_{Air} to a minimum value of T_{Sfc} in the upwind neighbourhood of the pixel adds more flexibility to the model and the resulting frequency distribution histogram is likely to be more realistic, and accordingly this approach is adopted in this study.

	$T_{Air} = aT_{Sfc} + b$		*Mean* Z_i	*Median* Z_i
	a	b	(m)	(m)
1	*1.00*	*0.40*	0.20	0.17
2	*1.00*	*0.00*	0.23	0.18
3	*1.03*	*-9.01*	0.25	0.19
4	*9 x 1 rectangle*		0.29	0.21

Table 13 Median and mean ice thicknesses for histograms generated with three different sets of coefficients used to derive T_{Air} through a linear relationship with T_{Sfc} (**1** to **3**), along with values for the histogram obtained using the minimum T_{Sfc} value within a rectangle measuring 9 x 1 pixels oriented upwind (**4**).

Following studies such as *Vihma* [1995], *Andreas* [1996] and *Wu et al.* [1997], which motivated the development of the method employed to estimate T_{Air} in this study, one has to consider two other correlated factors to which the model might be sensitive: the size and shape of the neighbourhood from which the minimum T_{Sfc} is selected, and the influence of wind speed and direction. Figure 27 shows frequency distribution histograms of sea ice thickness resulting from the application of square neighbourhoods with sizes varying from 1 x 1 to 9 x 9 pixels. The means and medians of these histograms are listed in Table 14.

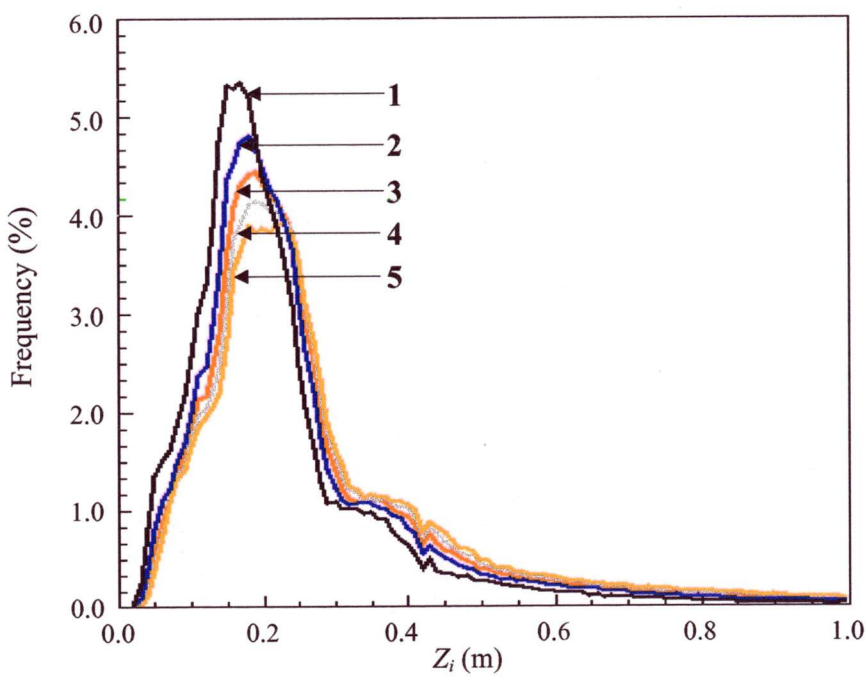

Figure 27 Frequency distribution histograms of sea ice thickness corresponding to the use of square neighbourhoods of varying sizes:1 x 1 (**1**–black), 3 x 3 (**2**–blue), 5 x 5 (**3**–red), 7 x 7 (**4**–grey), and 9 x 9 (**5**–yellow). These histograms correspond to the rows labelled **1** through **5** in Table 14, respectively.

	Box Size	*Mean* Z_i (m)	*Median* Z_i (m)
1	*1* x *1*	0.20	0.17
2	*3* x *3*	0.28	0.20
3	*5* x *5*	0.32	0.22
4	*7* x *7*	0.35	0.23
5	*9* x *9*	0.39	0.24
6	*1* x *9*	0.29	0.21
7	*3* x *9*	0.33	0.22
8	*1* x *n*	0.28	0.20

Table 14 Median and mean ice thicknesses for frequency distribution histograms generated with increasing box size (numbers **1** to **5**). Numbers **6** and **7** refer to a rectangular region oriented upwind (results shown in Figure 28). Number **8** refers to a rectangular region of variable size (in pixels), where *n* is chosen from 5, 7, 9, 11 or 13, depending on wind speed (results shown in Figure 29).

As can be seen from Figure 27 and Table 14, increasing the size of the area used to select T_{Air} effectively increases the average Z_i for the whole image, as the air temperature attains smaller values over larger portions of the image. It also increases the number of pixels excluded from the final thickness image (through failing to reach equilibrium during the looping process). The use of large square neighbourhoods (5 x 5, 7 x 7, 9 x 9) seems to produce higher thickness values compared to the 9 x 1 rectangular shape. The mean ice thickness produced using a 9 x 1 rectangle is comparable with that in a 3 x 3 square, which suggests that the value of T_{Air} is influenced more by the number of pixels analysed rather than the shape of the area. Increasing the width of the rectangle from 1 to 3 pixels (entries **6** and **7** in Table 14) produces very little change in the overall thickness histogram, as can be seen from Figure 28, although the mean ice thickness increases by 0.04 m.

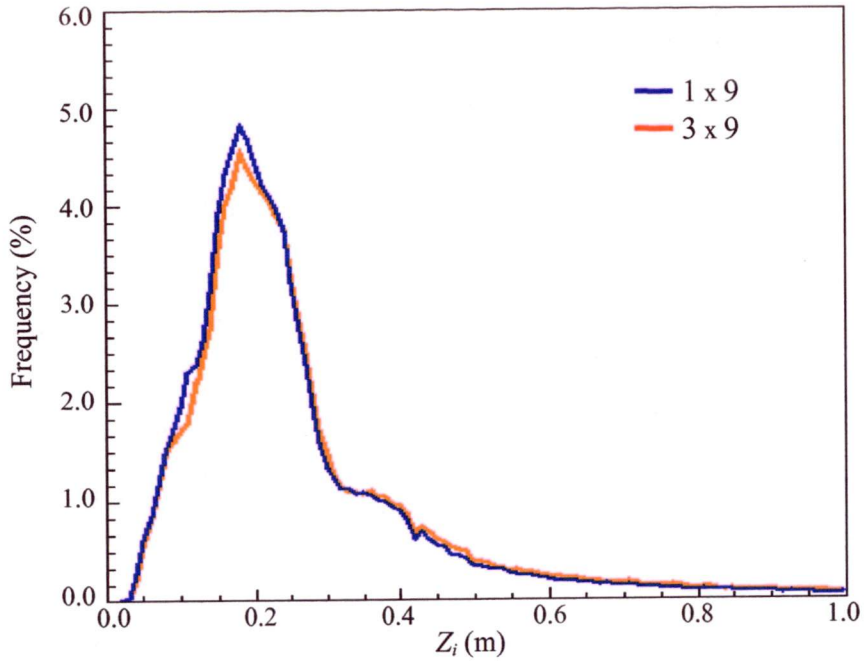

Figure 28 A comparison between the frequency distribution histograms of sea ice thickness generated by using a 1 x 9 rectangle (blue) and a 3 x 9 rectangle (red). The corresponding mean and median values are listed in Table **14**.

Based on the principle that the association between T_{Air} and T_{Sfc} would be extended over thin ice areas with increasing wind speeds (*Vihma* [1995], as shown in Figure 22), the sensitivity of the model was also tested by varying the length of the rectangle according to wind speed in the following manner: 5 pixels for speeds up to 5 $m \cdot s^{-1}$, 7 for speeds up to 10 $m \cdot s^{-1}$, 9 for speeds up to 15 $m \cdot s^{-1}$, 11 for speeds up to 20 $m \cdot s^{-1}$, and 13 for speeds greater than 20 $m \cdot s^{-1}$. As can be seen from Figure 29 and from the mean and median values listed in Table 14, this test produced very little change in the overall histogram.

The two previous tests support the notion that, in the absence of independent information on the near-surface air temperature, using the minimum value of the ice/snow surface temperature within an area around the pixel is a better alternative. The shape and wind speed-dependency are of little influence on the overall thickness histogram, and the number of pixels that comprise the neighbourhood is the more influential parameter. Ideally, these tests should have been conducted using dimensions and values that bear some relationship with *in situ* measurements. The collection of such measurements for the Antarctic sea ice zone would be a valuable source of corroborative information.

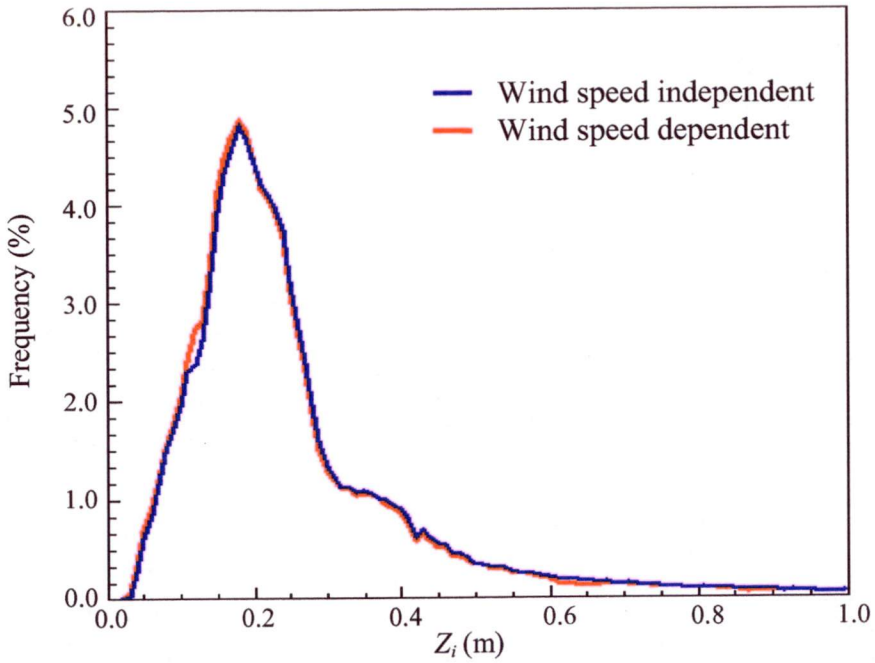

Figure 29 Frequency distribution histograms of sea ice thickness generated using a rectangle with a fixed length of 9 (blue) and a rectangle of varying extent (5,7,9,11 or 13) that depends on the wind speed (red).

4.4.2 Effective Thermal Conductivity of Snow

In this study, the effective thermal conductivity of ice (k_i) was calculated as a function of both the temperature and salinity of the ice slab (Equation 17) , using the relationship proposed by *Untersteiner* [1964]. However, the thermal conductivity of snow (k_s) was fixed at 0.164 $W \cdot m^{-1} \cdot K^{-1}$, a value significantly lower than the 0.31 $W \cdot m^{-1} \cdot K^{-1}$ adopted by *Yu and Rothrock* [1996] and typically employed by other sea ice models such as those of *Hibler* [1979], *Parkinson and Washington* [1979] and *Semtner* [1976].

This parameterisation of k_s uses new results from *Massom et al.* [1998b] and *Sturm et al.* [1998]. They combine measured values of snow thermal conductivity as a function of snow type, incorporating all measurements from entire cruises, to derive a *bulk effective thermal conductivity* based upon the proportions of different snow types encountered in the field. A review of measured k_s values as a function of snow type is given by *Sturm et al.* [1997] and *Massom et al.* [in press-a].

Snow thermal conductivity is defined as the proportionality constant between the temperature gradient within the snow layer and the total heat transport across this layer. It is generally expressed as an "effective" thermal conductivity to account for all of the processes in the snow pack, including conduction and vapour diffusion [*Sturm and Johnson*, 1992]. A few studies, such as *Jordan* [1991], have suggested that k_s can be calculated as a function of snow density (ρ_s). For example, *Abels* [1892] proposed the following relationship which, according to *Maykut and Untersteiner* [1971], satisfactorily described a wide range of *in situ* measurements.

$$k_s = 2.849\rho_s^2 \qquad \textbf{Equation 30}$$

Some of these proposed formulations have resulted in values even higher than 0.31 $W \cdot m^{-1} \cdot K^{-1}$. Recent studies by *Sturm et al.* [1997], *Sturm et al.* [1998] and *Massom et al.* [in press-a] have demonstrated that, for most types of snow, k_s is highly dependent on snow morphological and structural characteristics such as grain size and shape. *Sturm et al.* [1997] have also demonstrated that in certain types, such as new snow, there is no clear relationship between k_s and ρ_s.

In the case of the *Massom et al.* [1998b] study, data were taken from 46 snow pits collected in East Antarctica during Voyage 1(95) to derive a bulk effective thermal conductivity value of 0.164 $W \cdot m^{-1} \cdot K^{-1}$. Details of the location and dates of these snow pits can be found in *Lytle et al.* [1998b]. This value is used in an effort to account for the range of stratigraphy and textural complexity of the most frequent types of snow encountered on East Antarctic sea ice. Further details on the rationale for the use of a bulk effective thermal conductivity in sea ice models can be found in a review study by *Massom et al.* [in press-a].

	k_s ($W \cdot m^{-1} \cdot K^{-1}$)	*Mean* Z_i (m)	*Median* Z_i (m)
1.	*0.07*	0.22	0.16
2.	*0.16*	0.29	0.21
3.	*0.31*	0.34	0.24
4.	*2.20*	0.48	0.35

Table 15 Median and mean ice thicknesses for histograms generated with four different values of k_s.

Figure 30 shows variations in sea ice thickness of the five test pixels in response to changes in k_s between limiting values of 0.07 $W \cdot m^{-1} \cdot K^{-1}$ (for low-density new snow [*Sturm, et al.*, 1997]) and 2.2 $W \cdot m^{-1} \cdot K^{-1}$ (for icy melt layers [*Ratcliffe*, 1962]). "Warmer" and "darker" pixels (**1**, **2**, and **3**) show little or no response to changes in this parameter, with variations of less than 0.01 m. Pixels that are "colder" and "brighter" (**4** and **5**) presumably have a thicker layer of snow and therefore are more sensitive to changes in k_s. Even in these cases, however, the most noticeable changes occur only when k_s is less than 0.2 $W \cdot m^{-1} \cdot K^{-1}$.

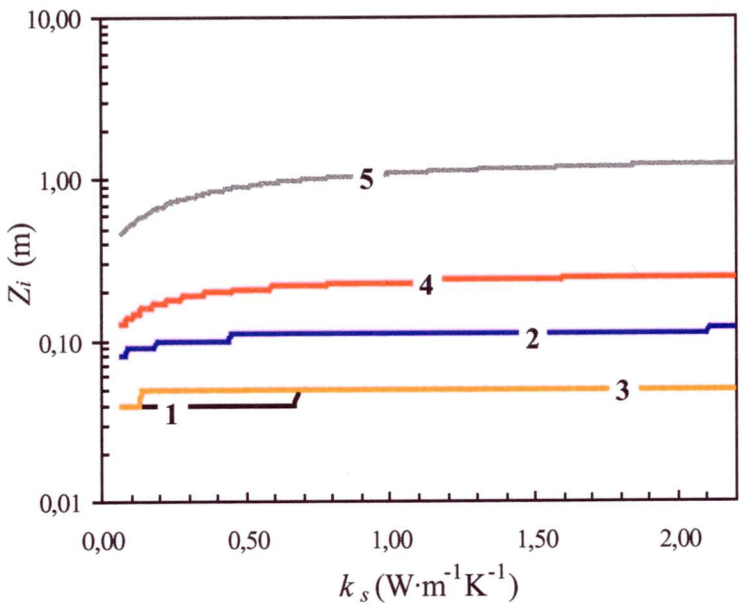

Figure 30 Variations in sea ice thickness of the test pixels **1** to **5** (see Table 12 above) in response to changes in k_s.

Figure 31 shows frequency distribution histograms of sea ice thickness obtained with four different values of k_s: 0.07 $W \cdot m^{-1} \cdot K^{-1}$, the lower limit from Figure 30 (histogram **1**), 0.164 $W \cdot m^{-1} \cdot K^{-1}$, the value employed in this study (histogram **2**), 0.31 $W \cdot m^{-1} \cdot K^{-1}$, which is the value proposed by *Yu and Rothrock* [1996] (histogram **3**), and 2.20 $W \cdot m^{-1} \cdot K^{-1}$, which is upper limit from Figure 30 (histogram **4**). The median and mean ice thicknesses of these histograms are listed in Table 15. It is clear from Figure 31 that the choice of an appropriate value for this coefficient is important. The use of extreme values, such as the ones for low-density new snow and icy melt layers (histograms **1** and **4** respectively), produces histograms, with mean ice thicknesses that are too small or too large if compared with histograms **2** and **3**.

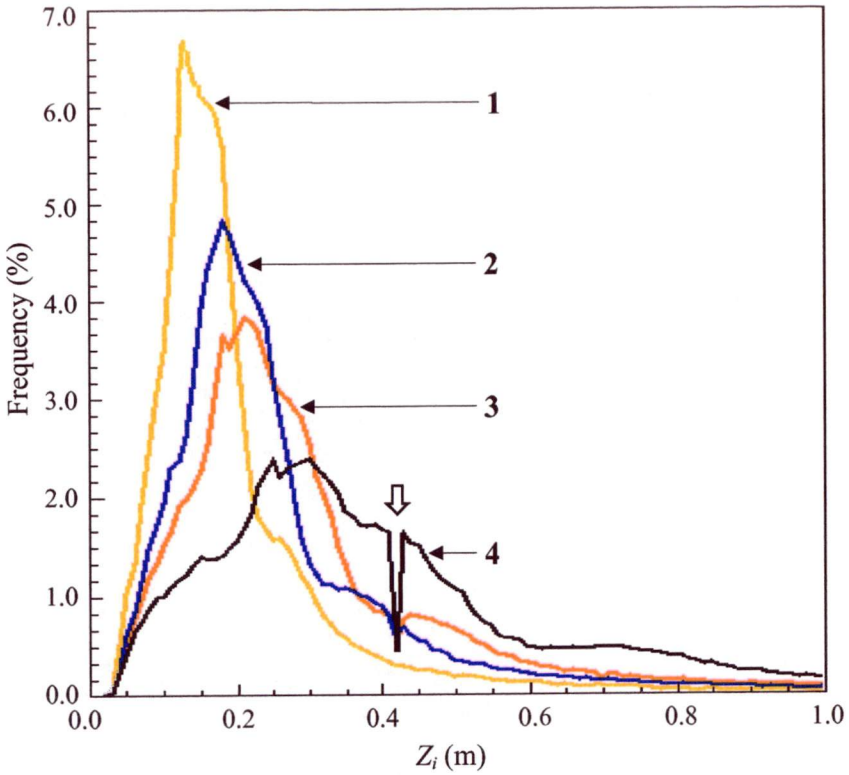

Figure 31 Frequency distribution histograms of sea ice thickness (Z_i) obtained with four values of k_s: (**1**–yellow) 0.07, (**2**–blue) 0.164, (**3**–red) 0.31 and (**4**–black) 2.20 $W \cdot m^{-1} \cdot K^{-1}$. The depression around 0.4 m (⇩) found in (**4**) occurs, albeit to a lesser extent, in all histograms generated through this model and is a numerical anomaly caused by the introduction of the second equation of *Cox and Weeks*' [1974] empirical relationship used to calculate the sea ice salinity (see Equation 18).

In spite of its widespread use in other sea ice models, including *Yu and Rothrock* [1996], the value of 0.31 $W \cdot m^{-1} \cdot K^{-1}$ (histogram **3**) is higher than estimates of bulk k_s obtained from direct measurements of Antarctic snow [*Sturm, et al.*, 1997; *Sturm, et al.*, 1998]. The application of this value leads to a scenario with more thick ice and a large number of pixels that do not reach the equilibrium at the end of the model's iterations.

In summary, this study will therefore employ a value of 0.164 $W \cdot m^{-1} \cdot K^{-1}$ for the thermal conductivity for snow, as it has been found to be a more representative value for Antarctic sea ice. In addition, the histograms of sea ice thickness compiled with this value of snow thermal conductivity are more physically reasonable. For a fuller discussion of the rationale behind the development of this value for the snow thermal conductivity, see *Massom et al.* [in press-a].

4.4.3 Bulk Transfer Coefficients

Bulk transfer coefficients for heat and evaporation are notoriously difficult to measure over polar surfaces [*Andreas*, 1996]. They are an integral part of the formulations of the turbulent sensible and latent heat fluxes, which are the only two fluxes in Equation 8 that can assume either positive or negative signs (i.e., removing heat from, or adding heat to the ice/snow surface respectively), depending on T_{Sfc} and on the meteorological conditions. It is therefore important to evaluate the effect of varying C_h and C_e in the overall heat budget and the corresponding ice thickness frequency distribution histograms.

Figure 32 shows variations in sea ice thickness of the five test pixels resulted from variations of C_h and C_e. The selection of the upper and lower limits in this figure was based on the maximum and minimum values of modelled results published by *Andreas* [1987], shown in Figure 13. They bracket the values chosen by *Yu and Rothrock* [1996] and also include the range over which these coefficients are permitted to vary in this study (i.e., from 1.0×10^{-3} to 1.5×10^{-3}). As expected, little change occurs in the thickness of the test pixels with increasing C_h and C_e. The variation in the magnitude of the coefficients is too small to produce any noticeable variations in the net flux. Moreover the fluxes themselves are too small.

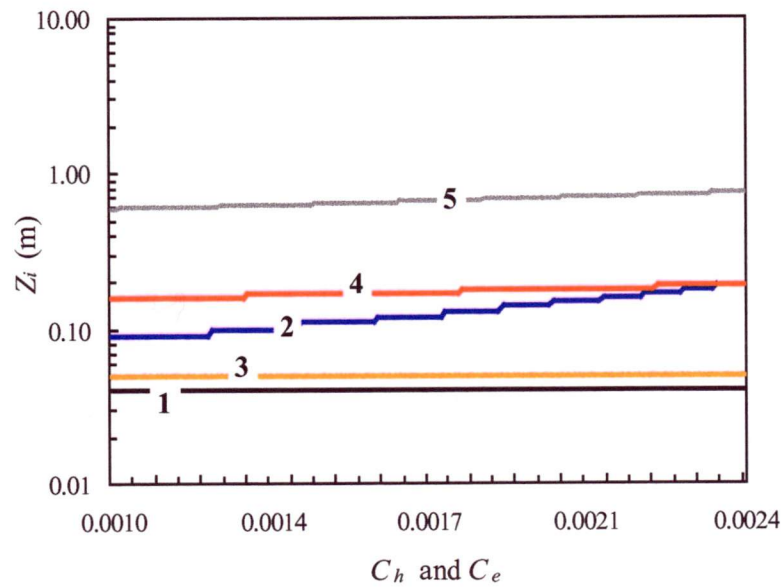

Figure 32 Variations in sea ice thickness of the test pixels 1 to 5 (see Table 12 above) in response to changes in C_h and C_e.

Figure 33 shows frequency distribution histograms of ice thickness obtained with C_h and C_e set to the same lower and upper limits from Figure 32 (histograms **1** and **3**) plus the histograms obtained with coefficients for thin and thick ice chosen by *Yu and Rothrock* (**4**) and the method to obtain the coefficients employed in this study (**2**). Table 16 shows the median and mean ice thicknesses for these histograms. Figure 32 implies that the model is not very sensitive to variations in the bulk transfer coefficients, although "dark" and "warm" pixels are less affected than "cold" and "bright" pixels. However, the choice of correct values for those coefficients is important. Figure 33 and Table 16 show that, in comparison with the fixed values chosen by *Yu and Rothrock* [1996], the method utilised in this study to calculate C_h and C_e (histogram **2**) produces results that are closer, both in the shape of the histogram and the mean ice thickness, to those produced through model predictions by *Andreas* [1996], especially in the lower limit (histogram **1**).

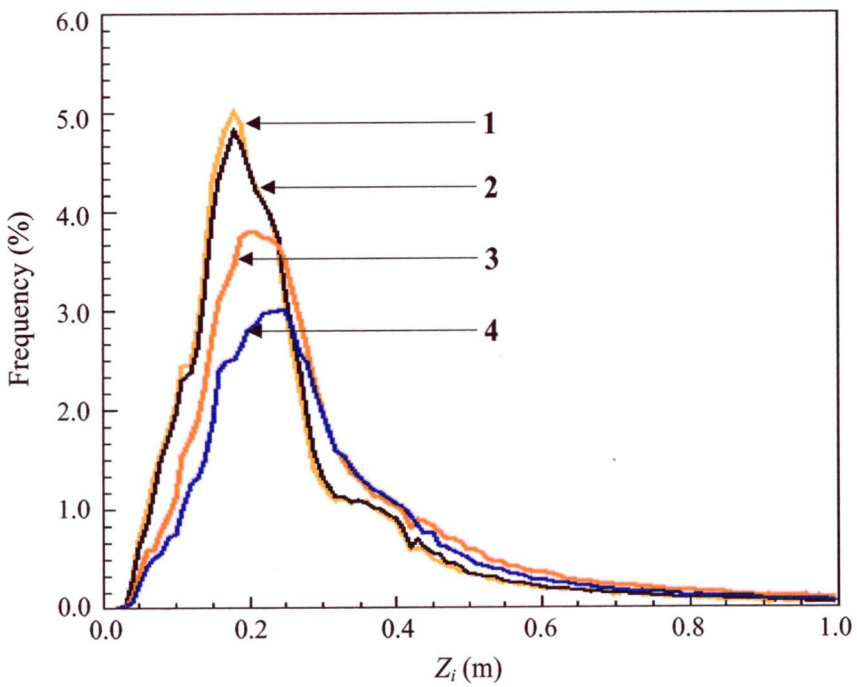

Figure 33 Frequency distribution histograms of sea ice thickness obtained with four sets of values for C_h and C_e: (**1**–yellow) $C_h = C_e = 0.0010$, (**2**–black) the method employed in this study, (**3**–red) $C_h = C_e = 0.0022$, and (**4**–blue) the values employed by *Yu and Rothrock* [1996]: $C_h = C_e = 0.003$ for thin ice and $C_h = C_e = 0.00175$ for thick ice.

	C_h and C_e	*Mean* Z_i (m)	*Median* Z_i (m)
1.	*0.0010*	0.27	0.20
2.	*This study*	0.29	0.21
3.	*0.0022*	0.41	0.25
4.	*Yu and Rothrock* [1996]	0.40	0.30

Table 16 Median and mean ice thicknesses for histograms generated with four different conditions for C_h and C_e.

4.4.4 Calibration Gains

As discussed in Section 4.3.2.1, the post-launch drift in the gains (g_1 and g_2) used to retrieve the narrow-band radiance from the digital counts of channels 1 and 2 (Equation 20) are the largest source of uncertainty in the method of albedo retrieval from AVHRR data. Figure 34 shows variations in ice thicknesses of the five test pixels in response to changes in g_1 and g_2. The upper and lower limits used in this figure are the pre-launch values listed in *Kidwell* [1998] and the post-launch values from *Rao and Chen* [1994] respectively (see Table 10).

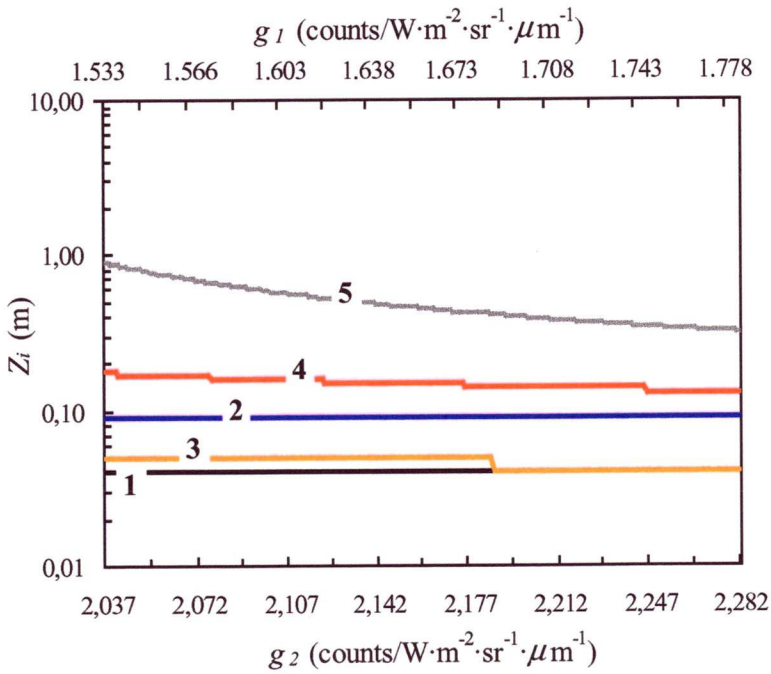

Figure 34 Variations in sea ice thickness of the test pixels **1** to **5** (see Table 12 above) in response to changes in g_1 and g_2.

Figure 35 shows the frequency distribution histograms of ice thickness generated using the same upper and lower limit values of g_1 and g_2 mentioned above (histograms **1** and **2**), together with the histogram generated using the new values of g_1 and g_2 employed in this study. The median and mean ice thicknesses corresponding to these histograms are given in Table 17. The use of pre-launch values (histogram **1**) caused a decrease in the average albedo, allowing more solar radiation to enter the ice, so that on average, pixels took fewer iterations to reach equilibrium and were consequently assigned smaller thicknesses. The sets of coefficients employed in this study and those obtained through the piecewise linear calibration method (histograms **2** and **3** respectively) led to similar histograms, with both the mean and median values being considerably larger than in histogram **1**.

	g_1 ($W \cdot m^{-2} \cdot sr^{-1} \cdot \mu m^{-1}$)	g_2	*Mean* Z_i (m)	*Median* Z_i (m)
1.	*1.73*	*2.28*	0.20	0.17
2.	*1.54*	*1.99*	0.37	0.23
3.	*1.58*	*2.09*	0.29	0.21

Table 17 Median and mean ice thicknesses for histograms generated with three different sets of values for g_1 and g_2.

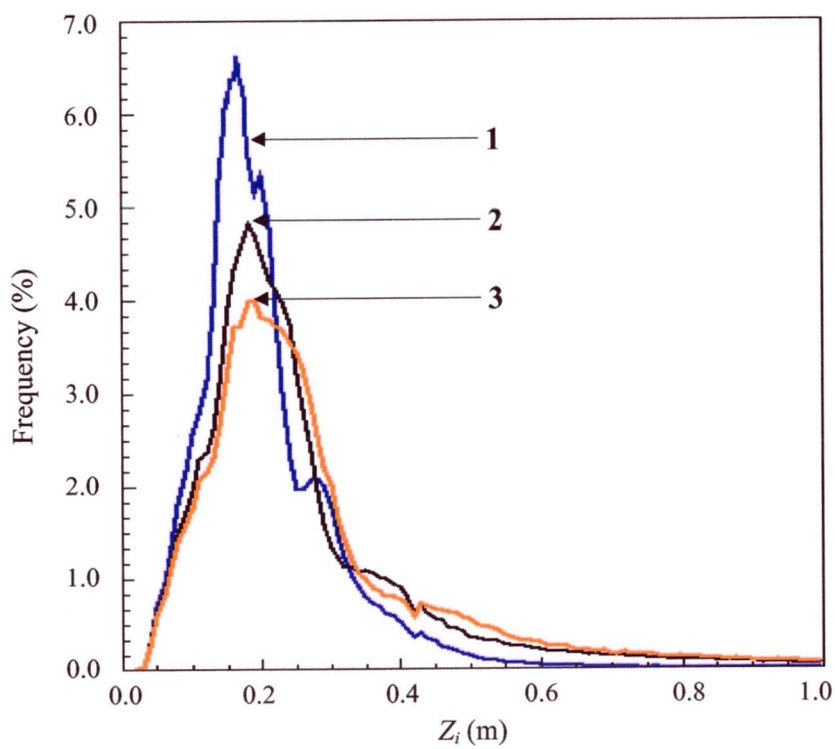

Figure 35 Frequency distribution histograms of sea ice thickness obtained with three sets of values for g_1 and g_2: (**1**–blue) the pre-launch values from *Kidwell* [1998], (**2**–black) the values used in this study and, (**3**–red) the PWL post-launch values published by *Rao and Chen* [1994].

4.5 Analysis of the Model's Response to Sub-Pixel Scale Features

The spatial resolution of the model presented in this study is determined by the size of the AVHRR pixel (approximately 1.0 x 1.0 km). The radiances and brightness temperatures from which the normalised albedo and the ice/snow surface temperature are respectively derived are an integration of the radiances emitted by all targets (i.e., types of surfaces) present within that ~ 1 km^2 area. In the case of Antarctic sea ice, several types of surfaces can typically occur within a single pixel, such as open water, nilas, pancake ice, new ice, first-year and multiyear ice (with or without snow cover) etc. In addition, radiances measured by the satellite's sensor may also be contaminated by the presence of sub-pixel clouds, which are especially difficult to detect and remove.

In this section, the model's response to pixels containing more than one surface type is tested. Sets of typical cloud, open water, snow-free sea ice and snow-covered sea ice pixels were manually retrieved from the same test image used in the sensitivity tests. Their original radiances and brightness temperatures (shown in Table 18) were averaged and then employed to re-create pixels with varying concentrations of ice (with and without a snow cover), water and cloud. In each case, a pixel was composed of two different surfaces in varying proportions. The combination of types of surface employed were: cloud x open water, cloud x snow-free ice, cloud x snow-covered ice, snow-free ice x cloud, snow-free ice x snow-covered ice, and snow-covered ice x cloud.

Surface Type	*Radiance 1* ($W \cdot m^{-2}$)	*Radiance 2* ($W \cdot m^{-2}$)	*Temp. 3* (K)	*Temp. 4* (K)	*Temp. 5* (K)
Cloud	64.57	61.67	261.95	242.46	241.78
Open Water	4.04	2.55	272.69	270.93	270.13
Snow-free ice	51.24	48.94	263.45	257.25	256.60
Snow-covered ice	70.38	70.30	261.06	252.87	252.07

Table 18 Typical cloud, open water, snow-free ice and snow-covered ice averaged radiances (from AVHRR channels 1 and 2) and brightness temperatures (from AVHRR channels 3, 4 and 5) employed in the combinations to create pixels with more than one feature.

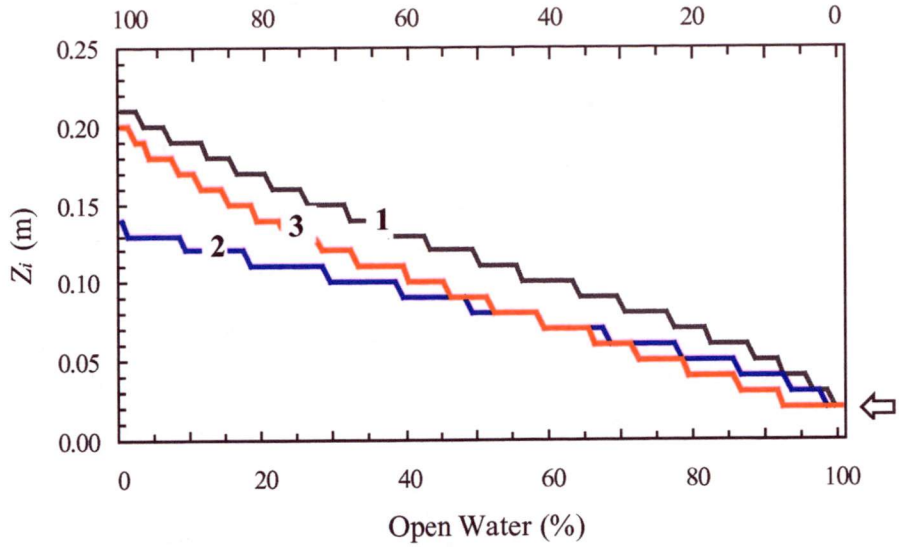

Figure 36 Apparent sea ice thickness variations in response to changes in sub-pixel concentrations of (**1**–black) open water x cloud, (**2**–blue) open water x snow-free ice and (**3**–red) open water x snow-covered ice. The bottom scale indicates the percentage of open water and the top scale indicates the percentage of the other three features. The model does not in fact deal with open water pixels, and assigns them a default thickness of 0.02 m (marked by ⇦).

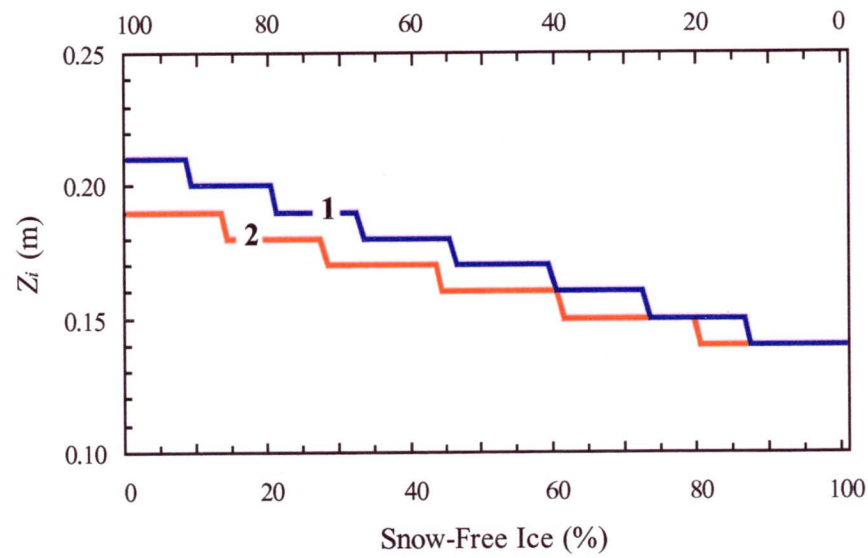

Figure 37 Apparent sea ice thickness variations in response to changes in sub-pixel concentrations of (**1**–blue) snow-free ice x cloud and (**2**–red) snow-free ice x snow-covered ice. The bottom scale indicates the percentage of snow-free ice and the top scale indicates the percentage of cloud and snow-covered ice. In the sixth scenario (snow-covered ice x cloud) the ice thickness remained at 0.20 m regardless of variations in the concentration of the two features.

Figure 36 and Figure 37 show variations in apparent sea ice thickness in response to changes in sub-pixel concentrations of cloud, open water and various types of ice. From the analysis of these figures it is possible to conclude that, because of the thermodynamic nature of the model, the apparent ice thickness of a pixel containing more than one surface type depends approximately on the concentration of each feature. This is particularly critical in the case of pixels containing a mixture of open water and cloud. In this scenario, unless the pixel is classified by the ICEMAPPER system as open water (which would preclude it from further sea ice thickness calculations), the model returns an unrealistic ice thickness for this pixel for any concentration of cloud greater than zero. This effect is further investigated in Chapter 5. The apparent ice thickness of pixels containing various concentrations of ice (with or without snow cover) and open water is also affected in the same manner.

The Antarctic sea ice zone is a very diverse region, with a large variety of surface types typically present in even small areas of a satellite image. Furthermore, sub-pixel clouds are very common. This analysis is useful to help understand the model's response to such diversity, in spite of the relative simplicity of the scenarios investigated.

4.6 Error Analysis

In this section, the accuracy of the apparent sea ice thicknesses returned by the model is estimated through an analysis of the uncertainties that arise from the various parameterisations employed to calculate each of the fluxes in the model (Equation 8). The general equation to calculate this error is given by *Young* [1962]:

$$\sigma_H^2 = \sigma_{(1-\tau)(1-\alpha)Q_s}^2 \left(\frac{\partial H}{\partial (1-\tau)(1-\alpha)Q_s}\right)^2 + \sigma_{Q_L^{\downarrow}}^2 \left(\frac{\partial H}{\partial Q_L^{\downarrow}}\right)^2 + \sigma_{Q_L^{\uparrow}}^2 \left(\frac{\partial H}{\partial Q_L^{\uparrow}}\right)^2 + \sigma_{H_S}^2 \left(\frac{\partial H}{\partial H_S}\right)^2 + \sigma_{H_L}^2 \left(\frac{\partial H}{\partial H_L}\right)^2 + \sigma_{H_C}^2 \left(\frac{\partial H}{\partial H_C}\right)^2 \qquad \textbf{Equation 31}$$

where σ_X^2 is the uncertainty associated with a flux X (see Equation 8). Each of these uncertainties is calculated separately using the error estimates shown in Table 19. Where appropriate, the typical values used to calculate the partial derivatives from Equation 31 were obtained by averaging the dataset.

The resulting uncertainty (σ_H = 11.23 W·m^{-2}) was then used to calculate ice thickness uncertainties (σ_{z_i}) for four selected thicknesses (0.05, 0.11, 0.25 and 0.37 m). These were obtained from pixels extracted from the test image (see Section 4.4) and were judged to be representative of the values found in the spring dataset.

Parameter (Unit)	*Fractional Error (%)*	*Source*
α	10.0	*De Abreu et al.* [1994]
τ	4.0	*Grenfell* [1979]
ε_{Sfc}	1.0	*Key and Haefliger* [1992]*
ε_{Air}	1.0	*Maykut and Church* [1973]*
C_e and C_h	10.0	*Andreas* [1987]*
T_{Sfc} (K)	1.5	*Key et al.* [1997a]
T_{Air} (K)	1.5	*Key et al.* [1997a]
k_i (W·m^{-1}·K^{-1})	5.0	*Untersteiner* [1964]*
k_s (W·m^{-1}·K^{-1})	1.0	*Massom et al.* [in press-a]
Q_s (W·m^{-2})	5.0	*Shine* [1984]
Z_s (m)	1.0	*Massom* [pers. comm., 1999]
U (m·s^{-1})	10.0	*Adams* [pers. comm., 1999]
f (%)	5.0	*Davey* [1997]

Table 19 Fractional error estimates used to calculate the accuracy of the AVHRR-derived apparent sea ice thicknesses. An asterisk indicates that the fractional error was not available in the publication, and typical values were employed to produce best estimates of the error.

Figure 38 shows plots of net flux and the resulting values of Z_i and σ_{z_i} at equilibrium (net flux = 0). These values are also shown in Table 20. The uncertainties in the turbulent and latent heat fluxes (9.8 and 3.9 W·m^{-2} respectively) are the greatest contributions to the value of 11.23 W·m^{-2} for σ_H. Still, this value is less than the sum of the uncertainties reported by *Yu and Rothrock* [1996], mainly because of the smaller error in the estimation of T_{Sfc} and T_{Air} and the smaller uncertainty for the downwelling longwave radiation flux (1.64 W·m^{-2} in comparison with 13.7 W·m^{-2} reported by *Yu and Rothrock* for the Arctic spring).

From the analysis of Figure 38 and Table 20, it is concluded that σ_{z_i} increases with Z_i and that $+\sigma_{z_i}$ increases more rapidly than $-\sigma_{z_i}$. This is due to the fact that the net flux does not vary linearly, which means that the longer it takes for a pixel to reach the equilibrium (i.e. the greater the number of iterations), the wider the gap between Z_i and σ_{z_i} is. Since the variation of net fluxes assumes a logarithmic form, $+\sigma_{z_i}$ will always be larger than $-\sigma_{z_i}$.

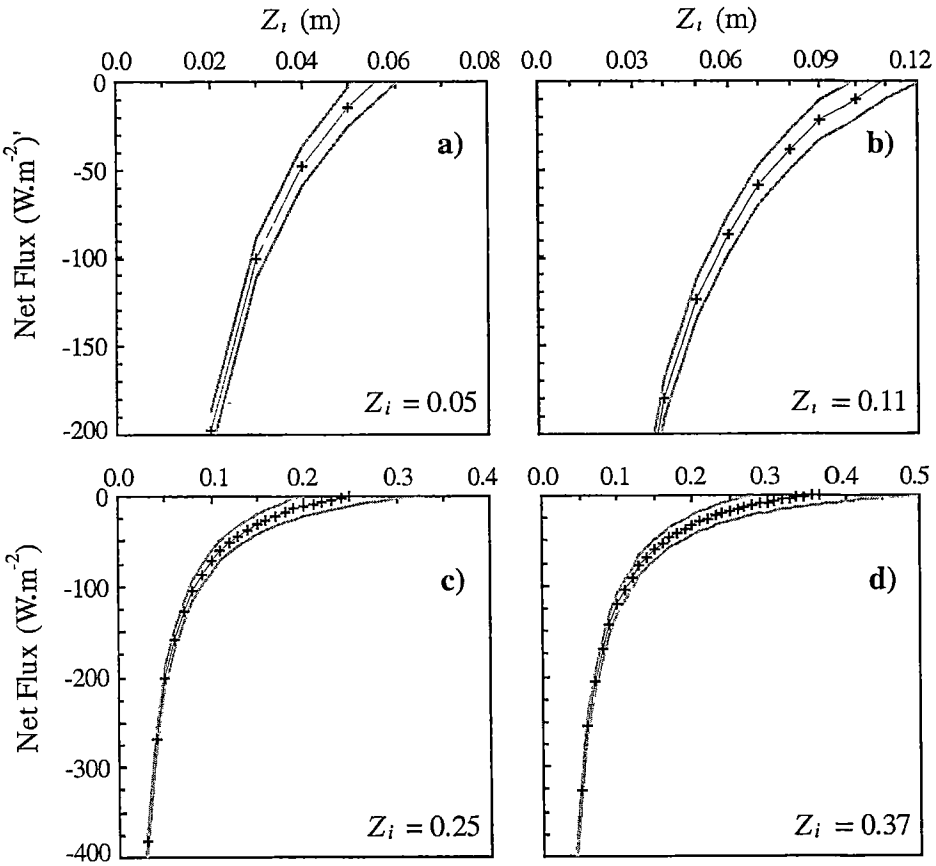

Figure 38 Net flux (black line with crosses) and corresponding ranges of uncertainties (σ_H, grey lines) for four representative ice thicknesses: (**a**) 0.05 m; (**b**) 0.11 m; (**c**) 0.25 m and; (**d**) 0.37 m.

For thicknesses up to 0.1 m, σ_{z_i} is approximately ± 0.01 m, which is the minimum thickness increment employed by the model. For thicknesses between 0.1 and 0.2 m, $-\sigma_{z_i}$ is 10% and $+\sigma_{z_i}$ is 20%. These error estimates increase to 16% and 32% respectively for thicknesses between 0.2 and 0.3 m, reaching up to 22% and 35% for thicknesses above 0.3 m. Considering that 55.7% of the pixels analysed in the 1996 dataset are between 0.02 and 0.20 m and 24.8% are between 0.2 and 0.4 m, the incorporation of these error estimates in the 33 images from that period will incur uncertainties of no more than 35% for more than 80% of the pixels analysed.

Z_i (m)	$-\sigma_{z_i}$ (m)	$+\sigma_{z_i}$ (m)
0.06	0.05	0.07
0.11	0.10	0.13
0.25	0.21	0.33
0.37	0.29	0.50

Table 20 Positive and negative uncertainties in estimated ice thickness.

Results

This chapter presents the results of the application of the sea ice thickness model described in Chapter 4 to a set of 35 NOAA-14 images from the austral winter of 1995 and spring of 1996. In Section 5.2, these results are interpreted in light of the current knowledge of albedo, IST and sea ice thickness distributions in East Antarctica. Comparisons between these data and concurrent digital aerial photography and ship-based observations are presented in Section 5.3. In Section 5.4, the results are compared with "climatological" data such as ship-based observations and drill-hole measurements collected in East Antarctica since 1991. A discussion of the results is presented in Section 5.5.

5.1 Data Summary

Table 21 presents the complete list of NOAA-14 images which provided input data for the sea ice thickness model, along with relevant sea ice thickness statistics obtained from them. In the V2(96) dataset, an average of 2.3% of valid pixels did not attain equilibrium after 198 iterations, while 14.9% of valid pixels from the two V1(95) images did not attain equilibrium after 398 iterations. These pixels were initially classified as sea ice pixels and were assigned the maximum thicknesses permitted by the system (2.0 m and 4.0 m, respectively). However, an analysis of their spatial distribution in the V2(96) dataset (exemplified in Figure 39) showed that these pixels occur on the periphery of large areas that were classified by the ICEMAPPER system as "clouds", leading to the conclusion that they had been erroneously inserted into the system as valid sea ice pixels. For this reason, they were removed from further sea ice calculations.

Considering the analysis of the model's sensitivity to sub-pixel scale features (Section 4.5), it is important to evaluate the spatial distribution of pixels that reached equilibrium in the first iteration and were therefore assigned a thickness of 0.02 m. In the same test image (Figure 39), only 159 pixels satisfied this condition. These occur in the vicinity of areas classified by the ICEMAPPER system as "open water" and "clouds", such as in the Cape Darnley polynya (Figure 39, **A**), which could indicate that they are accurately reflecting the process of ice formation in those areas.

Another possibility, however, is that these are actually open water pixels contaminated by cloud, fog or frost smoke emanating from the open water itself. Figure 36 shows that open water pixels containing even a small percentage (less than 5%) of cloud contamination will be erroneously classified as thin ice by the model, provided that its surface temperature is lower than 271.35 K (the approximate freezing point of sea water). Unfortunately, there is insufficient evidence to differentiate between these two possibilities.

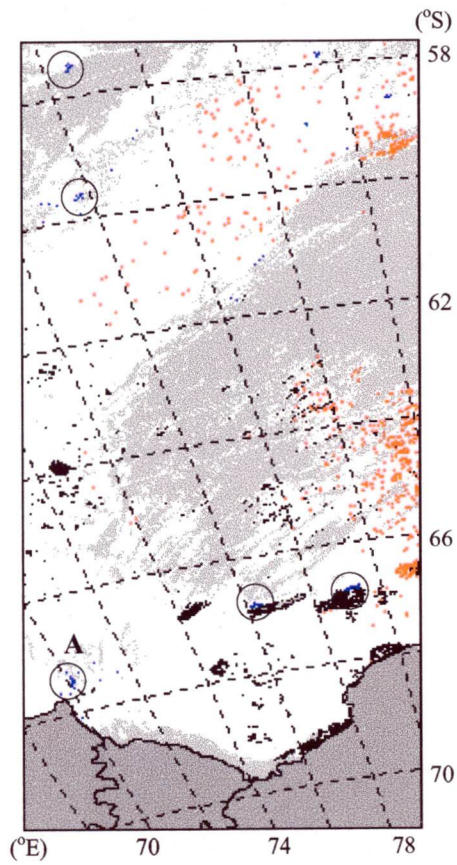

Figure 39 The spatial distribution of pixels in a test image from the Prydz Bay region, during the austral spring of 1996 (30-Sep, 0909Z). Pixels classified by the ICEMAPPER system as clouds are coloured in light grey, pixels classified as "very compact ice" (including icebergs or fast ice) are in black, pixels that were classified as valid by the ICEMAPPER but did not reach the equilibrium after 198 iterations are red, and pixels assigned a thickness of 0.02 m are blue and their position is highlighted by the circles. The location of the Cape Darnley polynya is indicated by (**A**).

As expected, the number of cloud-free images available for the period coinciding with the austral winter of 1995 was very small (only two), which limits the validation process for this period. Cloud cover also played a major role in limiting the amount of data available for processing in the spring of 1996, as can be seen by the percentage of valid data in Table 21.

Orbit Number	*Date/Time* (dd-mmm-yy, hhmm Z)	$\bar{\theta}_0$ (°)	*Valid Data* (%)	Z_t *>limit* (%)	$\bar{Z}_t$ (m)	*Median* (m)	σ_{Z_t} (m)
	Voyage 1 (95)	*limit* = 4.0 m					
3270	19-Aug-1995, 0549	82.37	22.71	12.60	1.84	0.82	1.63
3284	20-Aug-1995, 0539	81.91	21.41	17.28	1.01	1.18	0.73
Average values for dataset:		**82.14**	**22.06**	**14.94**	**1.43**	**1.00**	**1.18**
	Voyage 2 (96)	*limit* = 2.0 m					
9028	30-Sep-1996, 0909	67.02	49.52	0.75	0.29	0.21	0.30
9029	30-Sep-1996, 1050	76.67	12.95	20.20	1.44	2.00	0.74
9042	01-Oct-1996, 0858	66.96	24.11	0.13	0.24	0.20	0.19
9043	01-Oct-1996, 1039	75.18	14.55	18.19	1.31	2.00	0.80
9056	02-Oct-1996, 0848	64.62	18.52	0.00	0.14	0.13	0.05
9099	05-Oct-1996, 0955	70.53	6.70	4.21	1.07	0.77	0.80
9113	06-Oct-1996, 0945	68.72	11.81	3.34	0.77	0.41	0.73
9114	06-Oct-1996, 1124	78.39	8.70	4.69	1.19	1.11	0.71
9126	07-Oct-1996, 0752	61.52	4.45	0.00	0.10	0.10	0.03
9212	13-Oct-1996, 1009	68.60	8.64	2.82	0.67	0.20	0.79
9213	13-Oct-1996, 1149	77.27	6.15	1.84	0.89	0.63	0.73
9225	14-Oct-1996, 0817	61.40	3.25	0.00	0.09	0.10	0.04
9226	14-Oct-1996, 0958	68.86	5.05	1.44	0.67	0.24	0.76
9254	16-Oct-1996, 0936	65.19	9.98	0.76	0.37	0.18	0.50
9255	16-Oct-1996, 1116	73.34	8.56	2.05	0.67	0.28	0.71
9268	17-Oct-1996, 0925	64.81	4.18	0.04	0.24	0.19	0.23
9269	17-Oct-1996, 1106	72.51	2.14	1.46	1.06	0.64	0.82
9282	18-Oct-1996, 0914	61.29	5.79	0.01	0.09	0.07	0.10
9283	18-Oct-1996, 1055	72.37	3.40	1.43	0.97	0.71	0.76
9310	20-Oct-1996, 0852	58.50	11.17	0.00	0.05	0.04	0.08
9311	20-Oct-1996, 1033	68.59	3.55	1.70	0.91	0.47	0.80
9339	22-Oct-1996, 1011	66.61	4.05	3.49	1.15	1.12	0.84
9352	23-Oct-1996, 0820	58.99	4.17	0.00	0.12	0.12	0.03
9353	23-Oct-1996, 1000	65.95	5.95	4.13	1.10	0.85	0.80
9395	26-Oct-1996, 0928	61.41	5.83	0.19	0.26	0.16	0.36
9465	31-Oct-1996, 0833	54.82	1.31	0.00	0.05	0.04	0.04
9494	02-Nov-1996, 0953	62.12	7.43	0.52	0.34	0.14	0.52
9508	03-Nov-1996, 0941	60.45	4.03	0.01	0.08	0.06	0.11
9522	04-Nov-1996, 0930	58.93	8.81	0.01	0.08	0.05	0.11
9578	08-Nov-1996, 0846	53.54	7.32	0.00	0.05	0.03	0.04
9579	08-Nov-1996, 1027	63.13	10.56	1.10	0.39	0.15	0.58
9606	10-Nov-1996, 0824	51.69	6.46	0.01	0.03	0.03	0.06
9607	10-Nov-1996, 1006	59.52	8.93	0.19	0.18	0.10	0.32
Average values for dataset:		**65.44**	**9.03**	**2.26**	**0.52**	**0.41**	**0.44**

Table 21 Summary of the AVHRR images employed to derive apparent sea ice thickness distributions in this study, along with the resultant ice thickness mean ($\bar{Z}_t$), median and standard deviation (σ_{Z_t}) for each image. Average values for the V1(95) and V2(96) datasets are shown in bold. θ_0 is the solar zenith angle.

5.2 Albedo, Ice/Snow Surface Temperature and Sea Ice Thickness Distributions

In this section, the results summarised in Table 21 are interpreted in terms of what is currently known about the albedo, IST and sea ice thickness distributions of the two study areas. Examples of frequency distribution histograms and classified images are presented (Figure 40 to Figure 45), along with average ice thickness distributions for the entire V1(95) and V2(96) datasets (Figure 46). The analysis presented in this section concentrates on the images from 1996, as the two 1995 images from the Mertz area are spaced less than 24 hours apart, an interval which is insufficient to establish a sea ice climatology for that region.

Inter-comparisons between the albedo, IST and sea ice thickness data from individual images are complicated by the presence of a cloud cover as can be seen from Figure 40 to Figure 43. The images shown in these figures are the ones with the least cloud obscuration within the entire 1996 dataset. However, sea ice distribution patterns are discernible in some cases and can be explained in light of the meteorological and environmental conditions at the time of acquisition of the images.

For example, Figure 40 and Figure 41 are the ones with the least cloud obscuration and their acquisition time is only 24 hours apart. Data obtained from the RSV *Aurora Australis*' DLS and from the GASP system show no substantial alterations in the meteorological and environmental conditions during this period, suggesting that there should have been no major changes in the sea ice regime. Although atmospheric pressure at sea level was not available from the GASP dataset at this time, low temperatures observed at the coastline (~253 K) and moderate to strong winds blowing from southwest (15 to 25 $m \cdot s^{-1}$) suggest the occurrence of freezing and divergent conditions. The sea ice thickness distribution during this period, is consistent with the pattern described in the literature for such divergent conditions in the East Antarctic sector [*Allison*, 1989; *Massom, et al.*, 1999; *Worby and Massom*, 1995; *Worby, et al.*, 1998], with the inner pack consisting mostly of thin ice (0.02 to 0.10 m) and polynyas near the coast, the central pack, consisting of bands of thicker ice (up to 1 m) and icebergs, and the outer pack, characterised by areas of thinner ice (up to 0.10 m), probably brash and broken floes, mixed with open water areas near the ice edge.

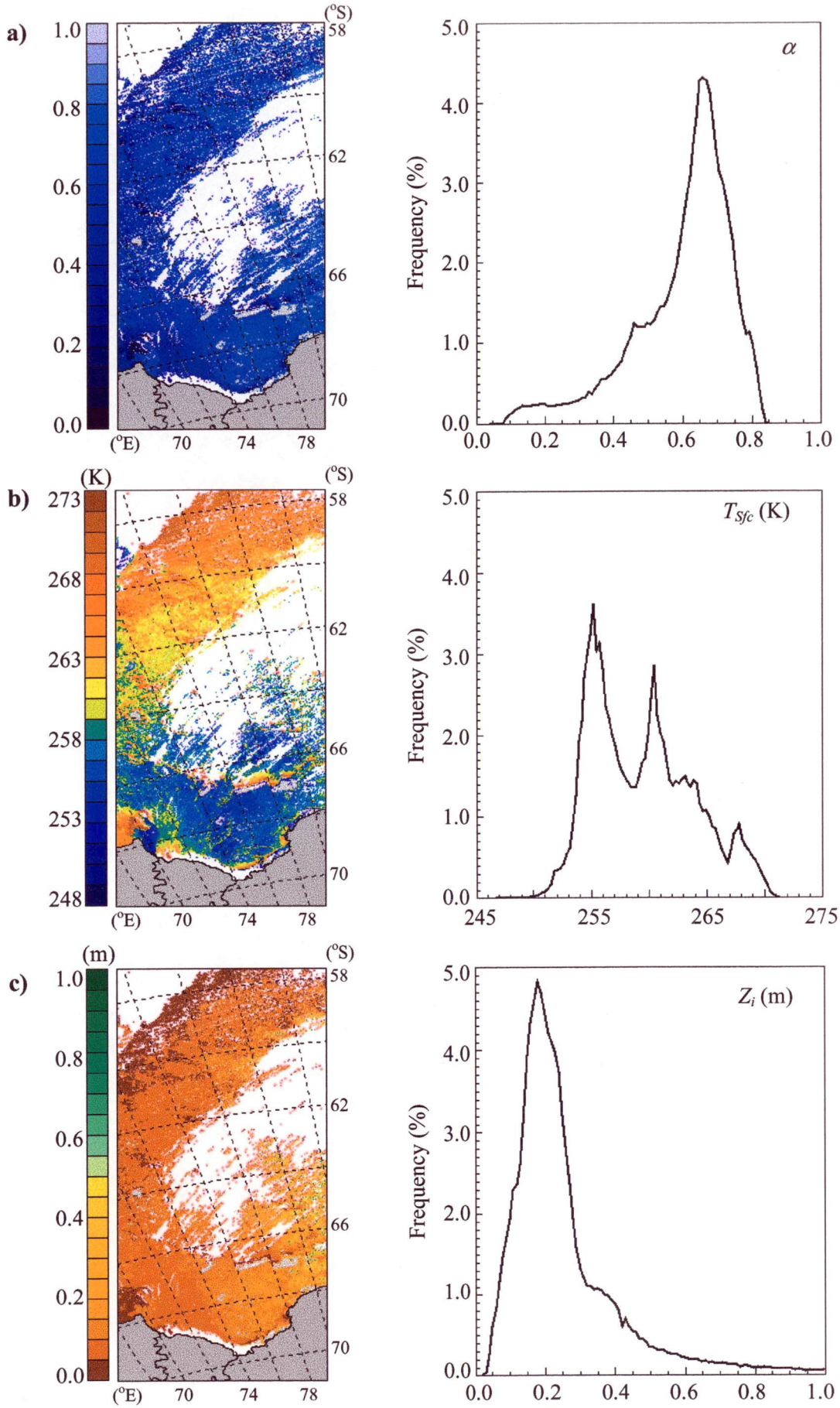

Figure 40 Classified AVHRR images and frequency distribution histograms of (**a**) albedo, (**b**) ice surface temperature and (**c**) sea ice thickness on 30-Sep-1996 at 0909 Z.

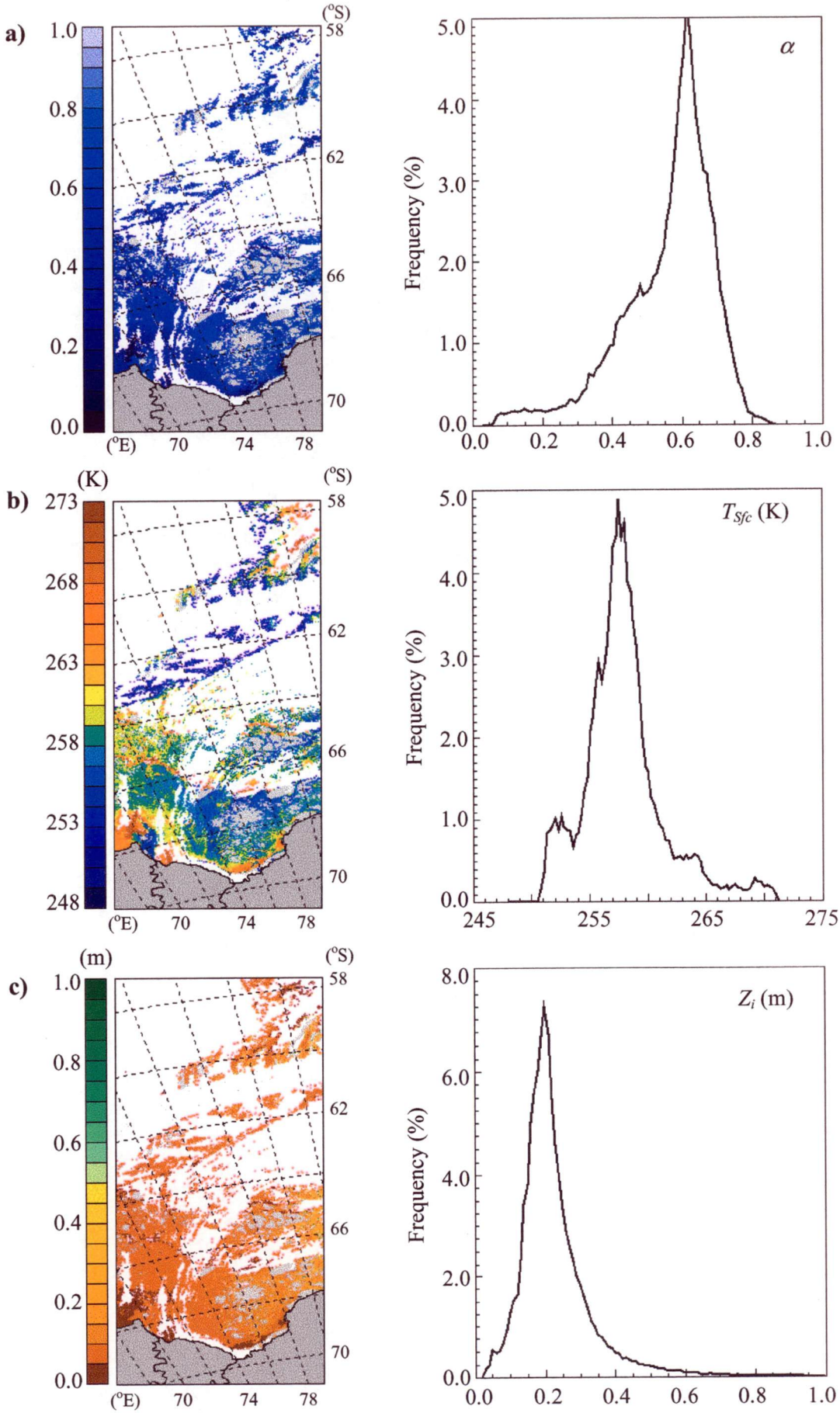

Figure 41 Classified AVHRR images and frequency distribution histograms of (**a**) albedo, (**b**) ice surface temperature and (**c**) sea ice thickness on 01-Oct-1996 at 0858 Z.

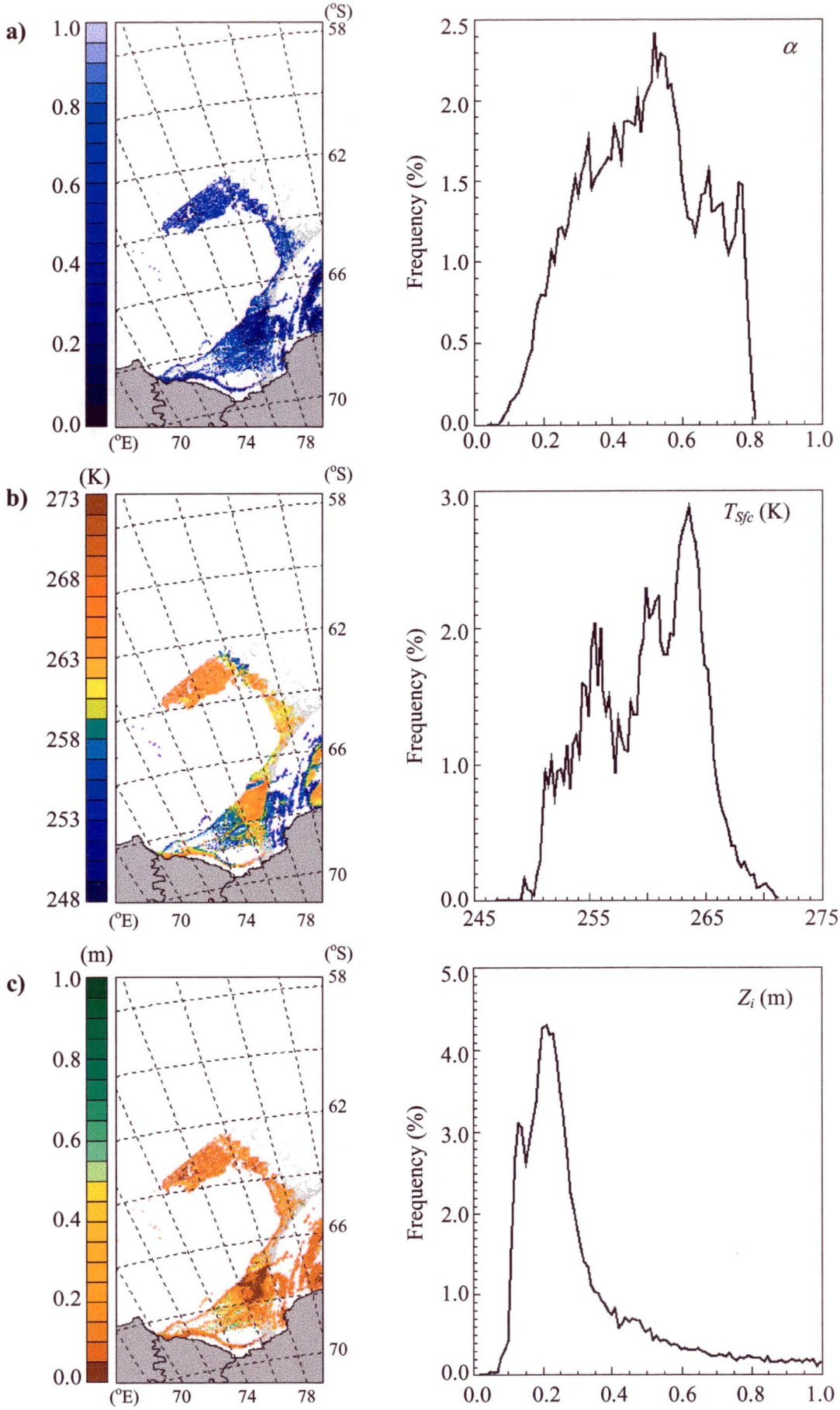

Figure 42 Classified AVHRR images and frequency distribution histograms of (**a**) albedo, (**b**) ice surface temperature and (**c**) sea ice thickness on 16-Oct-1996 at 1116 Z.

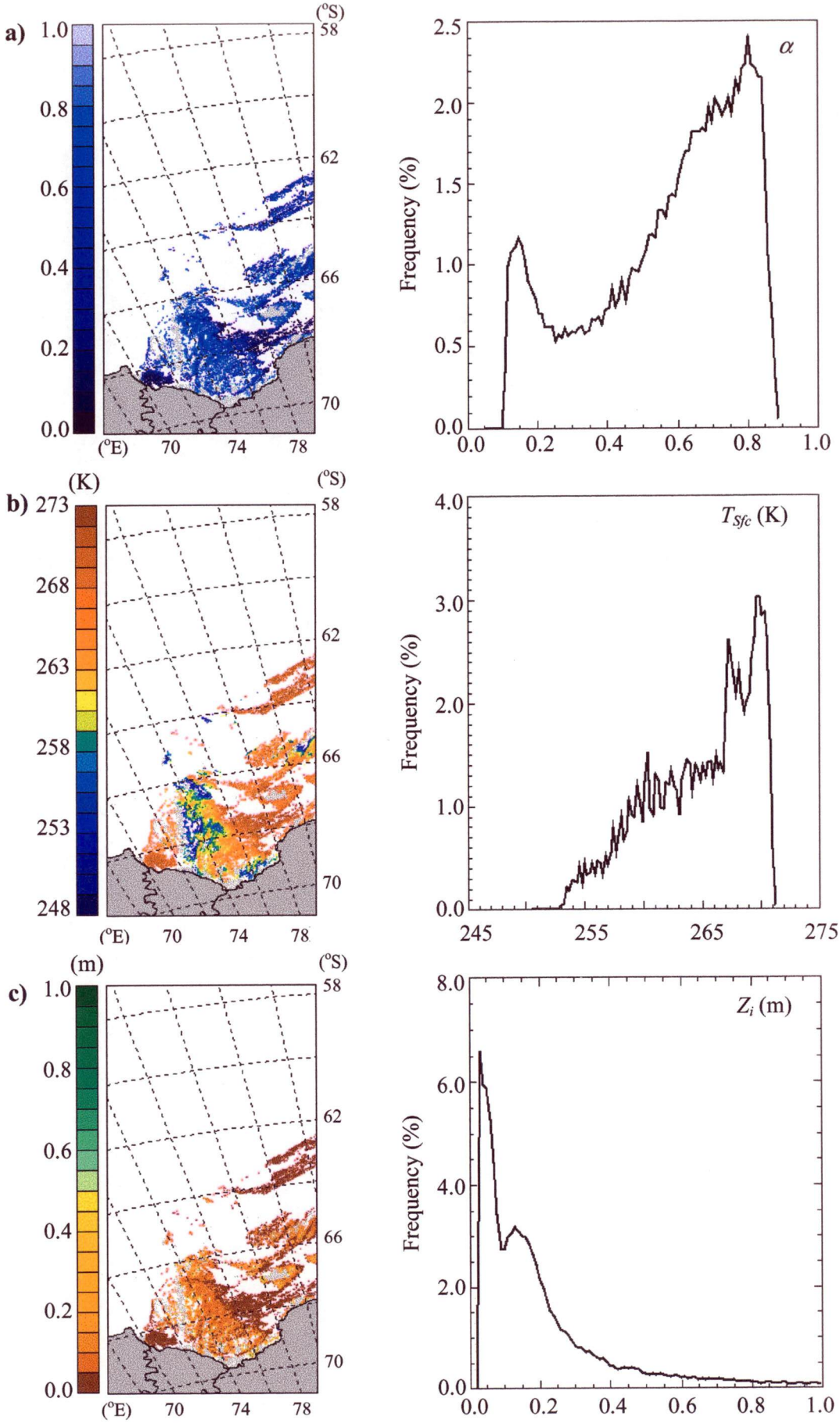

Figure 43 Classified AVHRR images and frequency distribution histograms of (**a**) albedo, (**b**) ice surface temperature and (**c**) sea ice thickness on 08-Nov-1996 at 1027 Z.

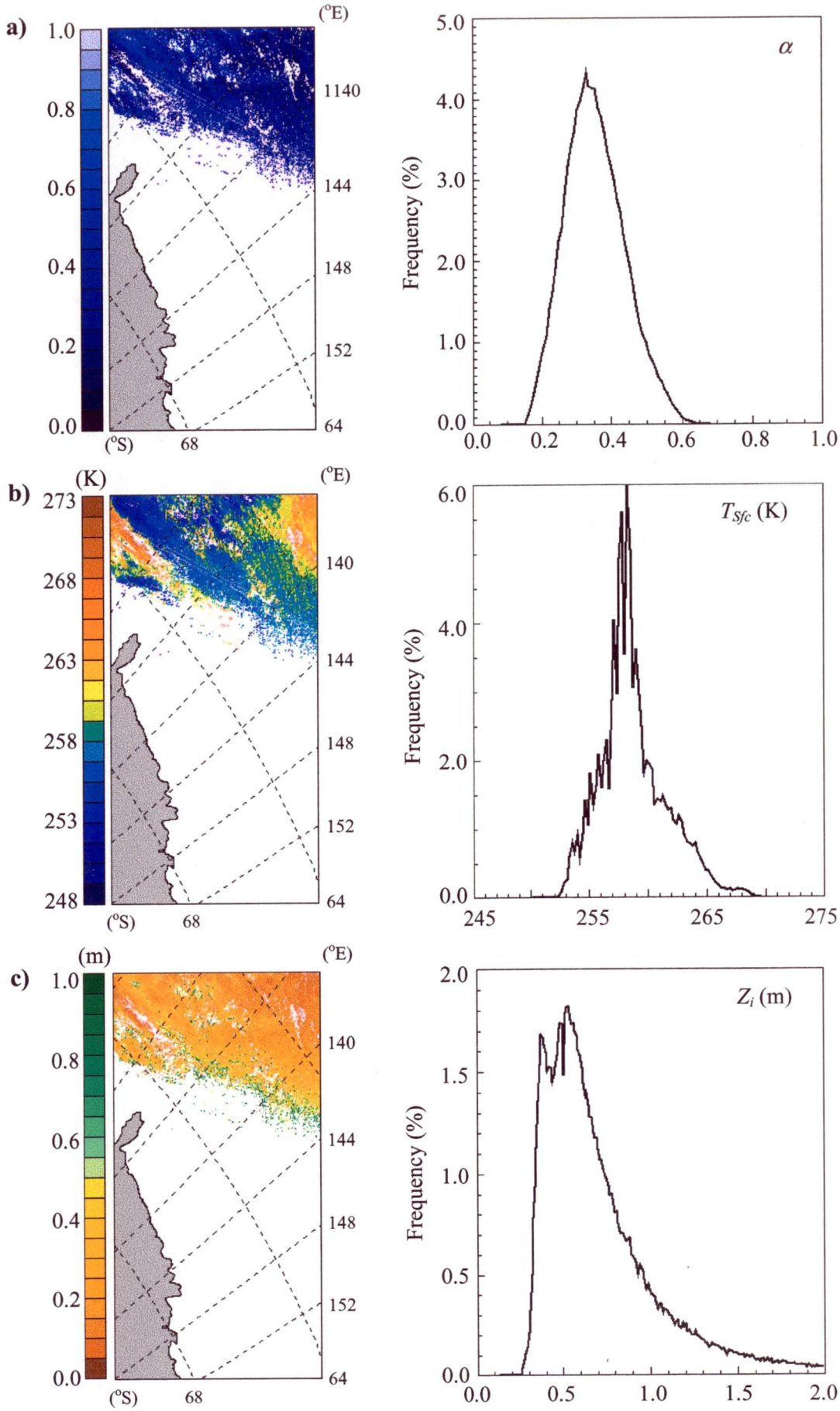

Figure 44 Classified AVHRR images and frequency distribution histograms of (**a**) albedo, (**b**) ice surface temperature and (**c**) sea ice thickness on 19-Aug-1995 at 0549 Z.

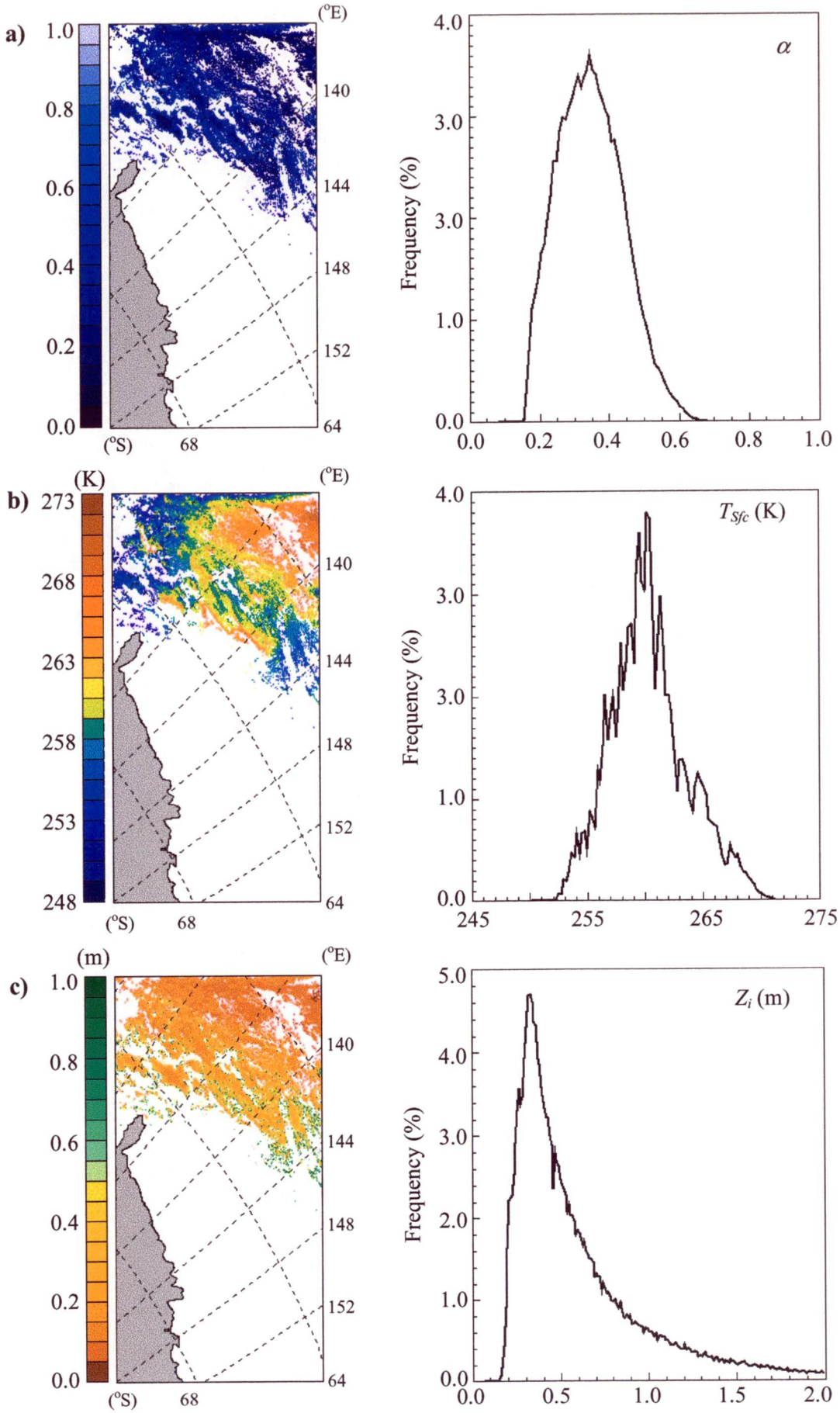

Figure 45 Classified AVHRR images and frequency distribution histograms of (**a**) albedo, (**b**) ice surface temperature and (**c**) sea ice thickness on 20-Aug-1995 at 0539 Z.

In general, the albedo and IST distributions observed in images from the Davis area follow the ice thickness distribution pattern closely. The model assigns apparent ice thicknesses below 0.2 m to dark pixels (albedo less than 0.4) with relatively high temperature (close to 273 K), and apparent thicknesses of 0.6 to 1.0 m to cold (below 255 K) and bright (albedo above 0.6) pixels. This pattern of association is also observed in the two images from the Mertz area. In this case however, the albedo values associated with thicknesses above 0.6 m are lower (0.4 to 0.5), due to the larger solar zenith angles that occur in winter. The range of IST values observed in the two winter images does not differ from that found in the spring images. The association of albedo values with sea ice thicknesses in the V2(96) dataset is not inconsistent with the *in situ* measurements of *Allison et al.* [1993] and *Brandt et al.* [1999] (see Table 3)

The presence of a cloud cover represents a major influence in the range of values and the shape of the albedo, IST and ice thickness frequency distribution histograms obtained from the V2(96) dataset. During periods of divergent conditions (Figure 40 and Figure 41), clouds tend to concentrate on the northern part of the scene, leaving large areas of thin ice near the coast exposed for analysis, which reflects on the narrow and uniform shape of the histograms. With the passage of synoptic weather systems, cloud cover increases taking up most of the scenes in a much less selective way (Figure 42 and Figure 43). In these cases, the shape of the histograms tends to be more irregular. The range of values however is roughly maintained throughout the V2(96) dataset: approximately 0.05 to 0.90 for albedo, 250 to 270 K for IST and 0.02 to 1.2 m for sea ice thickness.

The frequency distribution histograms from the two V1(95) images (Figure 44 and Figure 45) are less affected by cloud cover and therefore the range of values of albedo, IST and ice thickness and the shape of the histograms are likely to be more representative of the area analysed. In both images however, only the north-eastern sector contains valid data (corresponding to 22.06% of the area). It is clear from these two winter images that the ice is considerably thicker (median = 1.00) if compared to the images from the spring of 1996 (median = 0.41). Although there is no ice thickness data near the coast for the V1(95) dataset, it is possible to identify a pattern of gradual decrease northwards, with values ranging from 0.9 m around 64 °S to 0.1 m around 59 °S.

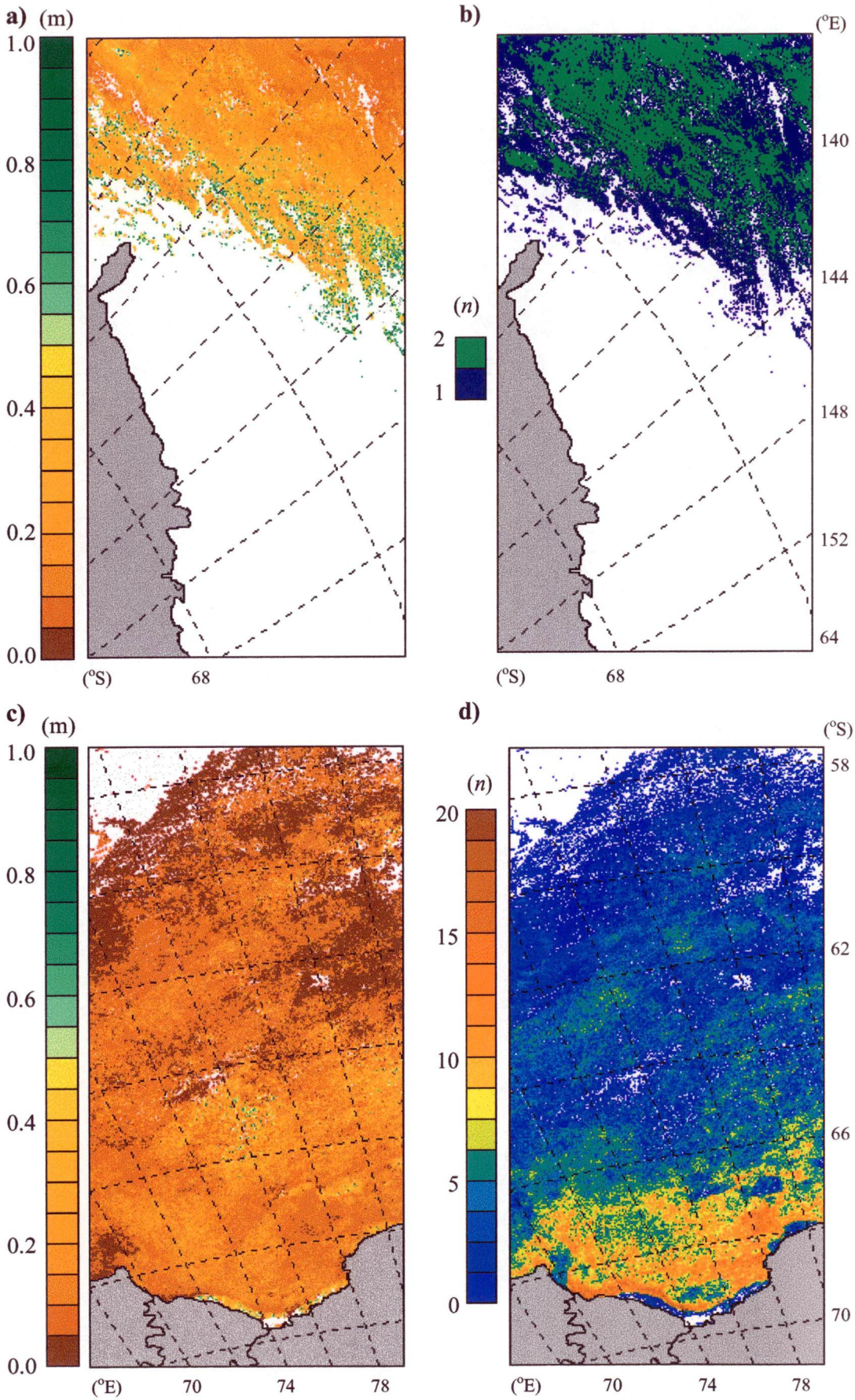

Figure 46 Classified AVHRR images of (**a**) average sea ice thickness and (**b**) number of pixels analysed (n) for the two images of 1995 and (**c**) average sea ice thickness and (**d**) number of pixels analysed for the 33 images of 1996.

Certain broad-scale morphological features of the Davis area are apparent in the albedo, IST and sea ice thickness classified images presented in Figure 40 to Figure 43 and especially in the average image presented in Figure 46 (**c**). For example, in Figure 40, Figure 41 and Figure 43 a region of generally thin sea ice is apparent in the south-western corner of the scenes, near Cape Darnley. *Massom et al.* [1998a] investigated the distribution of latent heat polynyas around the east coast of Antarctica with eight years (1987 to 1994) of SSM/I data. The Cape Darnley polynya (centred at approximately 67° 30' S and 69° 45' E) is described in that study as a recurring polynya with its maximum extent occurring in October and a mean area of 17.8×10^3 km^2. This feature is clearly visible in Figure 46 (**c**). By summing the pixels with an ice thickness less than 0.1 m in the area around Cape Darnley, the mean area of the polynya for the V2(96) period was estimated as 8.16×10^3 km^2. The difference between these two figures may be due to the fact that a large percentage of the Cape Darnley polynya lies outside the region of analysis. Furthermore, open water pixels were not counted as they were previously discarded by the ICEMAPPER system.

Another distinguishable feature in Figure 41, Figure 42 and in Figure 46 (**c**) is a narrow band of thin ice (up to 0.1 m) immediately north of the fast-ice edge in the Prydz Bay area. Ship-based observations made by several authors [*Allison and Worby*, 1994; *Worby*, 1998; *Worby and Massom*, 1995; *Worby, et al.*, 1998] showed a marked decrease in mean ice thickness in this region in spring between the central pack ice zone and the coast, due to the presence of a persistent flaw lead along the fast-ice edge.

Figure 40 and Figure 41 show a band of thicker ice (from 0.4 up to more than 1.0 m) between 68° and 64° S, with several large grounded icebergs lined up roughly around 67° S. Although icebergs are not classified as such by the model, they can be identified by their size, shape and orientation. In this instance, the ICEMAPPER system classified them as "compacted ice". Indeed several large icebergs have been reported in the Prydz Bay area by *in situ* observers and remote sensing surveys such as *Young* [1998] and *Young et al.* [1998]. This band of thick ice is also clearly distinguishable in Figure 46, although the average classified image do not show the icebergs. This feature is further discussed in Section 5.5.1

The northward gradation from thin ice/open water to thicker sea ice in the corridor between 70° and 76° E is also reflected in the albedo, IST and ice thickness classified images from the spring of 1996. Despite the more specific features described above, Figure 46 (**c**) show that, in general, the Davis area present the generally expected pattern where the northernmost sea ice is thinner (and therefore warmer and less bright) than the southernmost sea ice. This is also valid for the two images from the Mertz area, as can be observed in Figure 46 (**a**).

Another advantage of using remote sensing information to derive sea ice thickness is the ability to resolve temporal variations in an Eulerian fashion. Figure 47 shows the variation of AVHRR-derived sea ice thickness in two sub-areas of the Davis region from late-September to mid-November 1996. The large time-dependent changes in sea ice thickness observed in both sub-areas cannot be attributed to thermodynamic growth alone, as this would require the formation and melting of an enormous volume of ice in the short period of a few days.

These changes in ice thickness are likely caused by dynamic processes such rafting and ridging and the advection of ice into and out of the two sub-areas [*Worby, et al.*, 1998]. There are two other hypotheses that could satisfactorily explain such variations. In the space of a few days, the presence of clouds can act as a "selective screener" of pixels within a given range of thicknesses. An example of this process is found by comparing the spatial distribution of cloud cover (obtained from the pixels classified as clouds by the ICEMAPPER system) and the ice-thickness distributions in Figure 40 and Figure 41. In less than 24 hours, the cloud cover increased from 47% to 76%, mostly because of a large cloud band that obscured the northern section of the second image. Even though the ice conditions did not change significantly over this period (as evidenced by comparing the cloud-free areas of the two images), the resulting ice thickness histograms are very different.

Another possible explanation for the variability shown in Figure 47 is also related to the presence of clouds. As demonstrated in Section 4.5, open water or thin-ice pixels containing even a small amount of cloud contamination will be generally misclassified by the ICEMAPPER system as snow-covered ice, and will therefore be assigned an unrealistic thickness value by the model. Depending on the amount of contamination, the ice in some of these pixels will not attain the thermodynamic equilibrium even after the system performs all its iterations. These pixels will be discarded.

Overall it is not certain how many of these contaminated pixels are incorporated into the ice thickness distribution. As can be seen in Figure 39, these pixels are usually found in the vicinity of cloud formations, which reinforces this hypothesis. Setting aside the influence of these sources of ambiguity, and notwithstanding the size of the error bars in Figure 47, it is possible to observe a thinning trend through the period of analysis (between September and November 1996). This trend can be attributed to a combination of dynamic and thermodynamic processes that occur as the season progresses and the temperatures increase.

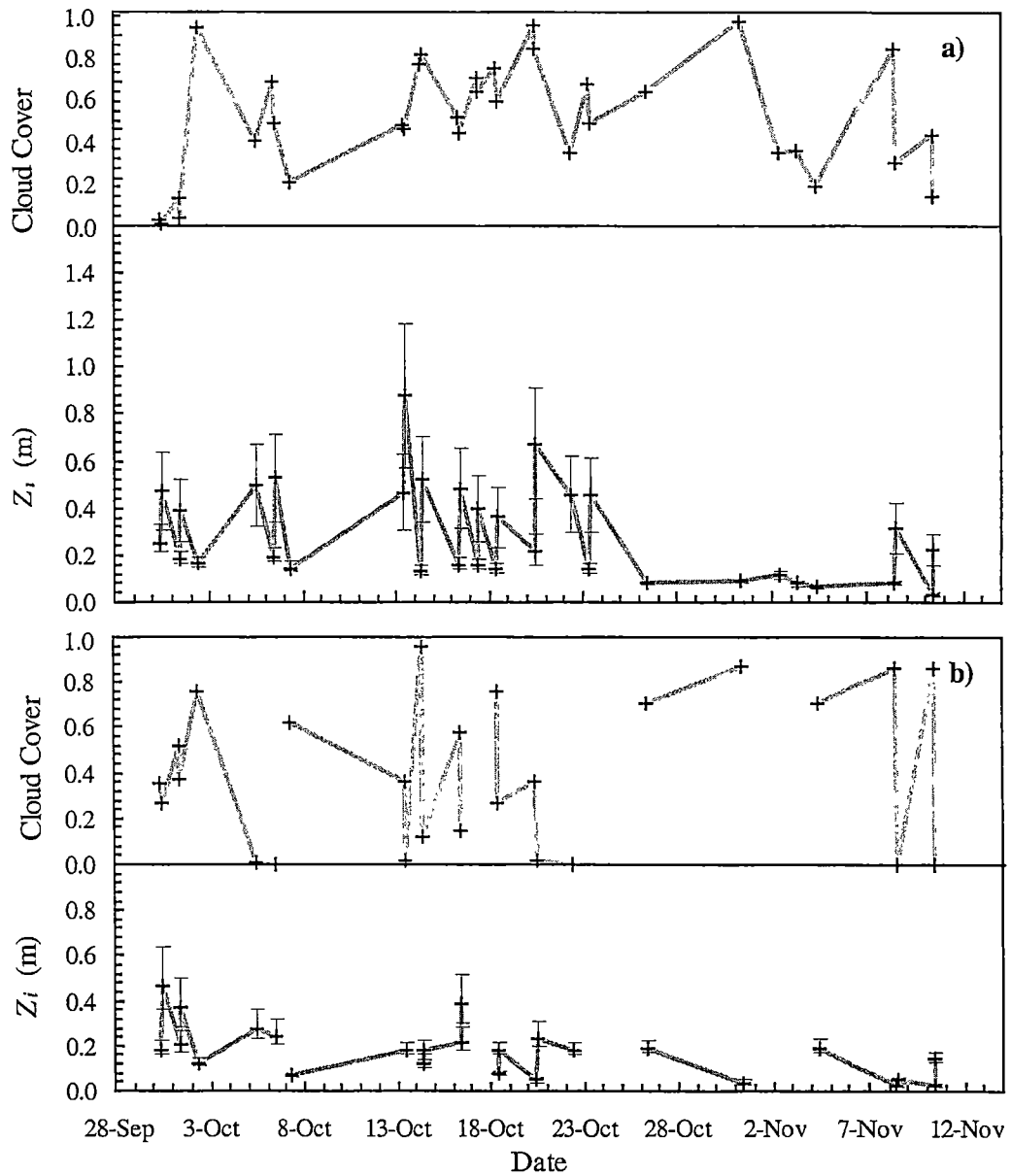

Figure 47 Average sea ice thickness and cloud cover variation in two sub-areas within the Davis area in 1996: (**a**) south of 68° S and (**b**) between 62° and 60° S. The error bars for ice thicknesses were estimated through the error analysis described in Section 4.6.

By determining the position of pixels located at the northern end of the average image of the Davis area (Figure 46 - **c**) that were assigned the minimum thickness of 0.02 m by the system, it is possible to estimate the average position of the ice edge for the spring of 1996. A comparison between the model outputs and data obtained from the Antarctic CRC's SSM/I dataset provides useful information on the system's ability to estimate two important parameters besides sea ice thickness: sea ice extent and areal coverage.

Figure 46 (**c**) shows that the sea ice cover in the Davis area in late spring extends roughly up to 58° S. The position of the ice edge is consistent with the analysis conducted by *Worby et al.* [1998] of four years (1991-1994) of daily sea ice concentration maps derived from SSM/I data. The authors of that study found that at 75° E the position of the ice edge ranges from 57° to 59° S at this time of the year.

A period of 10 years (from 1987 to 1996) of SSM/I data analysed with the same method employed by *Worby et al.* [1998] showed that, for the Davis area, the average areal coverage for the months of October and November is 5.65 x 10^5 km^2 with extremes of 3.68 and 6.51 x 10^5 km^2 (see Figure 48). Comparatively, the average areal coverage obtained from the 33 images from this same period is 5.91 x 10^5 km^2. The fact that this value is roughly in the middle of the range observed in the SSM/I dataset is a good indication that the system is capable of satisfactorily estimate sea ice areal coverage in East Antarctica.

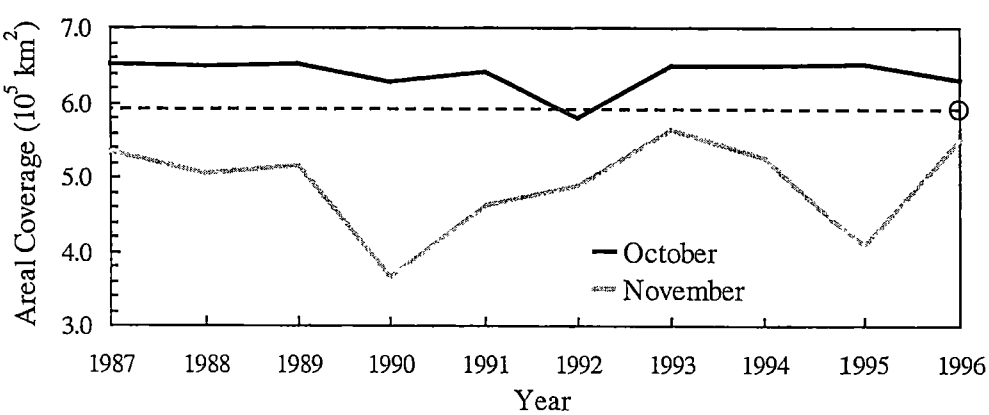

Figure 48 Variations in areal coverage within the Davis area obtained from SSM/I data. The dashed line and the circle indicate the area coverage value derived from the AVHRR dataset, referring to a period between late September and early November 1996.

5.3 Comparisons with Concurrent *In Situ* Data

In this section, the sea ice thickness distributions resulting from the application of the model to the 1995 and 1996 AVHRR datasets are more formally compared with information from other sources, namely ship-based observations and digital aerial photography. Unfortunately, the number of images with pixels coinciding with data from either of these sources is limited, which prevents the completion of a statistically-meaningful validation of the model. It also must be noted that these comparisons are largely of a qualitative nature, as the results obtained from the model bear little similarity (in terms of synoptic coverage, resolution and accuracy) to the data obtained from other methods. In spite of these discrepancies, certain large-scale similarities are apparent.

5.3.1 Ship-Based Sea Ice Thickness Observations

Considering that the model output is the result of the thermodynamic analysis of an area approximately 1 km^2 in size (i.e. one AVHRR pixel), the resulting apparent ice thickness is an average that reflects the characteristics of albedo and ice surface temperature of the various ice types and open water fraction present within this area. Therefore, in order to compare this information with ship-based sea ice observations, the *in situ* weighted-average ice thickness (Z_{Obs}) must be recalculated to include the open water fraction. This can be achieved by employing the following equation:

$$Z_{Obs} = \frac{C_{1st}}{C_{OW} + C_T} Z_{1st} + \frac{C_{2nd}}{C_{OW} + C_T} Z_{2nd} + \frac{C_{3rd}}{C_{OW} + C_T} Z_{3rd} \qquad \textbf{Equation 32}$$

where C_{1st}, C_{2nd} and C_{3rd} are the primary, secondary and tertiary sea ice concentrations (in tenths) respectively, Z_{1st}, Z_{2nd} and Z_{3rd} are the primary, secondary and tertiary sea ice thicknesses (in metres) respectively, C_T is the total sea ice concentration (in tenths) and C_{OW} is the open water fraction (in tenths), as determined by the ship observations. The sum of C_{OW} and C_T is always 10. Table 22 presents a comparison between the AVHRR-derived apparent thicknesses and the ice thickness calculated from ship-based observations.

Of the 33 images from the spring of 1996, 19 could not contribute to the analysis in this section because, at the time of their acquisition, the ship was located outside the Davis area. Of the remaining 14 images, 9 had coincident pixels that were covered with clouds and only 5 contained useful data. Unfortunately, for the winter of 1995, there were no contemporary ship observations corresponding with either of the AVHRR images obtained for that period.

Date/Time	Z_{AVHRR}	Z_{Obs}	*Total*		*Primary*		*Secondary*		*Tertiary*	
			C_{ow}	C_{ice}	C_{1st}	Z_{1st}	C_{2nd}	Z_{2nd}	C_{3rd}	Z_{3rd}
20-Oct-1996 0852 Z	0.19	0.45	0	10	5	0.65	4	0.30	1	0.05
26-Oct-1996 0928 Z	0.29	0.51	0	10	1	0.90	8	0.50	1	0.20
04-Nov-1996 0930 Z	0.03	0.08	1	9	7	0.10	2	0.05	0	0.00
08-Nov-1996 1027 Z	0.61	0.65	0	10	9	0.70	1	0.15	0	0.00
10-Nov-1996 1006 Z	0.03	0.18	1	9	9	0.20	0	0.00	0	0.00

Table 22 Comparison between AVHRR-derived ice thicknesses (Z_{AVHRR}) and co-located data from ship-based observations (Z_{Obs}). Z_{Obs} is the weighted average of the three ice-thickness categories (see Section 3.2.2), considering the open water fraction. Concentrations are expressed in tenths and thicknesses in metres.

As can be observed in Table 22, in each of the five co-located points, Z_{Obs} is larger than Z_{AVHRR}. The smallest difference between Z_{Obs} and Z_{AVHRR} (6.15% or 0.04 m) was found on the 8th of November when no open water was present and the region observed was almost entirely covered with snow-covered first-year ice 0.7 m thick. At the thinner end of the thickness spectrum, the difference between Z_{Obs} and Z_{AVHRR} on the 4th of November was 0.05 m.

Assuming that this pixel is not contaminated by clouds, the analysis of curve (**3**) in Figure 36 indicates that the AVHRR-derived sea ice thickness of a pixel containing 9 tenths of snow-covered ice and 1 tenth of open water is 15% thinner than the value returned by the model, which in theory could reduce the difference between Z_{Obs} and Z_{AVHRR} to 0.03 m. Considering the margins of error for this method (see Section 4.6) and the accuracy of individual ship-based observations (± 20% as reported by *Allison et al.* [1993]), this can be considered a reasonably good agreement.

The largest difference between the *in situ* observations and the model outputs (600% or 0.15 m) was found on the 10th of November. In this case, the application of the sub-pixel resolution test does not improve this figure significantly. The margins of error in the estimation of α and T_{Sfc} for thin, snow-free ice and the geo-location of the AVHRR pixels may be possible explanations for the model's underestimation in this situation.

Figure 49 compares the histogram of weighted-average sea ice thicknesses from all the ship-based observations made during V2(96) with the frequency distribution histogram of sea ice thickness derived from the 33 AVHRR images that coincided with this period (from September 30 to November 10, 1996). In both histograms, the data are arranged in 0.2 m bins.

It is important to note the differences between the methods employed to generate these histograms. The average AVHRR-derived ice thickness frequency distribution histogram (Figure 49 - **a**) was created by summing all valid pixels in the 33 images and dividing them by the number of occurrences throughout the period (shown in Figure 46 - **d** in the form of an image). The lower histogram in Figure 49 (**b**) was obtained by calculating the weighted-average sea ice thickness from each ship-based observation from V2(96) that fell within the Davis area, through Equation 32. Although the two datasets refer to the same period, the latter covers an area of less than 500 km^2 while the AVHRR-derived thickness values refer to an area of approximately 6×10^5 km^2.

Another important aspect to be considered in this comparison is the fact that, during V2(96), a problem in the ship's engine prevented it from maintaining a straight course, which led to the introduction of two biases in the sampling program. Firstly, in order to facilitate navigation under reduced power, routes with open water and thinner ice (i.e. nilas, pancakes etc) were preferred. Secondly, when the vessel encountered areas of thicker ice, the speed was reduced more than usual and a greater number of observations per unit distance was made. Although the sea ice observation analysis software discards subsequent observations made within 20 km of each other (see Section 3.2.2), this bias is still apparent when the V2(96) dataset is compared to others collected under normal navigation conditions.

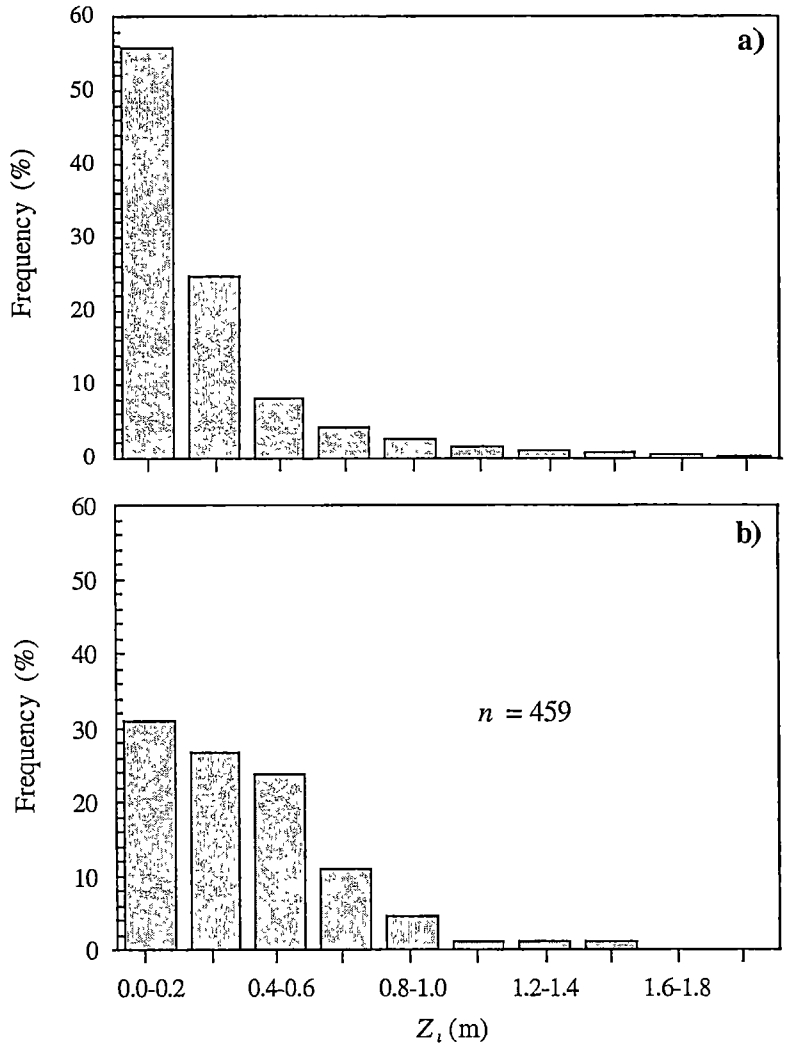

Figure 49 Frequency distribution histograms of (**a**) average AVHRR-derived sea ice thickness from the 33 images of 1996 and (**b**) weighted-average sea ice thickness obtained from 459 ship-based observations from the same period.

The largest difference between the two histograms in Figure 49 is in the open water/thin ice class (0.0 to 0.2 m). Whereas 31% of the ship-based observations have a weighted-average thickness of less than 0.2 m, 56% of all AVHRR-derived ice thicknesses fall within this category. This discrepancy is most likely caused by the inclusion of a large number of open-water pixels contaminated by clouds into the AVHRR algorithm. The parameterisation of snow thickness also contribute to this discrepancy. The relationship between Z_i and Z_s employed in this study is based on winter measurements (see Figure 15). Since the snow-fall regime is probably different in spring [*Bromwich*, 1990], it is likely that changes in this parameterisation will affect the AVHRR-derived ice thickness distribution.

The fraction of ice with thicknesses between 0.2 m and 0.4 m is similar in both histograms (25% for the model and 27% for the ship-based observations), but there is a large (16%) difference in the bin centred at 0.5 m. The subsequent bins have similar frequencies in both histograms, with the ship-based observations presenting lower values. Possible explanations for the discrepancies between the two histograms in Figure 49 are discussed in Section 5.5.

Figure 50 shows the ice thickness frequency distribution histogram derived from the two 1995 images. Although there is no direct sea ice thickness information from the ship-based observations for this period, it is possible to comment on this histogram in light of meteorological data from both GASP and the RSV *Aurora Australis*' DLS. The most noticeable feature in Figure 50 is the near-absence of thin ice (between 0.02 and 0.2 m), which is consistent with the findings of other winter studies conducted in this area [*Lytle, et al.*, 1998b; *Worby, et al.*, 1998]. *Worby et al.* [1998] showed that in August, the East Antarctic pack ice is very consolidated, with an open water fraction of approximately 12%. *Worby et al.* attributed this small percentage of thin sea ice and open water to *a)* low air temperatures typical of this time of the year which leads to the rapid freezing of leads (to ice thicknesses of more than 0.4 m), and *b)* the effects of deformation.

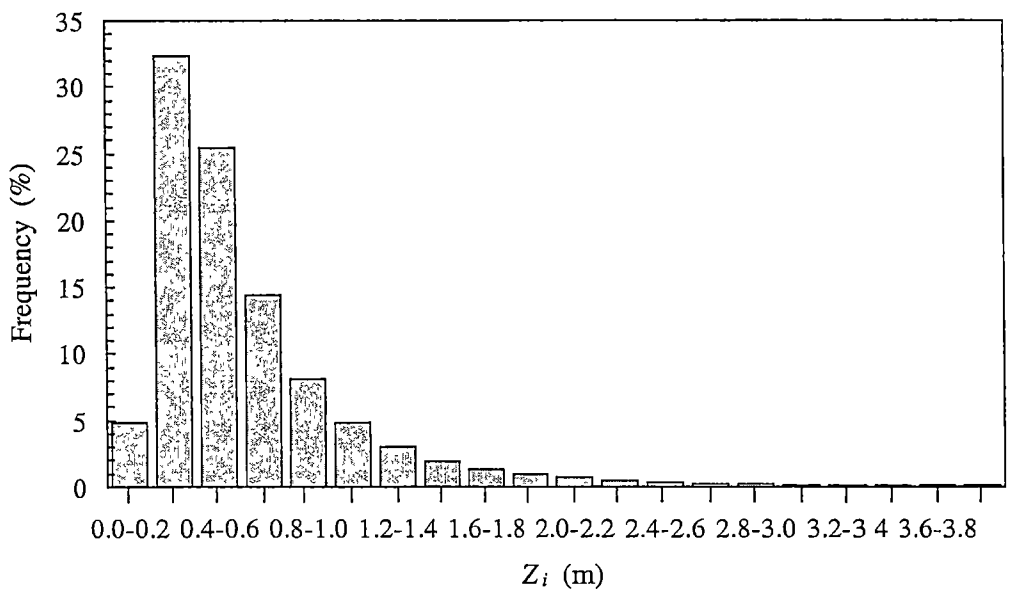

Figure 50 Frequency distribution histograms of sea ice thickness generated from the two AVHRR images from August 1995.

The dominance of 0.4 to 0.6 m thick ice in the winter ice thickness distribution histogram shown in Figure 50 is supported by *Lytle et al.* [in press-a] who showed that the pack ice in wintertime in the vicinity of 65° S; 140° E attains an equilibrium thermodynamic thickness of approximately 0.5 to 0.6 m, observing both basal freezing and melting in ice of this thickness range. These findings also agree with those of *Allison and Worby*, [1994].

An alternative explanation for the near-absence of thin ice in the AVHRR histogram can be formulated by analysing the synoptic conditions over the 24-hour period when the two AVHRR images were collected. The analysis of the data from the DLS onboard the RSV *Aurora Australis* (Figure 52) and the outputs from the GASP system (Figure 51) show the occurrence of persistent westerly winds on the period from 17th to 19th of August, which originated a swell that penetrated more than 350 km into the ice pack. The effect of this swell was to alter the floe-size distribution and promote rafting in the subsequent convergent regime. It also introduced sea water onto the ice surface. This same event was reported by *Worby et al.* [1998] and *Massom et al.* [1999]. Under these circumstances, relatively little thermodynamic ice formation is expected (even at low temperatures), which is consistent with the relative absence of ice between 0.02 and 0.2 m in the AVHRR-derived frequency histogram of ice thickness.

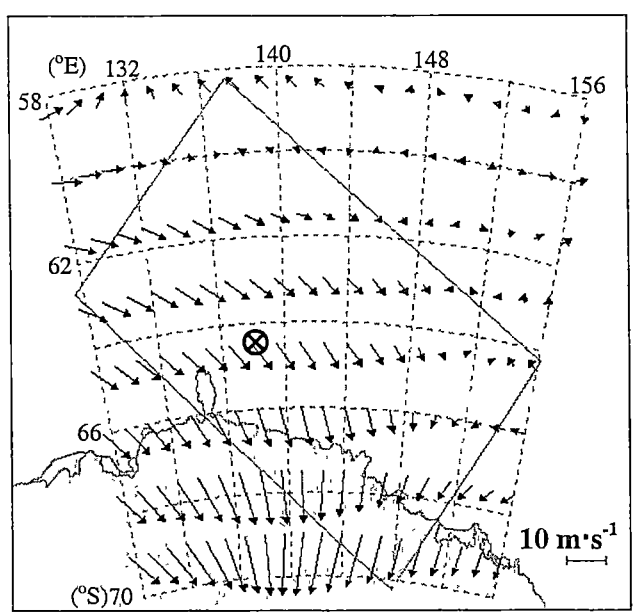

Figure 51 GASP predictions of wind speed and direction temporally interpolated to coincide with an AVHRR image from 19-Aug-1995 at 0549 Z. The polygon indicates the Mertz area (Figure 4) and the circle indicates the approximate position of the RSV *Aurora Australis* at the time.

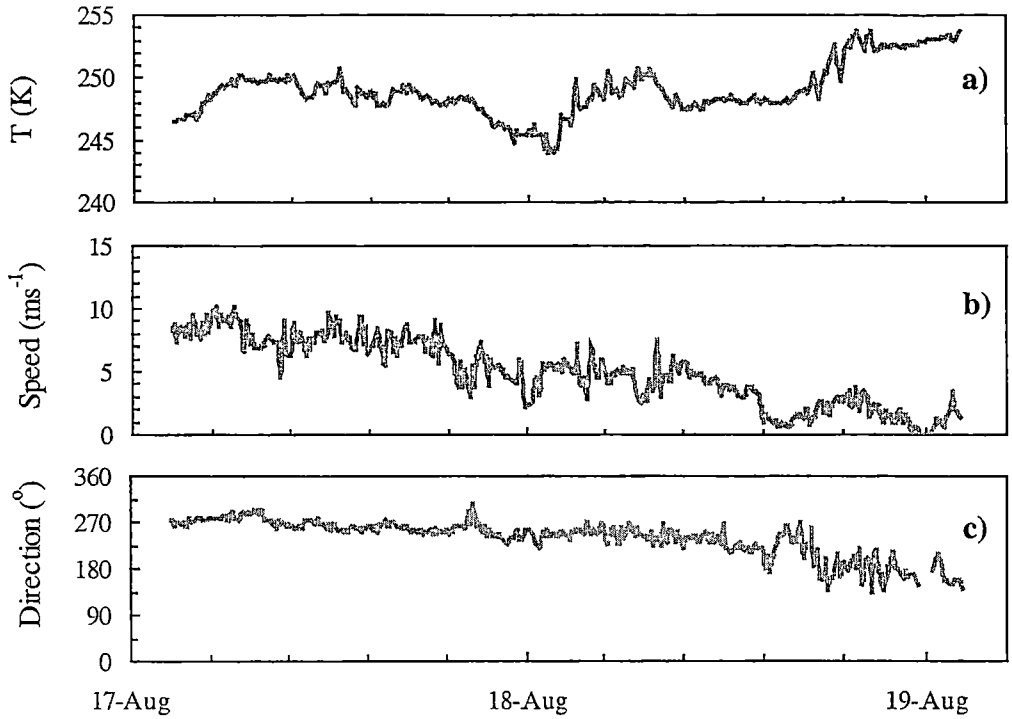

Figure 52 (**a**) Air temperature, (**b**) wind speed and (**c**) wind direction data from the DLS onboard the RSV *Aurora Australis* collected during V1(95).

5.3.2 Digital Aerial Photography

A visual analysis of grey tones, textures and the presence and morphology of features such as rafts, ridges, folds and fractures was used in conjunction with the WMO classification scheme (see Table 6) to identify ice types and assign thickness ranges within each photograph. These values were then compared with thicknesses retrieved from pixels that coincided with the path of the helicopter flights, similarly to the method employed by *Eppler and Farmer* [1992] and *Ackley et al.* [1992].

Of the eleven aerial photography flights from 1995 and 1996 that fell within the Davis and Mertz areas, only Flights 7 and 8 (see Table 8) coincided with an AVHRR image, namely that collected on 26-Oct-1996 at 0928 Z. The flight paths, along with the AVHRR-derived ice thickness distribution obtained from that image, are shown in Figure 53. The analysis conducted in this section concentrates on Flight 8, as the number of valid pixels available for comparison is considerably larger than in Flight 7. Furthermore, Flight 7 occurred between 0245 and 0530 Z, while Flight 8 occurred between 0850 and 1100 Z, bracketing the image's acquisition time.

During Flight 8, the helicopter flew at approximately 185 km/h and at an altitude of 2438 m (8000 ft). A navigator recorded the time, aircraft position (latitude and longitude), elevation, speed, heading, photograph frame number and an estimation of the total ice concentration once every 60 seconds. The average dimensions of the frames, calculated using Equation 7 are 1172 x 785 m, which corresponds to an area approximately 8% smaller than the size of one AVHRR pixel.

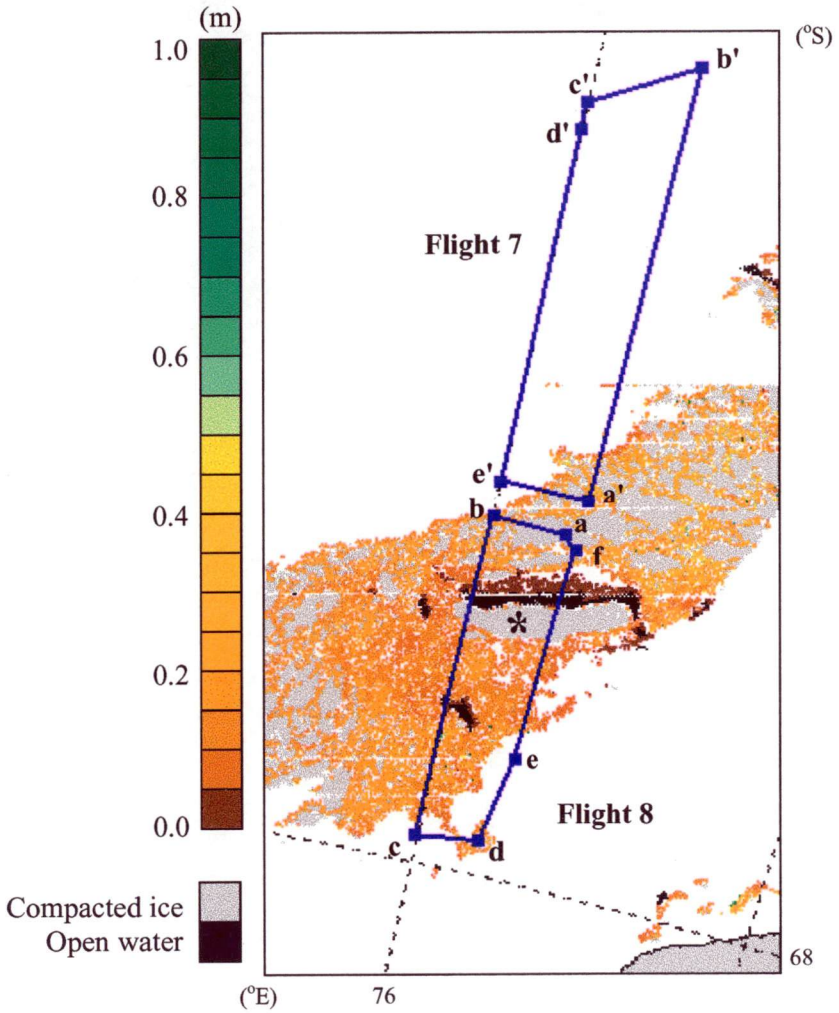

Figure 53 Paths of helicopter flights 7 and 8 plotted on top of the ice thickness distribution obtained through an AVHRR image from the same day (26-Oct-1996). Letters **a'** to **f'** and **a** to **e** indicate the starting point of each section of flights 7 and 8, respectively. The asterisk indicates a large tabular iceberg.

Analysis of photographs from the first leg of Flight 8 (from **a** to **b** in Figure 53), showed that the helicopter flew over areas of large (> 500 m diameter) snow-covered first-year floes separated by leads less than 100 m in width. The total ice concentration recorded by the navigator varied between 9 and 10 tenths. In the AVHRR image, most of the pixels corresponding to this section of the flight were classified as "compacted ice" by the ICEMAPPER system and were therefore excluded from the ice thickness calculations. The second leg (from **b** to **c** in Figure 53) was approximately 160 km in length, and it followed the 76° E parallel southwards to approximately 67° 50' S. Figure 54 shows the AVHRR-derived sea ice thicknesses along the path of this section of the flight. In the first 20 km, the navigator assigned concentrations of 9 to 10 tenths to most of the ice underneath the helicopter, and the corresponding pixels in the AVHRR image were also classified as "compacted ice" by the ICEMAPPER.

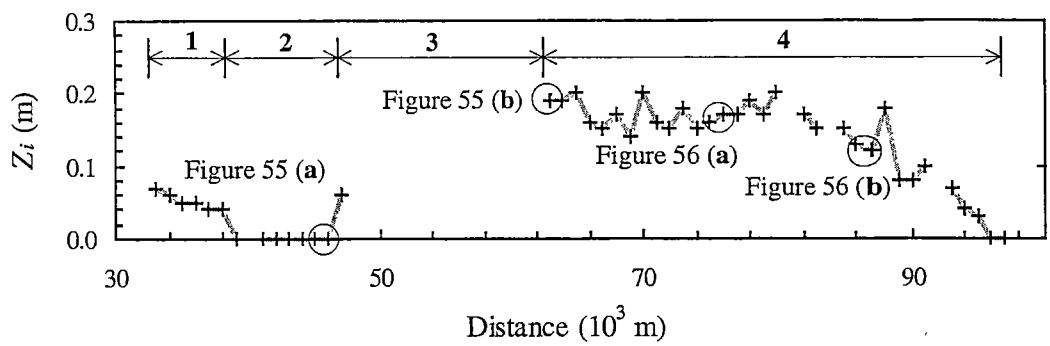

Figure 54 AVHRR-derived sea ice thicknesses along the path of the second section of Flight 8. The numbers indicate sub-sections as follows: (**1**) field of nilas with finger rafting; (**2**) section of the field of nilas misclassified as "open water" by the ICEMAPPER system; (**3**) iceberg; (**4**) large floes of snow-covered ice. Circles indicate the approximate location of the photographs shown in Figure 55 and Figure 56.

After a distance of 30 km, the total ice concentration remained unchanged but most of the ice observed in the pictures was classified as snow-free nilas, with finger rafting. This area of thin sea ice was accurately described by the model, with thicknesses varying from 0.04 to 0.07 m (Section **1** in Figure 54). However, as the ice thickness decreased southwards, the ICEMAPPER misclassified some of these pixels as "open water", preventing the model from assigning a thickness to them (Section **2** in Figure 54).

A large tabular iceberg located between 66° 45'and 66° 55' S and measuring approximately 18.5 km across was observed immediately south of the field of dark nilas (Section **3** in Figure 54). The corresponding pixels in the image were classified as "compacted ice". However, the model described accurately the transition from the nilas field to the iceberg and from the iceberg to an area of medium size, snow-covered first-year floes (Section **4** in Figure 54), as can be seen in Figure 55.

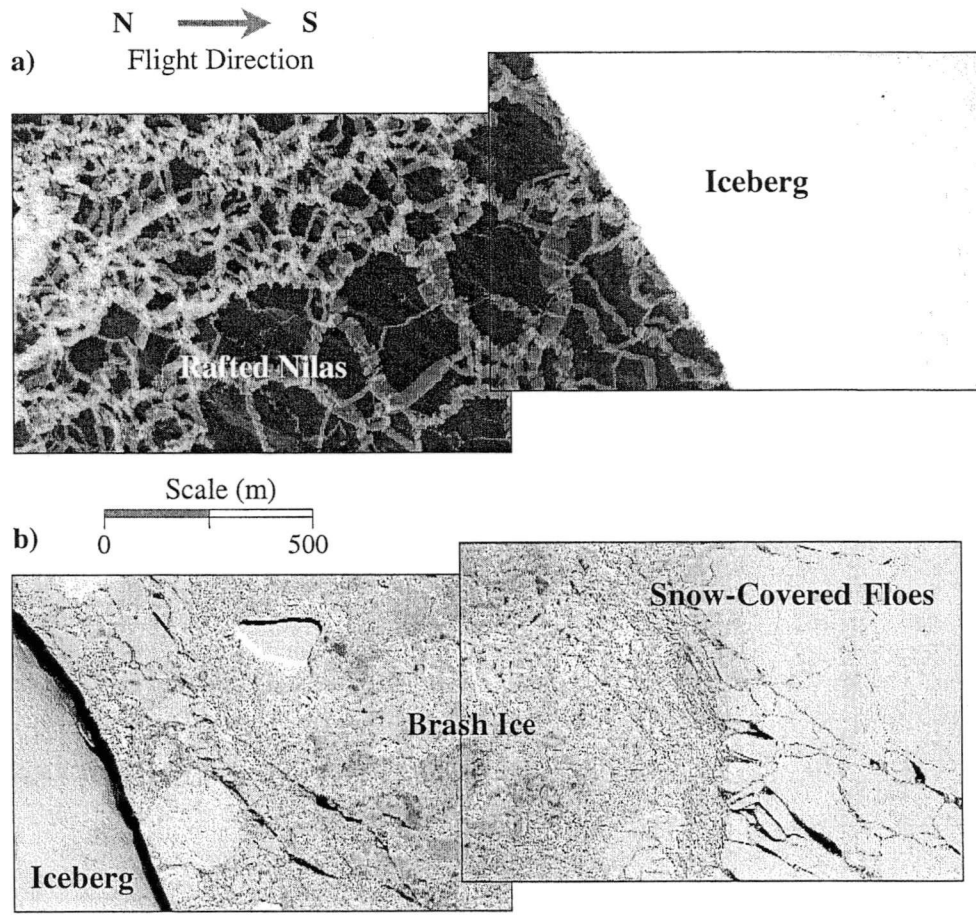

Figure 55 Mosaics of digital aerial photographs showing two parts of the second section of Flight 8: (**a**) a field of nilas north of an iceberg and (**b**) an area of brash ice and snow-covered first-year ice immediately south of the same iceberg.

Between 65 and 80 km into the same section of Flight 8, the aircraft flew over an area of snow-covered consolidated ice (10/10 concentration), constituting large expanses of level refrozen lead ice with small ridges covering an area of 10% to 20% of the floes. The model recorded apparent thicknesses varying from 0.12 m to 0.18 m for this region. Figure 56 (**a**) shows a mosaic of two photographs representative of this area. About 85 km into this section, the navigator observed a field of rafted light nilas or young grey ice with finger rafting.

The apparent ice thickness given by the model for that area was 0.08 m, which is consistent with this type of ice [*WMO*, 1970]. The corresponding mosaic (Figure 56 - **b**) also shows that, preceding this field of thin ice, was a large snow-covered first-year floe of levelled ice, to which the model assigned an apparent thickness of 0.18 m.

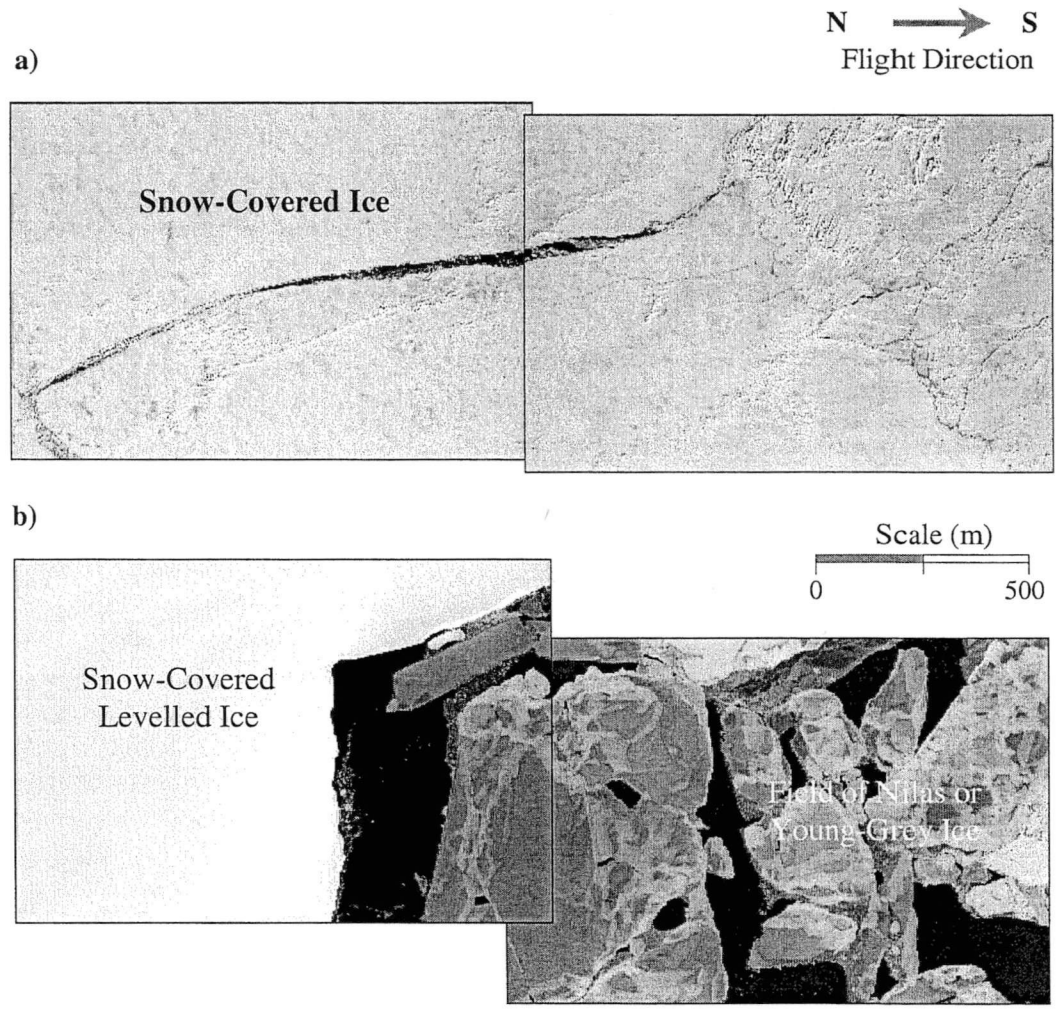

Figure 56 Mosaics of digital aerial photographs showing two parts of the second section of Flight 8: (**a**) An area of snow-covered first-year ice and (**b**) the transition between that area and a field of rafted light nilas or young grey ice.

In the third section of Flight 8 (from **c** to **d** in Figure 53), the aircraft flew over areas of snow-covered "cemented" floes with practically no open water (10/10 concentration). The navigator observed the presence of clouds, which were also recorded by the ICEMAPPER system. Therefore, there are no thickness data for most of the pixels in this section. The same pattern occurred in the fourth section (from **d** to **e** in Figure 53).

The fifth section of Flight 8 (from **e** to **f** in Figure 53) was approximately 110 km in length. It followed the 76° 55' parallel northwards to 66° 28' S. The variation in AVHRR-derived sea ice thicknesses coinciding with this section is shown in Figure 57 below.

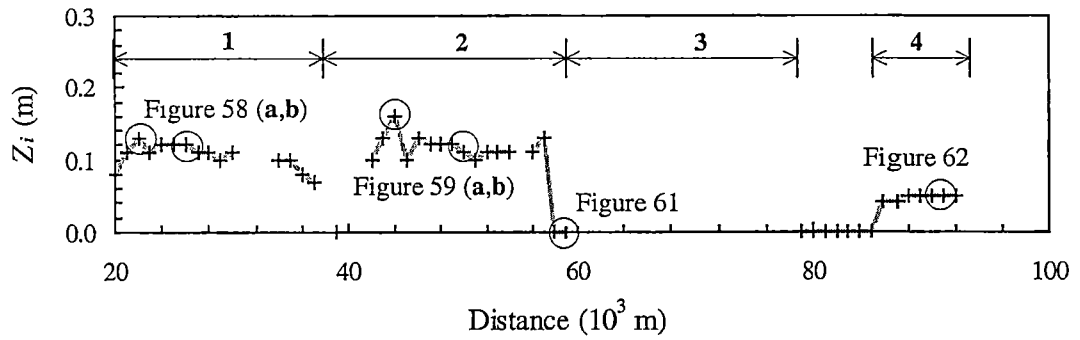

Figure 57 AVHRR-derived sea ice thickness along the path of the fifth section of Flight 8. The numbers indicate sub-sections as follows: (**1**) Snow-free ice with finger rafting; (**2**) open water with frazil streams; (**3**) iceberg; and (**4**) snow-covered young grey-white ice with portions of rafted nilas and open water. Circles indicate the approximate location of the photographs shown in Figure 58 to Figure 62.

The same band of clouds observed in the two previous sections of the flight prevented the recording of ice thicknesses by the model for the first 20 km of this section. The photographs of the next cloud-free area showed a field of snow-free ice with rafting (either light nilas or grey-white ice), shown in Figure 58 (**b**). The ice thickness assigned by the model for this area varied from 0.10 to 0.12 m, which is again consistent with the expected values for rafted light nilas or young grey-white ice [*WMO*, 1970]. The first photograph of this area, however, showed a large (greater than 500 m) snow-covered first-year floe with some cloud contamination in the middle of the scene (Figure 58 - **a**). This is probably the cause of an increasing trend (from 0.08 to 0.13 m) in the AVHRR-derived thickness for the first three pixels of this section.

This field of light nilas, mentioned above, extended for approximately 20 km. The last photographs depicting this formation show an increasing concentration of open water and, more importantly, a decrease in the degree of rafting, which possibly explains the drop in AVHRR-derived thickness from 0.10 to 0.07 m. The model also registered a few pixels as open water which were not encountered in the photographs.

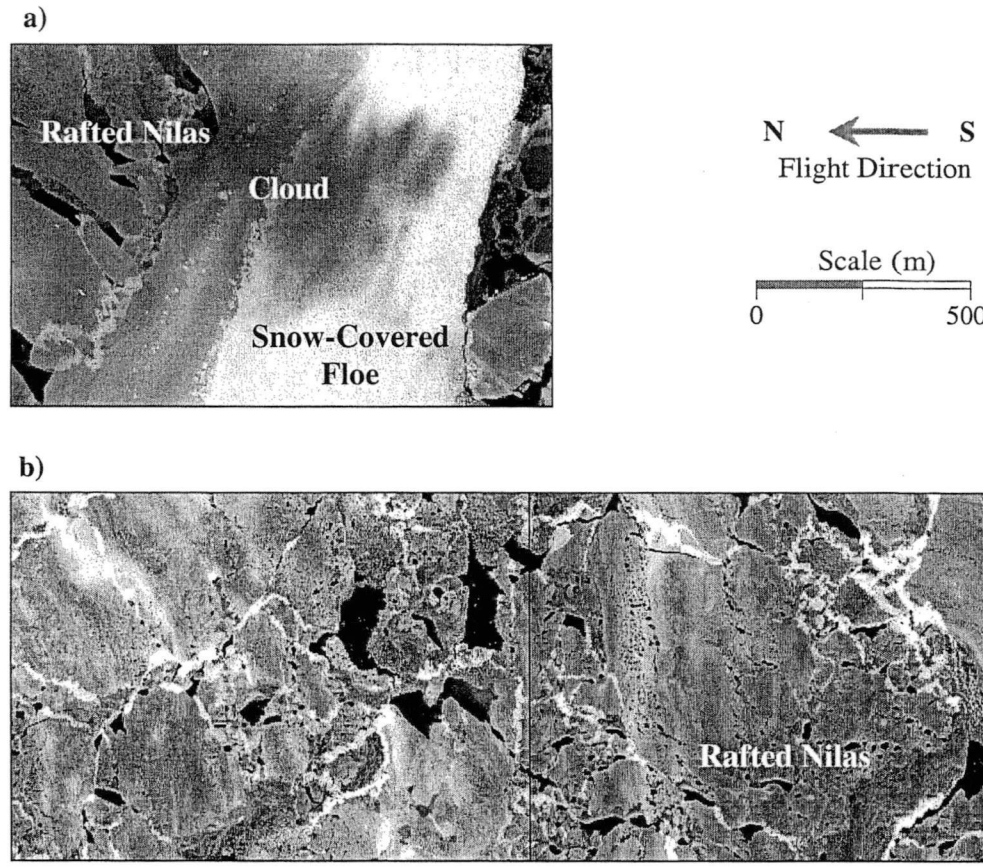

Figure 58 Digital aerial photographs showing two parts of the fifth section of Flight 8: (**a**) Transition between a large snow-covered floe to a field of snow-free ice, with cloud contamination in the centre of the scene. (**b**) Mosaic of two photographs showing a field of light nilas or young grey-white ice with rafting.

Immediately to the south of the field of nilas mentioned above, the photographs show the presence of a large area of open water with frazil streamers crossing the surface at an angle of approximately 235°, which is consistent with the wind direction recorded by the DLS on the RSV *Aurora Australis*. The transition between the two types of surfaces (Figure 59 - **a**) is recorded accurately by the model. However, it assigns thicknesses (from 0.10 to 0.13 m) to the open water pixels, most likely due to the presence of the bright frazil streamers (Figure 59 - **b**). This process is presumably similar to the cloud-contamination scenario described in Section 4.5. It is possible to observe a relationship between the concentration of frazil in each scene and the AVHRR-derived thickness of the corresponding pixel.

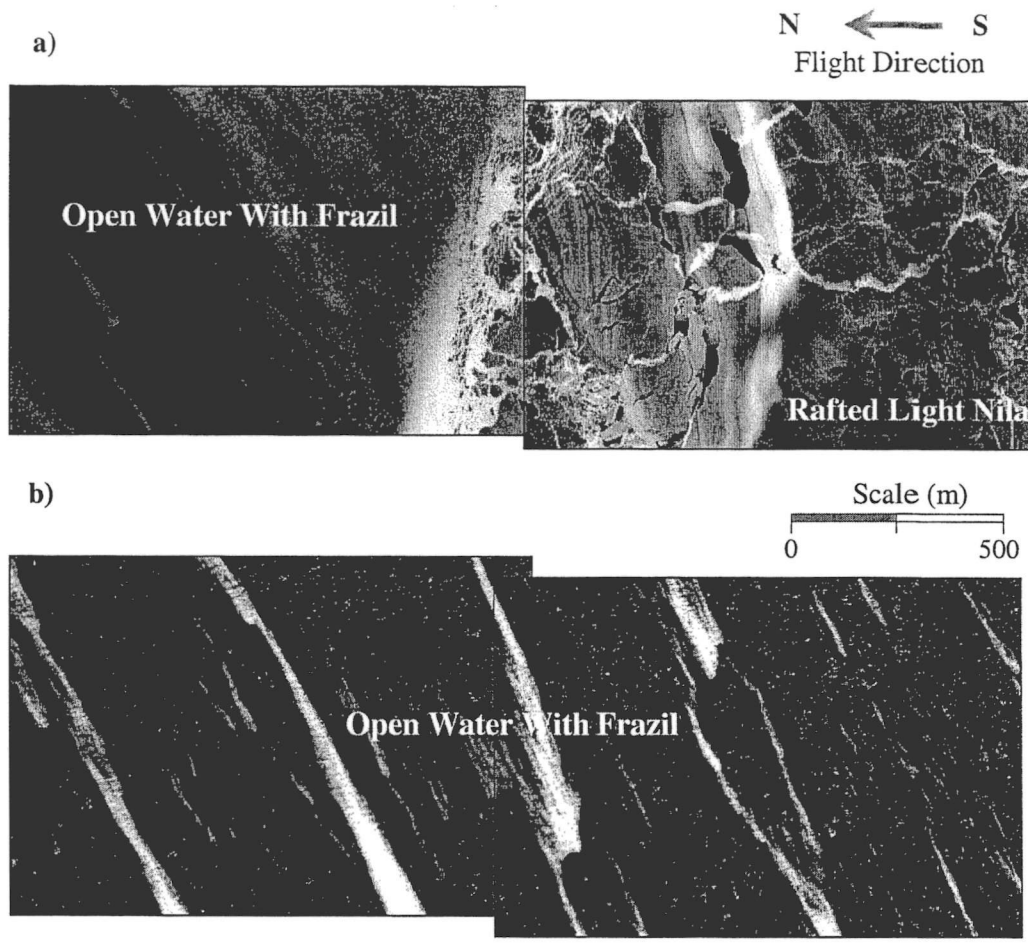

Figure 59 Mosaics of digital aerial photographs showing two parts of the fifth section of Flight 8: (**a**) Transition between a field of light nilas or grey-white ice with rafting to an area of open water with frazil streamers, and (**b**) a large extension of open water with frazil streamers.

Figure 60 (**a**) shows a concentration of frazil of 60 to 70% with the presence of some brash ice or newly formed pancakes in the centre of the scene. The corresponding AVHRR-derived ice thickness is 0.12 m. The frazil concentration drops to 10 - 15% in Figure 60 (**b**) and, although a few small pieces of ice are present, the apparent thickness assigned by the model is 0.10 m.

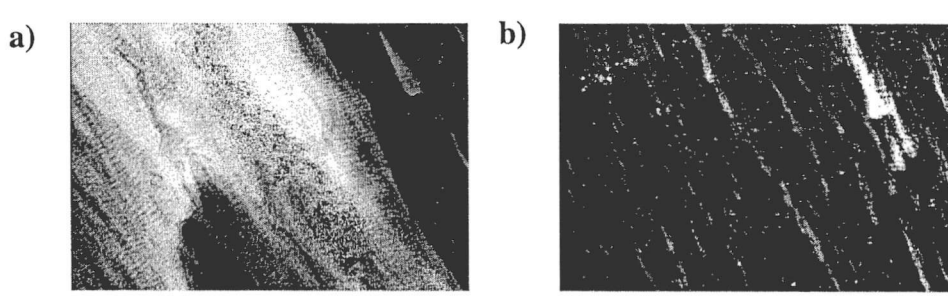

Figure 60 Changes in the concentration of frazil ice in two scenes from Flight 8.

In this section of the flight, the aircraft also flew over the large iceberg described earlier, this time travelling from south to north. The iceberg was preceded by a region of open water with hardly any frazil ice present, which was accurately recorded by the model (Figure 61). Once again, the pixels that correspond to the iceberg were classified by the ICEMAPPER system as "compacted ice" and therefore no AVHRR-derived sea ice thickness data exist for them. Photographs of the transition between the iceberg and the next section of sea ice were not available, as the camera was subject to a mechanical problem. Immediately north of the iceberg, approximately 80 km into the flight, the navigator recorded the presence of open water and grease/frazil ice. The ICEMAPPER classified the corresponding pixels as "open water" and therefore no ice thickness data exist for them.

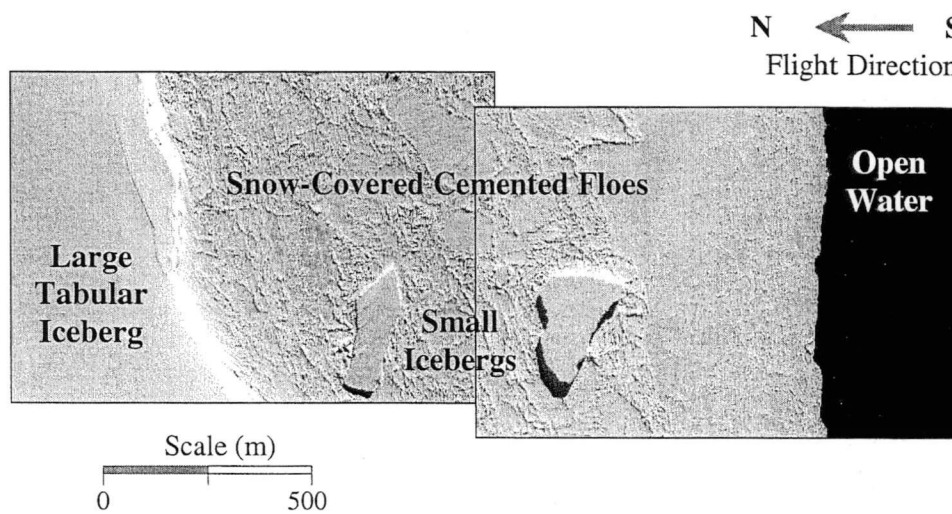

Figure 61 A mosaic of digital aerial photographs showing a part of the fifth section of Flight 8. From right to left are: an area of open water followed by a band of medium-size, cemented, snow-covered floes and the tabular iceberg.

The first available photographs for this part of the flight show a mixture of surfaces, including open water (around 2/10), grease and rafted nilas and medium to large young grey-white ice floes, generally snow-free or with a thin snow cover (Figure 62). This pattern extends to approximately 10 km and is the last section of the flight that has corresponding pixels with valid AVHRR-derived ice thicknesses. These vary between 0.04 and 0.05 m.

In the last section of Flight 8 (from **e** to **f** in Figure 53), the helicopter flew over an area of compacted snow-covered floes with hardly any open water. The corresponding pixels were classified as "compacted ice" by the ICEMAPPER system and therefore no ice thicknesses were assigned to them.

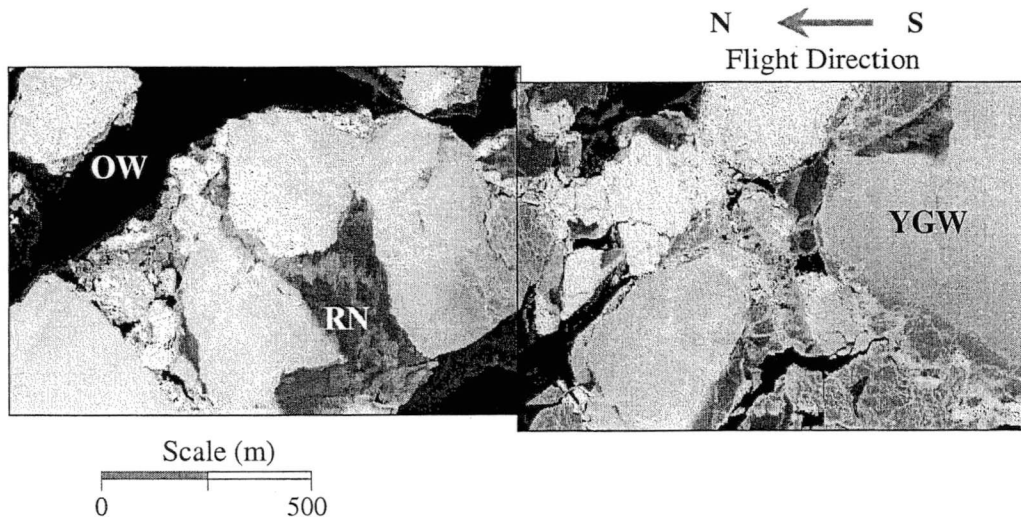

Figure 62 Mosaic of digital aerial photographs showing a characteristic scene from the last part of the fifth section of Flight 8. Noticeable features are: open water (**OW**), rafted nilas (**RN**) and snow-free young grey-white ice (**YGW**).

An important aspect observed in the analysis conducted in this section is the effectiveness of the preliminary classification performed by the ICEMAPPER system. Although this classification was useful in that it removed from the thickness calculations some unwanted features such as clouds and icebergs, the photographs showed that some pixels classified as "open water" and "compacted ice" contained valid information from which the model could have derived an apparent sea ice thickness.

The co-geolocation of the photographs and the corresponding pixels in the AVHRR image is another issue to be considered. The first difficulty is that there are no ground control points in the sea ice, so the accuracy of the geo-location cannot be determined. Furthermore, the manual recording of the aircraft's altitude, speed, latitude and longitude by the navigator during the flight is an inadequate method of registering the real location of the scenes as the camera generally collects between 4 and 10 pictures within the 60 seconds between two records.

Finding the corresponding pixels in the image is also a source of uncertainty, as the accuracy of the AVHRR geo-location is reported to be between ± 1 to ± 3 pixels [*Turner, et al.*, 1999]. In this study, photographs were located based on the position of a large iceberg or based on features reported by the navigator. This method however is not practical if a large number of scenes is being analysed.

The analysis of the digital aerial photography data in this section does not allow a quantitative comparison with the model results, as it is not possible to obtain ice thickness directly from the photographs. However this comparison has demonstrated that the model is capable of identifying major morphological features in the pack and, in some cases, the AVHRR-derived thickness were comparable with the type of ice observed in the photographs. However, in most photographs analysed, more than one type of ice was present along with varying concentrations of open water. In those cases, the ice thickness given by the model can be interpreted by using the relationships derived from the analysis of the response of the model to sub-pixel features (Section 4.5).

5.4 Comparisons With Climatological Data

This section presents comparisons between the AVHRR-derived sea ice thickness estimates and climatological estimates of sea ice thickness from both drill holes and ship-based observations. Historical data employed in Sections 5.4.1 and 5.4.2 were collected by the Antarctic CRC in several expeditions to the East Antarctic sector since 1986. These results have been reported in numerous publications such as *Allison et al.* [1993], *Allison and Worby* [1994], *Lytle et al.* [1998b], *Massom et al.* [1998a], *Massom et al.* [1999], *Massom et al.* [in press-b], *Worby and Massom* [1995], *Worby* [1998], *Worby et al.* [1998], *Worby and Allison* [1999] and *Worby and Ackley* [2000]. A summary of published Antarctic sea ice and snow thickness data derived from drilled measurements and ship-based observations can be found in Table 2.2 in *Worby* [1998]. As in Section 5.3, the comparisons discussed here should be analysed taking into consideration the differences in terms of synoptic coverage, spatial resolution and accuracy between the sea ice thickness model and the other two methods.

5.4.1 Drill-Hole Measurements

Drill-hole measurements in East Antarctica were typically made along 100 m transects (spacing 1 - 2 m) and ice core sites. The data presented in this section were collected in six voyages between 1991 and 1996 (see Table 23), totalling 849 drilled measurements and 134 ice cores. With the exception of V1 1995/96, all of the voyages listed in Table 23 collected data in the Prydz Bay area.

Voyage Name Season	*Drilled Measurements*	*Ice Cores*
V1 1991/92	0	4
V2 1991/92	31	8
V1 1992/93	43	18
V9 1992/93	133	18
V1 1994/95	54	34
V1 1995/96	588	52
Total	849	134

Table 23 Summary of drilled measurements made since 1991 in the East Antarctic sector. Adapted from *Worby* [1998].

Sea ice thicknesses obtained from drill-hole measurements are inherently biased in two ways: *a)* undersampling regions of very thin ice (less than 0.1 m) and open water [*Wadhams, et al.*, 1987], and *b)* undersampling the proportion of thick ridged ice [*Worby*, 1998], although this is less important for the comparison presented in this study. The first bias is evidenced by the fact that the 0.0-0.1 m and the 0.1-0.2 m thickness categories together contributed less than 2% of the total ice thickness range, while the 0.0-0.2 m bin in the AVHRR-derived sea ice thickness frequency distribution histogram (Figure 49 - **a**) contributes to almost 56% of its total range of thicknesses.

Figure 63 presents a sea ice thickness frequency distribution histogram obtained from drill-hole measurements collected in East Antarctica between 1991 and 1996. The histogram shows a sharp modal peak in the 0.6-0.7 m thickness category and, according to *Worby* [1998], its shape is similar to that of the histograms derived from other regions of the Antarctic pack ice such as the Weddell Sea [*Wadhams, et al.*, 1987] and the Bellingshausen and Amundsen Seas [*Worby, et al.*, 1996a]. This overall shape is also present in the AVHRR-derived sea ice thickness frequency distribution histogram for the V1(95) period (Figure 50), although the modal peak is centred on the 0.3-0.5 m thickness category.

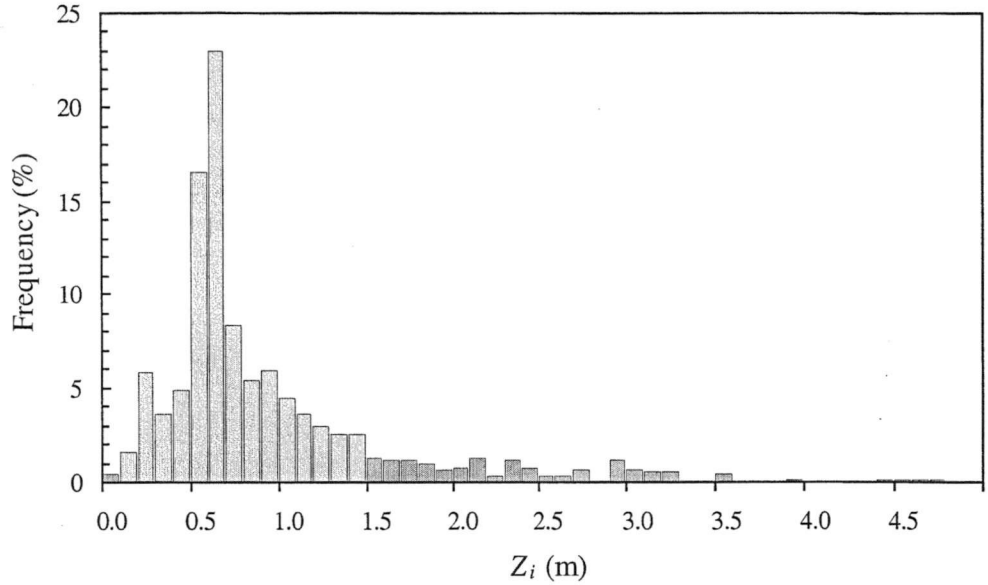

Figure 63 Sea ice thickness frequency distribution histogram obtained from drill-hole measurements collected in East Antarctica between 1991 and 1996. Adapted from *Worby* [1998].

Worby [1998] reported a mean ice thickness value of 0.80 m (± 0.41 m), corresponding to 614 ice thickness measurements (combining drilled measurements and core sites) for the V1(95) voyage. The average ice thickness value for the two AVHRR images is 1.43 m (± 1.18 m). The difference between these two figures can be attributed to the fact that, while the voyage spent a total of 28 days in the pack ice, the two images are spaced less than 24 hours apart. Furthermore, strong convergent conditions occurred during that period (see Section 5.3.1), contributing to the reduction of the open water and thin ice fraction and also to the overall thickening of the pack ice through mechanical forcing. Therefore, the model results for the V1(95) dataset are not representative of the average sea ice conditions of the Mertz area for the winter of 1995.

For the remaining voyages shown in Table 23, the mean ice thickness is 0.97 m (± 0.89 m), a value almost twice the mean ice thickness for the V2(96) spring dataset (0.52 m ± 0.44 m). Despite the undersampling of ridged ice mentioned above, these figures indicates that drill-hole measurements perform better than the method proposed in this study for ice thicknesses above 1.0 m. The reason for this poor performance of the model is that, once the ice floe is covered with a layer of fresh snow and its surface temperature is in equilibrium with the near-surface air temperature, the thermodynamic analysis of the model is not capable of resolving thickness increments that occurred through mechanical processes.

5.4.2 Ship-Based Sea Ice Thickness Observations

In this section, the AVHRR-derived sea ice thickness estimates are compared with data from 10 field experiments conducted in the Prydz Bay area between 1986 and 1995, representing a total of 1965 sea ice thickness observations. Table 24 shows the details of these expeditions, along with their corresponding mean ice thickness values. Unlike the results published by *Worby* [1998] and *Worby et al.* [1998], where the open water fraction is shown in a separate bin, the results presented in the current section show the open water fraction distributed proportionally throughout the thickness range (Figure 64) using the same process described in Section 5.3.1.

Voyage Number Season	*Dates in Ice*	*Region* (°E)	*Number of Observations*	*Mean Ice Thickness* (m)
V1 1986/87	22-Oct To01-Dec	60 - 120	213	0.40
V3 1987/88	21-Oct To31-Oct	60 - 120	33	0.40
V1 1988/89	28-Oct To23-Nov	60 - 120	299	0.28
V1 1989/90	22-Oct To03-Dec	60 - 120	230	0.43
V2 1990/91	16-Oct To10-Nov	60 - 120	202	0.19
V2 1991/92	08-Nov To19-Nov	60 - 100	101	0.24
V1 1992/93	25-Oct To05-Nov	60 - 100	213	0.37
V2 1993/94	20-Oct To01-Nov	60 - 100	113	0.30
V1 1994/95	08-Sep To12-Oct	75 - 140	315	0.47
V2 1994/95	27-Oct To23-Nov	60 - 120	246	0.41
			Total = 1965	$\overline{Z}_t$ = 0.35

Table 24 Summary of ship-based sea ice thickness observations made since 1986 in the Prydz Bay area. Adapted from Worby [1998].

The largest difference between the two histograms in Figure 64 is a 10% increase in the 0.0-0.2 m thickness class from October to November, which is accompanied by a 10% decrease in the 0.2-0.4 m bin, evidencing the mechanic and thermodynamic processes that occur as the season progresses and the temperatures increase. Compared with this 10-year dataset of ship-based sea ice observations, it is possible to conclude that the model overestimates the percentages of thin ice (up to 0.4 m) and underestimates percentages of ice thicker than 0.4 m. The mean ice thickness for the V2(96) dataset (0.52 m) is 32.7 % higher than the average obtained from the ship-based observations (0.35 m).

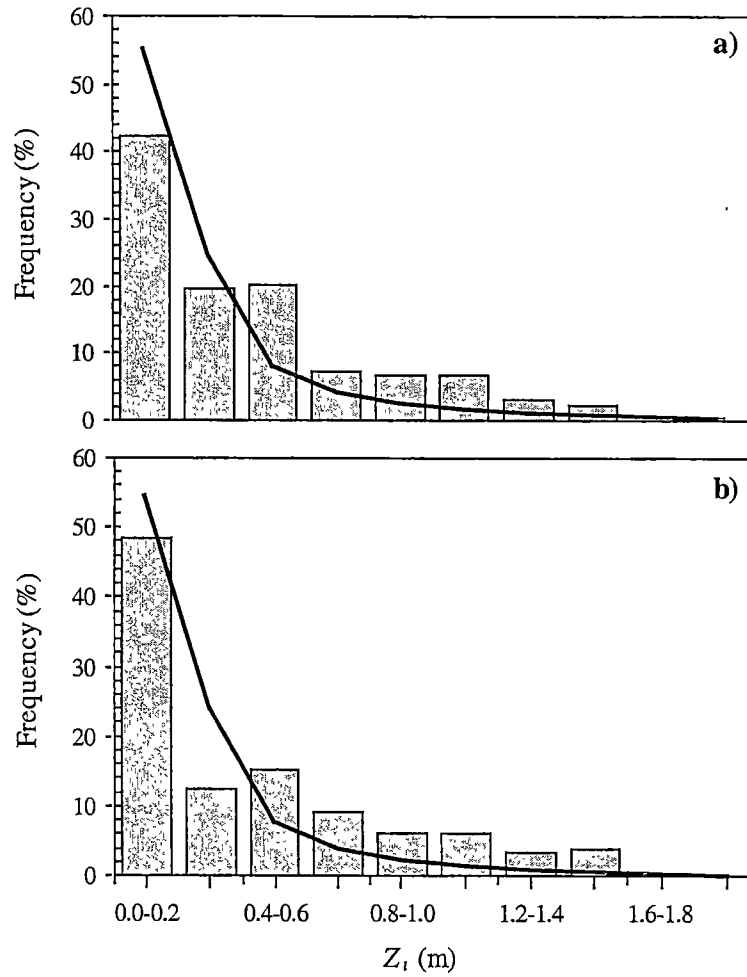

Figure 64 Average frequency distribution histograms of sea ice thickness obtained from ship-based observations for the months of (a) October and (b) November. The black lines represent the mean sea ice thickness frequency distribution histogram derived from the analysis of the 33 AVHRR images from the spring of 1996.

Two reasons can be enumerated to explain this overestimation of thin ice in the AVHRR results when compared to ship-based observations. According to *Worby* [1998], the ship-based observation method has an estimated accuracy of 20% for ice thinner than 0.3 m, which certainly affects the thin ice categories of the histograms in Figure 64. On the other hand, if the model's sensitivity to sub-pixel scale features (Section 4.5) is taken into consideration, a large number of open water pixels (which would otherwise be removed from ice thickness calculations) may have been inserted into the system due to cloud contamination, thereby increasing the contribution of the first thickness category (0.0-0.2 m) to the total range of ice thicknesses.

Regarding the data from the winter of 1995, the mean ice thickness value for the two AVHRR images for this period is 1.43 m. Ship-based observation values for specific periods within the V1(95) voyage were reported by *Worby et al.* [1996b]. Between 5 and 10-Aug-1995 mean ice thickness values ranged from 1.08 to 1.66 m. Closer to the date of acquisition of the two images (between 12 and 23-Aug-1995), mean values decreased from 1.66 to 1.03 m which, given then uncertainties and biases mentioned previously, can be considered a good agreement.

It became clear from the data presented in the current section, that comparing the model outputs with historical sea ice thickness data is not only an alternative to the absence of concurrent *in situ* data but also an essential source of information to assess the feasibility of the method proposed in this study. In spite of problems such as seasonal and interannual variability, synoptic coverage, spatial resolution and accuracy, the comparisons shown in this section contributed to highlight some of the strengths of the method that were not evident during the validation process conducted in Section 5.3.

5.5 Discussion of Results

This section presents a discussion of the results in comparison to recently published data on the spatial and temporal distribution of sea ice thickness in East Antarctica, aiming to identify similarities and present possible explanations for discrepancies. Similar but less detailed analyses are also presented for ice/snow surface temperature and albedo. This discussion focuses on the 1996 results for the Davis study area. Besides the fact that only two images of the Mertz study area were available for analysis in this study, there is a general lack of winter sea ice data published in the sector between 120° and 150° E.

5.5.1 Sea Ice Thickness

Comparisons between the frequency distribution histograms of sea ice thickness obtained through the method proposed in this study and concurrent (Figure 49) and climatological (Figure 64) data indicate that the AVHRR-based method tends to overestimate the amount of sea ice thinner than 0.4 m. Besides the issues of accuracy and cloud contamination of open water pixels discussed in Section 5.3.1, a complex mixture of factors contribute to explain such discrepancy. In order to highlight the importance of each of these factors, the analysis conducted in the current section takes three different approaches:

a) Overall Sea Ice Thickness Distribution

Seasonal variability is one important aspect that regulates the overall sea ice thickness distribution in East Antarctica. Based on the analysis of ten years of ship-based observation data (see Table 24), *Worby et al.* [1998] found that the greatest seasonal change in sea ice thickness distribution lies in the open water and thin ice categories, with values varying from 60% in December to less than 10% in August. Figure 47 and Table 21 show that the results of the present study are in accordance with this conclusion. The analysis of individual AVHRR images and histograms (Figure 40 to Figure 45) also show little or no variation in the amount of ice thicker than 1.0 m, which is consistent with the results of *Worby et al.* [1998].

Worby [1998] showed that the greatest variability in sea ice conditions occurs in the austral spring. During this time, open water and ice thicker than 0.3 m accounted for 60% to 90% of the total pack ice zone, with thinner ice in the form of nilas and pancake ice in leads being observed in lower and more variable concentrations. In October, there is a general flattening of the thickness distribution, histogram with virtually equal ice in many thickness categories. *Worby* [1998] attributes this to the continuing formation of sea ice, but at a lower rate than in winter, combined with the presence of thick ice formed earlier. The AVHRR-based sea ice thickness histogram for the Davis area in Figure 49 (**a**) shows a dominance of thin ice (0.02 - 0.2 m), corresponding to 56% of the data. This pattern is comparable to the average results for the month of November published by *Worby et al.* [1998] (shown in their Figure 12). The flattening of the sea ice thickness histogram however is observed to a lesser extent in the thicker ice categories of Figure 49 (**a**).

Interannual variability also plays an important role in determining East Antarctic sea ice thickness distribution. Analysing ship-based observation data from six field experiments conducted in the austral spring between 60° and 90° E (an area which brackets the Davis study area), *Allison and Worby* [1994] observed that the relative percentages of open water and ice categories varied considerably from season to season, as can be seen in Figure 65. Such interannual variability was also observed in the comparisons presented in this study. In fact, the differences (both in the overall shape of the histograms and the percentages of each ice thickness categories) between concurrent ship-based sea ice thickness observations and the AVHRR results (Figure 49) are larger than the differences between the later and the average of ship-based observations from 10 field experiments (Figure 64).

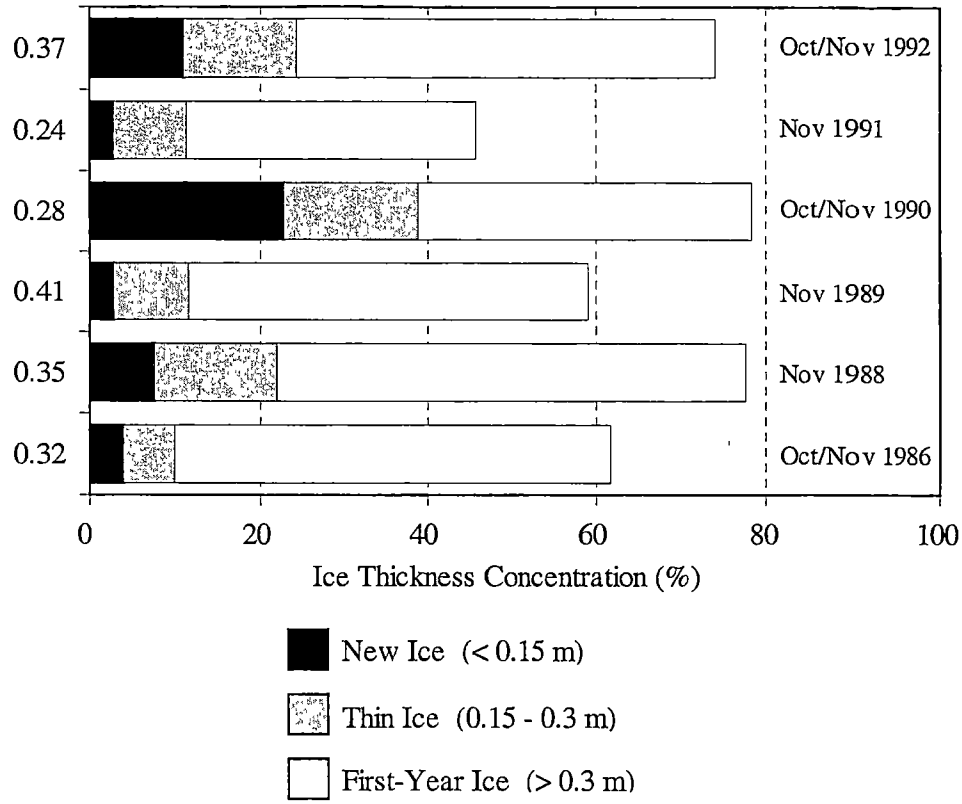

Figure 65 Relative concentrations for three ice-thickness categories (New Ice, Thin Ice and First-Year Ice) obtained from ship-based observation data collected in six spring field experiments in East Antarctica, between 60° and 90° E. Numbers in the vertical axis correspond to the area-averaged, undeformed mean ice thickness for each voyage (in metres). Adapted from *Allison and Worby* [1994].

Another factor that could help to account for the apparent underestimate in the mean thickness distributions computed from the present study is related to mechanical processes of ice thickening. *Worby* [1998] and *Worby et al.* [1998] have shown that deformation and ridging make a substantial contribution to the ice thickness distribution across East Antarctica. This is also highlighted in *Lytle et al.* [1998a]. Analysis of ice cores show that dynamic forcing plays a central role in the evolution of East Antarctic sea ice from its earliest stages of formation. These studies concluded that ship-based sea ice observations corrected for the presence of pressure ridges, which contain a significant volume of ice, generally provide better estimates of the overall sea ice thickness distribution in a given area. *Worby* [1998] and *Worby et al.* [1998] presented a detailed treatment of adjusting the distribution of level undeformed ice for the presence of pressure ridges based upon its areal extent and sail height.

Based on eight East Antarctic field experiments where surface ridging is calculated, *Worby* [1998] and *Worby et al.* [1998] also showed that ridged ice represents an increase in the mean thickness for East Antarctica of 70% compared to uncorrected level ice. In other words, there appears to be a 70% increase in the mean East Antarctic sea-ice thickness for dynamical compared to thermodynamic forcing. It should also be noted that this parameterisation does not account for rafting, which is a common mechanism for the thickening of level floes and may be dominant over ridging in terms of its effect on the thickness distribution of East Antarctic sea ice [*Worby, et al.*, 1998]. Presently, the AVHRR-based method proposed in this study does not account for mechanical processes of ice thickening, which is probably the most influential factor in the underestimation of sea ice thicker than 0.3 m. Chapter 6 presents possible alternatives for the incorporation of such processes.

b) Latitudinal Variations

Analysing East Antarctic data from ship-based observations between 1986 and 1992, *Allison and Worby* [1994] concluded that, between 60° and 90° E, the change in mean undeformed ice and snow thickness with distance from the ice edge is remarkably constant from year to year. In the outer zone (up to 150 km from the ice edge), sea ice concentration is only 20 - 30% and the area-averaged ice thickness is strongly biased by the presence of open water. Ice-covered areas are usually composed of new ice formed due to localized cooling and small floes 0.5 - 2.0 m thick. Figure 46 (**c**) shows this pattern of low ice concentration with new ice formation. Floes thicker than 0.5 m however are not observed near the ice edge, which can be explained by the analysis of the model's response to sub-pixel features presented in Section 4.5. In a low ice concentration scenario, the model tends to underestimate the thickness of small floes because of the presence of open water and/or new ice in the space of the same pixel.

According to *Allison and Worby* [1994], there is an increase in ice concentration in the central zone (between 150 km and 550 km from the ice edge), mostly due to the presence of ice thicker than 0.3 m. The concentration of new ice also increases with the appearance of leads. A trend towards thicker ice south of the ice edge is observed. At the inner pack, more than 550 km from the ice edge, there is a decrease in the area-average undeformed ice thickness caused by increasing concentrations of open water and ice thinner than 0.3 m and the presence of a flaw lead between the fast ice and the pack.

This pattern of zonation presented by *Allison and Worby* [1994] is similar to the results for the spring of 1996 presented in Section 5.2, as well as to other East Antarctic studies found in the literature (see Section 2.1.3). Figure 66 shows a comparison between the changes in undeformed area-averaged ice thickness with distance from the ice edge and an average longitudinal transect (centred at 75° E) of AVHRR-based sea ice thicknesses. Despite the variations inherent to the AVHRR method, it is possible to identify the ice regimes described by *Allison and Worby* [1994]. An analysis of Figure 46 (**c**) also confirms the model's ability to resolve latitudinal variations in East Antarctic sea ice thickness distribution.

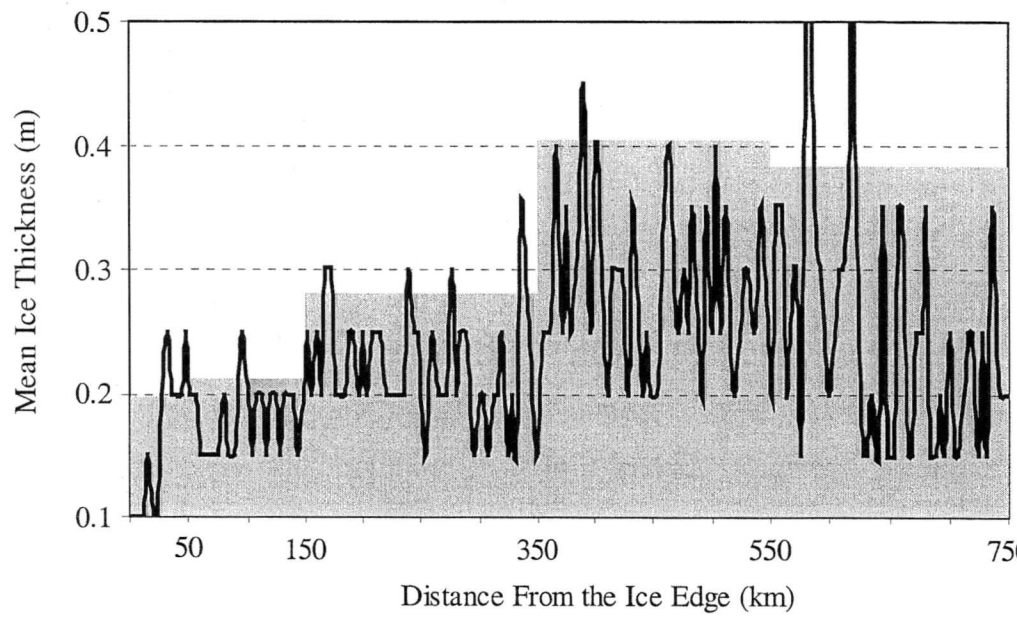

Figure 66 Changes in sea ice thickness with distance from the ice edge. Grey bars indicate the area-averaged ice thicknesses from ship-based observations collected between 1986 and 1992. Adapted from *Allison and Worby* [1994]. The black line refers to a longitudinal transect centred at 75° E, retrieved from the average image for the Davis area.

Allison and Worby [1994] also analysed the latitudinal variations in autumn between 120° and 150° E (an area which brackets the Mertz study area) and concluded that a high proportion of ice trapped near iceberg tongues along the coast survives the summer melt and tends to drift north. This ice, which accounts for a high percentage of floes 2.0 - 5.0 m thick near the ice edge, is formed by a continuous deformation of thinner floes. Figure 46 (**a**) shows a band of floes thicker than 1 m lined up at approximately 62° S, but not as close to the ice edge as described by *Allison and Worby* [1994]. This discrepancy is probably due to convergent regime caused by the swell penetration event described in Section 5.3.1.

c) Zonal Variations

The analysis of the average sea ice thickness distribution for the spring of 1996 (Figure 46 - **c**) clearly shows that the characteristics of the outer pack, the central zone and the inner pack, described in item *a)* above, are not constant throughout the longitude range of the Davis area. Superimposed on the large-scale patterns of ice thickness distribution are smaller scale regimes related to factors such as bottom topography, coastal features and the distribution of grounded icebergs.

Figure 46 (**c**) shows that the most prominent feature to break the zonal sea ice distribution pattern in the Davis area is a band of thick ice (from 0.4 up to more than 1.0 m) that stretches from 74° to 82° E, occupying a latitudinal range between 68° and 64° S. Climatological analyses of ship-based sea ice observations from previous years (11 sets of observations between September and November from 1986 to 1995) confirm that this is indeed a common feature of the region [*Allison and Worby*, 1994; *Worby*, 1998; *Worby and Massom*, 1995; *Worby, et al.*, 1998]. *Worby and Ackley* [2000], in a summary of these studies, noted a persistent band of thick ice with primary ice thicknesses up to 2.5 m, which can be attributed to the cyclonic circulation pattern in the Prydz+ Bay area (described by *Wong et al.* [1998]) and the barrier provided by the frequent presence of grounded icebergs.

The bathymetry of this region is dominated by the Four Ladies Bank with depths as shallow as 200 m (as shown in Figure 67), which explains the presence of grounded icebergs. The latter act as obstacles to sea ice drifting within the cyclonic circulation of the Prydz Bay gyre [*Wong, et al.*, 1998], causing the pack to accumulate and thicken through rafting and ridging "upstream" of the blocking feature. As such, icebergs play a significant but as yet unquantified role in the local production and thickness distribution of sea ice, and the concomitant rejection of brine into the underlying ocean.

Southerly winds and the lee effect "downstream" promote the appearance of areas of thin ice and open water immediately north of the icebergs (as can be seen in Figure 40), a phenomenon which has been reported in previous studies [*Heil and Allison*, 1999; *Wong, et al.*, 1998]. This presence of thin ice and open water, along with the pattern of narrow cloud strings north of the icebergs, is a possible indication that these areas may be related to ice formation processes during periods of divergent conditions.

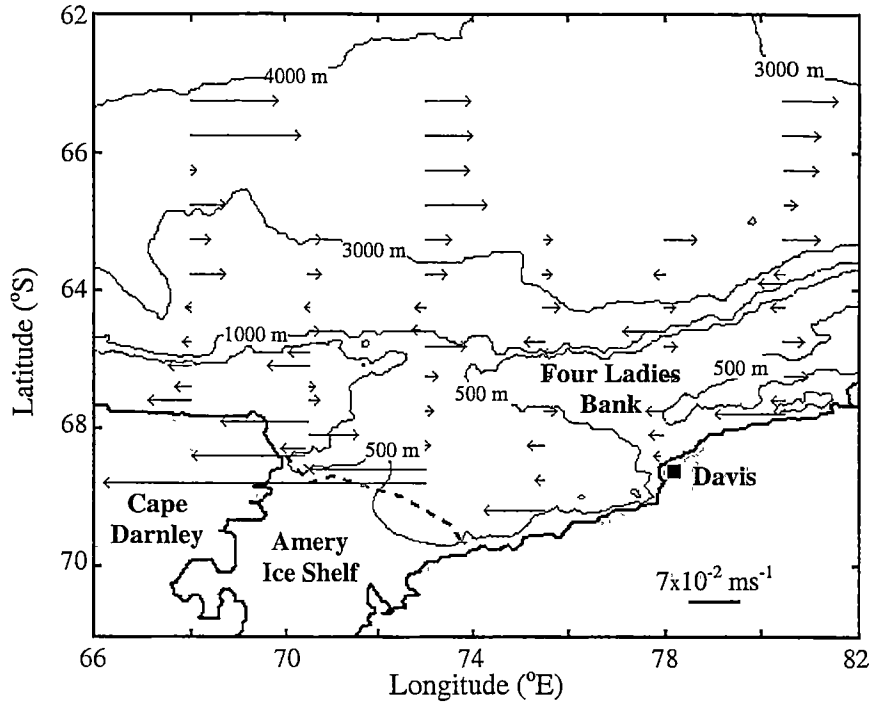

Figure 67 The bathymetry and ocean circulation at the Prydz Bay area. Plotted east-west geostrophic velocities at the surface were obtained from CTD data collected in 1992. Adapted from *Wong et al.* [1998].

Ice drift is another important process controlling zonal variations in the Prydz Bay area. Through their analysis of drifting buoy data, *Heil and Allison* [1999] show that oceanic circulation along the East Antarctic coast is generally barotropic, with the ice drift being strongly correlated with bottom topography. However, northward outflows occur in certain locations due to the effects of both the bottom topography and seasonal changes in the position of the zonal shear zone. One important such outflow is in the Prydz Bay region, allowing the discharge of ice from the westward drift in the south to the predominantly eastward drift to the north.

Within the Prydz Bay region, *Heil and Allison* [1999] identify two regions which are dominated by net northward advection, namely around 67° E and 77° E. These are likely associated with the presence of a large-scale cyclonic oceanic gyre in Prydz Bay itself (Figure 67), and an eddy at 79° E. Due to their close proximity, the two current axes act as broad conveyors of sea ice from the coastal current region and into the ACC [*Heil and Allison*, 1999]. Drift rates in the Prydz Bay sector are moderate, being lowest in the northernmost pack and the far south. In their buoy drift analysis, *Heil and Allison* [1999] and *Worby et al.* [1998] have also identified the regions around 125° and 135° E as being zones of net northward sea-ice transport out of the East Wind Drift. These northward deflections are clearly related to the sea bottom topography.

5.5.2 Albedo and Ice/Snow Surface Temperature

Total albedo and surface physical temperature retrievals from the AVHRR data, while a key input to drive the thermodynamic model described in this study, are in themselves important climate variables. While no contemporary data were available for validation, comparison are made with previous field observations and climatological data from East Antarctica.

a) Albedo

Most measurements of sea ice albedo have either been made in the Arctic (e.g. *Grenfell and Perovich* [1984], and *Perovich et al.* [1986]) or in the laboratory (e.g. *Perovich* and *Grenfell* [1981]). However, sufficient data have been collected in East Antarctica by *Allison et al.* [1993] and *Brandt et al.* [1999], to evaluate the albedo results presented in this study, and to infer information on the ice type (and indirectly ice thickness) from this comparison. Other albedo measurements in the Southern Ocean were made by *Spano* [1965] and *Andreas and Makshtas* [1982]

The most influential factor controlling the surface albedo of Antarctic sea ice is snow cover. In fact, *Allison et al.* [1993] mention that a snow cover of a few centimetres is sufficient to hide the underlying ice, so that the albedo becomes essentially that of the snow. Snowfall is frequent in the Southern Ocean because of the passage of synoptic storms. As such, young sea ice acquires a covering of snow within a few days after it forms [*Allison, et al.*, 1993]. Throughout the 22 ship-based and helicopter-based observations conducted in East Antarctica between October and December 1988, *Allison et al.* [1993] noted that sea ice thicker than 0.15 m always had a snow cover.

Snow parameters that control the total surface albedo are: snow thickness, grain size and wetness [*Allison, et al.*, 1993]. *Zhou et al.* [in press] found for example that the total albedo of the snow on sea ice decreased between the continent and the ice edge, i.e. from south to north, due to an increase in snow wetness and grain size. Of secondary importance for snow-covered ice are the effects of the solar zenith angle and cloud cover [*Warren*, 1982; *Wiscombe and Warren*, 1980]. The most important variables determining the albedo of young snow-free ice are the size and number of air bubbles and ice thickness [*Allison, et al.*, 1993]. Snow-free ice albedo also increases significantly with decreasing solar elevation [*Grenfell*, 1979; *Grenfell and Maykut*, 1977].

Comparing the recommended East Antarctic values of albedo for each ice category (shown in Table 3) suggested by *Allison et al.* [1993] and *Brandt et al.* [1999] with average values for the spring of 1996 obtained from the AVHRR dataset (shown in Table 25), it is possible to evaluate the results of the present study.

Ice Type (Thickness)	*Albedo*
Grease (0.02 m)*	0.08
Nilas (<0.1 m)	0.15
Young Grey Ice (0.1 - 0.15 m)	0.46
Grey-White Ice (0.15 - 0.3 m)	0.57
First-Year Ice (0.3 - 0.7 m)	0.69
First-Year Ice (>0.7 m)	0.75

Table 25 Average albedos for each thickness class obtained from the 1996 AVHRR dataset. (*)The value for grease ice was to set to 0.02 m to allow a comparison with the model's minimum thickness.

The values in Table 25 are systematically smaller than those of Table 3, but the difference is never superior to 11.5%. It is important to notice however that, to estimate snow thickness, the model employs an empirical relationship with ice thickness in the parameterisation of the conductive heat flux (Section 4.1.6) and therefore the effects of snow cover in the model outputs might be underestimated (See Section 6.2). Furthermore, the albedos in Table 25 are averages for each ice type, regardless of the presence or absence of a snow cover. At the sub-pixel level, open water contamination may also contribute to the reduction of albedo estimated by the model, especially for ice classes thicker than 0.15 m.

The results presented in this study show an expected broad-scale variability in the total albedo, from the ice-edge region southwards to the coast. In the outer pack, wave-ice interaction removes much of the snow from the ice cover [*Massom, et al.*, in press-a], which is composed of smaller floes [*Lytle, et al.*, 1998a]. This results in a circumpolar zone of relatively low (intermediate) albedo. Although the ice edge is obscured by clouds in most images, values as low as 0.05 can be observed at lower latitudes (Figure 40) In contrast, the inner pack comprises large floes with a relatively thick snow cover and hence a high albedo (0.6 - 0.8). At the coast, significant areas of relatively low albedo (0.05 - 0.1) correspond to the presence of recurrent and persistent coastal polynyas. Adjacent to these, regions of higher albedo (0.2 – 0.4) can be fund near the fast ice which has been misclassified by the ICEMAPPER as clouds.

b) Ice/Snow Surface Temperature

Measurements of *in situ* surface temperature for the Antarctic ice sheet showed reasonably good results when compared to thermal infrared satellite data such as the Temperature Humidity Infrared Radiometer (THIR) [*Comiso*, 1983; *Comiso*, 1994], the ATSR [*Key, et al.*, 1997a] and AVHRR [*Comiso*, 2000; *Key, et al.*, 1997a]. Similar comparisons involving the sea ice cover of the Southern Ocean however are far more limited, mostly because of the lack of *in situ* data, which can be linked to the small number of platforms like buoys, drift stations and ships. Other issues such as the insulation of buoy thermistors by snow also contribute to limit the number of experiments conducted in the Southern Ocean [*Comiso*, 1994].

Variations in Antarctic sea ice extent have been correlated with interannual changes in surface temperature from continental stations [*Weatherly, et al.*, 1991], but the dataset may not reflect actual surface temperatures in sea-ice-covered regions because of large distances between the stations and the ice edge and the influence of local phenomena such as katabatic winds [*Comiso*, 1994]. Furthermore, *Comiso* [1994; 2000] noted that the seasonal fluctuation of surface temperature over the Antarctic ice sheet is larger than that of sea ice.

Comiso [2000] published AVHRR-derived average surface temperature values from 1992 for both descending (night) and ascending (day) data. The approximate day-time average values for the spring months were: 257 K for September, 260 K for October and 263 K for November. As expected the difference between day and night data increases (from +1 K to +2 K) within this three month period. At 55° S, the average values encountered for the entire year range from 257 K to 271 K. *Comiso* [2000] also noted that the temperature cycle is asymmetrical, with the cooling period being longer than the warming period, a phenomenon which has also been observed in other remote sensing studies such as *Gloersen et al.* [1992]. The average values published by *Comiso* [2000] show an increase of 7 K between September and November. Comparatively, the median values for the images from the 1996 AVHRR dataset show an increase of 7.7 K (from 257.5 K to 265.2 K) for the same period.

Parish and Bromwich [1987] and *Comiso* [2000] noted that the coldest regions within the pack ice of the Southern Ocean occur in the vicinity of drainage basins and ice shelves. Analysis of the Davis study area shows that one such region occurs north of the Amery Ice Shelf, which presents the lowest temperatures (below 250 K) within the 1996 AVHRR dataset, despite the presence of warmer areas such as leads and polynyas. This phenomenon is well depicted in the image of 30-Sep-1996 shown in Figure 40.

The expected spatial distribution pattern of colder areas near the coast and warmer areas to the north, closer to the ice edge, can be observed in the 1996 spring dataset, albeit the obscuration caused by cloud cover that occurs in some of the images (Figure 41 to Figure 43). Besides this overall warming trend towards the outer pack, the relatively small amount of clouds observed in Figure 40 allows the identification of important features. The flaw lead immediately north of the fast ice (which in this case is mis-classified as "Cloud" by the ICEMAPPER) between 74° and 78° E shows temperatures above 268 K which is consistent with values found in the literature for this type of feature [*Key, et al.*, 1993; *Worby*, 1998]. The temperatures of the Cape Darnley polynya (between 74° and 78° E) vary between 265 K and 271 K, which is an indication of the presence of newly-formed young ice [*Massom, et al.*, 1998a]. East of the Cape Darnley polynya is a region of very low temperatures (between 250 and 253 K) that extends from the tip of Cape Darnley to the western limit of the Amery Ice Shelf. The corresponding sea ice thickness for this area is less than 0.10 m which indicates that the low temperatures are not caused by the presence of thick, snow-covered ice floes but might be related to a cold and dry air parcel originated at the Amery Ice Shelf.

As can be observed in Figure 40, the central pack is dominated by large areas of relatively low temperatures (between 250 and 258 K), which is consistent with the band of thick ice mentioned in Section 5.5.1. The temperature decreases gradually towards the ice edge, reaching 263 K at 61° S. The only features to break this pattern are areas of high temperature (between 265 and 270 K) located immediately north of grounded icebergs which might be related to ice formation processes (see Section 5.5.1). The marginal ice zone is dominated by temperatures below 263 K, indicating the decrease in ice concentration and the contamination of sea ice pixels with open water.

Conclusions

This chapter presents an assessment of the technique in terms of the achievement of the objectives specified in the Introduction chapter (Section 6.1), followed by discussions of the limitations of the method (Section 6.2), and operational and future research requirements (Section 6.3). The chapter is concluded with an analysis of future remote sensing technology applicable to sea ice thickness research (Section 6.4) and a brief summary of this study (Section6.5).

The sea ice zone encircling the Antarctic continent acts as a highly variable interface between the ocean and the lower atmosphere, and is of immense global significance as a region of physical and biogeochemical interaction processes. An important characteristic governing these processes is the sea ice thickness distribution, and its variability. While there is still much work to be done towards a better understanding of the current conditions, a growing concern is the potential effect of global warming on sea ice, and the feedback processes involved [*Allison, et al.*, 2000].

Although decreasing trends in Arctic sea ice extent have been recently reported by several authors [*Cavalieri, et al.*, 1997; *Maslanik, et al.*, 1999; *Rothrock, et al.*, 1999; *Vinnikov, et al.*, 1999], projected changes and their timing in the extent of the Southern Hemisphere sea ice cover are less certain, with various coupled models predicting contradictory responses of the sea ice cover to an increased carbon dioxide atmosphere [*Barron*, 1995]. Moreover, it appears that there has been a slight increase (1.3% per decade) in Antarctic sea ice extent from 1978 to 1996 [*Cavalieri, et al.*, 1997]. Analysing satellite data from 1988 to 1994, *Parkinson* [1998] observed no indication of an overall lengthening or shortening of the ice season in the Southern Ocean as a whole. However, short-term changes of opposite sign in ice extent tend to occur in different regions and have been reported in recent studies such as *Jacobs and Comiso* [1997], *Gloersen and Mernicky* [1998] and *Parkinson* [1998].

A complicating factor in Antarctica is the role played by snow cover in a global change scenario. Possible changes in the sea ice mass balance or volume due to global warming may be complex, rather than simply a progressive thinning of the ice cover. The predicted enhanced precipitation [*Hunt, et al.*, 1995], for example, may increase the contribution of snow-ice formation, as suggested by modelling studies [*Wu, et al.*, 1999]. Indeed, snow-ice formation may act to counterbalance ice volume loss due to basal melting. Moreover, an increase in snowfall may increase the sea ice albedo, with significant implications for the ice-albedo feedback mechanism. This may also act to retard summer melt in certain regions [*Ledley*, 1991].

Recent modelling efforts such as *Wu et al.* [1999] and *Wu and Budd* [1998] show that the response of Antarctic sea ice to global change may manifest itself as a change in sea ice thickness or volume, with important climatic ramifications. However, model reproductions of current conditions, and predictions of change, are impossible to evaluate without more detailed knowledge of the Antarctic sea ice thickness distribution [*Allison, et al.*, 2000]. Indeed, it is currently difficult to ascertain which, if any, of the models yield realistic physical representations of the Antarctic sea ice cover.

Another complicating factor is the incomplete representation of much of the physics of sea ice in many of the current models [*Allison, et al.*, 2000]. *Rind et al.* [1995] for example, stress the importance of properly constraining the sea ice response to climate perturbations, through the use of more realistic sea ice and ocean models. As such, it is imperative to acquire long term, consistent and accurate time series of ice and snow thickness in order to evaluate whether potential changes in sea ice parameters reflect long-term global warming, natural variability on shorter time scales, or a complex combination of both.

While consistent data on Antarctic sea ice concentration and extent are routinely available from satellite passive microwave remote sensing to a reasonable accuracy [*Steffen, et al.*, 1992], a comparable large-scale determination of the thickness distribution represents a major challenge. As a result, the Antarctic sea ice thickness distribution, and its spatial and temporal variability, are typically poorly represented in numerical models [*Morales Maqueda and Fichefet*, 1996].

A procedure based on thermodynamic modelling combined with cloud-free visible and thermal infrared satellite data, as proposed in this study, has the potential to fill this gap, providing a monitoring tool that can be employed in conjunction with numerical models. While many aspects of such an approach need to be refined, this study has demonstrated that the combination of numerical modelling and remote sensing techniques has the ability to provide useful information on the distribution of albedo, ice/snow surface temperature and sea ice thickness in the Southern Ocean.

6.1 Assesment of Objectives

The main objective of this work has been to address the problem of lack of large-scale information on Antarctic sea ice thickness by developing a technique which combines the special attributes of satellite remote sensing with a thermodynamic sea ice growth model. This melding effectively addresses the issue that current satellite technology cannot directly measure Antarctic sea ice thickness, although future sensors show some promise (see Section 6.4). Due to the immense scales involved, the remoteness of the Antarctic sea ice zone, data sparsity and the need for consistent and repetitive coverage, satellite remote sensing is well suited to this problem. The work in this study incorporates data from the NOAA AVHRR sensor, which has the excellent attribute of providing coincident information on both surface reflective and thermal properties [*Cracknell*, 1997; *Steffen, et al.*, 1993].

This is the first time that such a technique has been developed and tested specifically for the Southern Ocean. While the concept of the method presented in this study is based on the Arctic technique proposed by *Yu and Rothrock* [1996], a number of significant changes and improvements have been made to adapt this technique to Antarctic conditions, which are considerably different to those encountered in the Arctic sea ice zone (see Section 2.1.1). Most of the parameterisations employed by *Yu and Rothrock*, which were based on empirical observations obtained from Arctic measurements, were replaced or updated with parameterisations based on data collected in the Southern Ocean, leading to the creation of a completely new algorithm. The main differences between this new technique and that of *Yu and Rothrock* can be summarised as follows:

a) The inclusion of a more accurate and flexible algorithm for the retrieval of ice-surface temperature following *Key et al.* [1997a], which includes coefficients derived specifically for Antarctica;

b) The incorporation of a more robust, wind-dependent system for retrieval of near surface air temperature;

c) The adoption of a recently published (*Massom et al.* [1998b] and *Sturm et al.* [1998]) value for the effective thermal conductivity of snow (k_s), which takes into account the presence of different snow types with different effective k_s values in the typical snow stratigraphy encountered in the East Antarctic sea ice zone;

d) The replacement of the original relationship between Z_i and Z_s for sea ice and snow in the Arctic (*Doronin* [1971]) by a more recent one obtained from data collected in East Antarctica and;

e) The replacement of the constant values of bulk transfer coefficients (C_e and C_h) by modelled data based on the work of *Andreas* [1987].

Another important modification was the introduction of the looping system described in Section 4.2. *Yu and Rothrock* [1996] calculated all of the terms in Equation 8, solving the system for Z_i for each AVHRR pixel. This approach creates a situation whereby more than one thickness can satisfy the equation. This problem is eliminated by using a looping system which checks the net flux for all pixels in the image at thickness increments of 0.01 m, ensuring that the minimum possible thickness is assigned to a pixel as soon as it attains thermodynamic equilibrium. When compared with *Yu and Rothrock*'s work, the improvements and modifications mentioned above led to considerably smaller error estimates (see Section 4.6).

Important by-products of this study are the classified images and frequency distribution histograms of total albedo and surface physical temperature of the East Antarctic sea ice zone, the variability of which is intimately tied to the variability in the sea ice thickness distribution. In themselves, these are also key parameters in the global climate system and are likely to respond to global climate change. The ice-albedo feedback, wherein warming leads to a reduced albedo which in turn leads to further warming, is, for example, an important topic in the discussion of global climate change [*Chu*, 1996; *Rind, et al.*, 1995], which could benefit from such products.

The recent study by *Comiso* [2000] has intriguingly indicated that, over the period 1979-1998, the sea-ice surface temperature around Antarctica exhibited a slight cooling trend. Both surface albedo and temperature are closely linked to seasonal and interannual variability in Antarctic sea ice surface melt [*Drinkwater and Liu*, 2000], the patterns of which may also change in response to long-term global warming. Again, the overall accuracy, reliability and predictive ability of numerical models depend strongly upon the input of accurate surface temperature and albedo data. Such data are also essential to the validation of the model results. The data from the current technique will complement those from the NSIDC's NOAA Polar Pathfinder compilation of AVHRR data, which covers the period from 1983 to 1996 [*Maslanik, et al.*, 1998]. Both the albedo and temperature outputs form useful data with which to run and test existing coupled models.

This study also demonstrated that the thermodynamic model adapted satisfactorily to the sea ice conditions of the Southern Ocean. Because of the assumption of a linear temperature profile within the ice-snow layer (see Section 4.1), the generally thinner ice of the Antarctic pack is more suitable for the application of this model than the thicker sea ice cover of the Arctic. On the other hand, the greater diversity that Antarctic sea ice types present at sub-pixel scales, and its greater mobility in comparison with the Arctic are clear disadvantages. The latter is a critical problem as the model focuses on the thermodynamic characterisation of each pixel and cannot resolve thickening due to ice dynamics or snow-ice formation. These limitations are further discussed in Section 6.2.

The validation process was impaired by a relative lack of coincident data. Of the whole dataset analysed, only five pixels had concurrent ship-based observations. In spite of this problem, the overall ice thickness frequency distribution histogram obtained from the 33 images from the spring of 1996 is in reasonably good agreement with concurrent ship-based observations (Figure 49 - **a**) and historical data published in several studies such as *Allison and Worby* [1994], *Lytle et al.* [1998b], *Worby and Massom* [1995], *Worby* [1998], *Worby et al.* [1998], *Worby and Allison* [1999] and *Worby and Ackley* [2000].

Although there were some significant differences between the apparent sea ice thickness returned by the model and the other methods investigated in this study, these could be largely explained by the margins of error and also by the model's response to the presence of more than one feature in the space of one pixel. Also important is the fact that the model outputs of albedo and IST are in agreement with results published by *Allison et al.* [1993], *Brandt et al.* [1999], *Comiso* [2000], *Key et al.* [1997a] and *Laine and Heikinheimo* [1996].

The comparison with digital aerial photographs showed that, on the scale of tens kilometres, the model is capable of resolving areas of transition between different ice regimens such as thick, snow-covered ice and areas of open water and/or thin ice (e.g. Figure 56). This is a crucial parameter for the characterisation of the heat budget in the Southern Ocean. In areas of homogeneous ice cover, the thickness returned by the model is in good agreement with the ranges associated with the ice types observed in the photographs.

Comparisons with the two AVHRR images from winter 1995 are, of course, less meaningful as these are separated by less than 24 hours. However, by analysing the synoptic conditions of that one-day period it was possible to satisfactorily explain the sea ice regime observed in the classified images.

The present work complements that of *Worby* [1998] and *Worby et al.* [1998], and also that of the current SCAR ASPeCt programme. A major objective of the latter is to assimilate all available ship observational data from various national programmes into a common dataset to produce a regionally and seasonally varying climatology of Antarctic sea ice thickness [*Worby and Ackley*, 2000]. The ASPeCt product will be a circumpolar climatology of sea ice and snow thickness in 30° longitudinal bands, covering the period from1980 to 1997. Another aim is to compile a circumpolar sea-ice and snow cover thickness climatology at a longitudinal spacing of 15° around the continent for the period from 1998 to 2007.

The regional and seasonal distribution of the entire dataset compiled by ASPeCt and presented in *Worby* [1999b] and *Worby and Ackley* [2000] show significant gaps, particularly in the Ross and Amundsen Seas in summer and autumn. It is hoped that transects, along-commonly-travelled routes to Antarctic bases and in regions of particular scientific interest, will be repeated more than once per season. Again, it is likely that significant spatial and temporal gaps will be present in this dataset [*Worby and Ackley*, 2000].

In East Antarctica, ship observations are largely limited to certain periods of the year, and datasets are collected on an opportunity basis or as part of dedicated sea ice cruises. The dataset analysed by *Worby et al.* [1998] and *Worby* [1998] largely emanates from the October-November period, with some data available for March-May, September and December for the eight-year dataset. Significant gaps exist in February, as well as May, June and July. Although further validation and development is essential, the technique proposed in this study has the potential to make a significant contribution by helping to fill in these seasonal gaps, as well as the spatial gaps between the ship tracks, which also tend to be concentrated in certain regions (see Figures 1 and 2 in *Worby and Ackley* [2000]).

6.2 Limitations of the Method

The technique proposed in this study shows considerable promise. However, a number of issues require attention before it can be used as a tool to routinely and systematically monitor sea-ice thickness over large areas to the accuracy and consistency required by climate studies.

a) Forecasting of the sea ice thickness distribution.

Unlike typical numerical models, the procedure presented in this study is not capable of forecasting changes with time, mostly because of the nature of the input data (i.e. the satellite image). The issue of modifying this model to work with consecutive images to characterise dynamic and thermodynamic processes in the pack ice is discussed in Section 6.3.

b) Water vapour contamination in polynyas and leads.

The effect of contamination by strong fluxes of water vapour from leads and polynyas on ice-thickness retrievals derived from the system proposed in this study is currently unknown. As demonstrated in Sections 4.5 and 5.3.1, cloud contamination may have a significant effect on the model retrievals of thin sea ice classes. This situation can only be improved with the collection of specific *in situ* data and further developments in the ICEMAPPER system, which are outlined in Section 6.3 below, and by further validation in the field.

c) *Sub-pixel scale features.*

The issue of how the model responds to the presence of more than one surface type within the space of a pixel has been discussed in Section 4.5. It is clear from that analysis that the apparent ice thickness returned by the model is the result of the radiometric characteristics and the relative concentrations of all features (i.e. ice, water, clouds etc.) present within the area of each pixel. By using this information in conjunction with fine resolution data such as digital aerial photography, it is possible to characterise regions of large ice diversity such as polynyas and the marginal ice zone. This analysis also exposed deficiencies in the ICEMAPPER system in its inability to unambiguously identify cloud-contaminated pixels in areas of open water, which may be related to the occurrence of strong moisture fluxes in such regions. Improvements to the ICEMAPPER system are discussed in Section 6.3.

d) *Dynamic processes and snow-ice formation.*

Studies by *Worby et al.* [1998], *Worby*, [1998] and *Lytle* [1998b] demonstrated that the ice-thickness distribution in East Antarctica is governed by a complex interaction of dynamic and thermodynamic processes. Ridging and rafting caused by episodes of convergence in the pack are the dominant processes of sea ice thickening beyond approximately 0.5 m. This may help to explain why the frequency distribution histogram of ice thickness obtained from ship-based observations is "thicker" than the one produced by the model (see Figure 49). Thickening due to snow-ice formation is another important mechanism that cannot be resolved by the sea ice model, which is currently concerned only with the thermodynamic characterisation of each suitable pixel within an image. The possible future incorporation of ice dynamics and snow-ice formation processes into the algorithm is discussed in Section 6.3.

e) *Night-time ice thickness data.*

Due to its reliance on albedo retrievals from channels 1 and 2, this technique is not applicable during periods of polar darkness.

f) Variations in snow depth and properties..

As mentioned in Section 2.1.8, the snow cover has both direct and indirect effects in the ice thickness distribution. The system proposed in this study cannot produce information on local variations of snow properties such as grain size or the thickness of the snow cover. Instead, it employs a relationship between Z_i and Z_s based on data collected on the field.

g) Ridge parameterisation.

The studies of *Allison and Worby* [1994], *Worby* [1998] and *Worby et al.* [1998] show that a large proportion of pack ice in East Antarctica is at any one time contained within pressure ridges. *Worby* [1998] points out that resolving the thick end of the thickness distribution spectrum is essential to accurately estimate climate parameters such as the total ice production and the resultant flux of salt into the underlying ocean. Obviously, thermodynamic modelling alone cannot account for this extra ice. As such, it may be that the mean thicknesses derived from this study should be adjusted by some factor (e.g. 1.7 as proposed by *Worby* [1998]) in order to more accurately parameterise this ridge ice. However, while the current technique may not be optimally adapted to yielding ice thicknesses at the thicker end of the spectrum, it does a reasonable job in identifying and measuring thin ice regions. The latter are of crucial importance to the surface heat and radiation budgets and to water mass modification due to rapid ice growth rates therein [*Allison and Moritz*, 1995; *Maykut*, 1978].

h) Temperature profile in the snow/ice column.

As mentioned in Section 4.1, the model assumes a linear ice/snow temperature profile which allows the estimatation of the conductive heat flux through the sea ice using theoretical relationships. Although reasonable for many situations encountered in the Antarctic sea ice cover, this assumption cannot be generalized.

6.3 Future Model Developments

This study has demonstrated the feasibility of a semi-automated method for obtaining Antarctic sea ice thickness distributions using visible and thermal infrared data from satellite remote sensing platforms. Such a system, once properly validated, can be employed both for logistical support and as a source of high-resolution, albedo, IST and sea ice thickness distribution data for input and validation of ice-ocean-atmospheric coupled numerical models. However, a number of issues remain to be addressed for this technique to achieve its full potential as a tool for monitoring changes in Antarctic sea ice thickness distribution.

a) Employment of large and more extensive datasets.

One of the major limitations of this study was the small amount of AVHRR images concurrent with *in situ* data. The causes of this are: extensive cloud cover typical of this region of the Southern Ocean and problems in the co-ordination between the collection of field data and the passage of satellites, especially during V2(96), when a problem with the RSV *Aurora Australis*' engine caused most of the *in situ* data to be collected outside the area of study. To overcome this problem, it is necessary to increase the number of images analysed, which can be achieved by extending the period of analysis, enlarging the areas of study and most importantly including other NOAA satellites. In this context, the recently launched NOAA-15, with its new 1.6 μm channel will offer potentially improved cloud masking capabilities over snow and ice surfaces. Retrospective analysis is also possible, with the AVHRR dataset extending back to 1978.

At present, the sea ice thickness model described in Chapter 4 is capable of running only on the seven-band DISIMP-based AVHRR images generated through the process described in Section 3.1.1. The use of larger datasets suggested here requires a greater flexibility, which includes the capacity to open, navigate and calibrate any Antarctic AVHRR image, including important datasets such as the NSIDC's Polar Pathfinder compilation [*Maslanik, et al.*, 1998]. The Pathfinder product series are available at 25-km, 5-km, and 1.25-km grid resolution.

This flexibility could also be extended to accommodate other visible and thermal infrared sensors such as the first spaceborne Moderate-resolution Imaging Radiometer (MODIS). Launched on the EOS Terra satellite in December 1999, MODIS forms an important continuation of the AVHRR programme, yielding improved surface albedo and physical temperature datasets. Superficially similar to the AVHRR, this sensor will provide higher radiometric resolution images of daylight-reflected solar radiation and day/night thermal emissions over all regions of the globe. Marked improvements are its precise spectral band, geometric registration and high calibration accuracy and precision, including sophisticated onboard calibration. This sensor will view the entire surface of the Earth every 1-2 days, making observations in 36 co-registered spectral bands (from 0.4 - 14.4 μm) at a spatial resolution of 0.25 - 1 km across a 2330 km-wide swath [*NASA*, 1999].

Section 5.2 demonstrated that it is possible to employ the method presented in this study to build a climatology of the sea ice for the region between 60° and 80° E, which could then be validated and compared with *in situ* information such as ship-based observations and ULS data. Prydz Bay is the largest embayment in East Antarctica and therefore very important in terms of its glaciological and oceanographic influence [*Wong, et al.*, 1998]. It is also geographically important because of the location of Davis and Mawson stations and the ship traffic they generate.

b) Validation.

Consistent with item *a)* above, to strive for larger and more extensive sets of satellite data, it is essential to incorporate more *in situ* data for further validation of the technique. This work will initially concentrate on periods and regions within which field observations are available. Ship-based sea ice observations provide the best means of comparing the AVHRR-derived ice thicknesses on a pixel-by-pixel basis. The number of coincident ship-based observations analysed in this study was too small to derive any robust statistical comparisons. Obtaining a statistically-representative relationship between Z_{Obs} and Z_{AVHRR}, and understanding the processes that account for possible differences between the two methods, is an essential step towards the operational use of the model. Apart from extending the analysis with more points from the same season, it is also desirable to replicate this procedure for winter and summer months.

Additional data are also necessary to evaluate specific topics raised by the method developed in this study as well as the strength of some of the model's assumptions, specially the employment of a linear temperature profile in the snow/ice column and the inability to account for variations in snow depth and properties over different areas in the ice pack.

As demonstrated by *Yu and Rothrock* [1996], moored ULS devices are also a suitable source of data for validation. There have been deployments of ULS in the East Antarctic sector in 1994 and 1996 [*Bush*, 1997] and more are planned for the near-future, which will permit new possibilities to calibrate and validate the AVHRR-derived ice thickness distributions. Prospective sources of suitable data include those from moored ULS sensors within the WCRP AnSITP programme. These datasets, which are from the Weddell Sea and East Antarctica, date back to 1990 (a data listing is given on the AnSITP web site at http://www.awi-bremerhaven.de/Research/IntCoop/Oce/ansitp.html). Transects of moored ULS arrays are also planned for the near future. Future validation efforts will also focus on data from dedicated field experiments, and will use extensive climatological data from the ASPeCt compilation.

c) *Improvements in the model's response to sub-pixel scale features.*

Although the spatial resolution of the procedure presented in this study is finer than most numerical models, it cannot differentiate features smaller than approximately 1 km. The sub-pixel resolution tests presented in Section 4.5 provide some indication of the response of the model when more than one feature (i.e. cloud, snow-free ice, snow-covered ice and open water) is present within a pixel.

The scenarios presented were, however, simplified and are probably different from the complex reality encountered in areas such as the marginal ice zone and polynyas. Digital aerial photography provides a suitable source of *in situ* data to assist in the development of a more complete view of this issue. Although it is not possible to obtain sea ice thickness directly from this technique, it provides important information on the distribution of thin ice and open-water areas. With a few improvements in the sampling method and the co-location of the satellite images and the photographs (discussed in Section 5.3.1), it will be possible to better calibrate the model outputs.

d) *Improvements in the parameterisation of the near-surface air temperature.*

The sensitivity tests presented in Section 4.4 demonstrated that a correct parameterisation of the air-surface temperature difference is essential for the successful application of the sea ice model. In this study, several techniques for estimating T_{Air} were tested. The chosen method uses a combination of wind direction and T_{Sfc} to obtain T_{Air} (see Section 4.3.2.3). In spite of the improvements achieved with this technique in comparison with the simplistic approach taken by *Yu and Rothrock* [1996], it still requires validation with field measurements. These should include detailed surface and air temperature data at various height levels, under different meteorological conditions and for different ice types.

As mentioned in section 4.3.2.3, TOVS is a possible alternative for an independent source of information on surface temperature and atmospheric temperature profiles, pending further studies to warrant its applicability over ice-covered surfaces. Comparisons between TOVS and *in situ* T_{Air} data may lead to a retrieval algorithm which can be employed in conjunction with this method

e) *Improvements to the cloud-screening algorithm.*

Extensive cloud cover around the coast of Antarctica is a well-reported phenomenon [*King and Turner*, 1997; *Orvig*, 1970; *Schwerdtfeger*, 1984]. The passage of synoptic systems and the persistent near-coastal effect of katabatic winds lead to a very dynamic environment where changes can occur in a matter of hours. Given these conditions, the use of a semi-automated system to screen pixels for cloud contamination is an essential part of the method proposed in this study. The principal issue to be considered in such a system is not the capacity to separate as many cloud-free pixels as possible (although this is a desirable outcome) but rather to ensure low levels of misclassification when screening the pixels to be analysed by the sea ice thickness model. The results presented in Chapter 5 demonstrated that under certain conditions, the ICEMAPPER system fails to provide reliable cloud-free data for the model.

Williams et al. [in press], reported that the performance of the ICEMAPPER deteriorates when it is used with non-summer images and images with solar zenith angles higher than 75°. This fact was confirmed by this study, as evidenced by the large number of open water pixels, especially in the two winter images, mis-classified by the algorithm as "sea ice" and introduced into the ice-thickness calculations. These pixels did not reach the thermodynamic equilibrium and were subsequently discarded, which is consistent with cloud contamination. However, it is not possible to estimate the percentage of these pixels that remained in the system and were erroneously assigned an ice thickness by the model. To overcome this problem, which would also contribute to increase the flexibility of the system, *Williams et al.* [in press] recommend that AVHRR datasets from different times of the year and different regions of the Southern Ocean should be employed to train the system and improve its classification skills. This process is to be conducted in the near-future at the Antarctic CRC using, in the first instance, the same set of spring AVHRR images employed in this study.

Other approaches like temporal analysis (i.e. subtraction of consecutive images to obtain velocity vectors) and spatial coherence methods could potentially be employed to assist the ICEMAPPER in the task of screening polar clouds. However this issue has to be considered carefully as most of these techniques are still the subject of current research [*Darzi*, 1992; *Steffen, et al.*, 1993] and their application has been restricted to case studies.

f) Investigation of dynamic processes.

Dynamic processes such as ridging and rafting can be investigated through this model by analysing temporal changes in the ice-thickness distributions derived from pairs of AVHRR images separated in time and/or by introducing wind and ocean current forcing into the system and tracking its effects. In both cases, it would be necessary to incorporate the equations that define mechanical processes and ice drift [*Gray and Killworth*, 1996; *Hibler*, 1979] as well as sources of atmospheric and oceanic forcing from coupled atmosphere/ocean models. Sea ice motion can also be estimated from the analysis of successive classified images in a method similar to that described by *Emery et al.* [1997].

In the long term, it may be possible to assimilate time-dependent ice motion fields into the thickness computation, in an effort to better account for ice thickening by dynamic processes. Such data would ideally come from coincident Radarsat SAR data products, produced using algorithms operating within the RGPS [*Kwok*, in press]. An alternative source of ice motion data for the period from 1982 to 1997 emanates from the NSIDC's Polar Pathfinder Programme.

g) *Characterisation of the ice/snow thickness relationship for non-winter months.*

The snow thickness is a critical parameter in the model. The presence of snow significantly decreases the heat loss to the atmosphere from the ice surface, and thus the thermodynamic ice growth rate. Furthermore, the snow cover can obscure the relationship between surface temperature and thin ice thickness [*Yu and Rothrock*, 1996]. In this study, an empirical relationship between Z_i and Z_s based on measurements made in the winter of 1995 was employed. Although this is an improvement from the Arctic relationship proposed by *Doronin* [1971], this parameterisation needs to be extended for autumn, spring and summer months.

The technique would also benefit from the assimilation of improved snow thickness data, in an effort to resolve the contribution of snow ice to the large-scale sea ice thickening process, and its spatial and temporal variability. Snow thickness data are available both from climatological datasets, such as the ASPeCt compilation [*Worby and Ackley*, 2000] and data from recent field observations, as summarised in *Massom et al.* [in press-a]. Larger-scale and possibly more suitable data may be available from passive microwave remote sensing techniques (e.g. *Arrigo et al.* [1998] and *Markus and Cavalieri* [1998]), although these new snow-thickness retrieval algorithms themselves require further validation.

h) *Improvements in the ice-surface temperature retrieval algorithm.*

The work of *Key et al.* [1997a] represented a considerable improvement over previous methods of retrieving Antarctic ice surface temperature from satellite thermal infrared data, reducing the error to an acceptable level of 0.3 K. In order to improve this result even further, the angle-dependent coefficients derived for the whole of Antarctica could be replaced by more localised coefficients derived with the aid of *in situ* data (i.e. radiosondes) and radiative transfer models such as LOWTRAN.

i) Improvements to the albedo retrieval algorithm.

The albedo controls the intensity of shortwave radiation that reaches the system, through two terms in Equation 8: the net solar radiation at the surface and the solar radiation that penetrates the snow/ice layer. The reported uncertainty for *Lindsay and Rothrock*'s [1994a] albedo retrieval algorithm is 10%. When translated into the net flux, this uncertainty accounts for $\pm$ 1.8 $W \cdot m^{-2}$, or 16%, of the total σ_H. Since this algorithm was originally designed for the Arctic, there is scope for further adaptation to the sea ice conditions of the Southern Hemisphere. This could be accomplished by comparing the albedo results with *in situ* measurements such as those conducted by *Allison et al.* [1993] and *Brandt et al.* [1999].

j) Synergistic utilisation of other remote sensing data.

The SAR and AVHRR sensors have complementary radiometric and geometric characteristics which can be combined to generate products that are capable of providing geophysical information on the Antarctic pack ice, which otherwise could not be acquired if the sensors were used separately. A good example of this synergistic approach is given by *Glueck and Groves* [1994]. In that study, the authors employed SAR backscatter and AVHRR thermal infrared data combined in a Hue, Lightness and Saturation (HLS) colour model to assist in the identification of open water and thin ice in leads and polynyas. This same approach, or a development of it can be incorporated in the system proposed in this study in order to assist in the resolution of ambiguities between cloud and snow-covered pixels and between icebergs and fast ice.

k) Provision of data for input to, and validation of, numerical models.

Comparisons between numerical models and observational data are essential for the verification of the models' treatment of processes such as melting and thermodynamic growth, ice dynamics, drift and the effect of oceanic and atmospheric circulation. Ice thickness is of particular interest in such comparisons [*Gates, et al.*, 1996]. Studies such as *Worby* [1998] and *Worby and Wu* [1998] presented extensive comparisons between *in situ* data and model outputs of sea ice thickness, concentration, rafting, ice volume and structural composition.

These comparisons demonstrated that most sea ice models are limited in their ability to describe the sea ice thickness distribution. The method proposed in this study has the potential to provide a synoptic, mesoscale view of the pack ice which can be employed by modellers to improve the parameterisation of these thickness distributions.

l) Data assimilation.

The method proposed in the current study is comparable to a *direct insertion* assimilation technique applied to the sea ice thickness model, providing the foundation for future studies in this area for the Southern Ocean. Other assimilation strategies are available to improve the effectiveness of the combination of AVHRR data and modelling techniques. Despite being focused on the Northern Hemisphere sea ice cover, the RGPS technique is a successful example of the operational data assimilation using, satellite imagery (in this case from Radarsat) in combination with well-documented algorithms.

6.4 Future Remote Sensing Technology

Although *in situ* measurements may never be replaced by remote sensing, the benefits of the unique, synoptic view of the Earth's surface provided by satellite technology is becoming increasingly important. This is evidenced by the growing number of missions that now concentrate on the generation of higher-level products destined to validate models and process studies [*Massom*, 1995; *Yu*, 1996]. The commitment to the maintenance of long-term datasets such as the AVHRR and passive microwave is essential for the detection of possible global trends [*Massom*, 1995]. It is envisaged that new technology will make a significant contribution to the problem of estimating sea ice thickness from space, as will the adaptation of existing technology.

A number of promising innovative satellite remote sensing techniques and sensors will potentially yield large-scale sea ice thickness data in the near future. For example, a method has recently been proposed to estimate spatially-averaged sea ice thickness using spaceborne altimetry [*Peacock, et al.*, 1998]. These estimates may become available on a routine basis from CryoSat, a satellite which has been approved for launch by the European Space Agency (ESA) in 2003. The goals of this dedicated mission are to measure large-scale sea ice thickness variability to within

the limit established by SAR and interferometric techniques in synergy with radar altimetry [*Wingham*, 1999].

With its ability to penetrate cloud and polar darkness, SAR also has the potential to make a significant contribution to the measurement of Antarctic sea ice thickness in the near future. Radarsat's RGPS system currently outputs estimates of ice age and thickness from repeat observations of Lagrangian cells in sequential SAR imagery, but for the Arctic Ocean basin only [*Kwok and Holt*, 2000]. The RGPS algorithm is unlikely to produce accurate results in the Antarctic sea ice zone without considerable development, due to the complex variability in the physical properties of Antarctic sea ice and its snow cover [*Massom, et al.*, in press-a].

At the moment, the SAR classification of Antarctic sea ice types as a proxy for ice thickness is limited by the lack of an Antarctic sea ice backscatter signature database equivalent to that in the Arctic [*Drinkwater*, 1998; *Drinkwater, et al.*, 1995]. This also applies to the forthcoming wide-swath SAR sensors onboard ESA's Envisat and the Japanese Advanced Land Observing Satellite (ALOS), to be launched in August 2002. However, the Phased Array type L-band Synthetic Aperture Radar (PALSAR) onboard ALOS and the Advanced SAR (ASAR) onboard Envisat will allow data collection at a number of different polarization combinations (i.e. HH or VV, and HH+HV or VV+VH). This may aid the distinction of different surface types, which is a difficult problem using single-frequency data [*Drinkwater, et al.*, 1992].

Another potentially useful new technology is ESA's Soil Moisture and Ocean Salinity Mission (SMOS) satellite, due for launch in 2005 [*Kerr, et al.*, 2000]. This satellite will carry, for the first time in space, an L-band (1.4 GHz) passive-microwave radiometer which has the potential to measure sea ice thickness. Theory indicates that it may be possible to determine the thickness of a slab of sea ice when it approximates the wavelength of the radiometer i.e. 21.4 cm for the 1.4 GHz instrument [*Comiso*, 1996]. As a result of the complexity of Antarctic sea ice, the monotonic increase in emissivity with thickness, as predicted by theory, may not necessarily always hold true as it depends on complex interactions of factors other than ice thickness. The potential capability of low-frequency radiometry as a tool to remotely measure Antarctic sea ice thickness was, however, demonstrated using a UHF radiometer (611 MHz) in the Weddell Sea onboard the German icebreaker *RV Polarstern*. These ship-borne observations indicated that emissivity is a function

of ice thickness up to a thickness of about 0.8 m, at which the emissivity saturates [*Menashi, et al.*, 1993]. Compared to the MODIS and AVHRR, however, the pixel size of SMOS data will be very poor, at approximately 50 x 50 km, and considerable uncertainties in accuracy may remain due to the complexity of the combined sea ice-snow substrate as a microwave target.

In all cases, there is great potential in the synergistic approach of combining satellite data with different attributes, such as SAR and AVHRR (see Section 6.3), and in the merging of satellite data with a modelling approach. However, a key to the usefulness of both these new and existing sensors as tools for measuring and monitoring important sea ice properties is their validation under the range of conditions encountered in the Southern Ocean. Compared to the Arctic, virtually no validation has been carried out of remotely-sensed geophysical data products collected from the Antarctic sea ice zone. Dedicated validation field experiments planned for the next few years should address this issue [*Massom*, 2000, pers. comm.].

6.5 Summary

In summary, this study presents a technique which can provide large-scale estimates of the thickness distribution of East Antarctic sea ice for a number of applications:

a) Creation of a baseline dataset or climatology, against which to gauge possible future large-scale changes related to global climate variation;

b) Provision of input into sea ice models and GCMs, as well as independent data for their validation;

c) Testing or validation of numerical models or new concepts about the rheology of Antarctic sea ice and;

d) Improvement of navigation and logistic operations in the Southern Ocean through the generation of sea ice thickness maps on an operational basis.

Ultimately, modelling is a key tool to enhance our understanding of the role played by sea ice in the global climate system, its complex feedback mechanisms, and the system's possible response to climate change. However, this can only be achieved if accurate independent large-scale Antarctic sea ice thickness data are available for input and validation.

The data produced through the application of the technique described in this study may not attain the absolute accuracy required to detect a thinning of the Antarctic sea ice cover. In this respect, the continuing operation and extension of the existing moored ULS arrays (see Section 2.2.2) is of great importance, as is the planned launch of a long-range autonomous unmanned mini-submarine (AutoSub) equipped with ULS devices [*NERC*, 2001]. Furthermore, it is hoped that civilian-run non-nuclear submarine programmes will in the future address the issue of collecting Antarctic sea ice thickness data along repeat transects in a manner similar to the Arctic [*Massom*, 2000, pers. comm.]. Constituting one-dimensional transects of sea ice draft (or, equivalently, thickness), these data are suitable for building up a climatology of mean sea ice thickness over extended periods of time, or for computing the volume transport of ice across a given region. However, such techniques do not produce a spatial picture of the sea ice thickness distribution over large areas. This is where the technique presented in this study has the potential make a very significant contribution.

This study has helped to demonstrate that, for Antarctic sea ice, many benefits can be derived from the integration of *in situ* and remote sensing techniques. While the meso- and macro-scale views of the pack ice are provided by satellite data at low cost and for relatively long periods, a more detailed view of the dynamic and thermodynamic processes is provided by field observations. While the combination of such distinct methods is a challenging task, the ultimate gain, a better understanding of the role played by the sea ice in the Southern Hemisphere's ocean/atmosphere system, is certainly worth the effort.

Bibliography

The journal abbreviations employed in the following list of references are based on the dataset published by the California Institute of Technology's Library System. This dataset was compiled originally by the Institute for Scientific Information® and is available for consultation in the following World Wide Web address: http://library.caltech.edu/admin/abbreviations/.

Abels, G., Measurement of the snow density at Ekaterinburg during the winter of 1890-1891, *Akad. Nauk. Mem. (Memorandum of the Russian Academy of Sciences)*, *69*, 1-24, 1892.

Ackley, S.F., Mass balance aspects of the Weddell Sea pack ice, *J. Glaciol.*, *24* (90), 391-406, 1979.

Ackley, S.F., A review of sea-ice weather relationships in the Southern Ocean, in *Sea Level, Ice, and Climatic Change*, edited by I. Allison, 127-159, IAHS Press, 1981.

Ackley, S.F., P. Wadhams and M. Lange, Antarctic ice thickness distributions obtained from aerial photography, in *Report of the Sea Ice Thickness Workshop*, edited by A.S. Thorndike, C.L. Parkinson and D.A. Rothrock, B16-B18, NASA, New Carrolton, Maryland, 1992.

Adolphs, U., Roughness variability of sea ice and snow cover thickness profiles in the Ross, Amundsen, and Bellingshausen Seas, *J. Geophys. Res.*, *104* (C6), 13577-13591, 1999.

Allison, I., The East Antarctic sea ice zone: Ice characteristics and drift, *GeoJournal*, *18* (1), 103-115, 1989.

Allison, I., Physical processes determining the Antarctic sea ice environment, *Aust. J. Phys.*, *50*, 759-771, 1997.

Allison, I., R.G. Barry and B.E. Goodison, Climate and Cryosphere (CLIC) Project. Science and Coordination Plan, World Climate Research Programme, Geneva, 2000.

Allison, I., R.E. Brandt and S.G. Warren, East Antarctic sea ice: albedo, thickness distribution, and snow cover, *J. Geophys. Res.*, *98* (C7), 12417-12429, 1993.

Allison, I. and R.E. Moritz, Sea ice in the global climate system: Requirements for an ocean observing system, *Ocean Observing System Development Panel Report* 7, 28 pp., Texas A&M University, College Station, Texas, 1995.

Allison, I., C.M. Tivendale, G.J. Akerman, J.M. Tann and R.H. Wills, Seasonal variations in the surface energy exchanges over Antarctic sea ice and coastal waters, *Ann. Glaciol.*, *3*, 12-16, 1982.

Allison, I. and A.P. Worby, Seasonal changes of sea-ice characteristics off East Antarctica, *Ann. Glaciol.*, *20*, 195-202, 1994.

Anderson, D.L., Growth rate of sea ice, *J. Glaciol.*, *3*, 1170-1172, 1961.

Andreas, E.L., A theory for the scalar roughness and the scalar transfer coefficients over snow and sea ice, *Bound.-Lay. Meteorol.*, *38*, 159-184, 1987.

Andreas, E.L., The atmospheric boundary layer over polar marine surfaces, *CRREL Monograph* 96-2, 38 pp., Hanover, New Hampshire, 1996.

Andreas, E.L. and S.F. Ackley, On the differences in ablation seasons of Arctic and Antarctic sea ice, *J. Atmos. Sci.*, *39* (3), 440-447, 1982.

Andreas, E.L. and K.J. Claffey, Air-ice drag coefficients in the western Weddell Sea. 1. Values deduced from profile measurements, *J. Geophys. Res.*, *100* (C3), 4821-4831, 1995.

Andreas, E.L., M.A. Lange, S.F. Ackley and P. Wadhams, Roughness of Weddell sea ice and estimates of the air-ice drag coefficient, *J. Geophys. Res.*, *98* (C7), 12439-12452, 1993.

Andreas, E.L. and A.P. Makshtas, Energy exchange over Antarctic sea ice in the spring, *J. Geophys. Res.*, *90*, 7119-7212, 1985.

AntCRC, International Programme for Antarctic Buoys [WWW site], AntCRC, Available from the Internet at: <http://www.antcrc.utas.edu.au/antcrc/special/buoys/buoys.html>, 1998.

Arrigo, K., D.L. Worthen, P. Dixon and M.P. Lizotte, Primary productivity of near surface communities within Antarctic pack ice, in *Antarctic Sea Ice Biological Processes, Interactions, and Variability*, edited by M.P. Lizotte and K.R. Arrigo, 23-43, AGU, Washington, DC, 1998.

Ball, F.K., Short communications: sea surface temperatures, *Aust. J. Phys.*, *7*, 649-652, 1954.

Barber, D.G. and E.F. LeDrew, Multivariate analysis of texture statistics for sea ice discrimination, in *International Geoscience and Remote Sensing Symposium (IGARSS'89)*, Vancouver, IGARSS, pp. 759-762, 1989.

Barnes, H.T., *Ice Engineering*, 364 pp., Renoulf, Montreal, 1928.

Barron, E.J., Global change researchers assess projections of climate change, *EOS Trans. AGU*, *76* (18), 185, 189-190, 1995.

Barton, I.J., Satellite-derived sea surface temperatures - Current status, *J. Geophys. Res.*, *100* (C5), 8777-8790, 1995.

Barton, I.J. and T. Takashima, An AVHRR investigation of surface emissivity near Lake Eyre, Australia, *Remote Sens. Environ.*, *20*, 153-163, 1986.

Barton, I.J., A.M. Zavody, D.M. O'Brien, D.R. Cutten, R.W. Saunders and D.T. Llewellyn-Jones, Theoretical algorithms for satellite-derived sea surface temperatures, *J. Geophys. Res.*, *94* (D3), 3365-3375, 1989.

Bevilaqua, R.M., P.M. Caplan and D.J.R. Nordemann, Trocas de massas atmosféricas entre latitudes altas e médias no modelo global NMC, in *II Conferência Latino-americana em Ciências Espaciais e Atmosféricas na Antártica*, Serra Negra, Brasil, edited by R.M. Medrano-B. and E.B. Pereira, Transtec Editorial Ltda, pp. 131-140, 1994.

Bilello, M., Formation, growth and decay of sea ice in the Canadian Arctic Archipelago, *Arctic*, *14*, 12-25, 1961.

Bilello, M., Method for predicting river and lake ice formation, *J. Appl. Meteorol.*, *3*, 38-44, 1964.

Bintanja, R. and J. Oerlemans, The influence of the albedo-temperature feed-back on climate sensitivity, *Ann. Glaciol.*, *21*, 353-360, 1995.

Bourke, W., T. Hart , R. Seaman, L. Rikus, P. Steinle, M. Naughton, P. Mullenmeister and G. Emberg, Operational global assimilation and prediction in the Australian Bureau of Meteorology, *BMRC Research Report* 27, pp. 54-72, Bureau of Meteorology, Melbourne, 1991.

Brandt, R.E., C.S. Rossler and S.G. Warren, Spectral albedo, absorptance, and transmittance of Antarctic sea ice, in *5th Conference on Polar Meteorology and Oceanography*, Boston, Amer. Meteorol. Soc., pp. 456-459, 1999.

Bromwich, D.H., Estimates of Antarctic precipitation, *Nature*, *343* (6259), 627-629, 1990.

Budd, W.F., The role of Antarctica in southern hemisphere weather and climate, *Aust. Meteorol. Mag.*, *30*, 265-272, 1982.

Budd, W.F., The Southern Hemisphere circulation of atmosphere, ocean and sea ice, *Working Group on Sea Ice and Climate Report* WCP-128, pp. 47-53, WMO, Geneva, 1987.

Budd, W.F., Antarctica and global change, *Climatic Change*, *18*, 217-299, 1991.

Budyko, M.I., Polar ice and climate, in *Proceedings of the Symposium on the Arctic Heat Budget and Atmospheric Circulation*, Santa Monica, California, edited by J.O. Fletcher, Rand Corporation, pp. 3-22, 1966.

Bush, G., Measuring Antarctic Sea Ice Draft With Upward Looking Sonar, PhD thesis, 242 pp., Curtin University of Technology, Perth, Australia, 1997.

Buynitskiy, V.K., Structure, principal properties, and strength of Antarctic sea ice, *Sov. Antarct. Exped. Inform. Bull.*, *65*, 504-510, 1967.

Campbell, W.J., P. Gloersen, W.J. Webster, T.T. Wilheit and R.O. Ramseier, Beaufort Sea ice zones as delineated by microwave imagery, *J. Geophys. Res.*, *81* (6), 1103-1110, 1976.

Carrol, J.J., Long-term means and short-term variability of the surface energy balance components at the South Pole, *J. Geophys. Res.*, *87*, 4277-4286, 1982.

Carsey, F.D., R.G. Barry, D.A. Rothrock and W.F. Weeks, Status and future directions for sea ice remote sensing, in *Microwave Remote Sensing of Sea Ice*, edited by F.D. Carsey, 443-446, AGU, Washington, DC, 1992.

Cavalieri, D.J., A microwave technique for mapping thin sea ice, *J. Geophys. Res.*, *99* (C6), 12561-12572, 1994.

Cavalieri, D.J., P. Gloersen and W.J. Campbell, Determination of sea ice parameters with the NIMBUS 7 SMMR, *J. Geophys. Res.*, *89* (D4), 5355-5369, 1984.

Cavalieri, D.J., P. Gloersen, C.L. Parkinson, J.C. Comiso and J.H. Zwally, Observed hemispheric asymmetry in global sea ice changes, *Science*, *278*, 1104-1106, 1997.

Cavalieri, D.J. and S. Martin, A passive microwave study of polynyas along the Antarctic Wilkes Land coast, in *Oceanography of the Antarctic Continental Shelf*, edited by S.S. Jacobs, 227-252, AGU, Washington, DC, 1985.

CCCO, The Ocean Observing System Development Panel (OOSDP) [WWW site], Committee on Climatic Changes in the Ocean, Available from the Internet at: <http://www-ocean.tamu.edu/OOSDP/oosdp.html>, 1996.

Che, N. and J.C. Price, Survey of radiometric calibration results and methods for visible and near infrared channels of NOAA-7, -9 and -11 AVHRRs, *Remote Sens. Environ.*, 19-27, 1992.

Chu, P.C., Effects of ice-albedo feedback on global climate change, in *Proc. of Workshop on Polar Processes in Global Climate*, Cancun, Mexico, Am. Met. Soc., pp. 24-27, 1996.

Cihlar, J. and P.M. Teillet, Forward piecewise calibration model for quasi-real time processing of AVHRR data, *Can. J. Rem. Sens.*, *21* (1), 22-27, 1995.

Colwell, N., *Manual of Remote Sensing*, 2440 pp., American Society of Photogrammetry, Falls Church, Virginia, 1983.

Comiso, J.C., Sea ice effective microwave emissivities from satellite passive microwave and infrared observations, *J. Geophys. Res.*, *88*, 7686-7704, 1983.

Comiso, J.C., Surface temperatures in the polar regions using Nimbus-7 THIR, *J. Geophys. Res.*, *99* (C3), 5181-5200, 1994.

Comiso, J.C., Applications of a low-frequency microwave sensor for sea ice research, in *Remote Sensing of Sea Surface Salinity, Ice Cover and Soil Moisture, Report of a Workshop During the American Geophysical Union Western Pacific Geophysical Meeting*, edited by D. Burrage, G. Lagerloef and R. Massom, 8-10, Australian Inst. of Marine Science, Brisbane, Australia, 1996.

Comiso, J.C., Variability and trends in Antarctic surface temperatures from *in situ* and satellite infrared measurements, *J. Climate*, *13* (10), 1674-1696, 2000.

Comiso, J.C., T.C. Grenfell, M.A. Lange, A.W. Lohanick, R.K. Moore and P. Wadhams, Microwave remote sensing of the Southern Ocean ice cover, in *Microwave Remote Sensing of Sea Ice*, edited by F.D. Carsey, 243-259, AGU, Washington, DC, 1992.

Coppin, P.A., E.F. Bradley, I.J. Barton and J.S. Godfrey, Simultaneous observations of sea surface temperature in the Western Equatorial Pacific Ocean by bulk, radiative and satellite methods., *J. Geophys. Res.*, *96* (Supplement), 3401-3409, 1991.

Cox, G.F.N. and W.F. Weeks, Salinity variations in sea ice, *J. Glaciol.*, *13* (67), 109-120, 1974.

Cracknell, A.P., *The Advanced Very High Resolution Radiometer*, 534 pp., Taylor & Francys, London, 1997.

Cracknell, A.P. and L. Hayes, *Introduction to Remote Sensing*, 621 pp., Taylor & Francis, London, 1991.

Darzi, M., Cloud screening for polar orbiting visible and infrared (IR) satellite sensors, *NASA Technical Memorandum* 104566, Volume 7, 7 pp., NASA, Greenbelt, Maryland, 1992.

Davey, J., Estimation of the Turbulent Heat Fluxes in the Sea Ice Zone From Continuous Ship-Based Measurements, Honours thesis, 94 pp., University of Tasmania, Hobart, Australia, 1997.

De Abreu, R.A., J.R. Key, J.A. Maslanik, M.C. Serreze and E.F. LeDrew, Comparison of *in situ* and AVHRR-derived broadband albedo over Arctic Sea ice, *Arctic*, *47* (3), 288-297, 1994.

Doronin, Y.P., Thermal interaction of the atmosphere and the hydrosphere in the Arctic, *Israel Program for Sci. and Trans.*, 85 pp., Jerusalem, 1971.

Drinkwater, M.R., Applications of SAR measurements in ocean-ice-atmosphere interaction studies, in *Oceanographic Applications of Remote Sensing*, edited by M. Ikeda and F. Dobson, 391-406, CRC Press, Boca Raton, Florida, 1995.

Drinkwater, M.R., Satellite microwave radar observations of Antarctic sea ice, in *Analysis of SAR Data of the Polar Oceans*, edited by C. Tsatsoulis and R. Kwok, 145-187, Springer-Verlag, Berlin, 1998.

Drinkwater, M.R., R. Hosseinmostafa and S.P. Gogineni, C-band backscatter measurements of winter sea ice in the Weddell Sea, Antarctica, *Int. J. Remote. Sens.*, *16* (17), 3365-3389, 1995.

Drinkwater, M.R., R. Kwok, E. Rignot, H. Israelsson, R.G. Onstott and D.P. Winebrener, Potential Applications of Polarimetry to the Classification of Sea Ice, in *Microwave Remote Sensing of Sea Ice*, edited by F.D. Carsey, 430-462, AGU, Washington, DC, 1992.

Drinkwater, M.R. and X. Liu, Seasonal to interannual variability in Antarctic sea-ice surface melt, *IEEE T. Geosci. Remote*, *38* (4), 1827-1842, 2000.

Drinkwater, M.R. and V.I. Lytle, ERS-1 SAR and field-observed austral fall freeze-up in the Weddell Sea, Antarctica, *J. Geophys. Res.*, *102* (C6), 12593-12608, 1997.

Ebert, E.E., Pattern recognition analysis of polar clouds during summer and winter, *Int. J. Remote. Sens.*, *13* (1), 97-109, 1992.

Ebert, E.E. and J.A. Curry, An intermediate one-dimensional thermodynamic sea ice model for investigating ice-atmosphere interactions, *J. Geophys. Res.*, *98* (C6), 10085-10109, 1993.

Eicken, H., The role of sea ice in structuring Antarctic ecosystems, *Polar Biol.*, *12*, 3-13, 1992.

Eicken, H., H. Fischer and P. Lemke, Effects of the snow cover on Antarctic sea ice and potential modulation of its response to climate change, *Ann. Glaciol.*, *21*, 369-376, 1995.

Emery, W.J., C.W. Fowler and J.A. Maslanik, Satellite-derived maps of Arctic and Antarctic sea ice motion: 1988-1994, *Geophys. Res. Lett.*, *24*, 897-900, 1997.

Eppler, D.T., D. Farmer, A.W. Lohanick, M.R. Anderson, D.J. Cavalieri, J.C. Comiso, P. Gloersen, C. Garrity, T.C. Grenfell, M. Hallikainen, J.A. Maslanik, C. Mätzler, R.A. Melloh, I. Rubinstein and C. Swift, Passive microwave signatures of sea ice, in *Microwave Remote Sensing of Sea Ice*, edited by F.D. Carsey, 47-71, AGU, Washington, DC, 1992.

Eppler, D.T. and L.D. Farmer, Sea ice thickness distribution derived from archived aerial photographs of the Arctic sea ice pack, in *Report of the Sea Ice Thickness Workshop*, edited by A.S. Thorndike, C.L. Parkinson and D.A. Rothrock, B10-B15, NASA, New Carrolton, Maryland, 1992.

Fetterer, F.M. and J.D. Hawkins, Data set of Arctic AVHRR imagery for the study of leads, *Ann. Glaciol.*, *17*, 398-404, 1993.

Fisher, R. and V.I. Lytle, Atmospheric drag coefficients of Weddell Sea ice computed from roughness profiles, *Ann. Glaciol.*, *27*, 455-460, 1998.

Fletcher, J.O., *The Heat Budget of the Arctic Basin and Its Relation to Climate*, 179 pp., Rand Corporation, Santa Monica, California, 1965.

Fletcher, J.O., Ice extent on the Southern Ocean and its relation to world climate, RM-5793-NSF, 108 pp., Rand Corporation, Santa Monica, California, 1969.

Foster, T.D., Abyssal water mass formation off the eastern Wilkes Land coast of Antarctica, *Deep-Sea Res., Part I, 42* (4), 501-522, 1995.

Francis, J.A., Improvements to TOVS retrievals over sea ice and applications to estimating Arctic energy fluxes, *J. Geophys. Res.*, *99*, 10395-10408, 1994.

Gallegos, S.C., J.D. Hawkins and C.F. Cheng, Cloud screening in AVHRR digital data over Arctic regions, *Ann. Glaciol.*, *17*, 386-390, 1993.

Gates, W.L., A. Henderson-Sellers, G.J. Boer, C.K. Folland, A. Kioth, B.J. MacAvaney, F. Semazzi, N. Smith, A.J. Weaver and Q.C. Zeng, Climate models: Evaluation, in *Climate Change 1995 - The Science of Climate Change*, edited by J.T. Houghton, L.G. Meira Filho, B.A. Callander, N. Harris, A. Kettemberg and K. Maskell, 229-284, Cambridge University Press, Cambridge, 1996.

Gesell, G., An algorithm for snow and ice detection using AVHRR data: An extension to the APOLO software package, *Int. J. Remote. Sens.*, *10* (4-5), 897-905, 1989.

Gloersen, P., W.J. Campbell, D.J. Cavalieri, J.C. Comiso, C.L. Parkinson and J.H. Zwally, Arctic and Antarctic Sea Ice, 1978-1987: Satellite Passive-Microwave Observations and Analysis, *Special Publication* 511, 290 pp., NASA, Washington, DC, 1992.

Gloersen, P. and A. Mernicky, Oscillatory behaviour in Antarctic sea ice concentrations, in *Antarctic Sea Ice: Physical Processes, Interactions and Variability*, edited by M.O. Jeffries, 161-171, AGU, Washington, DC, 1998.

Glueck, M. and J.E. Groves, Use of the HLS color model as a technique for combining AVHRR and ERS-1 imagery to evaluate near shore ice processes in the St. Lawrence Island polynya, in *3rd Circumpolar Symposium on Remote Sensing of Arctic Environments*, Fairbanks, Alaska, edited by M.O. Jeffries and D.G. Kenneson, Univ. of Alaska, Fairbanks, pp. 25, 1994.

Gordon, A.L., Seasonality of Southern Ocean sea ice, *J. Geophys. Res.*, *86* (C5), 4193-4197, 1981.

Gordon, A.L., The Southern Ocean and global climate, *Oceanus*, *31* (2), 39-46, 1988.

Gordon, H.B. and S.B. O'Farrell, Transient climate change in the CSIRO coupled model with dynamic sea ice, *Mon. Weather Rev.*, *125*, 875-907, 1997.

Gow, A.J. and W.B. Tucker III., Sea ice in the polar regions, in *Polar Oceanography: Part A Physical Science*, edited by W.O. Smith, 47-122, Academic Press, New York, 1990.

Gray, J.M.N.T. and P.D. Killworth, Sea ice ridging schemes, *J. Phys. Oceanogr.*, *26*, 2420-2428, 1996.

Grenfell, T.C., The effects of ice thickness on the exchange of solar radiation over the polar oceans, *J. Glaciol.*, *22* (87), 305-320, 1979.

Grenfell, T.C., A theoretical model of the optical properties of sea ice in the visible and near infrared, *J. Geophys. Res.*, *88*, 9723-9735, 1983.

Grenfell, T.C., D.J. Cavalieri, J.C. Comiso, M.R. Drinkwater, R.G. Onstott, I. Rubinstein, K. Steffen and D.P. Winebrener, Considerations for microwave remote sensing of thin sea ice, in *Microwave Remote Sensing of Sea Ice*, edited by F.D. Carsey, 291-301, AGU, Washington, DC, 1992.

Grenfell, T.C. and G.A. Maykut, The optical properties of ice and snow in the Arctic Basin, *J. Glaciol.*, *18* (80), 445-463, 1977.

Grenfell, T.C. and D.K. Perovich, Spectral albedos of sea ice and incident solar irradiance in the southern Beaufort Sea, *J. Geophys. Res.*, *89*, 3573-3580, 1984.

Groves, J.E. and W.J. Stringer, The use of AVHRR thermal infrared imagery to determine sea ice thickness within the Chukchi Polynya, *Arctic*, *44* (Supp. 1), 130-139, 1991.

Grumbine, R.W., The thermodynamic predictability of sea ice, *J. Glaciol.*, *40* (135), 277-282, 1994.

Guest, P.S., Surface longwave radiation conditions in the Eastern Weddell Sea during winter, *J. Geophys. Res.*, *103*, 30761-30771, 1998.

Guest, P.S. and K.L. Davidson, Factors affecting variations of snow surface temperature and air temperature over sea ice in winter, in *The Polar Oceans and their Role in the Shaping of the Global Environment*, edited by O.M. Johannessen, R.D. Muench and J.E. Overland, 435-442, AGU, Solstrand, Norway, 1994.

Gurney, A., *Below the Convergence - Voyages Towards Antarctica 1699 - 1839*, 315 pp., Pimlico, London, 1998.

Gurney, R.J., J.L. Foster and C.L. Parkinson, *Atlas of Satellite Observations Related to Global Change*, 470 pp., Cambridge University Press, Cambridge, 1993.

Haas, C., D.N. Thomas, M. Steffens and J. Bareiss, Physical and biological investigations of sea-ice, in *The Expedition ANTARKTIS-XIV of RV "Polarstern" in 1997, Report of Leg ANT-XIV/3*, edited by W. Jokat and H. Oerter, 18-30, *Rep. on Pol. Res.*, 267/98, 1998.

Haefliger, M., K. Steffen and C. Fowler, AVHRR surface temperature and narrow-band albedo comparison with ground measurements for the Greenland Ice Sheet, *Ann. Glaciol.*, *17*, 49-54, 1993.

Häkkinen, S., Models and their applications to polar oceanography, in *Polar oceanography, Part A: Physical Science*, edited by W.O. Smith Jnr., 335-384, Academic Press, San Diego, California, 1990.

Hallikainen, M. and D.P. Winebrenner, The physical basis for sea ice remote sensing, in *Microwave Remote Sensing of Sea Ice*, edited by F.D. Carsey, 29-46, AGU, Washington, DC, 1992.

Haverkamp, D., C. Tsatsoulis and G. Sivaprasad, The combination of algorithmic and heuristic methods for the classification of sea ice imagery, *Remote. Sens. Rev.*, *9*, 135-159, 1994.

Heil, P. and I. Allison, The pattern and variability of Antarctic sea-ice drift in the Indian Ocean and Western Pacific sectors, *J. Geophys. Res.*, *104* (C7), 15789-15802, 1999.

Heil, P., I. Allison and V.I. Lytle, Seasonal and interannual variations of the oceanic heat flux under a landfast Antarctic sea ice cover, *J. Geophys. Res.*, *101* (C11), 25741-25752, 1996.

Hepplewhite, C.L., Remote observations of the sea surface and atmosphere: The oceanic skin effect, *Int. J. Remote. Sens.*, *10* (4 and 5), 801-810, 1989.

Hibler, W.D., III, A dynamic thermodynamic sea ice model, *J. Phys. Oceanogr.*, *9*, 815-846, 1979.

Hibler, W.D., III, Modelling a variable thickness sea ice cover, *Mon. Weather Rev.*, *108* (12), 1943-1973, 1980.

Hibler, W.D., III and J. Zhang, On the effect of sea-ice dynamics on oceanic thermohaline circulation, *Ann. Glaciol.*, *21*, 361-368, 1995.

Hill, K., Antarctic CRC AVHRR Processing System, *Research Report* 16, 216 pp., Antarctic CRC, Hobart, Australia, 2000.

Holt, B., D.A. Rothrock and R. Kwok, Determination of sea ice motion from satellite images, in *Microwave Remote Sensing of Sea Ice*, edited by F.D. Carsey, 343-354, AGU, Washington, DC, 1992.

Horner, R., S.F. Ackley, G.S. Dieckman, B. Gulliksen, T. Hoshiai, L. Legendre, I.A. Melnikov, W.S. Reeburgh and W. Spindler, Ecology of sea ice biota. 1. Habitat and terminology, *Polar Biol.*, *12*, 3-13, 1992.

Hunt, B.G., H.B. Gordon and H.L. Davies, The impact of the greenhouse effect on sea-ice characteristics and snow accumulation in the polar regions, *Int. J. Climatol.*, *15* (1), 3-23, 1995.

IPAB, International Programme of Antarctic Buoys - Activities [WWW site], IPAB, Available from the Internet at: <http://www.antcrc.utas.edu.au/antcrc/special/buoys/buoys.html>, 1998.

Jacobs, S.S. and J.C. Comiso, A recent sea-ice retreat west of the Antarctic Peninsula, *Geophys. Res. Lett.*, *20* (12), 1171-1174, 1993.

Jacobs, S.S. and J.C. Comiso, A climate anomaly in the Amundsen and Bellingshausen Seas, *J. Climate*, *10* (4), 697-709, 1997.

Jeffries, M.O. and U. Adolphs, Early winter snow and ice thickness distribution, ice structure and development of the western Ross Sea pack ice between the ice edge and the Ross Ice Shelf, *Antarct. Sci.*, *9* (2), 188-200, 1997.

Jeffries, M.O., B. Hurst-Cushing, H.R. Krouse and T. Maksym, The role of snow in the thickening and mass budget of first-year floes in the eastern Pacific sector of the Antarctic pack ice, *UAG Report* 327, Geophysical Institute, University of Alaska, Fairbanks, Alaska, 1998a.

Jeffries, M.O., S. Li, R.A. Jaña, H.R. Krouse and B. Hurst-Cushing, Late winter first-year ice floe thickness variability, seawater flooding and snow ice formation in the Amundsen and Ross Seas, in *Antarctic Sea Ice: Physical Processes, Interactions and Variability*, edited by M.O. Jeffries, 69-88, AGU, Washington, DC, 1998b.

Jeffries, M.O., A.P. Worby, K. Morris and W.F. Weeks, Seasonal variations in the properties, and structural and isotopic composition of sea ice and snow cover in the Bellingshausen and Amundsen Seas, Antarctica, *J. Glaciol.*, *43* (143), 138-151, 1997.

Jordan, R., A one-dimensional temperature model for a snow cover: technical documentation for SNTHERM.89, *CRREL Report* 91, 16 pp., U.S. Army Corps of Eng., Hanover, New Hampshire, 1991.

Kaufman, Y.J., The atmospheric effect on remote sensing and its correction, in *Theory and Applications of Optical Remote Sensing*, edited by G. Asrar, 336-412, John Wiley & Sons, New York, 1989.

Kaufman, Y.J. and B.N. Holben, Calibration of the AVHRR visible and near-IR bands by atmospheric scattering, ocean glint and desert reflection, *Int. J. Remote. Sens.*, *14* (1), 21-52, 1993.

Kerr, Y.H., J. Font, P. Waldteufel and M. Berger, The Soil Moisture and Ocean Salinity Mission - SMOS, *ESA Earth Obs. Q.*, *66*, 18-25, 2000.

Kerr, Y.H., J.P. Lagouarde and J. Imbernon, Accurate land surface temperature retrieval from AVHRR with use of an improved split-window algorithm, *Remote Sens. Environ.*, *41*, 197-209, 1992.

Key, J.R., Cloud cover analysis with Arctic Advanced Very High Resolution Radiometer data: Classification with spectral and textural measures, *J. Geophys. Res.*, *95* (D6), 7661-7675, 1990.

Key, J.R., J.B. Collins, C. Fowler and R.S. Stone, High-latitude surface temperature estimates from thermal satellite data, *Remote Sens. Environ.*, *61*, 302-309, 1997a.

Key, J.R. and M. Haefliger, Arctic ice surface temperature retrieval from AVHRR thermal channels, *J. Geophys. Res.*, *97* (D5), 5885-5893, 1992.

Key, J.R., J.A. Maslanik, M.C. Papakyriakou, M.C. Serreze and A.J. Schweiger, On the validation of satellite-derived sea ice surface temperature, *Arctic*, *47* (3), 280-287, 1994.

Key, J.R., A.J. Schweiger and R.S. Stone, Expected uncertainty in satellite-derived estimates of the surface radiation budget at high latitudes, *J. Geophys. Res.*, *102* (C7), 15837-15847, 1997b.

Key, J.R., R.A. Silcox and R.S. Stone, Evaluation of surface radiative flux parameterizations for use in sea ice models, *J. Geophys. Res.*, *101* (C2), 3839-3849, 1996.

Key, J.R., R.S. Stone, J.A. Maslanik and E. Ellefsen, The detectability of sea-ice leads in satellite data as a function of atmospheric conditions and measurements scale, *Ann. Glaciol.*, *17*, 227-232, 1993.

Kidwell, K.B., Polar Orbiter Data User's Guide [WWW site], NOAA, Available from the Internet at: <http://perigee.ncdc.noaa.gov/docs/podug/index.htm>, 1998.

King, J.C. and J. Turner, *Antarctic Meteorology and Climatology*, 409 pp., Cambridge University Press, Cambridge, 1997.

Knap, W.H. and J. Oerlemans, The surface albedo of the Greenland ice sheet: satellite-derived and *in situ* measurements in the Søndre Strømfjord area during the 1991 melt season, *J. Glaciol.*, *42* (141), 364-374, 1996.

Koepke, P., Removal of atmospheric effects from AVHRR albedos, *J. Appl. Meteorol.*, *28*, 1341-1348, 1989.

Kuhn, P.M., L.P. Sterns and R.O. Ramseier, Airborne infrared imagery of Arctic sea ice thickness, *NOAA Technical Report* ERL 331 - APCL 34, Environmental Research Laboratories, Boulder, Colorado, 1975.

Kwok, R., Ice deformation, age and thickness: Summary of RGPS results from November 1996 to May 1997, *Ann. Glaciol.*, *33*, in press.

Kwok, R. and B. Holt, Sea ice thickness from kinematics, in *CEOS'99 SAR Workshop*, Toulouse, France, pp. 1843-1856, 2000.

Kwok, R., E. Rignot, B. Holt and R.G. Onstott, Identification of sea ice types in spaceborne Synthetic Aperture Radar data, *J. Geophys. Res.*, *97* (C2), 2391-2402, 1992.

Kwok, R., A.J. Schweiger, D.A. Rothrock, S. Pang and C. Kottmeier, Sea ice motion from satellite passive microwave imagery assessed with ERS SAR and buoy motion, *J. Geophys. Res.*, *103* (C4), 8191-8214, 1998.

Kwok, R., H.L. Stern, N. LaBelle-Hamer, B. Holt and D.A. Rothrock, Ice thickness derived from high-resolution radar imagery, *EOS Trans. AGU*, *80* (42), 495-497, 1999.

Laine, V. and M. Heikinheimo, Estimation of surface albedo from NOAA/AVHRR data in high latitudes, *Tellus*, *48A* (3), 424-441, 1996.

Lamb, H.H., The climate environment of the Arctic Ocean, in *The Arctic Ocean*, edited by L. Rey, 135-161, John Wiley & Sons, New York, 1982.

Lange, M.A., S.F. Ackley, P. Wadhams, G.S. Dieckman and H. Eicken, Development of sea ice in the Weddell sea, *Ann. Glaciol.*, *12*, 92-96, 1989.

Lange, M.A. and H. Eicken, The sea ice thickness distribution in the north-western Weddell Sea, *J. Geophys. Res.*, *96* (C3), 4821-4837, 1991.

Lange, M.A., P. Schlosser, S.F. Ackley, P. Wadhams and G.S. Dieckmann, ^{18}O concentrations in sea ice of the Weddell Sea, Antarctica, *J. Glaciol.*, *36* (124), 315-323, 1990.

Langhorne, P., V.A. Squire, C. Fox and T.G. Haskell, Break-up of sea ice by ocean waves, *Ann. Glaciol.*, *27*, 438-442, 1998.

Ledley, T.S., Snow on sea ice: Competing effects in shaping climate, *J. Geophys. Res.*, *96* (17), 17,195-17,208, 1991.

Leppäranta, M., The dynamics of sea ice, in *Physics of Ice-Covered Seas*, edited by M. Leppäranta, 305-342, Helsinki University Press, Helsinki, 1998.

Lide, D.R., *CRC Handbook of Chemistry and Physics*, 967 pp., CRC Press, Boca Raton, Florida, 1991.

Liljequist, G.H., Energy exchange of an Antarctic snow field: Short-wave radiation (Maudhein 71° 03' S, 10° 56' W), *Norwegian-British-Swedish Antarctic Expedition, 1949-1952, Scientific Results* Vol. 2, Part 1A, 304 pp., Norsk Polarinstitutt, Oslo, 1956.

Lillesand, T.M. and R.W. Kiefer, *Remote Sensing and Image Interpretation*, 721 pp., John Wiley & Sons, New York, 1987.

Lindsay, R.W., J.A. Francis, P.O.G. Person, D.A. Rothrock and A.J. Schweiger, Surface turbulent fluxes over pack ice inferred from TOVS observations, *Ann. Glaciol.*, *25*, 393-399, 1997.

Lindsay, R.W. and D.A. Rothrock, The calculation of surface temperature and albedo of Arctic sea ice from AVHRR, *Ann. Glaciol.*, *17*, 391-397, 1993.

Lindsay, R.W. and D.A. Rothrock, Arctic sea ice albedo from AVHRR, *J. Climate*, *7*, 1737-1749, 1994a.

Lindsay, R.W. and D.A. Rothrock, Arctic sea ice surface temperature from AVHRR, *J. Climate*, *7*, 174-183, 1994b.

Liu, A.K. and D.J. Cavalieri, On sea ice drift from the wavelet analysis of the Defense Meteorological Satellite Program (DMSP) Special Sensor Microwave Imager (SSM/I) data, *Int. J. Remote. Sens.*, *19* (7), 1415-1423, 1998.

Liu, A.K. and S. Häkkinen, Wave effects on ocean-ice interaction in the marginal ice zone, *J. Geophys. Res.*, *98* (C6), 10025-10036, 1993.

Long, D.G. and M.R. Drinkwater, Cryospheric applications of NSCAT data, *IEEE T. Geosci. Remote*, *37* (3), 1671-1684, 1999.

Lytle, V.I., R.A. Massom, N.L. Bindoff, A.P. Worby and I. Allison, The wintertime heat flux to the underside of East Antarctic pack ice, *J. Geophys. Res.*, in press-a.

Lytle, V.I., A. Worby and R.A. Massom, Sea-ice pressure ridges in East Antarctica, *Ann. Glaciol.*, *27*, 449-454, 1998a.

Lytle, V.I., A.P. Worby, I. Allison, X. Wu, R.A. Massom, M. Paget and A. Roberts, Ice formation in the Mertz Glacier polynya during winter, *Ann. Glaciol.*, *33*, in press-b.

Lytle, V.I., A.P. Worby, R.A. Massom, M. Wall, I. Allison, P. Heil and I. Knott, Winter conditions in the East Antarctic pack ice: A report on the 1995 HIHO HIHO ice drift and deformation experiment, *Research Report* 13, Antarctic CRC, Hobart, Australia, 1998b.

Makshtas, A.P., Thermodynamics of sea ice, in *Physics of Ice-Covered Seas*, edited by M. Leppäranta, 289-304, Helsinki University Press, Helsinki, 1994.

Manabe, S., R.J. Stouffer, M.J. Spelman and K. Bryan, Transient response of a coupled ocean-atmosphere model to gradual changes of atmospheric CO_2. Part I: Annual mean response., *J. Climate*, *4*, 785-818, 1991.

Markus, T. and D.J. Cavalieri, Snow depth distribution over sea ice in the Southern Ocean from satellite passive microwave data, in *Antarctic Sea Ice: Physical Processes, Interactions and Variability*, edited by M.O. Jeffries, 19-39, AGU, Washington, DC, 1998.

Martinson, D.G., Ocean heat and seasonal sea ice thickness in the Southern Ocean, in *Ice in the Climate System*, edited by W.R. Peltier, 597-610, Springer-Verlag, Berlin, 1998.

Maslanik, J., C. Fowler, J. Key, T. Scambos, T. Hutchinson and W. Emery, AVHRR-based Polar Pathfinder products for modeling applications., *Ann. Glaciol.*, *25*, 388-392, 1998.

Maslanik, J.A. and J.R. Key, Comparison and integration of ice-pack temperatures derived from AVHRR and passive microwave imagery, *Ann. Glaciol.*, *17*, 372-378, 1993.

Maslanik, J.A., M.C. Serreze and T. Agnew, On the record reduction in 1998 western Arctic sea-ice cover, *Geophys. Res. Lett.*, *26* (13), 1905-1908, 1999.

Massom, R.A., Observing advection of sea ice in the Weddell Sea using buoy and satellite passive microwave data, *J. Geophys. Res.*, *97* (C10), 15559-15572, 1992.

Massom, R.A., Satellite remote sensing of polar snow and ice: present status and future directions, *Polar Rec.*, *31* (177), 99-114, 1995.

Massom, R.A. and J.C. Comiso, The classification of Arctic Sea ice types and the determination of surface temperature using Advanced Very High Resolution Radiometer data, *J. Geophys. Res.*, *99* (C3), 5201-5217, 1994.

Massom, R.A., J.C. Comiso, A.P. Worby, V.I. Lytle and L. Stock, Regional classes of sea ice cover in the East Antarctic pack observed from satellite and *in situ* data during a winter time period, *Remote Sens. Environ.*, *68* (1), 61-76, 1999.

Massom, R.A., H. Eicken, C. Haas, M.O. Jeffries, M.R. Drinkwater, M. Sturm, A.P. Worby, X. Wu, V.I. Lytle, S. Ushio, K. Morris, P. Reid, S.G. Warren and I. Allison, Snow on Antarctic sea ice, *Rev. Geophys.*, in press-a.

Massom, R.A., P.T. Harris, K.J. Michael and M.J. Potter, The distribution and formative processes of latent-heat polynyas in East Antarctica, *Ann. Glaciol.*, *27*, 420-426, 1998a.

Massom, R.A., K.L. Hill, V.I. Lytle, A.P. Worby, M. Paget and I. Allison, Effects of regional fast-ice and iceberg distributions on the behaviour of the Mertz Glacier Polynya, East Antarctica, *Ann. Glaciol.*, *33*, in press-b.

Massom, R.A., V.I. Lytle, A.P. Worby and I. Allison, Winter snow cover variability on East Antarctic sea ice, *J. Geophys. Res.*, *103* (C11), 24837-24885, 1998b.

Maykut, G.A., Energy exchange over young sea ice in the Central Arctic, *J. Geophys. Res.*, *83*, 3646-3658, 1978.

Maykut, G.A., Large-scale heat exchange and ice production in the central Arctic, *J. Geophys. Res.*, *87* (C10), 7971-7984, 1982.

Maykut, G.A., An introduction to ice in the polar oceans, *Technical Report* 8510, 107 pp., Applied Physics Lab. Univ. of Washington, Seattle, Washington, 1985.

Maykut, G.A., The surface heat and mass balance, in *Geophysics of sea ice*, edited by N. Untersteiner, 395-463, Plenum Press, New York, 1986.

Maykut, G.A. and P.E. Church, Radiation climate of Barrow, Alaska, 1962-1966, *J. Appl. Meteorol.*, *12*, 620-628, 1973.

Maykut, G.A. and D.K. Perovich, On the role of shortwave radiation in the summer decay of sea ice cover, *J. Geophys. Res.*, *92* (C7), 7032-7044, 1987.

Maykut, G.A. and N. Untersteiner, Some results from a time-dependent thermodynamic model of sea ice, *J. Geophys. Res.*, *76*, 1550-1575, 1971.

McMillin, L.M. and D.S. Crosby, Theory and validation of the multiple window sea surface temperature technique, *J. Geophys. Res.*, *89* (C3), 3655-3661, 1984.

Menashi, J.D., K.M. St. Germain, C.T. Swift, J.C. Comiso and A.W. Lohanick, Low-frequency passive microwave observations of sea ice in the Weddell Sea, *J. Geophys. Res.*, *98* (C12), 22569-22577, 1993.

Michael, K.J., C.S. Hungria and R.A. Massom, Radiometric measurements of sea ice surface temperature in East Antarctica, *Ann. Glaciol.*, *27*, 466-470, 1998.

Morales Maqueda, M. and F. Fichefet, A case for including more complete representations of sea ice processes in numerical climate models, in *Proc. of Workshop on Polar Processes in Global Climate*, Cancun, Mexico, Am. Met. Soc., pp. 77-80, 1996.

Morris, K., M.O. Jeffries and S. Li, Sea ice characteristics and seasonal variability of ERS-1 SAR backscatter in the Bellingshausen Sea, in *Antarctic Sea Ice: Physical Processes, Interactions and Variability*, edited by M.O. Jeffries, 213-242, AGU, Washington, DC, 1998.

NASA, Earth Observing System - Terra, the EOS flagship [WWW site], NASA, Available from the Internet at: <http://www.terra.nasa.gov>, 1999.

NERC, AutoSub Science Missions Thematic Programme [WWW site], Natural Environment Research Council, Available from the Internet at: <http://www.soc.soton.ac.uk/PR/Autosub.html>, 2001.

Nicol, S. and I. Allison, The frozen skin of the Southern Ocean, *Am. Sci.*, *85*, 426-439, 1997.

Nunez, M., K.J. Michael, D. Turner, M. Wall and C. Nilsson, A satellite-based climatology of UV-B irradiance for Antarctic coastal regions, *Int. J. Climatol.*, *17* (10), 1029-1054, 1997.

Oke, T.R., *Boundary Layer Climates*, 435 pp., Methuen, New York, 1990.

Ono, N., Specific heat and heat of fusion of sea ice, in *Physics of Snow and Ice, Volume I*, edited by H. Oura, 599-610, Institute of Low Temperature Science, Hokkaido, Japan, 1967.

Orvig, S., *Climates of the Polar Regions*, 354 pp., Elsevier, Amsterdam, 1970.

Overland, J.E. and P.S. Guest, The Arctic snow and air temperature budget over sea ice during winter, *J. Geophys. Res.*, *98* (C3), 4651-4662, 1991.

Parish, T.R. and D.H. Bromwich, The surface wind field over the Antarctic Ice Sheet, *Nature*, *327* (6125), 51-54, 1987.

Parkinson, C.L., On the development and cause of the Weddell Polynya in a sea ice simulation, *J. Phys. Oceanogr.*, *13*, 501-511, 1983.

Parkinson, C.L., Recent sea-ice advances in Baffin Bay/Davis Strait and retreats in the Bellingshausen Sea, *Ann. Glaciol.*, *21*, 348-352, 1995.

Parkinson, C.L., Length of the sea ice season in the Southern Ocean, 1988-1994, in *Antarctic Sea Ice: Physical Processes, Interactions and Variability*, edited by M.O. Jeffries, 173-186, AGU, Washington, DC, 1998.

Parkinson, C.L. and D.J. Cavalieri, Arctic sea ice 1973-1987: seasonal, regional and interannual variability, *J. Geophys. Res.*, *94* (C10), 14499-14523, 1989.

Parkinson, C.L., J.C. Comiso, J.H. Zwally, D.J. Cavalieri, P. Gloersen and W.J. Campbell, Arctic sea ice, 1973-1976: Satellite passive-microwave observations, *Special Publication* 489, 296 pp., NASA, Washington, DC, 1987.

Parkinson, C.L. and P. Gloersen, Global Sea Ice Coverage, in *Atlas of Satellite Observations Related to Global Change*, edited by R.J. Gurney, J.L. Foster and C.L. Parkinson, 371-383, Cambridge University Press, Cambridge, 1993.

Parkinson, C.L. and W.M. Washington, A large-scale numerical model of sea ice, *J. Geophys. Res.*, *84* (C1), 311-337, 1979.

Payne, R.E., Albedo at the sea surface, *J. Atmos. Sci.*, *29*, 959-970, 1972.

Peacock, N.R., S.W. Laxon, R. Scharoo, W. Maslowski and D.P. Winebrenner, Geophysical signatures from precise altimetric height measurements in the Arctic Ocean, in *International Geoscience and Remote Sensing Symposium (IGARSS'98)*, Seattle, Washington, IGARSS, pp. 1964-1966, 1998.

Pease, C.H., The size of wind-driven coastal polynyas, *J. Geophys. Res.*, *92* (C7), 7049-7059, 1987.

Perey, F.G.J. and E.R. Pounder, Crystal orientation in ice sheets, *Can. J. Phys.*, *36*, 494-502, 1958.

Perovich, D.K., The Optical Properties of Sea Ice, *CRREL Monograph* 96-1, U.S. Army Cold Regions Research and Engineering Laboratory, Hanover, New Hampshire, 1996.

Perovich, D.K., The optical properties of sea ice, in *Physics of Ice-Covered Seas*, edited by M. Leppäranta, 195-239, Helsinki University Press, Helsinki, 1998.

Perovich, D.K. and T.C. Grenfell, Laboratory studies of the optical properties of young sea ice, *J. Glaciol.*, *27*, 331-346, 1981.

Perovich, D.K., G.A. Maykut and T.C. Grenfell, Optical properties of ice and snow in the polar regions. I: Observations, *Proc. SPIE Ocean Optics VIII*, *637*, 232-241, 1986.

Pinet, P.R., *Invitation to Oceanography*, 508 pp., West Publishing, St. Paul, Minnesota, 1996.

Ramstein, G. and S. Joussaume, Sensitivity experiments to sea surface temperatures, sea ice extent and ice-sheet reconstruction, for the last glacial maximum, *Ann. Glaciol.*, *21*, 343-347, 1995.

Rao, C.R.N. and J. Chen, Post-launch calibration of the visible and near-infrared channels of the Advanced Very High Resolution Radiometer on NOAA-14 spacecraft, *Int. J. Remote. Sens.*, *17*, 2743-2747, 1994.

Rapier, C.B., An Investigation of the Difference Between Skin and Bulk Sea Surface Temperatures in the Southern Ocean Between Australia and Antarctica, MSc thesis, 188 pp., University of Tasmania, Hobart, Australia, 1995.

Ratcliffe, E.H., The thermal conductivity of ice, new data on the temperature coefficient, *Philos. Mag.*, *7* (79), 1197-1203, 1962.

Reid, P.A. and W.F. Budd, Calculation of Antarctic surface ice mass accumulation through atmospheric parameters, in *Joint APOC-AMOS Conference*, Lorne, Australia, AMOS, pp. 104, 1995.

Rind, D., R. Healy, C.L. Parkinson and D. Martinson, Role of sea ice in 2 x CO_2 climate model sensitivity. Part I. The total influence of sea ice thickness and extent, *J. Climate*, *8* (3), 449-463, 1995.

Rintoul, S., On the origin and influence of the Adélie Land Bottom Water, in *Ocean, Ice, and Atmosphere: Interactions at the Antarctic Continental Margin*, edited by S. Jacobs and R. Weiss, 151-171, AGU, Washington, DC, 1998.

Rothrock, D.A., Y. Yu and G.A. Maykut, Thinning of the Arctic sea-ice cover, *Geophys. Res. Lett.*, *26* (23), 3469-3472, 1999.

Satiamurty, P., V.B. Rao and Y. Yamasaki, Características e processos físicos que afetam o clima na Antártica, in *Seminário Sobre Ciências Espaciais na Antártica*, São José dos Campos, Brasil, edited by E.B. Pereira and V.W.J.H. Kirchhoff, INPE, pp. 139-161, 1989.

Saunders, P.M., The temperature at the ocean-air interface, *J. Atmos. Sci.*, *24*, 269-273, 1967.

Schluessel, P., W.J. Emery, H. Grassl and T. Mammen, On the bulk temperature difference and its impact on the satellite remote sensing of sea surface temperature, *J. Geophys. Res.*, *95* (C8), 13341-13356, 1990.

Schluessel, P., H.-Y. Shin, W.J. Emery and H. Grassl, Comparison of satellite-derived sea surface temperatures with *in situ* skin measurements, *J. Geophys. Res.*, *92* (C3), 2859-2874, 1987.

Schweiger, A.J. and J. Key, Estimating surface radiation fluxes in the Arctic from TOVS HIRS and MSU brightness temperatures, *Int. J. Remote. Sens.*, *18*, 955-970, 1997.

Schweiger, A.J., M.C. Serreze and J.R. Key, Arctic sea ice albedo: A comparison of two satellite-derived data sets, *Geophys. Res. Lett.*, *20* (1), 41-44, 1993.

Schwerdtfeger, W., *Weather and Climate of the Antarctic*, 261 pp., Elsevier, Amsterdam, 1984.

Semtner, A.J., A model for the thermodynamic growth of sea ice in numerical investigations of climate, *J. Phys. Oceanogr.*, *6*, 379-389, 1976.

Setzer, A.W. and C.S. Hungria, Meteorologia na Península Antártica: alguns aspectos práticos, *Relatório de Pesquisa* INPE-5612-RPQ/668, Instituto Nacional de Pesquisas Espaciais, São José dos Campos, Brasil, 1994.

Shine, K.P., Parameterisation of the shortwave flux over high albedo surfaces as a function of cloud thickness and surface albedo, *Q. J. Roy. Meteor. Soc.*, *110*, 747-764, 1984.

Simmonds, I. and T.H. Jacka, Relationships between the interannual variability of Antarctic sea ice and the Southern Oscillation, *J. Climate*, *8* (3), 637-647, 1995.

Skirving, W.J., Radiometric Sea Surface Temperature in the Great Barrier Reef: Techniques and Algorithms, unpublished PhD thesis, James Cook University, Townsville, 2001.

Slater, P.N., *Remote Sensing, Optics and Optical Systems*, 562 pp., Addison-Wesley Publishing Co., London, 1980.

Smith, S.D., R.D. Muench and C.H. Pease, Polynyas and leads: An overview of physical processes and environment, *J. Geophys. Res.*, *95* (C6), 9461-9479, 1990.

Smolskaia, I., M. Nunez and K.J. Michael, Measurements of erythemal irradiance near Davis Station, Antarctica: effect of inhomogeneous surface albedo, *Geophys. Res. Lett.*, *26* (10), 1381-1384, 1999.

Snyder, J.P., Map projections - A working manual, *Professional Paper* 1395, 383 pp., U.S. Geological Survey, 1987.

Spano, A.F., Results of an airborne albedo program in Antarctica, 1963, *Mon. Weather Rev.*, *93*, 687-696, 1965.

Squire, V., The marginal ice zone, in *The Physics of Ice Covered Seas*, edited by M. Leppäranta, 381-446, Helsinki University Press, Helsinki, Finland, 1998.

Steffen, K., AVHRR applications for ice surface studies, in *Oceanographic Applications of Remote Sensing*, edited by M. Ikeda and F.W. Dobson, 307-320, CRC Press, Boca Raton, Florida, 1995.

Steffen, K., R. Bindschadler, G. Casassa, J.C. Comiso, D.T. Eppler, F.M. Fetterer, J.D. Hawkins, J.R. Key, D.A. Rothrock, D.R. Thomas, R. Weaver and R.M. Welch, Snow and ice applications of AVHRR in polar regions: report of a workshop held in Boulder, Colorado, 20 May 1992, *Ann. Glaciol.*, *17*, 1-16, 1993.

Steffen, K., J.R. Key, D.J. Cavalieri, J.C. Comiso, P. Gloersen, K.M. St. Germain and I. Rubinstein, The estimation of geophysical parameters using passive microwave algorithms, in *Microwave Remote Sensing of Sea Ice*, edited by F.D. Carsey, 201-231, AGU, Washington, DC, 1992.

Strass, V.H. and E. Fahrbach, Temporal and regional variation of sea ice draft and coverage in the Weddell Sea obtained from upward looking sonars, in *Antarctic Sea Ice: Physical Processes, Interactions and Variability*, edited by M.O. Jeffries, 123-139, AGU, Washington, DC, 1998.

Stroeve, J., A. Nolin and K. Steffen, Comparison of AVHRR-derived and *in situ* surface albedo over the Greenland Ice Sheet, *Remote Sens. Environ.*, *62*, 262-276, 1997.

Sturm, M., J. Holmgren, M. König and K. Morris, The thermal conductivity of seasonal snow, *J. Glaciol.*, *43* (143), 26-41, 1997.

Sturm, M. and J.B. Johnson, Thermal conductivity measurements of depth hoar, *J. Geophys. Res.*, *97* (B2), 2129-2139, 1992.

Sturm, M., K. Morris and R.A. Massom, The winter snow cover of the West Antarctic pack ice: its spatial and temporal variability, in *Antarctic Sea Ice: Physical Processes, Interactions and Variability*, edited by M.O. Jeffries, 1-18, AGU, Washington, DC, 1998.

Sverdrup, H.U., The Norwegian North Polar Expedition with the "Maud" Vol. II, Meteorology, 331 pp., Geophysical Institute, Bergen, Norway, 1933.

Taylor, V.R. and L.L. Stowe, Atlas of reflectance patterns for uniform earth and cloud surfaces (Nimbus 7 - 61 days), *Technical Report* 10, 66 pp., NOAA/NESDIS, Washington, DC, 1984.

Tchernia, P. and P.F. Jeannin, Circulation in Antarctic waters as revealed by iceberg tracks 1972-1983, *Polar Rec.*, *22* (138), 263-269, 1984.

Teillet, P.M. and B.N. Holben, Towards operational radiometric calibration of NOAA AVHRR imagery in the visible and near-infrared channels, *Can. J. Rem. Sens.*, *20* (1), 1-10, 1994.

Thomas, C.W., On the transfer of visible radiation through sea ice and snow, *J. Glaciol.*, *4*, 481-484, 1963.

Thomas, R.H., Polar research from satellites, 91 pp., Joint Oceanographic Institutions, Washington, DC, 1992.

Thorndike, A.S., C.L. Parkinson and D.A. Rothrock, Report of the Sea Ice Thickness Workshop, 56 pp., NASA, New Carrolton, Maryland, 1992.

Tin, T. and M.O. Jeffries, Sea ice thickness and roughness in the Ross Sea, Antarctica, *Ann. Glaciol.*, *33*, in press.

Tomczak, M. and S.J. Godfrey, *Regional Oceanography: An Introduction*, 422 pp., Pergamon Press, London, 1994.

Tucker, W.B., III, W.F. Weeks and M. Frank, Sea ice ridging over the Alaskan continetal shelf, *J. Geophys. Res.*, *84*, 4885-4897, 1979.

Turner, D., K.J. Michael and T. Adams, Mapping of sea ice with an artificial neural network, in *3rd National Australian Meteorological and Oceanographic Society Conference*, Hobart, Australia, pp. 165, 1996.

Turner, J., S. Pendlebury, L. Cowled, K. Jacka, M. Jones and P. Targett, Report on the First International Symposium on Operational Weather Forecasting in Antarctica, *B. Am. Meteorol. Soc.*, *81*, 75-94, 2000.

Turner, P., H. Davies, P. Tildesley and C. Rathbone, Common AVHRR processing software [WWW site], CSIRO, Available from the Internet at: <http://larry.dar.csiro.au/caps/oview/caps_paper.html>, 1999.

Untersteiner, N., Calculations of temperature regime and heat budget of sea ice in the Central Arctic, *J. Geophys. Res.*, *69* (22), 4755-4766, 1964.

Untersteiner, N., Calculating the thermal regime and mass budget of sea ice, in *Proceedings of the Symposium on the Arctic Heat Budget and Atmospheric Circulation*, Santa Monica, California, edited by J.O. Fletcher, Rand Corporation, pp. 203-214, 1966.

Untersteiner, N., *Geophysics of the Sea Ice*, 1196 pp., Plenum Press, New York, 1986.

USGCRP, Report on the Forum on Global Change Modelling [WWW site], U.S. Global Change Research Program, Available from the Internet at: <http://www.gcrio.org/ipcc/cover.html>, 1995.

Vihma, T., Subgrid parameterization of surface heat and momentum fluxes over the polar oceans, *J. Geophys. Res.*, *100* (C11), 22265-22646, 1995.

Vinnikov, K.I., D.A. Robock, R.J. Stouffer, J.E. Walsh, C.L. Parkinson, D.J. Cavalieri, J.F.B. Mitchell, D. Garrett and V.F. Zakharov, Global warming and Northern Hemisphere sea ice extent, *Science*, *286* (5446), 1934-1937, 1999.

Vowinkel, E. and S. Orvig, The Climate in the North Polar Basin, in *World Survey of Climatology*, 129-252, Elsevier, Amsterdam, 1970.

Wadhams, P., Beaufort Sea and its effect on oil containment, in *Arctic Ice Dynamics Joint Experiment*, 1-52, AIDJEX Bulletin, 1976.

Wadhams, P., Sea ice topography in the Arctic Ocean in the region of 70° W to 25° E, *Philos. T. Roy. Soc.*, *302* (1464), 45-85, 1981.

Wadhams, P., Sea ice thickness changes and their relation to climate, in *The Polar Oceans and Their Role in Shaping the Global Environment: The Nansen Centennial Volume*, edited by O.M. Johannessen, R.D. Muench and J.E. Overland, 337-362, AGU, Washington DC, 1994.

Wadhams, P., Sea ice morphology, in *The Physics of Ice Covered Seas*, edited by M. Leppäranta, 231-288, Helsinki University Press, Helsinki, Finland, 1998.

Wadhams, P. and J.C. Comiso, The ice thickness distribution inferred using remote sensing techniques, in *Microwave Remote Sensing of Sea Ice*, edited by F.D. Carsey, 375-383, AGU, Washington, DC, 1992.

Wadhams, P., M.A. Lange and S.F. Ackley, The ice thickness distribution across the Atlantic sector of the Antarctic Ocean in midwinter, *J. Geophys. Res.*, *92* (C13), 14535-14552, 1987.

Walton, C.C., W.G. Pichel, J.F. Sapper and D.A. May, The development and operational application of nonlinear algorithms for the measurement of sea surface temperatures with the NOAA polar-orbiting environmental satellites, *J. Geophys. Res.*, *103* (C12), 27999-28012, 1998.

Walton, D.W.H., *Antarctic Science*, 562 pp., Cambridge University Press, Cambridge, 1987.

Warren, S.G., Optical properties of snow, *Rev. Geophys. Space Phys.*, *20*, 67-89, 1982.

Warren, S.G., I.G. Rigor , N. Untersteiner, V.F. Radionov, N.N. Bryazgin, Y.I. Aleksandrov and R. Colony, Snow depth on Arctic sea ice, *J. Climate*, *12*, 1814-1829, 1999.

Warren, S.G. and W.J. Wiscombe, A model for the spectral albedo of snow II: Snow containing atmospheric aerosols., *J. Atmos. Sci.*, *37*, 2734-2745, 1980.

Washington, W.M. and C.L. Parkinson, *An Introduction to Three-Dimensional Climate Modelling*, 422 pp., University Science Books, Mill Valley, California, 1986.

Washington, W.M., A.J. Semtner Jr., C.L. Parkinson and L. Morrison, On the development of a seasonal change sea ice model, *J. Phys. Oceanogr.*, *6* (5), 679-685, 1976.

Weatherly, J.W., J.E. Walsh and H.J. Zwally, Antarctic sea ice variations and seasonal air temperature relationships, *J. Geophys. Res.*, *96*, 15119-15130, 1991.

Weeks, W.F., Growth conditions and the structure and properties of sea ice, in *Physics of Ice-Covered Seas*, edited by M. Leppäranta, 25-104, Helsinki University Press, Helsinki, 1998a.

Weeks, W.F., On the history of research on sea ice, in *Physics of Ice-Covered Seas*, edited by M. Leppäranta, 1-24, Helsinki University Press, Helsinki, 1998b.

Weeks, W.F. and S.F. Ackley, The growth, structure, and properties of sea ice, in *The Geophysics of Sea Ice*, edited by N. Untersteiner, 9-164, Plenum Press, New York, 1986.

Weeks, W.F., S.F. Ackley and J. Govoni, Sea ice ridging in the Ross sea, Antarctica as compared with sites in the Arctic, *J. Geophys. Res.*, *94*, 4984-4988, 1989.

Weeks, W.F., A. Kovacs and W.D. Hibler, III, Pressure ridge characteristics in the Arctic coastal environment, in *Proc. 1st Intl. Conf. Port & Eng. under Arctic Conditions*, Trondhein, Norway, edited by S.S. Wetteland and P. Bruun, Tech. Univ., Norway, pp. 152-183, 1971.

Welch, R.M., K.S. Kuo and S.K. Sengupta, Cloud and surface textural features in polar regions, *IEEE T. Geosci. Remote*, *28* (4), 520-528, 1990.

Welch, R.M., S.K. Sengupta, A.K. Goroch, P. Rabindra, N. Rangaraj and M.S. Navar, Polar cloud and surface classification using AVHRR imagery: An intercomparison of methods, *J. Appl. Meteorol.*, *31*, 405-420, 1992.

Weller, G., Spatial and temporal variations in the polar surface energy balance, *Mon. Weather Rev.*, *108*, 2007-2014, 1980.

Weller, G. and P. Schwerdtfeger, Radiation penetration in antarctic plateau and sea ice, *Tech. Note* 87, 120-141 pp., WMO, Geneve, 1967.

Wendler, G., B. Moore, D. Dissing and J. Kelley, On the radiation characteristics of Antarctic sea ice, *Atmos. Ocean*, *38* (2), 349-366, 2000.

Wensnahan, M., G.A. Maykut, T.C. Grenfell and D.P. Winebrener, Passive microwave remote sensing of thin ice using principal components analysis, *J. Geophys. Res.*, *98* (C7), 12453-12468, 1993.

White; W.B. and R.G. Peterson, Antarctic circumpolar wave in surface pressure, wind, temperature and sea-ice extent, *Nature*, *380* (6976), 699-707, 1996.

Williams, R.N., K.J. Michael, S. Pendlebury and P. Crowther, ICEMAPPER: An automated image analysis system for determining sea ice concentration and cloud cover from AVHRR images of the Antarctic, *Int. J. Remote. Sens.*, in press.

Wingham, D.J., The first of ESA's first Opportunity Missions: CryoSat, *ESA Earth Obs. Q.*, *63*, 21-24, 1999.

Wiscombe, W.J. and S.G. Warren, A model for the spectral albedo of snow I: pure snow, *J. Atmos. Sci.*, *37*, 2712-2727, 1980.

WMO, Sea ice nomenclature, terminology, codes, and illustrated glossary, *WMO Report* 259, 145 pp., World Meteorological Organisation, Geneva, 1970.

Wolfe, W., *Introduction to Infrared System Design*, 131 pp., SPIE, Bellingham, Washington, 1996.

Wong, A.P.S., N.L. Bindoff and A. Forbes, Ocean-ice shelf interaction and possible bottom water formation in Prydz Bay, Antarctica, in *Ocean, Ice and Atmosphere: Interactions at the Continental Margin*, edited by S.S. Jacobs and R.F. Weiss, 173-187, AGU, Washington, DC, 1998.

Woodcock, A.H. and H. Stommel, Temperature observations near the surface of a fresh water pond at night, *J. Meteorol.*, *4*, 102-103, 1947.

Worby, A.P. and S.F. Ackley, Antarctic research yields circumpolar sea ice thickness data, *EOS Trans. AGU*, *81* (17), 181,184-185, 2000.

Worby, A.P., M.O. Jeffries, W.F. Weeks, K. Morris and R.A. Jaña, The thickness distribution of sea ice and snow cover during late winter in the Bellingshausen and Amundsen Seas, Antarctica, *J. Geophys. Res.*, *101* (C12), 28441-28455, 1996a.

Worby, A.P., Thickness Distribution of East Antarctic Sea Ice, PhD thesis, 195 pp., University of Tasmania, Hobart, Australia, 1998.

Worby, A.P., Observing Antarctic Sea Ice: A Practical Guide for Conducting Sea Ice Observations from Vessels Operating in the Antarctic Pack Ice, CD-ROM produced by ASPeCt/SCAR/GLOCHANT, Hobart, Tasmania, Australia, 1999a.

Worby, A.P., Report on the ASPeCt sea ice thickness climatology project, *Antarctic Global Change Research*, *4*, 9-11, 1999b.

Worby, A.P. and I. Allison, A technique for making ship-based observations of Antarctic sea ice thickness and characteristics - Part I: Observational techniques and results, *Research Report* 14, 23 pp., Antarctic CRC, Hobart, Australia, 1999.

Worby, A.P., N.L. Bindoff, V.I. Lytle, I. Allison and R.A. Massom, Winter ocean/sea ice interactions studied in the East Antarctic, *EOS, Trans. AGU.*, *77* (46), 453, 453-457, 1996b.

Worby, A.P. and V. Dirita, A technique for making ship-based observations of Antarctic sea ice thickness and characteristics - Part II: Software user manual, *Research Report* 14, 39 pp., Antarctic CRC, Hobart, Australia, 1999.

Worby, A.P., P. Griffin, V.I. Lytle and R.A. Massom, On the use of electromagnetic induction sounding to determine winter and spring sea ice thickness in Antarctica, *Cold Reg. Sci. Technol.*, *29*, 49-58, 1999.

Worby, A.P. and R.A. Massom, The structure and properties of sea ice and snow cover in East Antarctic pack ice, *Research Report* 7, 191 pp., Antarctic CRC, Hobart, Australia, 1995.

Worby, A.P., R.A. Massom, I. Allison, V.I. Lytle and P. Heil, East Antarctic sea ice: a review of its structures properties and drift, in *Antarctic Sea Ice: Physical Processes, Interactions and Variability*, edited by M.O. Jeffries, 41-67, AGU, Washington, DC, 1998.

Worby, A.P. and W. Regester-Young, Antarctic Sea-Ice Processes and Climate (ASPeCt) [WWW site], SCAR-GLOCHANT, Available from the Internet at: <http://www.antcrc.utas.edu.au/aspect/>, 1999.

Worby, A.P. and X. Wu, East Antarctic sea ice: observations and modelling, *Ann. Glaciol.*, *27*, 427-432, 1998.

Wu, X. and W.F. Budd, Modelling global warming and Antarctic sea-ice changes over the past century, *Ann. Glaciol.*, *27*, 413-419, 1998.

Wu, X., W.F. Budd, V.I. Lytle and R.A. Massom, The effect of snow on Antarctic sea ice simulations in a coupled atmosphere-sea ice model, *Clim. Dynam.*, *15*, 127-143, 1999.

Wu, X., W.F. Budd, A.P. Worby and I. Allison, Sensitivity of the Antarctic sea ice distribution to oceanic heat flux in a coupled atmosphere-sea ice model, *Ann. Glaciol.*, *33*, in press.

Wu, X., I. Simmonds and W.F. Budd, Modelling Antarctic sea ice in a general circulation model, *J. Climate*, *10* (4), 593-609, 1997.

Yhann, S.R. and J.J. Simpson, Application of neural networks to AVHRR cloud segmentation., *IEEE T. Geosci. Remote*, *33* (3), 590-604, 1995.

Young, H.D., *Statistical Treatment of Experimental Data*, 174 pp., McGraw-Hill, New York, 1962.

Young, N.M., Antarctic iceberg drift and ocean currents derived from scatterometer image series, in *Proceedings of the Joint ESA-Eumetsat Workshop on Emerging Scatterometer Applications - From Research to Operations*, Noordwijk, The Netherlands, ESA, pp. 125-132, 1998.

Young, N.M., D. Turner, G. Hyland and R.N. Williams, Near-coastal iceberg distributions in East Antarctica, *Ann. Glaciol.*, *27*, 68-74, 1998.

Yu, Y., Regional Arctic Ice Thickness and Brine Flux from AVHRR, PhD thesis, 142 pp., University of Washington, Seattle, Washington, 1996.

Yu, Y. and D.A. Rothrock, Thin ice thickness from satellite thermal imagery, *J. Geophys. Res.*, *101* (C10), 25753-25766, 1996.

Zabel, I.H.H., K.C. Jezek, S.P. Gogineni and P. Kanagaratnam, Search for proxy indicators of young sea ice thickness, *J. Geophys. Res.*, *101* (C3), 6697-6709, 1996.

Zhou, X., S. Li and K. Morris, Measurement of all-wave and spectral albedo of snow surface on the summer sea ice in the Ross Sea, *Ann. Glaciol.*, *33*, in press.

Zibordi, G. and M.L. Van Woert, Antarctic sea ice mapping using the AVHRR, *Remote Sens. Environ.*, *45*, 155-163, 1993.

Zillman, J.W., A study of some aspects of the radiation budget of the Southern Hemisphere oceans, *Meteorological Study* 26, 562 pp., Bureau of Meteorology, Canberra, 1972.

Zwally, J.H., J.C. Comiso and A.L. Gordon, Antarctic offshore leads and polynyas and oceanographic effects, in *Oceanography of the Antarctic Continental Shelf*, edited by S.S. Jacobs, 203-226, AGU, Washington, DC, 1985.

Zwally, J.H., J.C. Comiso, C.L. Parkinson, W.J. Campbell, F.D. Carsey and P. Gloersen, Antarctic Sea Ice, 1973-1976: Satellite Passive Microwave Observations, *Special Publication* 459, 206 pp., NASA, Washington, DC, 1983.

Zwally, J.H. and P. Gloersen, Passive microwave images of the polar regions and research applications, *Polar Rec.*, *18* (116), 431-450, 1977.

Sea Ice Thickness Code

This section presents the IDL® source code used in the sea ice thickness model. The program consists of eight routines (procedures and functions), listed below. A more detailed description of the model and the flow of information within it is given in Chapter 4. Figure 17 shows a flow diagram with the model's sequence of events.

MAIN.PRO - This procedure automates the process of running the model in more than one image through a FOR loop. It also adds the data resulting from this process into "average images" of albedo, IST and ice thickness.

AVHRR.PRO - This procedure is responsible for the main processing and for calling all the other procedures and functions of the program. It achieves the following: *a)* opens an AVHRR image in the DISIMP format; *b)* reads the image headers to retrieve useful information such as the date and time of acquisition, satellite number etc; *c)* extracts the seven bands of data (2 albedos, 3 brightness temperatures, 1 sea ice map; and 1 angles band); *d)* extracts the relevant information (solar zenith angle, satellite zenith angle; sun-satellite azimuth) from the angles band; *e)* creates a "mask image" to remove invalid data (clouds, land, NaN values, etc); *f)* calls a procedure that applies a spatial filter (**DESPECKLE.PRO**) to remove random noise from the sea ice map band; *g)* plots histograms of original and valid data; *h)* calls the function that calculates the albedo (**ALBEDO.PRO**); *i)* calls the function that calculates IST (**TEMPER.PRO**); *j)* removes the pixels with albedo greater than 1.0 and pixels with temperatures warmer than the freezing point of sea water from the sea ice calculations; *k)* calls the function that processes the GASP data (**GASP.PRO**); *l)* calls the procedure that estimates the sea ice thickness of each valid pixel (**NET_FLUX.PRO**); calls the procedure that displays the map and histogram outputs on the screen (**WINDOW_OUTPUTS.PRO**); and *m)* appends the newly-created albedo, IST and ice thickness bands to the original AVHRR image.

DESPECKLE.PRO - This function applies a low-pass spatial filter based on a 3 x 3 matrix to remove random noise from the original AVHRR image.

HISTOGRAMS.PRO - Auxiliary function that plots frequency distribution histograms on the screen at various places within the program.

ALBEDO.PRO - This function calculates surface albedo using inputs from AVHRR channels 1 and 2, according to the method described by *Lindsay and Rothrock* [1994], through the following steps: *a)* restricting the processing to valid data only; *b)* undoing the solar zenith correction and the radiance correction; *c)* converting the digital counts for channels 1 and 2 to a narrow-band radiance; *d)* converting the narrow-band radiances to corrected narrow-band radiances; *e)* converting the corrected narrow-band radiances to TOA narrow-band albedos; *f)* calculating the narrow-band anisotropic reflectance factor; *g)* forming the TOA narrow-band albedos; *h)* calculating the surface narrow-band albedo corrected for atmospheric attenuation; *i)* estimating a broad-band albedo from the two narrow-band albedos; and *j)* normalising the albedo to a solar zenith angle of 70°.

TEMPER.PRO - This function calculates IST using the method proposed by *Key and Haefliger* [1992] and updated by *Key et al.*[1997] through the following steps: *a)* restricting the processing to valid data only; *b)* calculating the satellite scan angle using the satellite zenith angle; *c)* choosing the appropriate correction coefficients according to the satellite number and temperature range; *d)* applying the appropriate IST calculation equation based on the chosen coefficient; and *e)* plotting a IST frequency distribution histogram.

GASP.PRO - Opens the raw GASP files (see Section 4.3.1) and generates air temperature and wind vector (u, v) arrays that match the characteristics of the AVHRR image through the following steps: *a)* locating the two raw GASP files relevant to the satellite image (based on the acquisition date and time); *b)* opening the raw GASP files; *c)* performing a temporal interpolation to match the AVHRR's date and time of acquisition; *d)* performing a bilinear spatial interpolation to match the dimensions of the AVHRR image ; *e)* generating a three-dimensional array holding the GASP arrays (T_{Air}, u and v) and saving it as a file; *f)* plotting temperature contour curves and a wind vector field; and *g)* plotting frequency distribution histograms of wind speed and air temperature.

NET_FLUX.PRO - Calculates the sea ice thickness of each pixel of an AVHRR image using the thermodynamic model proposed by *Yu and Rothrock* [1996], through the following steps: *a)* retrieving air temperature and wind speed and direction from the GASP data; *b)* determining the position of the 9 x 1 shape based on the wind direction (see Section 4.3.2.3); *c)* choosing the appropriate bulk transfer coefficients for each pixel based on the wind speed; *d)* calculating incoming solar radiation; *e)* calculating the solar radiation reaching the ice surface; *f)* calculating the transmitted fraction of the solar radiation; *g)* calculating the solar radiation absorbed in the ice layer; *h)* ; calculating the upward longwave radiation; *i)* calculating the downward longwave radiation; *j)* calculating the turbulent sensible and latent heat fluxes; *k)* calculating the conductive heat flux; *l)* summing the heat fluxes (terms from *d)* to *k)* above) to calculate the net flux; and *m)* initialising an incremental looping system (see Section 4.2) that assigns an estimate of sea ice thickness to pixels with zero or positive net flux. Pixels with a negative net flux (those that lose heat to the atmosphere) are passed to the next iteration, until all of the valid pixels within the image are analysed or a thickness limit (2 or 4 m) is attained.

WINDOW_OUTPUTS.PRO - This procedure displays the data outputs of albedo, IST and sea ice thickness on the screen and saves them as bitmap files. Each display consists of a window containing the frequency distribution histogram, the image plotted on top of a gridded map and the appropriate colour legend.

In the following pages, characters preceded by a semi-colon (;) indicate comments to the program or pieces of code that were commented out. The code itself is shown in a different font (`Courier New - Size 10pt`).

8.1 MAIN.PRO

```
;-------------------------------------------------------------------------
;
; NAME:                    MAIN.PRO
; PURPOSE:                 Automate the process of calling more than one
;                          image and running the whole model
; CATEGORY:                None
; CALLING SEQUENCE:        None
; INPUTS:                  File name to process
; KEYWORD PARAMETERS:      None
; OUTPUTS:                 FILE: all the outputs from AVHRR plus an
;                          average thickness image and another array
;                          counting the number of images analysed per
;                          pixel
; COMMON BLOCKS:           None
; SIDE EFFECTS:            None
; SYSTEM VARIABLES:        None
; RESTRICTIONS:            None
; PROCEDURES & FUNCTIONS:  AVHRR.PRO
; AUTHOR(S):               Clemente Hungria, June 1999
; MODIFICATION HISTORY:    Clemente Hungria, August, 1999
;-------------------------------------------------------------------------

PRO Main
;-------------------------------------------------------------------------
```

; Initiate FOR LOOP to open images, create an average image and save the thickness images.

```
Displays = DIALOG_MESSAGE('Multi Images ?', /QUESTION)
Ims = ['t6ysb','t6ytb','t6z6b','t6z7b','t6zkb','t70rb','t715b',$
       't716b','t71ib','t73wb','t73xb','t749b','t74ab','t752b',$
       't753b','t75gb','t75hb','t75ub','t75vb','t76mb','t76nb',$
       't77fb','t77sb','t77tb','t78zb','t7axb','t7bqb','t7c4b',$
       't7cib','t7e2b','t7e3b','t7eub','t7evb','t2iub','t2j8b']
```

; Chooses a file name from the list, unzip it from the INPUTS directory and moves it to the
; main IDL directory.

```
Start  = 0
Finish = 34
IF Start EQ 33 AND Finish EQ 34 $
       THEN ImageYear = '95' & Cols = 1251 & Lins = 761
IF Start LT 33 AND Finish LT 33 $
       THEN ImageYear = '96' & COls = 1501 & Lins = 501

Ocr_Img = FLTARR(Cols,Lins)
Avg_Img = FLTARR(Cols,Lins)

FOR j = Start,Finish DO BEGIN
       ImageFile = Ims(j)+ '.dat'
       Unzip = DIALOG_MESSAGE('Unzip Images ?', /QUESTION, /DEFAULT_NO)
       IF Unzip EQ 'Yes' THEN BEGIN
              CD, 'inputs'
              SPAWN, str
              Str = 'mv ' + ImageFile + ' ..'
              SPAWN, str
              CD, '/u/chungria/idl'
       ENDIF
```

; Runs AVHRR using the file name selected.

```
h = 1
H_Zi            = HANDLE_CREATE()
H_Data_Mask     = HANDLE_CREATE()
H_File_Name     = HANDLE_CREATE()
HANDLE_VALUE    , H_Data_Mask , h, /SET, /NO_COPY
HANDLE_VALUE    , H_File_Name , h, /SET, /NO_COPY
HANDLE_VALUE    , H_Zi        , h, /SET, /NO_COPY
AVHRR, ImageFile , Displays   , H_Zi, H_Data_Mask, H_File_Name
HANDLE_VALUE    , H_Zi        , Zi
HANDLE_VALUE    , H_Data_Mask , Data_Mask
HANDLE_VALUE    , H_File_Name , File_Name
```

; Table of Codes for Data_Mask:
;----------
; 1....Bad data (Noise, NaN)
; 2....Open Water (Ts > Tw)
; 3....Very Compacted Ice (Class 23)
; 4....Zi > than limit
; 5....Cloud (all types 3>Icemap>13)
; 6....Coastline (Icemap = 25)
; 7....Land (Icemap = 29)

```
Good  = WHERE(Data_Mask EQ  1)
Land  = WHERE(Data_Mask EQ -7)
Coast = WHERE(Data_Mask EQ -6)
Cloud = WHERE(Data_Mask EQ -5)
```

; Data is added to the average image created from the original mask.
; In the Mask, -1 correspond to the coastline and -2 to land.

```
Avg_Img = Avg_Img + Zi
Ocr_Img(Good) = Ocr_Img(Good) + 1
```

; The Zi image is saved on the OUTPUTS directory and the original AVHRR image is
; removed from the main IDL directory.

```
CD, 'outputs'
File_Name = STRMID(File_Name, 4, 10)
File_Name = File_Name + '_Zi.dat'
OPENW, lun, File_Name, /GET_LUN
WRITEU, lun, Zi
FREE_LUN, lun
CD, '/u/chungria/idl' & Str = '/bin/rm ' + ImageFile
SPAWN, Str
PRINT, 'Number of images processed: ', j + 1
ENDFOR
```

; Average image is saved.

```
Avg_Img    = Avg_Img/Ocr_Img
File_Name = 'average' + ImageYear + '.dat'
CD, 'outputs'
OPENW      , lun, File_Name, /GET_LUN
WRITEU     , lun, Avg_Img
FREE_LUN   , lun
File_Name = 'occurence' + ImageYear + '.dat'
OPENW      , lun, File_Name, /GET_LUN
WRITEU     , lun, Ocr_Img
FREE_LUN   , lun
CD, '/u/chungria/idl'
END
```

;_____

8.2 AVHRR.PRO

```
;-------------------------------------------------------------------------
;
; NAME:                                   AVHRR.PRO
; PURPOSE:                                This function will undo the solar zenith
                                          correction and then the brightness temperature
                                          correction as used by the DISIMP routine
                                          CNVRT5. The resulting image is then restored
                                          to its original digital count values. It calls
                                          ALBEDO.PRO and TEMPER.PRO to generate
                                          albedo and ice/surface temperature images and
                                          then proceed to NET_FLUX.PRO where it
                                          finishes the calculation of the thickness of each
                                          valid pixel.
; CATEGORY:                               None
; CALLING SEQUENCE:                      AVHRR, image=image
; INPUTS:                                 IMAGE: file name to process (must be a
                                          processed image)
; KEYWORD PARAMETERS:                    None
; OUTPUTS:                               FILE: three "images" holding the normalized
                                          albedo, the IST and the ice thickness.
; COMMON BLOCKS:                         None
; SIDE EFFECTS:                          None
; SYSTEM VARIABLES:                      None
; RESTRICTIONS:                          None
; PROCEDURES & FUNCTIONS:                AVHRR.PRO
; AUTHOR(S):                             Clemente Hungria, February/March 1998
; MODIFICATION HISTORY:                  Katrina Hill, March 8, 1998. Altered to allow
                                          image to be open and processed utilizing IDL
                                          array processing techniques.
                                          Clemente Hungria, August, 1998. Final
                                          alterations to accommodate new image format
;-------------------------------------------------------------------------

PRO OPEN_DISIMP,file,hdrsize,ns,nl,nb,nbits,num_utr,b_utr,geo_type,descrip, null
;-------------------------------------------------------------------------

        !error = 0
        ON_IOERROR, trouble
        DEVICE, retain=2
        GET_LUN, unit
        OPENR, unit, file
        header = INTARR(256)
        READU, unit, header
        null = header(60) & nb = header(3) & nbits = header(26)
        ns = LONG(header(29)) & nl = LONG(header(30)) & num_utr = header(18)
        b_utr = header(19) * 2
        CASE nbits OF
                8: BEGIN
                        data_type = 1
                        IF ((ns MOD 2) EQ 1) THEN ns = ns + 1
                END
                16: data_type = 2
        ENDCASE
        hdrsize = Header(10)*2
        POINT_LUN, unit, hdrsize+(ns*nl*nb*data_type)
        no_user_recs = header(16) & no_bytes_ur  = header(17) *2
        user_rec = BYTARR(no_bytes_ur,no_user_recs)
        READU, unit, user_rec
```

; Image description record.

```
        IF (STRING(user_rec(0:1,3)) EQ 'I1') THEN BEGIN
                dlen    = user_rec(3,3) < (128-4)
                descrip = STRING(user_rec(4:4+dlen-1,3))
        ENDIF ELSE descrip = "DISIMP Image"
```

; Channel names record.

```
        IF (STRING(user_rec(0:1,2)) EQ 'C1') THEN BEGIN
                clen    = user_rec(3,2) + user_rec(2,2)*256
                nchns   = user_rec(5,2) + user_rec(4,2)*256
                bnames  = STRARR(nchns) & k = 6
                FOR i   = 0, nchns-1 DO BEGIN
                        bnames(i) = STRING(user_rec(k:k+clen-1,2))
                        k = k + clen
                ENDFOR
        ENDIF
        geo_type = header(64)
        emin = 0.0 & lmin = 0.0 & emax = 0.0 & lmax = 0.0
        IF (geo_type GT 0) THEN BEGIN
                einc = 10000.0 * header(66) + header(67) + 0.0001 * header(68)
                linc = 10000.0 * header(69) + header(70) + 0.0001 * header(71)
                emin = 10000.0 * header(72) + header(73) + 0.0001 * header(74)
                lmin = 10000.0 * header(75) + header(76) + 0.0001 * header(77)
                emax = 10000.0 * header(78) + header(79) + 0.0001 * header(80)
                lmax = 10000.0 * header(81) + header(82) + 0.0001 * header(83)
                rot  = header(84) + 0.0001 * header(85)
                descrip = descrip + STRING(format='(" [GeoType=",i0,"; $
                        Pixels=",i0,"(",i0,") ",i0,"; Lines=",i0,"(",i0,")",i0,";$
                        Rot=",i0,"]")', geo_type, emin, einc, emax, lmin, linc,$
                        lmax, rot)
        ENDIF
        !error = 0
        trouble:
        IF !error NE 0 THEN BEGIN
                PRINT,'Error reading DISIMP file (getting next image)'
        EXIT, status=1
        ENDIF
        FREE_LUN, unit
END
;_____________________________________________________________________

PRO AVHRR, ImageFile, Displays, H_Zi, H_Data_Mask, H_File_Name
;_____________________________________________________________________

        xy_start=[0,1000] & xy_dim=[200,200]
        T0 = SYSTIME(1)                                  ; Starts counting the time.
```

; The acquisition time will be used by GASP.PRO to retrieve the appropriate GASP files.

```
        IF (KEYWORD_SET(satcode))  THEN code     = satcode   ELSE code     = 'NULL'
        IF (KEYWORD_SET(xystart))  THEN xy_start = xy_start  ELSE xy_start = [-1,-1]
        IF (KEYWORD_SET(xydim))    THEN xy_dim   = xy_dim    ELSE xy_dim   = [-1,-1]
```

; Set the colour table (This colour table is already on IASOS system).

```
        GOTO, Skip_Table
        Rlocols       = [0,4,4,0,0,4,4,0,2,4,3,0,3,4,0,4] & rlocols = 63 * rlocols
        Glocols = [0,4,0,4,0,4,0,4,2,2,0,2,4,2,2,3] & glocols = 63 * glocols
        blocols = [0,4,0,0,4,0,4,4,2,0,0,2,4,4,2,1] & blocols = 63 * blocols
        rhicols = [0,0,1,2,3,4,1,3,3,0,0,1,2,3,2,4] & rhicols = 63 * rhicols
        ghicols = [0,0,1,2,3,4,1,3,3,2,3,4,4,4,0,3] & ghicols = 63 * ghicols
        bhicols = [2,3,4,4,4,2,1,3,1,0,0,1,2,3,0,4] & bhicols = 63 * bhicols
        rglevel = INDGEN(63) * 4  & greenglevel = INDGEN(63) * 4
        bglevel = INDGEN(63) * 4
```

```
A_r   = [0,0,0,0,0,0,0,0,0,0,0,0,0,25,60,85,120,140,180,215]
A_g   = [0,0,0,0,10,50,60,80,90,105,120,130,150,160,180,190,200,210,225,240]
A_b   = [30,65,90,110,140,170,180,190,205,210,230,240,255,255,255,255,255,255,255,255]
Ts_r  = [0,10,45,12,0,0,0,0,0,229,250,255,255,255,255,225,198,180,155,120]
Ts_g  = [0,0,0,0,85,137,187,238,255,255,255,199,112,70,20,0,0,0,0,0]
Ts_b  = [90,180,210,248,255,229,255,255,153,0,0,0,0,0,0,0,0,0,0,0]
Zi_b  = [0,0,0,0,0,0,0,0,0,0,0,150,130,160,180,150,130,110,90,70]
Zi_r  = [90,170,220,250,250,255,255,255,255,255,255,255,245,225,210,200,190,170,150,130,110]
Zi_g  = [0,0,0,0,100,140,160,180,200,220,240,255,225,210,200,190, 170,150,130,110]
red   = [rlocols, rhicols, rglevel, A_r, Ts_r, Zi_r]
green = [glocols, ghicols, gglevel, A_g, Ts_g, Zi_g]
blue  = [blocols, bhicols, bglevel, A_b, Ts_b, Zi_b]
colors = [red, green, blue]

       TVLCT, red, green, blue                    ; Creates the new colour table.

Skip_Table:

       DEVICE, PSEUDO_COLOR = 8
       DEVICE, DECOMPOSED = 0                     ; Tests the number of colours
       Number_colors=!D.N_COLORS                  ; used by the system.
       IF (Number_colors GT 256) THEN Color_Test=1
```

; Opens the DISIMP image and retrieve the satellite number and acquisition time.

```
       PRINT, 'Opening Disimp Image...'
       IF Displays EQ 'No 'THEN
              ImageFile = DIALOG_PICKFILE(/READ, FILTER = '*.dat')
       open_disimp,imagefile,skip,x,y,bands,bits,nr,nbyt,geot,img_description,null
       image1  = INTARR(x,bands,y)
       hdr     = INTARR(skip/2)
       userrec = BYTARR(128,4)
       IF (nr GT 0) AND (nbyt GT 0) THEN BEGIN
              textrec = BYTARR(nbyt, nr)
       ENDIF
       OPENR, lun, imagefile, /get_lun
       READU, lun, hdr
       READU, lun, image1
       READU, lun, userrec
       IF (nr GT 0) AND (nbyt GT 0) THEN BEGIN
              READU, lun, txtrec
       ENDIF
       FREE_LUN, lun
       IF (bands EQ 5) THEN BEGIN
              PRINT, 'Sorry - this is not a processed image. Exiting!'
              GOTO, end_stat
       ENDIF
       IF (bands EQ 6) THEN BEGIN
              PRINT, 'Sorry - probably only has the OLD angles band. Exiting!'
              GOTO, end_stat
       ENDIF
```

; Collects information from the image description string.

```
       n=STR_SEP(STRCOMPRESS(img_description),' ',/TRIM)
       sat_code = n(0) & orbit_no = n(2) &
       a_time   = n(6)
       a_hour   = STRMID(a_time, 0,2)
       a_minute = STRMID(a_time, 2,2)
       a_day    = n(3)
       a_month  = n(4)
       a_year   = '19' + n(5)
       PRINT, 'SATELLITE ID.....', sat_code
       PRINT, 'ORBIT NUMBER.....', orbit_no
       PRINT, 'ACQUISITION DATE.....', a_day + '/' + a_month + '/' + a_year
       PRINT, 'ACQUISITION TIME.....', a_hour + ':' + a_minute + ' Z'
```

; Generates a satellite code to be used; within ALBEDO.PRO and TEMPER.PRO.

```
CASE sat_code OF
        'TIROS-N'  : sat = 0
        'NOAA6'    : sat = 1
        'NOAA7'    : sat = 2
        'NOAA8'    : sat = 3
        'NOAA9'    : sat = 4
        'NOAA10'   : sat = 5
        'NOAA11'   : sat = 6
        'NOAA12'   : sat = 7
        'NOAA13'   : sat = 8
        'NOAA14'   : sat = 9
        'NOAA15'   : sat = 10
ENDCASE
```

; Transforms the month string into its; correspondent number from 1 to 12

```
CASE a_month OF
        'Jan'      : Month = '01'
        'Feb'      : Month = '02'
        'Mar'      : Month = '03'
        'Apr'      : Month = '04'
        'May'      : Month = '05'
        'Jun'      : Month = '06'
        'Jul'      : Month = '07'
        'Aug'      : Month = '08'
        'Sep'      : Month = '09'
        'Oct'      : Month = '10'
        'Nov'      : Month = '11'
        'Dec'      : Month = '12'
ENDCASE

Sat_Code   = STRMID(Sat_Code,0,1)   + STRMID(Sat_Code, 4,2)
File_time  = STRMID(a_hour,0, 2)    + STRMID(a_minute, 0,2)
File_date  = STRMID(a_year, 2,2)    + STRMID(month, 0,2)+STRMID(a_day, 0,2)
File_id    = Sat_Code+'_' + File_Date + File_Time
Image_Id = Sat_Code+'-'+a_day+'/'+a_month+'/'+a_year+','+a_hour+':'+a_minute+'Z'
```

; Extracts the 7 bands of data (2 albedos, 3 brightness temperatures, 1 sea ice map
; and 1 angles band - where there are five angles presented).

```
PRINT, 'Extracting channels to be used...'
albedo1 = REFORM(image1(*,0,*))*0.01
albedo2 = REFORM(image1(*,1,*))*0.01
temper1 = REFORM(image1(*,2,*))*0.01 + 273.15
temper2 = REFORM(image1(*,3,*))*0.01 + 273.15
temper3 = REFORM(image1(*,4,*))*0.01 + 273.15
icemap  = REFORM(image1(*,5,*))
angles  = REFORM(image1(*,6,*))
```

; Extracts the angles from the "angles" band.

```
PRINT, 'Extracting the angles from thr angle channel...'
a_x    = hdr(62) & a_y = hdr(63) & low_y = 0 & high_y = a_y
satdcE = angles(0:a_x-1,low_y:high_y-1)
low_y  = high_y & high_y = high_y + a_y
satdcN = angles(0:a_x-1,low_y:high_y-1)
low_y  = high_y & high_y = high_y + a_y
sundcE = angles(0:a_x-1,low_y:high_y-1)
low_y  = high_y & high_y = high_y+a_y
sundcN = angles(0:a_x-1,low_y:high_y-1)
high_y = high_y + a_y & low_y = high_y
sundcZ = angles(0:a_x-1,low_y:high_y-1)
```

; Alters the solar zenith angle data to begin processing.

```
PRINT, 'Calculating the angles into probable bands...''
satdcE = CONGRID (satdcE,x,y) & satdcN = CONGRID (satdcN,x,y) & $
sundcE = CONGRID (sundcE,x,y) & sundcN = CONGRID (sundcN,x,y) & $
                  sundcZ = CONGRID (sundcZ,x,y) & NULL=32767.
PRINT, 'Calculating the angles into cosine values...'
ND = WHERE(satdcE EQ NULL, cnt) & satdcE = TEMPORARY(satdcE)/16384.
IF (cnt GT 0) THEN satdcE(ND) = NULL
ND = WHERE(satdcN EQ NULL, cnt) & satdcN = TEMPORARY(satdcN)/16384.
IF (cnt GT 0) THEN satdcN(ND) = NULL
ND = WHERE(sundcE EQ NULL, cnt) & sundcE = TEMPORARY(sundcE)/16384.
IF (cnt GT 0) THEN sundcE(ND) = NULL
ND = WHERE(sundcN EQ NULL, cnt) & sundcN = TEMPORARY(sundcN)/16384.
IF (cnt GT 0) THEN sundcN(ND) = NULL
ND = WHERE(sundcZ EQ NULL, cnt) & sundcZ = TEMPORARY(sundcZ)/16384.
IF (cnt GT 0) THEN sundcZ(ND) = NULL
```

; Calculates the three angles to be used by the model:
; Solar Zenith Angle (solza), Satellite Zenith Angle (satza) and Sun-Satellite Azimuth (ssaz).

```
PRINT, 'Calculating Solar and Sat. Zenith Angles and Sun-Sat. Azimuth Angle...'
solza       = ACOS(sundcZ)
satza       = ACOS(SQRT(1-(satdcE)^2-(satdcN)^2))
ssaz        = ATAN(sundcN/sundcE) - ATAN(satdcN/satdcE)
```

; Creates the Data_Mask array with 1s corresponding to valid data and -1s for invalid data.

```
m = SIZE(albedo1) & AVHRR_Columns = m(1) & AVHRR_Lines = m(2)
AVHRR_Size  = [AVHRR_Columns, AVHRR_Lines]
Data_Mask   = FLTARR(AVHRR_Columns, AVHRR_Lines)
Data_Mask   = Data_Mask + 1
```

; Initial screening: Data will be considered invalid under the following conditions:
; 1) Non ice pixels as classified by icemap (Ice pixels are currently classified as 16,17,18,19).
; 2) Pixels with solar zenith angles higher than 80 degrees.
; 3) Pixels with values less than zero.
; 4) Maximum values of each channel (Null Data from DISIMP).

```
PRINT, 'Initial number of pixels:.....', AVHRR_Columns*AVHRR_Lines
PRINT, 'Screening invalid data...'
Max_albedo1 = MAX(albedo1) & Max_albedo2 = MAX(albedo2) & $
Max_temper2 = MAX(temper2) & Max_temper3 = MAX(temper3)
IF a_year EQ '1996' THEN Limit = 80*!dtor
IF a_year EQ '1995' THEN Limit = 85*!dtor
Bad = WHERE((icemap LT 16) OR (icemap  GT 19 ) OR $
       (albedo1 EQ Max_albedo1) OR (albedo1 LT 0.0) OR $
       (albedo2 EQ Max_albedo2) OR (albedo2 LT 0.0) OR $
       (temper2 EQ Max_temper2) OR (temper2 LT 0.0) OR $
       (temper3 EQ Max_temper3) OR (temper3 LT 0.0) OR $
       (solza GT Limit), Bad_cnt)
Good = WHERE(Icemap EQ 0, Good_cnt)          ; Include open water pixels.
IF (Bad_cnt) GT 0 THEN BEGIN
       Data_Mask(Bad) = -1
       Data_mask(Good) = 1
ENDIF
```

; Defines the valid pixels after the screening processes.

```
Good    = WHERE(Data_Mask EQ  1, Good_cnt)
Bad     = WHERE(Data_Mask EQ -1,  Bad_cnt)
PRINT, '1st screening (valid pixels):..... ', Good_cnt
PRINT, '1st screening (bad pixels):..... ', Bad_cnt
```

; Applies a spatial filter to the icemap image to remove noisy pixels.

```
Filter=DESPECKEL(Icemap)
ND = WHERE(Icemap EQ 0, Count)
Data_Mask(ND) = -1
```

; Defines the valid pixels after the filtering processes.

```
Good = WHERE(Data_Mask EQ  1, Good_cnt)
Bad  = WHERE(Data_Mask EQ -1,  Bad_cnt)
PRINT, '2nd screening: Filter (valid pixels):..... ', Good_cnt
PRINT, '2nd screening: Filter (bad pixels):..... ', Bad_cnt
```

; Prints the average Solar Zenith Angle.

```
Stats = MOMENT(Solza)
Avg_Solza = Stats(0)
PRINT, 'Average Solar Zenith Angle.....', Avg_Solza*!radeg
```

; Closes the program if no data is available for analysis.

```
IF (Good_cnt) EQ 0 THEN BEGIN
       PRINT, 'No data available for analysis. Terminating program...
       GOTO, End_Stat
ENDIF
```

; Generates pointers to pass data to other procedures.

```
H_Temper1   = HANDLE_CREATE() &  H_Temper2     = HANDLE_CREATE() & $
H_Temper3   = HANDLE_CREATE() &  H_Albedo1     = HANDLE_CREATE() & $
H_Albedo2   = HANDLE_CREATE() &  H_Ssaz        = HANDLE_CREATE() & $
H_Solza     = HANDLE_CREATE() &  H_Satza       = HANDLE_CREATE() & $
H_Icemap    = HANDLE_CREATE() &  H_Data_Mask   = HANDLE_CREATE()
HANDLE_VALUE, H_Albedo1, Albedo1   , /SET, /NO_COPY & $
HANDLE_VALUE, H_Albedo2, Albedo2   , /SET, /NO_COPY & $
HANDLE_VALUE, H_Temper1, Temper1   , /SET, /NO_COPY & $
HANDLE_VALUE, H_Temper2, Temper2   , /SET, /NO_COPY & $
HANDLE_VALUE, H_Temper3, Temper3   , /SET, /NO_COPY & $
HANDLE_VALUE, H_Solza, Solza       , /SET, /NO_COPY & $
HANDLE_VALUE, H_Satza,Satza        , /SET, /NO_COPY & $
HANDLE_VALUE, H_Ssaz, Ssaz         , /SET, /NO_COPY & $
HANDLE_VALUE, H_Icemap , Icemap    , /SET, /NO_COPY & $
HANDLE_VALUE, H_Data_Mask, Data_Mask,/SET, /NO_COPY

Auxiliar       = [H_Data_Mask, H_Icemap]
Albedos        = [H_Albedo1, H_Albedo2]
Temperatures   = [H_Temper1, H_Temper2, H_Temper3]
Angles         = [H_Solza, H_Satza, H_Ssaz]
```

; Plots histograms of the original data.

```
IF Displays EQ 'No' THEN GOTO, Skip_hst1
PRINT, 'Plotting histograms of the original data...
Title      = 'Original Data'
H_Data     = [H_Albedo1, H_Albedo2,H_Solza, H_Temper1, H_Temper2, H_Temper3]
Names      = ['Albedo Ch1', 'Albedo Ch2', 'Solar Zenith', 'Temperature $
                                    Ch3','Temperature Ch4', 'Temperature Ch5']
RangeX     = [0,0,60,240,240,240,100,100, 90,280,280,280]
RangeY     = [0,0,0,0,0,0,0.1,0.1,0.1,0.1,0.1,0.1]
Bin        = [2.0,2.0,0.5,0.5,0.5,0.5]
Wnumber    = 1
Selection  = LONARR(1)
HISTOGRAMS, H_Data, Title, Names, RangeX, RangeY, Image_ID, WNumber, Bin
```

```
Selection;

        WSET, WNumber
        File_Name = 'Original_' + File_Date + '.bmp'
        WRITE_BMP, File_Name, TVRD()
        WSHOW, WNumber, /ICONIC

Skip_hst1:
```

; Plots histograms of valid data.

```
        Process = 0

Plot_Histograms:

        IF Displays EQ 'No' THEN GOTO, Skip_hst2
        PRINT, 'Plotting histograms of valid data...'
        Title   = 'Valid Data After Screening and Filtering'
        H_Data  = [H_Albedo1,H_Albedo2,H_Solza,H_Temper1,H_Temper2,H_Temper3]
        Names   = ['Albedo Ch1','Albedo Ch2','Solar Zenith','Temperature $
                                              Ch3','Temperature Ch4', 'Temperature Ch5']
        Range   = [0,0,60,240,240,240,100,100, 90,280,280,280]
        RangeY  = [0,0,0,0,0,0,0,0.12,0.12,0.12,0.12,0.12,0.12]
        Bin     = [2.0,2.0,0.5,0.5,0.5,0.5]
        WNumber = 2 Selection = Good
        HISTOGRAMS, H_Data,Title,Names,RangeX,RangeY,Image_ID,WNumber,Bin,Selection
        WSET, WNumber
        File_Name = 'Filtered_' + File_Date + '.bmp'
        WRITE_BMP, File_Name, TVRD()
        WSHOW, WNumber, /ICONIC

Skip_hst2:

        IF Process EQ  1 THEN GOTO, End_Stat
```

; Calls the function ALBEDO.PRO to calculate a normalised albedo based on Channels
; 1 and 2 and the three angles generated above. Calibrates the gain if requested.

```
        PRINT, 'Calculating the normalized broadband albedo (ALBEDO.PRO)...'
        H_Alpha = ALBEDO(Albedos, Angles, Auxiliar, Avg_Solza, Image_Id, $
                File_Id, Sat, AVHRR_Size, Displays)
        HANDLE_VALUE, H_Alpha, Alpha
```

; Calls the function TEMPER.PRO to calculate an IST based on Channels
; 1 and 2 brightness temperatures and the solar zenith angle generated above.

```
        PRINT, 'Calculating the IST (TEMPER.PRO)...'
        H_Ts = TEMPER(Temperatures, Angles, Auxiliar, Sat, Image_Id, $
                File_Id, AVHRR_Size, Displays)
        HANDLE_VALUE, H_Ts, Ts
        HANDLE_VALUE, H_Data_Mask , Data_Mask
        HANDLE_VALUE, H_Icemap, icemap
        H20_Sal = 34.2743
```

; Calculates the temperature of freezing sea water based on average salinity for V2(96)

```
        Tw = 273.15 + (-0.055 * H20_Sal)
```

; Excludes from the dataset the pixels that have albedo greater than 100% or ice surface
; temperature greater than -1.8C or less than -53C. Also removes NaN occurrences.

```
Bad = WHERE((Data_Mask EQ -1) OR (Alpha LT 0) OR (Alpha GT 1) $
       OR (Ts LT 220) OR (Ts GT Tw), Bad_cnt)
IF Bad_cnt GT 0 THEN Data_Mask(Bad) = -1
Bad = WHERE(Ts NE Ts, Bad_cnt)
IF Bad_cnt GT 0 THEN Data_Mask(Bad) = -1
Bad = WHERE(Alpha NE Alpha, Bad_cnt)
IF Bad_cnt GT 0 THEN Data_Mask(Bad) = -1
Bad = WHERE((Icemap EQ 0) AND (Ts GT Tw), Bad_cnt)
IF Bad_cnt GT 0 THEN Data_Mask(Bad) = -2
VCIce = WHERE(Icemap EQ 23, VCIce_cnt)
IF VCIce_cnt GT 0 THEN Data_Mask(VCIce) = -3
Cloud = WHERE((Icemap GE 3) AND (Icemap LE 13), Cloud_cnt)
IF Cloud_cnt GT 0 THEN Data_Mask(Cloud) = -5
Coast = WHERE(Icemap EQ 25, Coast_cnt)
IF Coast_cnt GT 0 THEN Data_Mask(Coast) = -6
Land  = WHERE(Icemap EQ 29, Land_cnt)
IF Land_cnt GT 0  THEN Data_Mask(Land)  = -7
Good = WHERE(Data_Mask EQ  1, Good_cnt)
Bad = WHERE(Data_Mask LT  0,  Bad_cnt)

PRINT, 'Number of valid pixels:..... ', Good_cnt
PRINT, 'Number of bad pixels:..... ', Bad_cnt
```

; Calls the function GASP.PRO to locate and open the two sets of neighbour GASP files.
; Performs a temporal interpolation to match the AVHRR acquisition time and also performs
; a spatial interpolation to match the size of the AVHRR array.

```
PRINT, 'Generating wind and air temperature data from GASP...'
GASP_Data = GASP(AVHRR_Size, File_id, Image_id, Displays, WNumber)
H_Ta = Gasp_Data(0) & H_u  = Gasp_Data(1)
H_v  = Gasp_Data(2) & Gasp_Data = [H_Ta, H_u, H_v]
```

; Generates 3D arrays to pass the outputs to other procedures.

```
H_Alpha = HANDLE_CREATE() & H_Ts = HANDLE_CREATE()
HANDLE_VALUE, H_Alpha, Alpha, /SET  & HANDLE_VALUE, H_Ts , Ts, /SET
HANDLE_VALUE, H_Data_Mask, Data_Mask, /SET
HANDLE_VALUE, H_Icemap, Icemap, /SET
Auxiliar = [H_Data_Mask, H_Icemap ] & Outputs = [H_Alpha, H_Ts]
```

; Calls the function NET_FLUX.PRO to calculate ice thickness using the normalised albedo
; and IST from AVHRR.

```
PRINT, 'Calculating the ice thickness (NET_FLUX.PRO)...'
Zi = NET_FLUX(Outputs,Angles,GASP_Data,Auxiliar,AVHRR_Size,Image_Id,File_Id)
H_Zi = zé[0] & H_Ta = zé[1] & H_Data_Mask = zé[2]
HANDLE_VALUE, H_Zi, Zi & HANDLE_VALUE, H_Ta, Ta
HANDLE_VALUE, H_Data_Mask , Data_Mask
Good = WHERE(Data_Mask EQ  1, Good_cnt) & Bad = WHERE(Data_Mask LT 0, Bad_cnt)
PRINT, 'Final number of valid pixels:..... ', Good_cnt
PRINT, 'Final number of bad pixels:..... ', Bad_cnt
```

; Calls the procedure WINDOW_OUTPUTS.PRO to display data on the screen.

```
HANDLE_VALUE, H_Data_Mask , Data_Mask
Auxiliar = [H_Data_Mask, H_Icemap ] & WNumber = 6
Outputs  = [H_Alpha, H_Ts, H_Ta, H_Zi]
WINDOW_OUTPUTS, Image_Id,Auxiliar,Outputs,Colors,File_ID,AVHRR_Size,WNumber
```

; Calls a widget that displays portions of the data based on conditions specified by the user.

```
IF Displays EQ 'No' THEN GOTO, End_Stat
Dialog_Box = DIALOG_MESSAGE('Display portions of data set?',/QUESTION, /DEFAULT_NO)
IF Dialog_Box EQ 'No ' THEN GOTO, End_Stat
IF Dialog_Box EQ 'Yes' THEN BEGIN
        WSHOW, 1, /ICONIC & WSHOW, 2, /ICONIC
        DISPLAYER, Albedos,Temperatures, Outputs, Auxiliar, AVHRR_Size, Colors
        HANDLE_VALUE, H_Data_Mask, New_Mask
        Count_Test = WHERE(New_Mask EQ -1, New_Cnt)
        IF Bad_cnt NE New_cnt THEN BEGIN
                Data_Mask = New_Mask
                HANDLE_VALUE, H_Data_Mask, Data_Mask
                Auxiliar = [H_Data_Mask, H_Icemap] & Process = 1
                WINDOW_OUTPUTS, Image_Id, Auxiliar, Outputs, Colors
                HANDLE_VALUE, H_Solza   , Solza
                HANDLE_VALUE, H_Albedo1 , Albedo1
                HANDLE_VALUE, H_Albedo2 , Albedo2
                HANDLE_VALUE, H_Temper2 , Temper2
                HANDLE_VALUE, H_Temper3 , Temper3
                HANDLE_VALUE, H_Icemap  , Icemap
                GOTO, Plot_Histograms
        ENDIF
ENDIF

End_Stat:
```

; Attaches the three new bands (Alpha Ts and Zi) to the original file and saves is as new
; *.dat file ready to be opened by ENVI.

```
GOTO, Skip_Save
CD, '..' & CD, 'envi'
output_image = File_Id + '.dat'
Noise = WHERE((Icemap EQ 3) OR (Icemap EQ 5) OR (Icemap EQ 13) $
        OR (Data_Mask LT 0), Noise_cnt)
Alpha(Noise) = -1 & Ts(Noise) = -1 & zé(Noise) = -1
Land = WHERE(Icemap EQ 29)
Alpha(Land)= -2 & Ts(Land) = -2 & Zi(Land) = -2 & Coast = WHERE(Icemap EQ 25)
Alpha(Coast)= -3 & Zi(Coast)= -3 & Ts(Coast)= -3 & Alpha(Good)= 100*Alpha(Good)
Ts (Good) = 100 * Ts(Good) & Zi (Good) = 100 * Zi(Good)
new_bands = 10 & hdr(3) = new_bands
image2 = INTARR(AVHRR_Columns,new_bands,AVHRR_Lines)
image2(0,0,0) = image1
image2(0,new_bands-1,0) = REFORM(TEMPORARY(Alpha),x,1,y)
image2(0,new_bands-2,0) = REFORM(TEMPORARY(Ts),x,1,y)
image2(0,new_bands-3,0) = REFORM(TEMPORARY(Zi),x,1,y)
OPENW, lun, output_image, /get_lun & WRITEU, lun, hdr
WRITEU, lun, image2 & WRITEU, lun, userrec & FREE_LUN, lun

Skip_Save:
```

; Create handlers to pass to MAIN.PRO.

```
H_File_Name = HANDLE_CREATE()
HANDLE_VALUE, H_Data_Mask, Data_Mask, /SET
HANDLE_VALUE, H_File_Name, File_ID, /SET
HANDLE_VALUE, H_Zi, Zi, /SET
```

; Calculates the running time before closing the program.

```
T1 = SYSTIME(2)
Running_Time = T1 - T0
PRINT, ' Running Time (min):.....' , Running_Time/60
Fim:
END
;
```

8.3 DESPECKLE.PRO

```
;_____________________________________________________________________
;
; NAME:                    DESPECKLE.PRO
; PURPOSE:                 Remove random noise from the image by using
                           a 3 x 3 matrix smoothing filter.
; CATEGORY:                None
; CALLING SEQUENCE:        None
; INPUTS:                  Image being processed by the main routine.
; KEYWORD PARAMETERS:      None
; OUTPUTS:                 Alterations in the ICE MAP band.
; COMMON BLOCKS:           None
; PROCEDURES & FUNCTIONS:  None
; AUTHOR(S):               Katrina Hill, January 1999
; MODIFICATION HISTORY:    None
;_____________________________________________________________________

FUNCTION FILT, t_data,x,y
;_____________________________________________________________________
```

; Common values for mask, size mask and edge (use as columns).

```
        col = 0 & w = 3 & edge = 1 & out_edge = 2
        data2 = INTARR(x,y)

        FOR i = edge,x-out_edge DO BEGIN
                FOR j = edge,y-out_edge DO BEGIN
                        c = t_data(i,j)
                        n = t_data(i-edge:i+edge,j-edge:j+edge)
                        n = WHERE(n EQ c, cnt)
                        IF ((cnt EQ 1) OR (cnt EQ 2)) THEN data2(i,j) = 1
                ENDFOR
        ENDFOR

        ND = WHERE(data2 EQ 1)
        t_data(ND)=col
        RETURN, t_data
END
;_____________________________________________________________________

FUNCTION DESPECKEL, data, icemap=icemap
;_____________________________________________________________________

        im_size=SIZE(data)
        IF (im_size(0) EQ 3) THEN data=REFORM(data(*,0,*))
        IF (im_size(2) EQ 5) THEN data=REFORM(data(*,5,*))
        PRINT, 'Filtering data. Please wait...'
        IF (KEYWORD_SET(icemap)) THEN BEGIN
                1 =(data EQ 5 )&l1_f=FILT(l1,im_size(1),im_size(2))        ; yellow
                2 =(data EQ 0 )&l2_f=fILT(l2,im_size(1),im_size(2))        ; black
                3 =(data EQ 17)&l3_f=FILT(l3,im_size(1),im_size(2))        ; blue
                4 =(data EQ 19)&l4_f=FILT(l4,im_size(1),im_size(2))        ; light blue
                5 =(data EQ 7 )&l5_f=FILT(l5,im_size(1),im_size(2))        ; aqua
                6 =(data EQ 12)&l6_f=FILT(l6,im_size(1),im_size(2))        ; light aqua
                7 =(data EQ 23)&l7_f=FILT(l7, im_size(1),im_size(2))       ; grey
                8 =(data EQ 8 )&l8_f=FILT(l8, im_size(1),im_size(2))       ; dark grey
                9 =(data EQ 29)&l9_f=FILT(l9, im_size(1),im_size(2))       ; light green
                10=(data EQ 28)&l10_f=FILT(l10,im_size(1),im_size(2))      ; green
                11=(data EQ 25)&l11_f=FILT(l11,im_size(1),im_size(2))      ; dark green
                12=(data EQ 1 )&l12_f=FILT(l12,im_size(1),im_size(2))      ; white
```

```
            filt_data = (low_cloud)*5B + (high_cloud)*5B $
                      + (ice_under_low_cloud) *5B $
                      + (ice_under_high_cloud)*5B   + (very_open_sea_ice)*17B $
                      + (open_sea_ice)*19B + (close_sea_ice)*7B $
                      + (very_close_sea_ice)*12B + (compact_sea_ice)*23B $
                      + (interference)*1B + (continental_ice)*8B + (open_water)*0B
        ENDIF ELSE filt_data=FILT(data,im_size(1),im_size(2))
        RETURN, filt_data
END
;_____________________________________________________________________
```

8.4 ALBEDO.PRO

```
;_____________________________________________________________________

; NAME:                                   ALBEDO.PRO
; PURPOSE:                                Calculate surface albedo as a function of
                                          AVHRR channels 1 and 2 based on Lindsay
                                          and Rothrock [1994].
; CATEGORY:                               None
; CALLING SEQUENCE:                       None
; INPUTS:                                 Digital counts from AVHRR's channels 1 and
                                          2; angles generated by AVHRR.PRO and
                                          satellite number.
; KEYWORD PARAMETERS:                     None
; OUTPUTS:                                Albedo image.
; COMMON BLOCKS:                          None
; SYSTEM VARIABLES:                       None
; PROCEDURES & FUNCTIONS:                 None
; AUTHOR(S):                              Clemente Hungria, February 1998
; MODIFICATION HISTORY:                   Katrina Hill, March 1999
;_____________________________________________________________________

FUNCTION ALBEDO,Albedos,Angles,Auxiliar,Avg_Solza,Image_Id,File_Id,Sat,AVHRR_Size, Displays
;_____________________________________________________________________

; Arrays of constants:
; Slope, Intercept, Gain, Offset, Width and Solar were all obtained from the NOAA POD
; user's guide (Kidwell [1991]).

        Offset     = FLTARR (11, 2)
        Width      = FLTARR (11, 2)
        Solar      = FLTARR (11, 2)
        Atm_Slope  = FLTARR (2, 1)
        Slope      = FLTARR (11, 2)
        Int        = FLTARR (11, 2)
        Gain       = FLTARR (11, 2)
        Atm_Int    = FLTARR (2, 1)

Slope(*,0) = [.1071,.1071,.1068,.1060,.1063,.1059,.0906,.104025,.1076,.1115,1]
Slope(*,1) = [.1051,.1078,.1069,.1060,.1075,.1061,.0900,.103193,.1035,.1337,1]
Gain(*,0)  = [1.00,1.79,1.79,1.73,1.81,1.79,2.03,1.87149,1.00,1.583017,1.0000]
Gain(*,1)  = [1.00,2.83,2.79,2.81,2.77,2.85,2.81,2.91017,1.00,2.087248,1.0000]
Width(*,0) = [0.325,0.109,0.108,0.113,0.117,0.108,0.113,0.124,0.121,0.136,0.0]
Width(*,1) = [0.303,0.223,0.249,0.230,0.239,0.222,0.229,0.219,0.243,0.245,0.0]
Solar(*,0) = [443.3,179,177.5,183.4,191.3,178.8,184.1,200.1,194.09,221.42,100]
Solar(*,1) = [313.5,233.7,261.9,242.8,251.8,231.5,241,229.9,249.42,252.29,100]
Int(*,0)   = [-3.9,-4.1136,-3.44,-4.1619,-3.8464,-3.5279,-3.73,-4.16098,-3.9747,-4.5715,0]
Int(*,1)   = [-3.5,-3.4539,-3.488,-4.1492,-3.877,-3.4766,-3.39,-4.12770,-3.828,-5.4817,0]
```

```
; NOAA 14              Ch. 1          Ch. 2
;-------------------------------------------------------------
; Pre Launch Gains:    1.730600       2.281840
; New Gains:           1.583017       2.087248
; Rao and Chen [1994]  1.540000       1.990000
;-------------------------------------------------------------
```

; Atmospheric correction coefficients obtained from *Koepke* [1989].

```
Atm_Slope = [ 0.791 , 0.804] & Atm_Int = [ 0.086  , 0.035]
```

; Define the arrays that came from AVHRR.PRO.

```
H_Albedo1  = Albedos(0)  & H_Albedo2   = Albedos (1)
H_Solza    = Angles (0)  & H_Satza     = Angles (1)
H_Ssaz     = Angles (2)  & H_Data_Mask = Auxiliar(0)
H_Icemap   = Auxiliar(1)

HANDLE_VALUE, H_Albedo1     , Albedo1
HANDLE_VALUE, H_Albedo2     , Albedo2
HANDLE_VALUE, H_Solza       , Solza
HANDLE_VALUE, H_Satza       , Satza
HANDLE_VALUE, H_Ssaz        , Ssaz
HANDLE_VALUE, H_Data_Mask   , Data_Mask
HANDLE_VALUE, H_Icemap      , Icemap
AVHRR_Columns = AVHRR_Size(0) & AVHRR_Lines = AVHRR_Size(1)
```

; Initial IF statement to restrict the calculation only to the valid data using Data_Mask.

```
Good = WHERE((Data_Mask EQ  1), Good_cnt)
Bad  = WHERE((Data_Mask EQ -1),  Bad_cnt)
PRINT, '2nd screening: Filter (valid pixels):..... ', Good_cnt
PRINT, '2nd screening: Filter (bad pixels):..... ', Bad_cnt
```

; Undoes the solar zenith correction and the radiance correction.

```
PRINT, 'Undoing the solar zenith correction on channels 1 and 2...'
Revert_1 = albedo1(Good) * COS(solza(Good))
Revert_2 = albedo2(Good) * COS(solza(Good))
PRINT, 'Returning the values back in to digital counts (di)...'
Digital_counts_1 = (Revert_1 - Intercept[sat,0]) / Slope[sat,0]
Digital_counts_2 = (Revert_2 - Intercept[sat,1]) / Slope[sat,1]
```

; Converts digital counts for channels 1 and 2 to narrow-band radiances.

```
PRINT, 'Obtaining the calibrated narrowband radiances (Li)...'
L1 = (Digital_counts_1 - Offset[sat,0]) / Gain[sat,0]
L2 = (Digital_counts_2 - Offset[sat,1]) / Gain[sat,1]
```

; Converts the narrow-band radiances to corrected narrow-band radiances.

```
PRINT, 'Converting narrowband radiances to corrected narrowband radiances (Ri)...'
R1 = (!pi * Width[sat,0] * L1) / (Solar[sat,0] * COS(solza(Good)))
R2 = (!pi * Width[sat,1] * L2) / (Solar[sat,1] * COS(solza(Good)))
```

; Converts the corrected narrow-band radiances to TOA narrow-band albedos and
; calculate the variables x, y and μ (as functions of the angles).

```
PRINT, 'Converting corrected narrowband radiances to TOA narrowband albedos '
x  = SIN(satza(Good)) * SIN(ssaz(Good))
y  = SIN(satza(Good)) * COS(ssaz(Good)) & mu = COS(solza(Good))
```

; Calculates the narrow-band anisotropic reflectance factor f = f(x,y, μ).

```
Beta_0 =  0.681 & Beta_1 = -0.185 & Beta_2 = -0.222 & Beta_3 =  0.310
Beta_4 =  0.413 & Beta_5 =  0.608 & Beta_6 =  0.338
f = Beta_0+Beta_1*x+Beta_2*y+Beta_3*mu+Beta_4*x^2+Beta_5*y^2+Beta_6 *y*mu
```

; Forms the TOA narrow-band albedos.

```
TOA_1 = R1 / f & TOA_2 = R2 / f
```

; Calculates the surface narrow-band albedo, corrected for atmospheric attenuation.

```
PRINT, 'Calculating the surface narrowband albedo...'
Narrow_Band_1 = (TOA_1 - Atm_Int[0])/Atm_Slope[0]
Narrow_Band_2 = (TOA_2 - Atm_Int [1])/Atm_Slope[1]
```

; Estimates the broad-band albedo from the two narrow-band albedos.

```
PRINT, 'Estimating the broad band albedo...'
Broad_band = 0.43 * Narrow_band_1 + 0.47 * Narrow_band_2
```

; Normalises the albedo to a solar zenith angle of 70 degrees and calculates the normalised
; albedo.

```
Avg      = STRTRIM(STRING(Avg_Solza*!radeg),2)
h_avg    = 0.85 - 0.075 * COS(avg_solza)
h        = 0.85 - 0.075 * COS(solza(Good))
Alb      =  Broad_band * ((h_avg)/(h))
PRINT, 'Calculating normalized albedo to a solar zenith angle of '+ Avg + '...'
IF Displays EQ 'No' THEN GOTO, Skip_Hst
H_Alpha = HANDLE_CREATE()
HANDLE_VALUE, H_Alpha, Alb, /SET, /NO_COPY
Title  = 'Albedo' & H_Data = [H_Alpha] & Names = ['Albedo']
Range = [0,1] & RangeY = [0,0.04] & Bin = [ 0.01] & WNumber = 3
Selection = LONARR(1)
HISTOGRAMS, H_Data,Title,Names,RangeX,RangeY,Image_ID,WNumber,Bin,Selection
WSET, WNumber
File_Date = STRMID(File_ID, 4,6)
File_Name = 'Albedo_' + File_Date + '.bmp'
WRITE_BMP, File_Name, TVRD()
WSHOW, WNumber, /ICONIC

Skip_Hst:
```

; Reconstruct the albedo array to the size of the AVHRR image and return it to
; AVHRR.PRO.

```
HANDLE_VALUE, H_Alpha, Alb
Alpha = FLTARR (AVHRR_Columns, AVHRR_Lines)
Alpha[Good] = Alb
HANDLE_VALUE, H_Alpha, Alpha, /SET, /NO_COPY
RETURN, H_Alpha
Fim:
END
;
```

8.5 TEMPER.PRO

```
;-------------------------------------------------------------------------------

; NAME:                                   TEMPER.PRO
; PURPOSE:                                Calculate the IST using the method proposed
                                          by Key and Haefliger [1992] and updated by
                                          Key et al. [1997]. The air temperature deltas
                                          will be calculated as a function of wind
                                          direction obtained from GASP.
; CATEGORY:                               None
; CALLING SEQUENCE:                       None
; INPUTS:                                 Digital counts from AVHRR's channels 4 and 5,
                                          satellite zenith angle generated by
                                          AVHRR.PRO and satellite number.
; KEYWORD PARAMETERS:                     None
; OUTPUTS:                                Temperature image.
; PROCEDURES & FUNCTIONS:                 None
; AUTHOR(S):                              Clemente Hungria, February 1998
; MODIFICATION HISTORY:                   None
;-------------------------------------------------------------------------------

FUNCTION TEMPER, Temperatures,Angles,Auxiliar,Sat,Image_Id,File_Id,AVHRR_Size,Displays
;-------------------------------------------------------------------------------
```

; Defines the arrays that were brought from AVHRR.PRO.

```
H_Temper2  = Temperatures(1) & H_Temper3    = Temperatures(2)
H_Solza    = Angles(0)       & H_Data_Mask  = Auxiliar(0)
H_Satza    = Angles(1)       & H_Icemap     = Auxiliar(1)
H_Ssaz     = Angles(2)
HANDLE_VALUE, H_Temper2,  Temper2  & HANDLE_VALUE, H_Temper3,    Temper3
HANDLE_VALUE, H_Solza,    Solza    & HANDLE_VALUE, H_Satza,      Satza
HANDLE_VALUE, H_Ssaz,     Ssaz     & HANDLE_VALUE, H_Data_Mask,  Data_Mask
HANDLE_VALUE, H_Icemap,   Icemap

AVHRR_Columns  = AVHRR_Size(0)
AVHRR_Lines    = AVHRR_Size(1)
```

; Initial IF statement to restrict the calculation only to the valid data using Data_Mask.

```
Good    = WHERE((Data_Mask EQ  1),Good_cnt)
Bad     = WHERE((Data_Mask EQ -1), Bad_cnt)
T11     = Temper2(Good) &T12 = Temper3(Good)
```

; Calculates the satellite scan angle (Ssa) using the satellite zenith angle obtained from
; AVHRR.PRO and calculates the secant (1/cos) of Ssa.

```
Ssa = ASIN(0.99986501 * SIN(Satza(Good))) & Sec = 1/COS(Ssa)
```

; Coefficients were determined through a least squares regression procedure where surface
; temperatures are regressed against modelled brightness temperatures. The values for the
; arrays were provided by *Key et al* [1997]. NOAA14 coefficients provided by Jeff Key.

```
PRINT, 'Choosing the coefficients based on temperature range...'
Cfs = FLTARR (11,12)
```

```
        Cfs(*,0)  = [1,1,-1.216191,1,-1.762823,1,-1.466105,-0.800189,1,-1.180768,1]
        Cfs(*,1)  = [1,1,-6.400722,1,-8.083512,1,-7.100426,-4.823715,1,-5.647743,1]
        Cfs(*,2)  = [1,1,-7.000356,1,-7.985411,1,-7.398464,-6.114496,1,-6.602028,1]
        Cfs(*,3)  = [1,1, 1.004336,1, 1.007446,1, 1.005666, 1.002277,1, 1.003950,1]
        Cfs(*,4)  = [1,1, 1.025619,1, 1.032868,1, 1.028625, 1.019081,1, 1.022697,1]
        Cfs(*,5)  = [1,1, 1.027369,1, 1.031757,1, 1.029138, 1.023614,1, 1.025938,1]
        Cfs(*,6)  = [1,1, 1.365568,1, 0.477679,1, 1.092875, 1.729552,1, 1.616824,1]
        Cfs(*,7)  = [1,1, 0.981037,1, 0.600573,1, 0.857094, 1.138661,1, 0.919952,1]
        Cfs(*,8)  = [1,1, 1.079770,1, 0.921390,1, 1.035730, 1.174924,1, 0.963384,1]
        Cfs(*,9)  = [1,1,-0.650609,1,-0.080109,1,-0.477556,-0.757764,1,-0.729174,1]
        Cfs(*,10) = [1,1, 0.562568,1, 1.158426,1, 0.766613, 0.383119,1, 0.552105,1]
        Cfs(*,11) = [1,1, 0.889363,1, 1.433513,1, 1.073912, 0.676141,1, 0.793529,1]
```

; Selects the appropriate coefficients for the estimation of surface temperature from
; Temper2 and Temper3, based on the value of Temper2 (as per *Key et al.* [1997]) and
; applies the equation to calculate Ts.

```
        PRINT, 'Calculating the snow/ice surface temperatures...'
        Ist = FLTARR(Good_cnt) & Low = WHERE((T11 LT 240), Low_cnt)
        Hi  = WHERE((T11 GT 260), Hi_cnt )
        Med = WHERE((T11 GE 240) AND (T11 LE 260), Med_cnt)
        IF Low_cnt GT 0 THEN BEGIN
               a=Cfs(sat,0) & b=Cfs(sat,3) & c=Cfs(sat,6) & d=Cfs(sat,9)
               Ist(Low) = a + b*(T11(Low)) + c*(T11(Low)-T12(Low)) $
                                           + d*((T11(Low) - T12(Low))*(Sec(Low)-1.0))
        ENDIF
        IF Med_cnt GT 0 THEN BEGIN
               a=Cfs(sat,1) & b=Cfs(sat,4) & c=Cfs(sat,7) & d=Cfs(sat,10)
               Ist(Med) = a + b*(T11(Med)) + c*(T11(Med)-T12(Med)) $
                                           + d*((T11(Med)-T12(Med))*(Sec(Med)-1.0))
        ENDIF
        IF Hi_cnt GT  0 THEN BEGIN
               a=Cfs(sat,2) & b=Cfs(sat,5) & c=Cfs(sat,8) & d=Cfs(sat,11)
               Ist(Hi) = a + b*(T11(Hi)) + c*(T11(Hi) -T12(Hi))  + d*((T11(Hi) $
                                                        - T12(Hi))*(Sec(Hi)-1.0))
        ENDIF
        PRINT,'Pixels calculated with low temperature range coeff.',Low_cnt
        PRINT,'Pixels calculated with medium temperature range coeff.',Med_cnt
        PRINT,'Pixels calculated with high temperature range coeff.',Hi_Cnt
```

; Plots the IST histogram.

```
        IF Displays EQ 'No'THEN GOTO, Skip_Hst
        H_Ts       = HANDLE_CREATE()
        HANDLE_VALUE, H_Ts, Ist, /SET, /NO_COPY
        Title      = 'Surface Temperature'
        H_Data     = [H_Ts]
        Names      = ['Surface Temperature']
        Range      = [245,275] & RangeY = [0,.1]
        Bin        = [0.5] & WNumber = 4 & Selection = LONARR(1)
        HISTOGRAMS,H_Data,Title,Names,RangeX,RangeY,Image_ID,WNumber,Bin,Selection
        WSET, WNumber
        File_Date  = STRMID(File_ID, 4,6)
        File_Name  = 'SfcTemp_' + File_Date + '.bmp'
        WRITE_BMP, File_Name, TVRD() & WSHOW, WNumber, /ICONIC

Skip_Hst:
```

; Returns the Ts array containing the surface temperature through a pointer.

```
        HANDLE_VALUE, H_Ts, Ist
        Ts = FLTARR(AVHRR_Columns, AVHRR_Lines) & Ts[Good] = Ist
        HANDLE_VALUE, H_Ts, Ts, /SET
RETURN, H_Ts
END
;_____________________________________________________________________
```

8.6 GASP.PRO

```
;-------------------------------------------------------------------------
; NAME: ..... GASP.PRO
; PURPOSE: This function opens the GASP files, generates
;          two 3d arrays, with temperature and wind
;          (u and v), that are the closest to the AVHRR
;          acquisition time. It interpolates them temporally
;          to match the acquisition time and spatially to
;          match the size of the AVHRR pixel.
; CATEGORY: None
; CALLING SEQUENCE: None
; INPUTS: GASP files, AVHRR number of lines and
;         corner coordinates.
; KEYWORD PARAMETERS: None
; OUTPUTS: Three arrays containing GASP temperature,
;          wind direction and speed.
; COMMON BLOCKS: None
; SYSTEM VARIABLES: None
; PROCEDURES & FUNCTIONS: None
; AUTHOR(S): Clemente Hungria, May 1998
; MODIFICATION HISTORY: None
;-------------------------------------------------------------------------

FUNCTION GASP, AVHRR_Size, File_id, Image_id, Displays, WNumber
;-------------------------------------------------------------------------

; Constants (AVHRR and GASP box coordinates).

    AVHRR_Columns = AVHRR_Size[0] & AVHRR_Lines = AVHRR_Size[1]
    LOADCT, 43
    DEVICE, PSEUDO_COLOR=8 & DEVICE, DECOMPOSED=0 & DEVICE, RETAIN=2
    Number_colors=!D.N_COLORS
    IF (Number_colors GT 256) THEN Color_Test=1

; Locates the two GASP probable neighbour files in relation to the satellite image using
; its acquisition date and time.

    PRINT, 'Locating nearest GASP files based on the acquisition time...'

; Retrieves date and time of acquisition from the original strings obtained from the image
; header at AVHRR.PRO.

    AVHRR_Year  = '19'+ STRMID (File_id, 4, 2)
    AVHRR_Month = STRMID (File_id, 6, 2)
    AVHRR_Day   = STRMID (File_id, 8, 2)
    AVHRR_Hour  = STRMID (File_id,10, 4)
    AVHRR_Date  = Julday(AVHRR_Month, AVHRR_Day, AVHRR_Year)
    Acquisition = AVHRR_Date + AVHRR_Time
    AVHRR_Time  = FLOAT(((60.*STRMID(AVHRR_Hour, 0, 2)) + $
                                        (STRMID(AVHRR_Hour, 2, 2))) / 1440.)
    Dec_Hour    = 1.0/24.0
    Dec_05      =  5.0 * Dec_Hour & Dec_06 =  6.0 * Dec_Hour
    Dec_11      = 11.0 * Dec_Hour & Dec_17 = 17.0 * Dec_Hour
    Dec_23      = 23.0 * Dec_Hour

    CD, 'gasp'
```

```
IF AVHRR_Time GT 0.0    AND AVHRR_Time LT Dec_05 THEN BEGIN
        Pre_Dec   = AVHRR_Date - 1 & Post_Dec  = AVHRR_Date
        Pre_Hour  = Dec_23 & Post_Hour = Dec_05
ENDIF
IF AVHRR_Time GE Dec_05 AND AVHRR_Time LT Dec_11 THEN BEGIN
        Pre_Dec   = AVHRR_Date & Post_Dec  = AVHRR_Date
        Pre_Hour  = Dec_05 & Post_Hour = Dec_11
ENDIF
IF AVHRR_Time GE Dec_11 AND AVHRR_Time LT Dec_17 THEN BEGIN
        Pre_Dec   = AVHRR_Date & Post_Dec  = AVHRR_Date
        Pre_Hour  = Dec_11 & Post_Hour = Dec_17
ENDIF
IF AVHRR_Time GE Dec_17 AND AVHRR_Time LT Dec_23 THEN BEGIN
        Pre_Dec   = AVHRR_Date        & Post_Dec  = AVHRR_Date
        Pre_Hour  = Dec_17 & Post_Hour = Dec_23
ENDIF
IF AVHRR_Time GE Dec_23 AND AVHRR_Time LT 1.0    THEN BEGIN
        Pre_Dec   = AVHRR_Date        & Post_Dec  = AVHRR_Date + 1
        Pre_Hour  = Dec_23 & Post_Hour = Dec_05
ENDIF
```

```
Build_Pre:

        CALDAT, FLOOR(Pre_Dec) , Pre_Month , Pre_Day , Pre_Year
        Pre_Year   = STRING(STRMID(STRTRIM(Pre_Year,2 ),2,2))
        IF Pre_Month LT 10 THEN Pre_Month = '0'+STRING(STRTRIM(Pre_Month, 2))
        IF Pre_Month GE 10 THEN Pre_Month = STRING(STRTRIM(Pre_Month, 2))
        IF Pre_Day LT 10 THEN Pre_Day = '0' + STRING(STRTRIM(Pre_Day, 2))
        IF Pre_Day GE 10.0 THEN Pre_Day = STRING(STRTRIM(Pre_Day, 2))
        IF Pre_Hour EQ Dec_05 THEN Str_Hour ='0' + STRING(STRTRIM((FLOOR(Pre_Hour*24)),2))
        IF Pre_Hour GT Dec_05 THEN Str_Hour = STRING(STRTRIM((FLOOR(Pre_Hour*24)),2))
        Pre_U_Filename ='u'+Pre_Year + Pre_Month + Pre_Day + Str_Hour + '.dat'
        Pre_V_Filename ='v'+Pre_Year + Pre_Month + Pre_Day + Str_Hour + '.dat'
        Pre_T_Filename = 'temperature' + Pre_Year + Pre_Month + Pre_Day + Str_Hour + '.dat'
```

; Searches the dataset for a file with such a name.

```
        File_Test = FINDFILE(Pre_U_Filename, COUNT=cnt)
        IF cnt EQ 0 THEN BEGIN
                Pre_Hour = Pre_Hour - Dec_06
                IF Pre_Hour LT 0 THEN  Pre_Hour = Dec_23 & Pre_Dec  = Pre_Dec - 1
                GOTO, Build_Pre
        ENDIF
```

; Repeats the process for the "POST" files.

```
Build_Post:

        CALDAT, FLOOR(Post_Dec) , Post_Month , Post_Day , Post_Year
        Post_Year   = STRING(STRMID(STRTRIM(Post_Year,2 ),2,2))
        IF Post_Month    LT 10 THEN Post_Month ='0'+STRING(STRTRIM(Post_Month, 2))
        IF Post_Month    GE 10 THEN Post_Month = STRING(STRTRIM(Post_Month, 2))
        IF Post_Day      LT 10 THEN Post_Day   ='0' + STRING(STRTRIM(Post_Day, 2))
        IF Post_Day      GE 10 THEN Post_Day   = STRING(STRTRIM(Post_Day, 2))
        IF Post_Hour EQ Dec_05 THEN Str_Hour   = '0' + $
                                    STRING(STRTRIM((FLOOR(Post_Hour*24)),2))
        IF Post_Hour GT Dec_05 THEN Str_Hour = STRING(STRTRIM((FLOOR(Post_Hour*24)),2))
        Post_U_Filename = 'u'+Post_Year+Post_Month+Post_Day+Str_Hour+'.dat'
        Post_V_Filename = 'v'+Post_Year+Post_Month+Post_Day+Str_Hour+'.dat'
        Post_T_Filename = 'temperature'+Post_Year+Post_Month+Post_Day+ Str_Hour + '.dat'
```

; Searches the dataset for a file with such a name.

```
File_Test = FINDFILE(Post_U_Filename, COUNT=cnt)
IF cnt EQ 0 THEN BEGIN
        Post_Hour = Post_Hour + Dec_06
        IF Post_Hour GT 1 THEN Post_Hour=Dec_05 & Post_Dec=Post_Dec + 1
        GOTO, Build_Post
ENDIF
```

; Opens the 6 neighbour GASP files (PRE and POST acquisition time).

```
PRINT, 'Opening the files...'
        IF AVHRR_Year EQ '1996'THEN BEGIN
                Nlins=11 & Ncols = 13 & Cols = 51 & Lins = 151 & Col0 = 4900
                Lin0 = 2060 & X_Size = 52 & Lon_Lab = -55.9 & Lat_Lab = 65.5
                x1=4 & x2=14 & y1=11 & y2=23
                Lats = INDGEN(Nlins)*(1.5) - 71 & Lons = INDGEN(Ncols)*1.5 + 66
                Border = [-70.95,66.0,-56.02,84.0]
                Box_x  = [ 66.3998, 79.0113, 83.5892, 75.8124, 66.3998]
                Box_y  = [-69.5220,-70.8592,-57.8646,-57.1023,-69.5220]
        ENDIF

        IF AVHRR_Year EQ '1995'THEN BEGIN
                Nlins = 10 & Ncols= 22 & Cols = 77 & Lins= 126 & Col0 = 2160
                Lin0  = 1150 & X_Size = 22 & Lon_Lab = -57.3 & Lat_Lab = 125
                x1=5 & x2=14 & y1=0 & y2=21
                Lats = INDGEN(Nlins)*(1.5) - 70.5 & Lons = INDGEN(Ncols)*1.5 + 126
                Border =[-70.5,126,-57.0,157.5]
                Box_x = [ 127.476,  137.291,  156.140,  147.995,  127.476]
                Box_y = [-62.6756, -58.2403, -64.2586, -70.2206, -62.6756]
        ENDIF
        Junk=' ' &      Array = FLTARR(18,X_Size)

FOR i=0,5 DO BEGIN
                CASE i OF
                0:BEGIN
                        Name =  Pre_U_Filename
                        OpenR, LUN, Name, /GET_LUN
                        ReadF, LUN, junk
                        ReadF, LUN, Array
                        Pre_U = Array[x1:x2, y1:y2]
                        FREE_LUN, LUN
                END
                1:BEGIN
                        Name =  Pre_V_Filename
                        OpenR, LUN, Name, /GET_LUN
                        ReadF, LUN, junk
                        ReadF, LUN, Array
                        Pre_V = Array[x1:x2, y1:y2]
                        FREE_LUN, LUN
                END
                2:BEGIN
                        Name =  Pre_T_Filename
                        OpenR, LUN, Name, /GET_LUN
                        ReadF, LUN, junk
                        ReadF, LUN, Array
                        Pre_T = Array[x1:x2, y1:y2]
                        FREE_LUN, LUN
                END
                3:BEGIN
                        Name =  Post_U_Filename
                        OpenR, LUN, Name, /GET_LUN
                        ReadF, LUN, junk
                        ReadF, LUN, Array
                        Post_U = Array[x1:x2, y1:y2]
                        FREE_LUN, LUN
                END
```

```
                4:BEGIN
                        Name =  Post_V_Filename
                        OpenR, LUN, Name, /GET_LUN
                        ReadF, LUN, junk
                        ReadF, LUN, Array
                        Post_V = Array[x1:x2, y1:y2]
                        FREE_LUN, LUN
                END
              5:BEGIN
                        Name =  Post_T_Filename
                        OpenR, LUN, Name, /GET_LUN
                        ReadF, LUN, junk
                        ReadF, LUN, Array
                        Post_T = Array[x1:x2, y1:y2]
                        FREE_LUN, LUN
                END
        ENDCASE
ENDFOR
CD, '/u/chungria/idl'
```

; Temporal interpolation.

```
PRINT, 'Performing linear temporal interpolation...'
IF Pre_U_Filename EQ Post_U_Filename THEN BEGIN
        GASP_u = Pre_U & GASP_v = Pre_V & GASP_t = Pre_T
        GOTO, Spatial_Interpolation
ENDIF
GASP_Gap =1440.* (((Post_Dec-Pre_Dec) + Post_Hour) -  Pre_Hour)
AVHRR_Gap=(1440.* (AVHRR_Date-Pre_Dec)) + 60*(FIX(STRMID(AVHRR_Hour, $
                0, 2))) + FIX(STRMID(AVHRR_Hour, 2,2)) - (1440.*Pre_hour)

U_Difference = Post_U - Pre_U
V_Difference = Post_V - Pre_V
T_Difference = Post_T - Pre_T
GASP_U = Pre_U + ((U_Difference / GASP_Gap) * AVHRR_Gap)
GASP_V = Pre_V + ((V_Difference / GASP_Gap) * AVHRR_Gap)
GASP_T = Pre_T + ((T_Difference / GASP_Gap) * AVHRR_Gap)
```

; Spatial Interpolation. Firstly the GASP data is rotated 270 degrees counter clockwise.

```
        PRINT, 'Rotating the GASP data...'

Spatial_Interpolation:

        Gasp_U = ROTATE(GASP_U,4)
        Gasp_V = ROTATE(GASP_V,4)
        Gasp_T = ROTATE(GASP_T,4)
```

; Step 1: Create two arrays containing the x's and y's.

```
        PRINT, 'Interpolating the GASP data...'
        Column = INDGEN(Cols)*(-10) + Col0 & Line = INDGEN(Lins)*10 + Lin0
        Y_array=REPLICATE(1,Cols) # Line & X_array=Column # REPLICATE(1,Lins)
```

; Step 2: Run Map_Loc to generate 2 arrays containing the latitudes and longitudes that
; correspond to the x's and y's from Step 1.

```
        LL = LAT_CONVERT(Y_array, X_array)
        Y_Size = Cols -1 & X_Size = Cols*2 -1
        Lts = LL[0:Y_Size   ,*] & Lns = LL[Cols:X_Size,*]
```

; Convert the latitudes and longitudes to grid coordinates.

```
        Lts = (- Lats(0) + Lts)/1.500 & Lns = (Lns - Lons(0))/1.500
```

; Step 3: Interpolate the three GASP arrays into an array 10 times smaller than the AVHRR
; using the latitudes and longitudes from Step 2.

```
U  = INTERPOLATE(Gasp_U, Lns, Lts)
V  = INTERPOLATE(Gasp_V, Lns, Lts)
Ta = INTERPOLATE(Gasp_T ,Lns, Lts)
```

; Generates a three dimensional array holding the GASP data and saves the file using the
; name structure 'GASP_YYMMDDHH', saving it as a file.

```
CD, 'gasp/outputs'
PRINT, 'Generating a 3D array...'
File_Name = 'gasp_'+ File_Id + '.dat'
GASP_Data = FLTARR(Cols,Lins,3)
GASP_Data(0,0,0) = Ta  & GASP_Data(0,0,1) = U & GASP_Data(0,0,2) = V
PRINT, 'Saving array as ' + File_Name + ' ...'
OPENW, lun, File_Name, /GET_LUN
WRITEU, lun, GASP_Data
FREE_LUN, lun
CD, '/u/chungria/idl'
```

; Calculates the statistics for wind speed and air temperature and plots histograms.

```
Ws = SQRT(v^2 + u^2)
Speed_Stats = MOMENT(Ws) & Mean_Speed = Speed_Stats[0]
Temp_Stats  = MOMENT(Ta) & Mean_Temp  = Temp_Stats [0]
PRINT, 'Mean Wind Speed:.....', Mean_Speed
PRINT, 'Mean Air Temperature:....', Mean_Temp
```

; Plots contour curves of temperature data and a wind vector field.

```
PRINT, 'Plotting temperature contour and wind vector maps...'
!P.BACKGROUND = 1 & WNumber = WNumber + 1
WINDOW, WNumber, XSIZE=1000, YSIZE=500, XPOS=750, YPOS=1, $
                                TITLE= 'GASP data corresponding to :' + Image_id
!P.MULTI = [0,2,1] & !P.FONT  = 0
DEVICE, FONT=Times
Lat_Center = Border(2) + ((Border(0)-Border(2))/2)
Lon_Center = Border(3) + ((Border(1)-Border(3))/2)
MAP_SET, Lat_Center, Lon_Center, /STEREO, LIMIT=Border, /HIRES
MAP_GRID, GLINESTYLE=1, LABEL=1, COLOR=8, LONLAB=Lon_Lab, LATLAB=Lat_Lab
MAP_CONTINENTS, /COASTS, /HIRES, COLOR=8
Gasp_T = Gasp_T - 273.15
CONTOUR, Gasp_T, Lons, Lats,/OVERPLOT, C_CHARSIZE=0.8, COLOR=0, $
                                    LEVELS=[-40,-35,-30,-25,-20,-15,-10,0,5]
PLOTS, Box_x, Box_y, COLOR=2, /DATA
MAP_SET,Lat_Center,Lon_Center,/STEREO,LIMIT=Border,/NOERASE,/HIRES
MAP_GRID, GLINESTYLE=1, LABEL=1, COLOR=8, LONLAB=Lon_Lab, LATLAB=Lat_Lab
MAP_CONTINENTS, /COASTS, /HIRES, COLOR=8
FOR i = 0,Ncols - 1 DO BEGIN
       FOR j = 0,NLins - 1 DO BEGIN
              Pos_0 = CONVERT_COORD(Lons(i), Lats(j), /DATA, /TO_DEVICE)
              X0 = Pos_0(0) & Y0 = Pos_0(1)
              X1 = X0 - Gasp_U(i,j)*3 & Y1 = Y0 - Gasp_V(i,j)*3
              ARROW, X0,Y0,X1,Y1, /SOLID, COLOR=0, HSIZE=7
       END
END

PLOTS, Box_x, Box_y, COLOR=2, /DATA
XYOUTS, 945, 40, '10 m/s'                    , COLOR=0, ALIGNMENT=0, /DEVICE
XYOUTS, 250, 485, 'Temperature (C)'   , COLOR=0, ALIGNMENT=0, /DEVICE
XYOUTS, 750, 485, 'Wind (m/s)'        , COLOR=0, ALIGNMENT=0, /DEVICE
Box_x = [950, 950, 980, 980, 950]
Box_y = [ 30,  30,  30,  30,  30]
PLOTS, Box_x, Box_y, COLOR=0, /DEVICE
```

; Stops the program to display the window. Restarts it when right mouse button is pressed.

```
CURSOR, X, Y
IF !MOUSE.BUTTON EQ 4 THEN BEGIN
        WSHOW, 3, /ICONIC
ENDIF
```

; Plots the histograms of wind speed and air temperature.

```
Title      = 'Gasp Data'      & Ws          = SQRT(v^2 + u^2)
H_Ta       = HANDLE_CREATE()  & H_Ws        = HANDLE_CREATE()
HANDLE_VALUE, H_Ta, Ta, /SET  & HANDLE_VALUE, H_Ws, Ws, /SET
H_Data     = [H_Ws, H_Ta]     & Names       = ['Wind Speed', 'Air Temperature']
Range      = [0,240, 20,280]  & RangeY      = [0,  0,0.1,0.1] & Bin = [0.5,1.0]
Wnumber    = WNumber + 1      & Selection   = LONARR(1)
HISTOGRAMS,H_Data,Title,Names,RangeX,RangeY,Image_ID,WNumber,Bin,Selection
WSET, WNumber
File_Date  = STRTRIM(STRMID(File_Id, 4, 6),2)
File_Name  = 'Gasp_' + File_Date + '.bmp'
WRITE_BMP, File_Name, TVRD()
WSHOW, WNumber, /ICONIC
```

; Creates Pointers to pass the GASP data to other procedures.

```
H_u = HANDLE_CREATE() & H_v  = HANDLE_CREATE() & H_Ta = ANDLE_CREATE()
HANDLE_VALUE, H_Ta, Ta, /SET & HANDLE_VALUE, H_u , U,  /SET
HANDLE_VALUE, H_v , V,  /SET
GASP_Data = [H_Ta, H_u, H_v]
RETURN, GASP_Data

END
;_____
```

8.7 NET_FLUX.PRO

```
;_____

; NAME:                    NET_FLUX.PRO
; PURPOSE:                 Calculate the ice thickness of each pixel using
                           the thermodynamic model proposed by Yu and
                           Rothrock [1996].
; CATEGORY:                None
; CALLING SEQUENCE:        None
; INPUTS:                  Normalised averaged albedo values obtained
                           from ALBEDO.PRO, Ice/snow surface and air
                           temperature obtained from TEMPER.PRO,
                           Solar Zenith Angle from AVHRR.PRO, Wind
                           vector components and air temperatures
                           obtained from GASP.PRO.
; KEYWORD PARAMETERS:      None
; OUTPUTS:                 Thickness image, thickness distribution
                           histogram.
; COMMON BLOCKS:           None
; SYSTEM VARIABLES:        None
; PROCEDURES & FUNCTIONS:  None
; AUTHOR(S):               Clemente Hungria, February 1998
; MODIFICATION HISTORY:    Katrina Hill, March 1999
;_____

FUNCTION NET_FLUX, Outputs, Angles, GASP_Data, Auxiliar, AVHRR_Size, Image_Id,File_ID
;_____
```

; Data retrieved from the pointers.

```
H_Alpha = Outputs(0) & H_Ts = Outputs(1) & H_Solza = Angles(0)
H_Data_Mask = Auxiliar(0) & H_Icemap = Auxiliar(1) & H_u= GASP_Data(1)
H_v = GASP_Data(2)
HANDLE_VALUE, H_Alpha, Alb
HANDLE_VALUE, H_Ts, Ist
HANDLE_VALUE, H_Solza, Sza
HANDLE_VALUE, H_Data_Mask, Data_Mask
HANDLE_VALUE, H_Icemap, Icemap
HANDLE_VALUE, H_u, u
HANDLE_VALUE, H_v, v

Atm_emissivity  = 0.7855       ;.....Effective atmospheric emissivity.
Sfc_emissivity  = 0.995608     ;.....Average emissivity of snow/ice.
Stefan_Boltzmann = 5.6693E-08  ;.....Stefan-Boltzmann constant.
Ro_air          = 1.295        ;.....Air Density.
Cp_air          = 1004.4       ;.....Specific heat of air in J.Kg-1.K-1.
Po              = 1013         ;.....Surface pressure in hPa.
L               = 2.49E06      ;.....Latent heat of vaporisation in J.Kg-1.
Ko              = 2.034        ;.....thermal conductivity of ice in W.m-1.K-1.
Beta            = 0.13         ;.....Constant expressed in W.m-2.kg-1.
Zo              = 0.02         ;.....Initial ice thickness in m.
ks              = 0.164        ;.....thermal conductivity of snow from V1 95
                               ;..... [Massom et al., 1998]. ks = 0.3097 for
                               ;..... Yu and Rothrock [1996] .

AVHRR_Columns = AVHRR_Size[0] & AVHRR_Lines = AVHRR_Size[1]
```

; Initial statement to restrict the calculation only to the valid data using Data_Mask.

```
Good    = WHERE((Data_Mask EQ 1), Good_cnt)
Bad     = WHERE((Data_Mask LT 0),  Bad_cnt)
```

; Defines the initial ice and snow thicknesses for the first run.
; The snow thickness relationship was derived from data from V1-95.

```
Zs = 0.28 * Zo - 0.035 + 0.035 * EXP(-8.0 * Zo)
```

; Calculates the wind speed based on u and v data from GASP and subscribe.
; all the variables to "good" to make sure the arrays have the same size.

```
PRINT, 'Generating wind speed and direction data..'
u = CONGRID(u, AVHRR_Columns, AVHRR_Lines, INTERP)
v = CONGRID(v, AVHRR_Columns, AVHRR_Lines, INTERP)
Ws = SQRT (u^2 + v^2)
Ws = Ws/1.4710297       ; This step converts the GASP wind speed from the 0.991
W_Speed = Ws(Good)      ; sigma level (approximately 71.76m) to 2 m using
                        ; the logarithmic wind profile [Oke, 1990].

Q1 = WHERE((u GE 0.0) AND (v GE 0.0), cnt1)
Q2 = WHERE((u GE 0.0) AND (v LE 0.0), cnt2)
Q3 = WHERE((u LE 0.0) AND (v LE 0.0), cnt3)
Q4 = WHERE((u LE 0.0) AND (v GE 0.0), cnt4)
Wd = FLTARR(AVHRR_Columns, AVHRR_Lines)

IF cnt1 GT 0 THEN Wd(Q1)      = 180 + !RADEG*ATAN(u(Q1)/v(Q1))
IF cnt2 GT 0 THEN Wd(Q2)      = 360 + !RADEG*ATAN(u(Q2)/v(Q2))
IF cnt3 GT 0 THEN Wd(Q3)      = !RADEG*ATAN(u(Q3)/v(Q3))
IF cnt4 GT 0 THEN Wd(Q4)      = 180 + !RADEG*ATAN(u(Q4)/v(Q4))
Ts = Ist(Good) & Solza = Sza(Good) & Alpha = Alb(Good)
PRINT, 'Generating an air temperature image..'
Sat = FLTARR (AVHRR_Columns, AVHRR_Lines)
```

; Several methods of estimating the air temperature.

```
; Ta = 1.0337*Ts -9.0091          ; Ta based on in situ measurements
; Ta = Ts + 0.4                   ; Ta used by Yu and Rothrock [1996].
```

; Change the size of the box according to wind speed

```
; IF Ws(Col, Lin) GT 5  THEN m = 7 & IF Ws(Col, Lin) GT 10 THEN m = 9
; IF Ws(Col, Lin) GT 15 THEN m = 11 & IF Ws(Col, Lin) GT 20 THEN m = 13
```

; Uses the wind direction to find the minimum Ts of a 9x1 strip.

```
FOR i = 0L, Good_cnt-1 DO BEGIN
Point = Good(i)
Lin   = FIX(Point/AVHRR_Columns)
Col   = Point - (Lin * AVHRR_Columns)
Min_t = Ist(Col, Lin) - 4.0 & m=9
```

; 1. Northerly Wind.

```
IF Wd(Col,Lin) GE 157.5 AND Wd(Col,Lin) LT 202.5 THEN BEGIN
       Lin1    = MIN([AVHRR_Lines-1,Lin+(m-1)]) & Col1 = Col
       Box     = Ist(Col:Col1, Lin:Lin1)
ENDIF
```

; 2. North-easterly Wind.

```
IF Wd(Col,Lin) GE 202.5 AND Wd(Col,Lin) LT 247.5 THEN BEGIN
       IF Lin GT (AVHRR_Lines-m  )    THEN m = AVHRR_Lines-Lin
       IF Col GT (AVHRR_Columns-m)    THEN m = AVHRR_Columns-Col
       xs = FINDGEN(m) + Col & ys = FINDGEN(m) + Lin
       Box = Ist(xs,ys)
ENDIF
```

; 3. Easterly Wind.

```
IF Wd(Col,Lin) GE 247.5 AND Wd(Col,Lin) LT 292.5 THEN BEGIN
       Col1    = MIN([AVHRR_Columns-1,Col+(m-1)]) & Lin1 = Lin
       Box     = Ist(Col:Col1, Lin:Lin1)
ENDIF
```

; 4. South-easterly Wind.

```
IF Wd(Col,Lin) GE 292.5 AND Wd(Col,Lin) LT 337.5 THEN BEGIN
       IF Col GT (AVHRR_Columns-m) THEN m = AVHRR_Columns - Col
       IF Lin LT (m-1) THEN m = Lin + 1
       xs = FINDGEN(m) + Col & ys = FINDGEN(m) *(-1) + Lin
       Box = Ist(xs,ys)
ENDIF
```

; 5. Southerly Wind.

```
IF Wd(Col,Lin) GT 337.5 OR Wd(Col,Lin) LT 22.5 THEN BEGIN
       Col1    = Col   & Lin1 = MAX([0,Lin-(m-1)])
       Box     = Ist(Col:Col1, Lin1:Lin)
ENDIF
```

; 6. South-westerly Wind.

```
IF Wd(Col,Lin) GE 22.5 AND Wd(Col,Lin) LT 67.5 THEN BEGIN
       IF Col LT (m-1) THEN m = Col + 1
       IF Lin LT (m-1) THEN m = Lin + 1
       Xs      = FINDGEN(m)*(-1) + Col & ys = FINDGEN(m)*(-1) + Lin
       Box     = Ist(xs,ys)
ENDIF
```

; 7. Westerly Wind.

```
        IF Wd(Col,Lin) GE 67.5 AND Wd(Col,Lin) LT 112.5 THEN BEGIN
                Col1    = MAX([0,Col-(m-1)]) & Lin1 = Lin
                Box     = Ist(Col1:Col, Lin:Lin1)
        ENDIF
```

; 8. North-westerly Wind.

```
        IF Wd(Col,Lin) GE 112.5 AND Wd(Col,Lin) LT 157.5 THEN BEGIN
                IF Col LT (m-1) THEN m = Col + 1
                IF Lin GT (AVHRR_Lines-m) THEN m = AVHRR_Lines - Lin
                xs = FINDGEN(m)*(-1) + Col & ys = FINDGEN(m) + Lin
                Box = Ist(xs,ys)
        ENDIF
        Valid = WHERE(Box GT 100.0)
        Max_T = MIN(Box(Valid))                         ; Establishes a minimum
        Sat(Col, Lin) = MAX([Min_t, Max_t])             ; value of 4K for delta T.
ENDFOR

Ta = Sat(Good) &        H_Ta = HANDLE_CREATE()
HANDLE_VALUE, H_Ta, Ta, /SET, /NO_COPY
Title   = 'Air Temperature'
H_Data  = [H_Ta]        & Names   = ['Air Temperature']
Range   = [245,275]     & RangeY  = [0,0.1] & Bin = [0.5] & WNumber = 7
Selection = LONARR(1)
HISTOGRAMS,H_Data,Title,Names,RangeX,RangeY,Image_ID,WNumber,Bin,Selection
WSET, WNumber
File_Date = STRMID(File_ID, 4,6)
File_Name = 'AirTemp_' + File_Date + '.bmp'
WRITE_BMP, File_Name, TVRD()
WSHOW, WNumber, /ICONIC
HANDLE_VALUE, H_Ta, Ta
```

; WHERE commands to choose the appropriate bulk transfer coefficients.
; Coefficients values for sea ice retrieved from modelled data by *Andreas* [1996] and
; *Andreas* [1987].

```
Wind1 = WHERE((W_Speed GE  0.0) AND (W_Speed LT  2.5), W1_Cnt)
Wind2 = WHERE((W_Speed GE  2.5) AND (W_Speed LT  7.5), W2_Cnt)
Wind3 = WHERE((W_Speed GE  7.5) AND (W_Speed LT 12.5), W3_Cnt)
Wind4 = WHERE((W_Speed GE 12.5) AND (W_Speed LT 17.5), W4_Cnt)
Wind5 = WHERE((W_Speed GE 17.5) AND (W_Speed LT 22.5), W5_Cnt)
Wind6 = WHERE((W_Speed GE 22.5) AND (W_Speed LT 27.5), W6_Cnt)
Wind7 = WHERE((W_Speed GE 27.5), W7_Cnt)
Ch    = FLTARR(Good_cnt) & Ce = FLTARR(Good_cnt)
IF W1_Cnt GT 0 THEN BEGIN
        Ch(Wind1) = 0.0007836735*Zo + 0.00116693
        Ce(Wind1) = 0.0007897959*Zo + 0.00123633
ENDIF
IF W2_Cnt GT 0 THEN BEGIN
        Ch(Wind2) = 0.0003013605*Zo + 0.00113061
        Ce(Wind2) = 0.0003115646*Zo + 0.00116816
ENDIF
IF W3_Cnt GT 0 THEN BEGIN
        Ch(Wind3) = 0.0002013605*Zo + 0.00110041
        Ce(Wind3) = 0.0002163265*Zo + 0.00113306
ENDIF
IF W4_Cnt GT 0 THEN BEGIN
        Ch(Wind4) = 0.000153741*Zo + 0.00107469
        Ce(Wind4) = 0.000170068*Zo + 0.00110571
ENDIF
IF W5_Cnt GT 0 THEN BEGIN
        Ch(Wind5) = 0.001052653*Zo + 0.00012517
        Ce(Wind5) = 0.000140136*Zo + 0.00108612
ENDIF
```

```
IF W6_Cnt GT 0 THEN BEGIN
        Ch(Wind6) = 0.000108843*Zo + 0.001032245
        Ce(Wind6) = 0.000117687*Zo + 0.001069796
ENDIF
IF W7_Cnt GT 0 THEN BEGIN
        Ch(Wind7) = 0.000094558*Zo + 0.001016326
        Ce(Wind7) = 0.000106122*Zo + 0.001054693
ENDIF
```

; Calculates the surface water vapour pressure using the fourth order polynomial
; proposed by *Maykut* [1982].

```
a =  2.7798202e-6
b = -2.6913393e-3
c = 0.97920849
d = -158.63779
e = 9653.1925
Sfc_sat = a * Ts^4 + b * Ts^3 + c * Ts^2 + d * Ts + e
Air_sat = a * Ta^4 + b * Ta^3 + c * Ta^2 + d * Ta + e
Air_s   = Air_sat * 0.81
```

```
;       a0 = 0.107799961
;       a1 = 4.436518521e-01
;       a2 = 1.428945805e-02
;       a3 = 2.650648471e-04        ; The equation below and the coefficients
;       a4 = 3.031240396e-06        ; were obtained from Kelvin's thesis but
;       a5 = 2.034080948e-08        ; didn't produce an acceptable result.
;       a6 = 6.136820929e-11
```

```
; E_air_saturation=a0 + a1*Ta + a2*Ta^2 + a3*Ta^3 + a4*Ta^4 + a5*Ta^5 + a6*Ta^6
; E_sfc_saturation=a0 + a1*Ts + a2*Ts^2 + a3*Ts^3 + a4*Ts^4 + a5*Ts^5 + a6*Ts^6
```

; Calculates incoming shortwave radiation (F_r). This equation is based on *Zillman* [1972] but
; modified by *Shine* [1984] and used again by *Heil* [1996].

```
PRINT, 'Calculating the incoming shortwave radiation (Qs)...'
Mu = COS(Solza)
Qs = 1368 * Mu^2/(1.2 * Mu + (1.0 + Mu) * Air_s * 0.001 + 0.0455)
```

; The original equation below proposed by *Yu and Rothrock* [1996] contained a typing error.

```
; Qs = 1368.0 * Mu/(1.2 * Mu + (1.0 + Mu) * E_air * 10e-3 + 0.046)
```

; The equation below was proposed by *Munk* [1964] but the results weren't very good.

```
; Qs = 1350 * Mu * (0.61 + 0.2 * Mu)
```

; The equation below was proposed by *Zillman* [1972] and used by *Maykut* [1977].

```
; Qs = 1368 * Mu^2/(1.085 * Mu + (2.7 + Mu)* E_air * 10e-3 + 0.1);
```

; Calculates the solar radiation at the surface.

```
PRINT, 'Calculating the solar radiation at the surface (Qs_Sfc)...'
Qs_Sfc = (1 - Alpha) * Qs
```

; Calculates the transmitted fraction of the shortwave spectrum (Z_o in metres)
; obtained from *Grenfell* [1979].

```
PRINT, 'Calculating transmitted fraction of the shortwave spectrum'
Trs = 0.3894 * EXP(-12.39 * Zo) + 0.350 * EXP(-1.578 * Zo)
```

; Calculates the solar radiation that passes through the interior of the ice slab.
; Sign is negative here because the energy is being removed from the ice despite the flux
; being directed downwards.

```
PRINT,'Calculating net solar radiation transmitted through the ice...'
Qs_Trs = -1 * (Qs * (1.0 - Alpha) * Trs)
```

; Calculates the upward longwave radiation.
; Sign is negative here because the flux is directed upwards.

```
PRINT, 'Calculating the upward longwave radiation (Ql_up)...'
Ql_up = -1 * (Sfc_emissivity * Stefan_Boltzmann * (Ts)^4)
```

; Calculates the downward longwave radiation.

```
PRINT, 'Calculating the downward longwave radiation (Ql_down)...'
Ql_down = Atm_emissivity * Stefan_Boltzmann * (Ta)^4
```

; Calculates the turbulent sensible heat flux.

```
PRINT, 'Calculating the turbulent sensible heat flux (Hs)...'
Hs = Ro_air * Cp_air * Ch * W_Speed * (Ta - Ts)
```

; Calculates the latent heat flux.
; The three equations below were tried without success.

```
; Hl = Ro_air * L * Ce * W_Speed * (Air_s - E_sfc_saturation)*(0.622/101300)
; Hl = 0.00005391 * W_Speed * (Air_s - E_sfc_saturation)
; Hl = 0.0179705 * Ce * W_Speed * (Air_s - E_sfc_saturation)
```

; The equation utilised below was obtained from *Maykut* [1982].

```
PRINT, 'Calculating the latent heat flux (Hl)...'
Hl = 0.622 * Ro_air * L * Ce * W_Speed * (Air_s - Sfc_sat)/Po
```

; Calculates the sea ice salinity based on an empirical relationship proposed by *Cox and*
; *Weeks* [1974].

```
PRINT, 'Calculating the sea ice salinity (Sal)....'
Ice_Sal = 14.24 - 19.39 * Zo                    ; Relationship for ice < 40 cm
```

; Calculates the thermal conductivity of sea ice.

```
PRINT, 'Calculating the thermal conductivity of sea ice (ki)....'
ki = ko + ((Beta * Ice_Sal)/(Ts - 273.15))
```

; Calculates the freezing temperature of sea water (T_f) in Degrees Kelvin using the average
; salinity for V2(96).

```
H20_Sal = 34.2743
Tf = 273.15 + (-0.055 * H20_Sal)
```

; Calculates the Conductive Heat Flux (F_C).

```
PRINT, 'Calculating the conductive heat flux (Hc)...'
Hc = -1*((ki * ks)/(Ks * Zo + ki * Zs))*(Tf-Ts)
```

; Adds all the terms to calculate the net flux.

```
PRINT, 'Calculating the net flux...'
Balance  = Qs_sfc + Qs_trs + Ql_up + Ql_down + Hs + Hl + Hc
Zi  = FLTARR(Good_cnt)
```

; Loop to adjust the thickness of all pixels with positive balance. The initial thickness of
; 2cm is increased by 1cm every iteration and this value will be set to the pixels that return a
; positive balance.

```
IF AVHRR_Columns EQ 1501 THEN Itr = 198
IF AVHRR_Columns EQ 1251 THEN Itr = 398
Exclude = WHERE(Balance GE 0, Exclude_cnt)
Include = WHERE(Balance LT 0, Include_cnt)
Inc = Include
IF Exclude_cnt GT 0 THEN Zi(Exclude) = Zo
OPENW, 1, 'histograms.txt', /APPEND
PRINTF, 1,'0.02', Exclude_cnt
PRINT, 'Thickness: ', Zo, ' .........', Exclude_cnt

FOR j = 1,Itr DO BEGIN
        Zo = j*.01 + 0.02
```

; Recalculates the sea ice salinity, bulk transfer coefficients and snow thickness based on
; Z_0 defined above.

```
Zs = 0.28 * Zo - 0.035 + 0.035 * EXP(-8.0 * Zo)
IF Zo GT 0.4  THEN BEGIN
        Ice_Sal = 7.88 -  1.59 * Zo
ENDIF
IF W1_Cnt GT 0 THEN BEGIN
        Ch(Wind1(Inc)) = 0.0007836735 * Zo + 0.00116693
        Ce(Wind1(Inc)) = 0.0007897959 * Zo + 0.00123633
ENDIF
IF W2_Cnt GT 0 THEN BEGIN
        Ch(Wind2(Inc)) = 0.0003013605 * Zo + 0.00113061
        Ce(Wind2(Inc)) = 0.0003115646 * Zo + 0.00116816
ENDIF
IF W3_Cnt GT 0 THEN BEGIN
        Ch(Wind3(Inc)) = 0.0002013605 * Zo + 0.00110041
        Ce(Wind3(Inc)) = 0.0002163265 * Zo + 0.00113306
ENDIF
IF W4_Cnt GT 0 THEN BEGIN
        Ch(Wind4(Inc)) = 0.000153741 * Zo + 0.00107469
        Ce(Wind4(Inc)) = 0.000170068 * Zo + 0.00110571
ENDIF
IF W5_Cnt GT 0 THEN BEGIN
        Ch(Wind5(Inc)) = 0.001052653 * Zo + 0.00012517
        Ce(Wind5(Inc)) = 0.000140136 * Zo + 0.00108612
ENDIF
IF W6_Cnt GT 0 THEN BEGIN
        Ch(Wind6(Inc)) = 0.000108843 * Zo + 0.001032245
        Ce(Wind6(Inc)) = 0.000117687 * Zo + 0.001069796
ENDIF
IF W7_Cnt GT 0 THEN BEGIN
        Ch(Wind7(Inc)) = 0.000094558 * Zo + 0.001016326
        Ce(Wind7(Inc)) = 0.000106122 * Zo + 0.001054693
ENDIF
```

; Recalculates the remaining parameters using the new ice thickness, ice salinity and
; bulk coefficients.

```
Trs(Inc) = 0.3894 * EXP(-12.39 * Zo) + 0.350 * EXP(-1.578 * Zo)
Qs_Trs(Inc) = -1 * (Qs(Inc)' * (1.0 - Alpha(Inc)) * Trs(inc))
Hs (Inc) = Ro_air*Cp_air*Ch(Inc)*W_Speed(Inc)*(Ta(Inc)-Ts(Inc))
Hl (Inc) =0.622*Ro_air*L*Ce(Inc)*W_Speed(Inc)*(Air_s(Inc)- Sfc_sat(Inc))/Po
ki (Inc) = ko+(Beta*Ice_Sal)/(Ts(Inc)-273.15)
Hc (Inc) = -1*((ki(Inc)*ks)/(ks*Zo+ki(Inc)*Zs))*(Tf-Ts(Inc))
Balance(Inc) = Qs_sfc(Inc)+Qs_trs(Inc)+Ql_up(Inc)+Ql_down(Inc) $
                                                +Hs(Inc)+Hl(Inc)+Hc(Inc)
```

; Tests the newly calculated balance for positive values.

```
            Exc = WHERE((Balance GE 0) AND (Zi EQ 0.0), Exc_cnt)
            Inc = WHERE((Balance LT 0) AND (Zi EQ 0.0), Inc_cnt)
```

; Redefine Z_i if at least 1 pixel with positive balance is found.

```
            IF Exc_cnt EQ 0.0 THEN BEGIN
                  PRINTF, 1, Exc_cnt
                  PRINT, 'Thickness: ', Zo, ' .........', Exc_cnt
            ENDIF
            IF Exc_cnt GT 0.0 THEN BEGIN
                  Zi (Exc) = Zo
                  PRINTF, 1, Exc_cnt
                  PRINT, 'Thickness: ', Zo, ' .........', Exc_cnt
            ENDIF
            IF Inc_cnt EQ 0 THEN GOTO, Fim
      ENDFOR
      PRINT , 'Thickness GT ', Itr*0.01 + 0.02, ' .........', Inc_cnt
      PRINTF, 1,'GT 2.0',  Inc_cnt
Fim:

CLOSE, 1
```

; Prints the Histogram.

```
      H_Zi = HANDLE_CREATE()
      HANDLE_VALUE, H_Zi, Zi, /SET, /NO_COPY
      Title = 'Ice Thickness' & H_Data = [H_Zi] & Names = ['Ice Thickness']
      Range = [0,1] & RangeY = [0,0.05] & Bin = [0.02] & WNumber = 8
      Selection = LONARR(1)
      HISTOGRAMS, H_Data,Title,Names,RangeX,RangeY,Image_ID WNumber,Bin,Selection
      WSET, WNumber
      File_Date = STRMID(File_ID, 4,6)
      File_Name = 'IceThick_' + File_Date + '.bmp'
      WRITE_BMP, File_Name, TVRD()
      WSHOW, WNumber, /ICONIC
      HANDLE_VALUE, H_Zi, Zi
```

; Creates the sea ice array. Adds a negative value (-4) to the Data_Mask according
; to pixels that didn't reach the equilibrium at the end of the iterations.

```
      Z_ice = FLTARR(AVHRR_Columns, AVHRR_Lines)
      Z_ice(Good) = Zi
      Thick = WHERE((Z_Ice EQ 0.0) AND (Data_Mask EQ 1), Thick_cnt)
      IF Thick_cnt GT 0 THEN Data_Mask(Thick) = -4
      Good    = WHERE((Data_Mask EQ 1), Good_cnt)
      Bad     = WHERE((Data_Mask LT 0),  Bad_cnt)
```

; Creates the handlers to output the Zi image and the Data_Mask.

```
      HANDLE_VALUE, H_Ta , Sat  , /SET
      HANDLE_VALUE, H_Zi , Z_ice, /SET
      HANDLE_VALUE, H_Data_Mask , Data_Mask, /SET
      Outputs = [H_Zi, H_Ta, H_Data_Mask]

      RETURN, Outputs

END
;_____
```

8.8 WINDOW_OUTPUTS.PRO

```
;-------------------------------------------------------------------------
; NAME: ... . . . . ... ... .WINDOW_OUTPUTS.PRO
; PURPOSE: . . . . ... ... This procedure displays the data on the screen
                           in the form of frequency distribution histograms
                           and images, saving the outputs into bitmap files.
; CATEGORY: . ... . .. . . . .. .. . .None
; CALLING SEQUENCE:. . . . .. . .. . . .None
; INPUTS: . . . . .. .. ... ..... . ... Colour tables and data outputs (albedo IST and
                           ice thickness).
; KEYWORD PARAMETERS: . . . . . ... None
; OUTPUTS: ..... ... .. ... . . ..... . . . . Three output windows and three bitmap files.
; COMMON BLOCKS:... . . . .... . . .... None
; PROCEDURES & FUNCTIONS:.. ... . . .. . .None
; AUTHOR(S):.... ..... . .... ..... . . .. .. .. .. .. . Clemente Hungria, November 1998
; MODIFICATION HISTORY: . . . ..... . . . None
;-------------------------------------------------------------------------

PRO WINDOW_OUTPUTS,Image_Id, Auxiliar, Outputs, Colors, File_ID, AVHRR_Size, WNumber
;-------------------------------------------------------------------------
```

; Retrieve the variables from the information passed to the procedure.

```
H_Data_Mask  = Auxiliar (0)  &  H_Icemap  = Auxiliar(1)
H_Alpha      = Outputs  (0)  &  H_Ts      = Outputs (1)
H_Ta         = Outputs  (2)  &  H_Zi      = Outputs (3)
HANDLE_VALUE, H_Data_Mask, Data_Mask  & HANDLE_VALUE, H_Icemap , Icemap
HANDLE_VALUE, H_Alpha , Alpha         & HANDLE_VALUE, H_Ts, Ts
HANDLE_VALUE, H_Ta, Ta                & HANDLE_VALUE, H_Zi, Zi
```

; Codes for Data_Mask:
;-1....Bad data (Noise, NaN).
;-2....Open Water ($T_s > T_w$).
;-3....Very Compacted Ice (Class 23).
;-4....Z_i > limit.
;-5....Cloud (all types 3>Icemap>13).
;-6....Coastline (Icemap = 25).
;-7....Land (Icemap = 29).

```
Bad    = WHERE(Data_Mask LT  0, Bad_cnt)
Good   = WHERE(Data_Mask EQ  1, Good_cnt)
OW     = WHERE(Data_Mask EQ -2, OW_cnt)
Ice    = WHERE(Data_Mask EQ -3, Ice_cnt)
Limit  = WHERE(Data_Mask EQ -4, Limit_cnt)
```

; Tests the number of colours used by the system.

```
LOADCT, 43
DEVICE, PSEUDO_COLOR=8 & DEVICE, DECOMPOSED=0
Number_colors=!D.N_COLORS
IF (Number_colors GT 256) THEN Color_Test=1
IF (Number_colors LE 256) THEN Color_Test=0
```

; Tests the size of the image to decide which mask to load.

```
AVHRR_Columns = AVHRR_Size(0) & AVHRR_Lines = AVHRR_Size(1)
IF AVHRR_Columns EQ 1501 THEN BEGIN
        Area = 0
        GOTO, Davis
ENDIF
```

```
        IF AVHRR_Columns EQ 1251 THEN BEGIN
                Area = 1
                GOTO, Mertz
        ENDIF
```

; Mask image containing the coastline and grids (valid for all three outputs).

```
Mertz:
        File  = 'mertz_mask' & Rotat = 4 & Limit = 4.0 & Top_x = 2.0
        OPENR, lun, file, /get_lun, ERROR=err
        IF (err EQ 0) THEN BEGIN
                Mask=BYTARR(400,200) & READU, lun, Mask
        ENDIF ELSE Mask=0
        FREE_LUN, lun
        Mask = ROTATE(Mask,1) & Grey = WHERE(Mask EQ 2) & Mask(Grey)=22
        GOTO, Start_Loop
```

; Opens and read a mask containing the coastline and grid from a file called 'davis.mask'.

```
Davis:
        File  = 'davis_mask' & Rotat = 4 & Limit = 2.0 & Top_x = 1.0
        OPENR, lun, file, /get_lun, ERROR=err
        IF (err EQ 0) THEN BEGIN
                Mask=BYTARR(200,400) & READU, lun, Mask
        ENDIF ELSE Mask=0
        FREE_LUN, lun

Start_Loop:
```

; FOR Loop that generates the albedo, IST and thickness outputs on the screen (histogram
; and map). Opens a window, and plot the albedo image, a colour legend and the histogram.

```
        FOR i = 1,4 DO BEGIN
                CASE i OF
                        1:BEGIN
                                Fname = '_Alpha' & Title = 'Albedo Outputs for: '
                                Bin_Size = 0.01 & Bin_Min = 0 & Image = Alpha
                                Color_Range = [0.0, 1.0, 20, 95] & X_Range = [0,1]
                                Legend = ['1.0','0.8','0.6','0.4','0.2','0.0']
                        END
                        2:BEGIN
                                Fname ='_Ts' & Title='Surface Temperature Outputs: '
                                Bin_Size = 0.25 & Bin_Min = 248 & Image = Ts
                                X_Range = [248,272] &  Color_Range = [248, 272, 20, 115]
                                Legend = ['273','268','263','258','253','248']
                        END
                        3:BEGIN
                                Fname = '_Ta' & Title = 'Air Temperature Outputs: '
                                Bin_Size = 0.25 & Bin_Min = 248 & Image = Ta
                                X_Range= [248,272] & Color_Range = [248, 272, 20, 115]
                                Legend= ['273','268','263','258','253','248']
                        END
                        4:BEGIN
                                Fname = '_Zi' & Title = 'Ice Thickness Outputs for: '
                                Bin_Size=0.01 & Bin_Min = 0.0015 & Image = Zi
                                X_Range=[0.0,Top_x] & Color_Range=[0, 2.5, 20.0, 135]
                                Legend=['1.0','0.8','0.6','0.4','0.2','0.0']
                        END
                ENDCASE
                WNumber = Wnumber + 1 & !P.BACKGROUND = 1
                WINDOW, WNumber, XSIZE=700, YSIZE=450, XPOS=750, YPOS=1, $
                                                        TITLE= Title + Image_Id
                !P.FONT = 0 & DEVICE, FONT = Times
```

; Histogram.

```
Y_Axis = HISTOGRAM(Image(Good), BINSIZE=Bin_Size, MIN=Bin_Min)
Y_Axis = (Y_Axis*100.0)/Good_cnt & Elements = N_ELEMENTS(Y_Axis)
X_axis = FINDGEN(Elements) * ((MAX(Image(Good)) - $
                MIN(Image(Good)))/(Elements - 1)) + MIN(Image(Good))
PLOT, X_axis, Y_Axis, YMARGIN=[0,2], POSITION=[350,25,685,420], $
/DEVICE, BACKGROUND=1,COLOR=0, XRANGE=[X_Range(0), X_Range(1)], $
                                                    THICK=2.0
```

; Image with a map plotted on top of it.

```
Img = BYTSCL (Image,MIN=Color_Range(0), MAX=Color_Range(1), $
                                        TOP=Color_Range(2)) + Color_Range(3)
Img(Ice) = 80 $ Img(Bad)  = 1 & IF OW_cnt GT 0 THEN Img(OW) = 0
Img = CONGRID(Img,400,200) & Img = ROTATE (Img, Rotat)
Land = WHERE(Mask EQ 1) & Line  = WHERE(Mask EQ 22)
Img(Land) = 70 & Img(Line) = 0
WSET, WINumber
TV, Img, 60, 25
```

; Frame for the image.

```
PLOTS, [59,59,260,260,59],[24,425,425,24,24], COLOR=0, /DEVICE
```

; Labels for the Map.

```
IF Area EQ 0 THEN BEGIN
       XYOUTS, 310, 413, '(%)', COLOR = 0, ALIGNMENT=0,  /DEVICE
       XYOUTS, 263, 50, '-70' , COLOR = 0, ALIGNMENT=0,  /DEVICE
       XYOUTS, 263, 170, '-66', COLOR = 0, ALIGNMENT=0,  /DEVICE
       XYOUTS, 263, 290, '-62', COLOR = 0, ALIGNMENT=0,  /DEVICE
       XYOUTS, 263, 410, '-58', COLOR = 0, ALIGNMENT=0,  /DEVICE
       XYOUTS, 120,  12,  '70', COLOR = 0, ALIGNMENT=0,  /DEVICE
       XYOUTS, 180,  12,  '74', COLOR = 0, ALIGNMENT=0,  /DEVICE
       XYOUTS, 240,  12,  '78', COLOR = 0, ALIGNMENT=0,  /DEVICE
ENDIF
IF Area EQ 1 THEN BEGIN
       XYOUTS, 310, 413, '(%)', COLOR=0, ALIGNMENT=0,  /DEVICE
       XYOUTS, 263,  41, '-64', COLOR=0, ALIGNMENT=0,  /DEVICE
       XYOUTS, 263, 315, '-60', COLOR=0, ALIGNMENT=0,  /DEVICE
       XYOUTS, 127,  12, '140', COLOR=0, ALIGNMENT=0,  /DEVICE
       XYOUTS,  55,  12, '138', COLOR=0, ALIGNMENT=0,  /DEVICE
ENDIF
```

; Box and colours for the legend.

```
Color_Box = BYTARR(20,20)
IF i LT 3 THEN k = I & IF i EQ 3 THEN k= 2 & IF i EQ 4 THEN k = 3
Color_Box = Color_Box+94+20*(k-1)
FOR j = 1,20 DO BEGIN
       Color_Box = Color_Box+1 & TV, Color_Box, 30, 5+20*j
ENDFOR
FOR j = 1,19 DO BEGIN
       Box_x=[30 , 30, 50, 50, 30]
       Box_y=[5+20*j , 45+20*j, 45+20*j, 5+20*j, 5+20*j]
       PLOTS, Box_x, Box_y,  COLOR=0, /DEVICE
ENDFOR
```

; Labels for the Legend.

```
XYOUTS, 5, 420, Legend(0),    COLOR=0, ALIGNMENT=0, /DEVICE
XYOUTS, 5, 340, Legend(1),    COLOR=0, ALIGNMENT=0, /DEVICE
XYOUTS, 5, 260, Legend(2),    COLOR=0, ALIGNMENT=0, /DEVICE
XYOUTS, 5, 180, Legend(3),    COLOR=0, ALIGNMENT=0, /DEVICE
XYOUTS, 5, 100, Legend(4),    COLOR=0, ALIGNMENT=0, /DEVICE
XYOUTS, 5, 20,  Legend(5),    COLOR=0, ALIGNMENT=0, /DEVICE
```

; Suspends the execution for a few seconds to display the output alone in the screen and then
; iconize the window. Program restarts when the mouse Right button is pressed.

```
CURSOR, X, Y
IF !MOUSE.BUTTON EQ 4 THEN BEGIN
       WSHOW, WNumber, /ICONIC
       GOTO, Next_output
ENDIF

Next_output:
```

; Saves the screen outputs into bitmap files and closes the program.

```
CD, 'outputs'
File_Name = File_ID + Fname + '.hst'
OPENW, 1, File_Name
Dim = SIZE(Y_Axis) & Dim = Dim(1)
PRINTF,1, '       X Axis     Y Axis'
FOR j= 1, Dim DO BEGIN
       PRINTF,1, X_Axis(j - 1), Y_Axis(j - 1)
ENDFOR
CLOSE, 1 &     LOADCT, 43
File_Name = File_ID + Fname + '.bmp'
WRITE_BMP, File_Name, TVRD()
CD, '/u/chungria/idl'
    ENDFOR
END
;
```